ORNL/TM-9947

ornl

OAK RIDGE NATIONAL LABORATORY

MARTIN MARIETTA

CERAMIC TECHNOLOGY FOR ADVANCED HEAT ENGINES PROJECT SEMIANNUAL PROGRESS REPORT FOR PERIOD APRIL - SEPTEMBER 1985

Prepared for
U.S. Department of Energy
Assistant Secretary for Conservation and Renewable Energy
Office of Transportation Systems
Advanced Materials Development Program

CERAMIC TECHNOLOGY PROJECT • DOE/ORNL •

OPERATED BY
MARTIN MARIETTA ENERGY SYSTEMS, INC.
FOR THE UNITED STATES
DEPARTMENT OF ENERGY

Printed in the United States of America. Available from
National Technical Information Service
U.S. Department of Commerce
5285 Port Royal Road, Springfield, Virginia 22161
NTIS price codes—Printed Copy: A12 Microfiche A01

ORNL/TM-9947

METALS AND CERAMICS DIVISION

CERAMIC TECHNOLOGY FOR ADVANCED HEAT ENGINES PROJECT SEMIANNUAL PROGRESS REPORT FOR PERIOD APRIL—SEPTEMBER 1985

D. R. Johnson
Project Manager

Date of Publication: May 1986

NOTICE: This document contains information of a preliminary nature. It is subject to revision or correction and therefore does not represent a final report.

Prepared for
U.S. Department of Energy
Assistant Secretary for Conservation and Renewable Energy
Office of Transportation Systems
Advanced Materials Development Program

Prepared by the
OAK RIDGE NATIONAL LABORATORY
Oak Ridge, Tennessee 37831
operated by
MARTIN MARIETTA ENERGY SYSTEMS, INC.
for the
U.S. DEPARTMENT OF ENERGY
under Contract No. DE-AC05-84OR21400

CONTENTS

CERAMIC TECHNOLOGY FOR ADVANCED HEAT ENGINES PROJECT SEMIANNUAL PROGRESS REPORT FOR PERIOD APRIL—SEPTEMBER 1985

SUMMARY

The Ceramic Technology For Advanced Heat Engines Project was developed by the Department of Energy's Office of Transportation Systems (OTS) in Conservation and Renewable Energy. This project, part of the OTS's Advanced Materials Development Program, was developed to meet the ceramic technology requirements of the OTS's automotive technology programs.

Significant accomplishments in fabricating ceramic components for the Department of Energy (DOE), National Aeronautics and Space Administration (NASA), and Department of Defense (DOD) advanced heat engine programs have provided evidence that the operation of ceramic parts in high-temperature engine environments is feasible. However, these programs have also demonstrated that additional research is needed in materials and processing development, design methodology, and data base and life prediction before industry will have a sufficient technology base from which to produce reliable cost-effective ceramic engine components commercially.

An assessment of needs was completed, and a five-year project plan was developed with extensive input from private industry. The objective of the project is to develop the industrial technology base required for reliable ceramics for application in advanced automotive heat engines. The project approach includes determining the mechanisms controlling reliability, improving processes for fabricating existing ceramics, developing new materials with increased reliability, and testing these materials in simulated engine environments to confirm reliability. Although this is a generic materials project, the focus is on structural ceramics for advanced gas turbine and diesel engines, ceramic bearings and attachments, and ceramic coatings for thermal barrier and wear applications in these engines. This advanced materials technology is being developed in parallel and close coordination with the ongoing DOE and industry proof-of-concept engine development programs. To facilitate the rapid transfer of this technology to U.S. industry, the major portion of the work is being done in the ceramic industry, with technological support from government laboratories, other industrial laboratories, and universities.

This project is managed by ORNL for the Office of Transportation Systems, Heat Engine Propulsion Division, and is closely coordinated with complementary ceramics tasks funded by other DOE offices, NASA, DOD, and industry. A joint DOE and NASA technical plan has been established, with DOE focus on automotive applications and NASA focus on aerospace applications. A common work breakdown structure (WBS) was developed to facilitate coordination. The work described in this report is organized according to the following WBS project elements:

0.0 Management and Coordination

1.0 Materials and Processing

  1.1 Monolithics
  1.2 Ceramic Composites
  1.3 Thermal and Wear Coatings
  1.4 Joining

2.0 Materials Design Methodology

  2.1 Modeling
  2.2 Contact Interfaces
  2.3 New Concepts

3.0 Data Base and Life Prediction

  3.1 Structural Qualification
  3.2 Time-Dependent Behavior
  3.3 Environmental Effects
  3.4 Fracture Mechanics
  3.5 NDE Development

4.0 Technology Transfer

This report includes contributions from all currently active project participants. The contributions are arranged according to the WBS outline.

0.0 PROJECT MANAGEMENT AND COORDINATION

D. R. Johnson
Oak Ridge National Laboratory

Objective/scope

This task includes the technical management of the project in accordance with the project plans and management plan approved by the Department of Energy (DOE) Oak Ridge Operations Office (ORO) and the Office of Transportation Systems. This task includes preparation of annual field task proposals, initiation and management of subcontracts and interagency agreements, and management of ORNL technical tasks. Monthly management reports and bimonthly reports are provided to DOE; highlights and semiannual technical reports are provided to DOE and program participants. In addition, the program is coordinated with interfacing programs sponsored by other DOE offices and federal agencies, including the National Aeronautics and Space Administration (NASA) and the Department of Defense (DOD). This coordination is accomplished by participation in bimonthly DOE and NASA joint management meetings, annual interagency heat engine ceramics coordination meetings, DOE contractor coordination meetings, and DOE Energy Materials Coordinating Committee (EMaCC) meetings, as well as special coordination meetings.

Technical progress

During this reporting period seven research contracts were signed. In addition, formal coordination and/or review meetings were held as listed in Table 1.

Table 1. Formal coordination or review meetings involving the Ceramic Technology Project

Agency	Dates of meetings
Department of Energy (sponsor)	4/24; 5/30; 6/18; 7/23; 8/22; 9/23
Department of Energy (other programs)	4/23 & 24
National Aeronautics and Space Administration	4/17; 4/18; 5/20 & 21; 6/27; 8/20; 9/18
Defense Advanced Research Projects Agency	5/21
Department of Commerce	7/10 & 11
Office of Technology Assessment	4/23 & 24
International groups	
DFVLR[a]	4/29; 7/22
Japanese study mission	5/1
IEA working group[b]	5/7

[a] Deutsche Forschungs- und Versuchsanstalt fuer Luft- und Raumfahrte. V.

[b] Working group for the International Energy Agency's Annex II — Cooperative Programme On Ceramics For Advanced Engines and Other Conservation Applications.

1.0 MATERIALS AND PROCESSING

INTRODUCTION

This portion of the project is identified as project element 1.0 within the work breakdown structure (WBS). It contains four subelements: (1) Monolithics, (2) Ceramic Composites, (3) Thermal and Wear Coatings, and (4) Joining. Ceramic research conducted within the Monolithics subelement currently includes work activities on green state ceramic fabrication, characterization, and densification and on structural, mechanical, and physical properties of these ceramics. Research conducted within the Ceramic Composites subelement currently includes silicon carbide and oxide-based composites, which, in addition to the work activities cited for Monolithics, include fiber synthesis and characterization. Research conducted in the Thermal and Wear Coatings subelement is currently limited to oxide-base coatings and involves coating synthesis, characterization, and determination of the mechanical and physical properties of the coatings. Research conducted in the Joining subelement currently includes studies of processes to produce strong stable joints between zirconia ceramics and iron-base alloys.

A major objective of the research in the Materials and Processing project element is to systematically advance the understanding of the relationships between ceramic raw materials such as powders and reactant gases, the processing variables involved in producing the ceramic materials, and the resultant microstructures and physical and mechanical properties of the ceramic materials. Success in meeting this objective will provide U.S. companies with new or improved ways for producing economical highly reliable ceramic components for advanced heat engines.

1.1 MONOLITHICS

1.1.1 Silicon Carbide

Synthesis of High-Purity Sinterable Silicon Carbide (SiC) Powders

J. M. Halstead and V. Venkateswaren [SOHIO Engineered Materials Company (Carborundum)] and B. L. Mehosky (SOHIO Research and Development)

Objective/Scope

The objective of this program is to develop a volume scaleable process to produce high purity, high surface area sinterable silicon carbide powder.

The program is organized in two phases. Phase I includes the following elements:

- Verify the technical feasibility of the gas phase synthesis route.
- Identify the best silicon feedstock on the basis of performance and cost.
- Optimize the production process at the bench scale.
- Fully characterize the powders produced and compare with commercially available alternatives.
- Develop a theoretical model to assist in understanding the synthesis process, optimization of operating conditions and scale-up.

Phase II, when authorized will scale the process to 5 - 10 times the bench scale quantities in order to perform confirmatory experiments, produce process flowsheets and to perform economic analysis.

Technical Highlights

Background - The Gas Phase Synthesis Route

Given the objective of producing a submicron silicon carbide powder purer and with more controllable properties than could be produced via the Acheson process, Sohio-Carborundum evaluated three candidate process routes:

1) Sol-Gel
2) Polymer Pyrolysis
3) Gas Phase Reactions

As gas phase route utilizing plasma heating was chosen as having the most proven technology, the highest product yield and good scaleability potential.

Further, Carborundum had previously sponsored proprietary research in gas phase synthesis and had demonstrated the feasibility of the approach.

---

[1] Research sponsored by the Advanced Materials Development Program, Office of Transportation Systems, U.S. Department of Energy under Contract DE-AC05-84OR21400 with Martin Marietta Energy Systems, Inc.

Workplan

A breakdown of major tasks and milestones is shown in Figure 1. Subtasks have been developed for Task 4 - Screening Experiments and will be developed for Task 5 - Extended Parametric Studies.

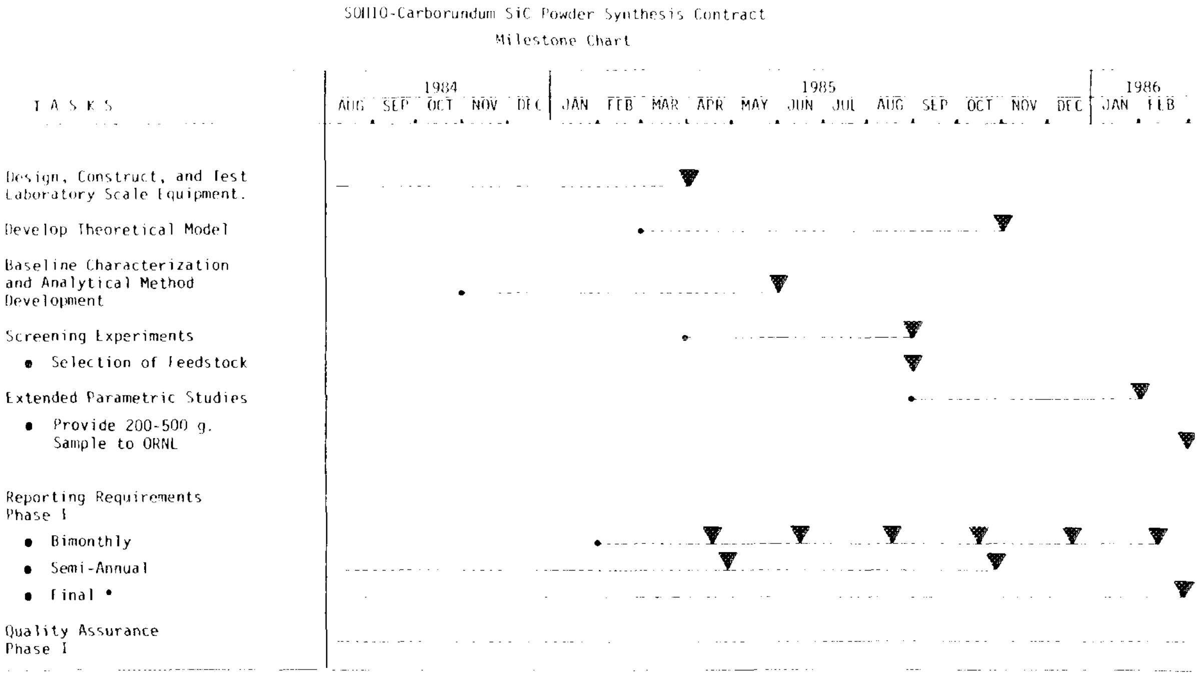

* Only required if decision is made not to go on to Phase II.

Revised 3/15/85

Figure 1. Milestone Chart

Task 1. Design, Construct and Test Laboratory Scale Equipment.

The Sohio Research and Development Center at Warrensville, Ohio was chosen as the site for the laboratory scale gas phase synthesis system due to the ready availability of applicable engineering and technical resources. The proximity to other related research which is being performed by Sohio on behalf of Sohio-Carborundum's structural ceramics effort was also a factor.

The design phase involved a complete review of the preliminary conceptual design and specifying appropriate subsystems in order to evaluate and control critical process parameters.

The conceptual design is shown in Figure 2.

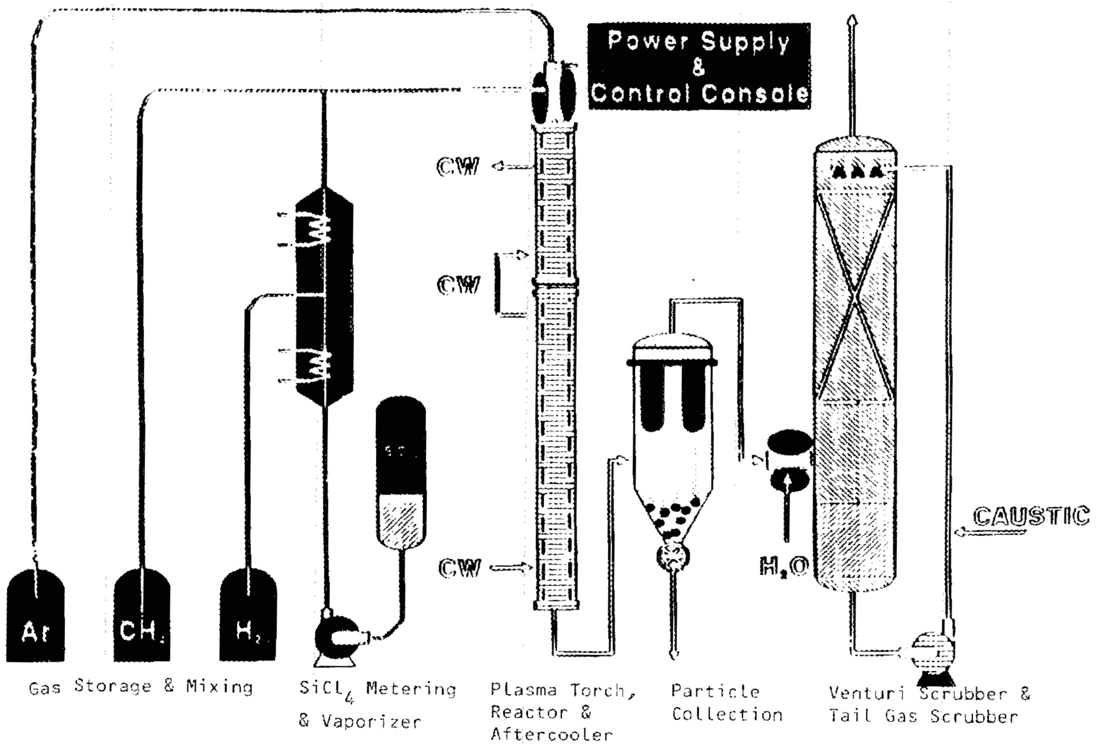

Figure 2. Conceptual Design and Simplified Process Flow Chart

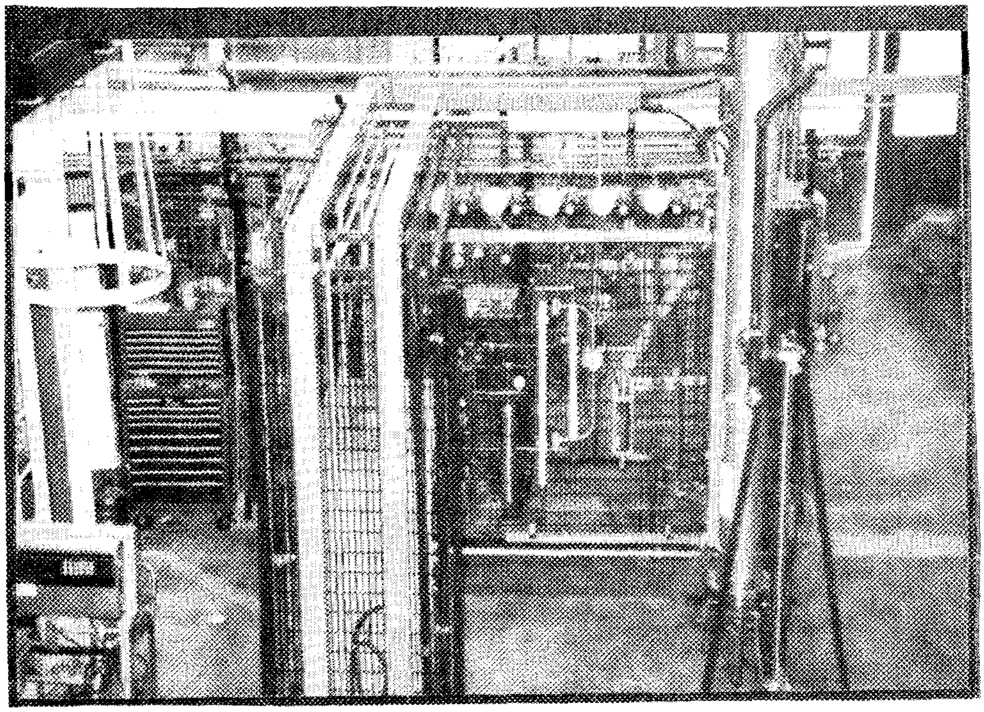

Figure 3. Photographic Overview of Laboratory Scale System

Plasma Torch Subsystem

The heart of the system is the plasma torch. This was obtained from Plasma Materials, Inc. with whom Sohio-Carborundum has previously worked. The torch system is rated at 50KW. This is significantly higher than required for this application, but the unit has excellent turn-down capability and will be sufficient for future scale-up. It is installed atop the reactor vessel which is constructed of copper and wrapped with copper tubing through which the cooling water flows. Thermocouples are installed along the entire length of the reactor.

The DC power supply has a 75KW effective rating. A simple thimble type collector with an isolation valve is affixed to the lower end of the reactor. Alternative powder collection techniques will be evaluated in preparation for Phase II scale-up.

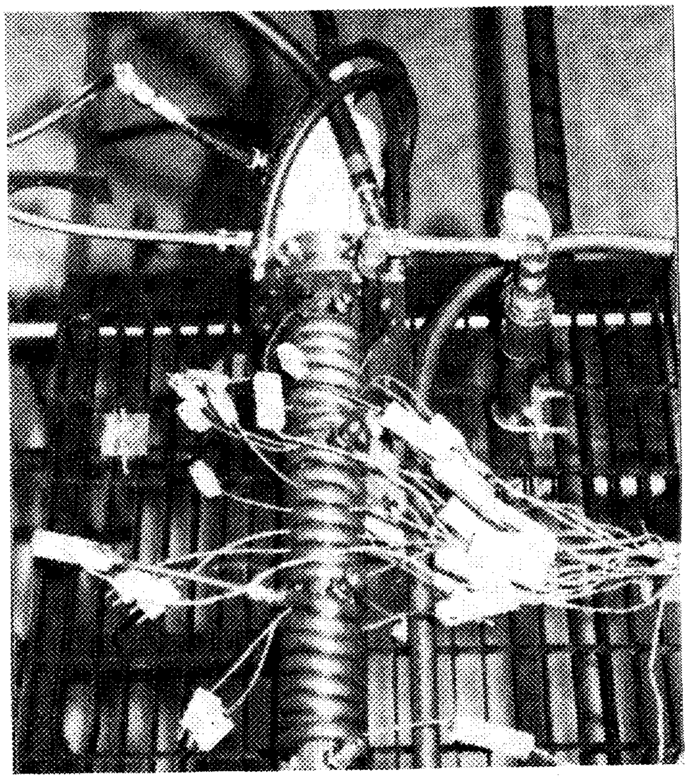

Figure 4. Plasma Torch Atop Water Cooled Reactor

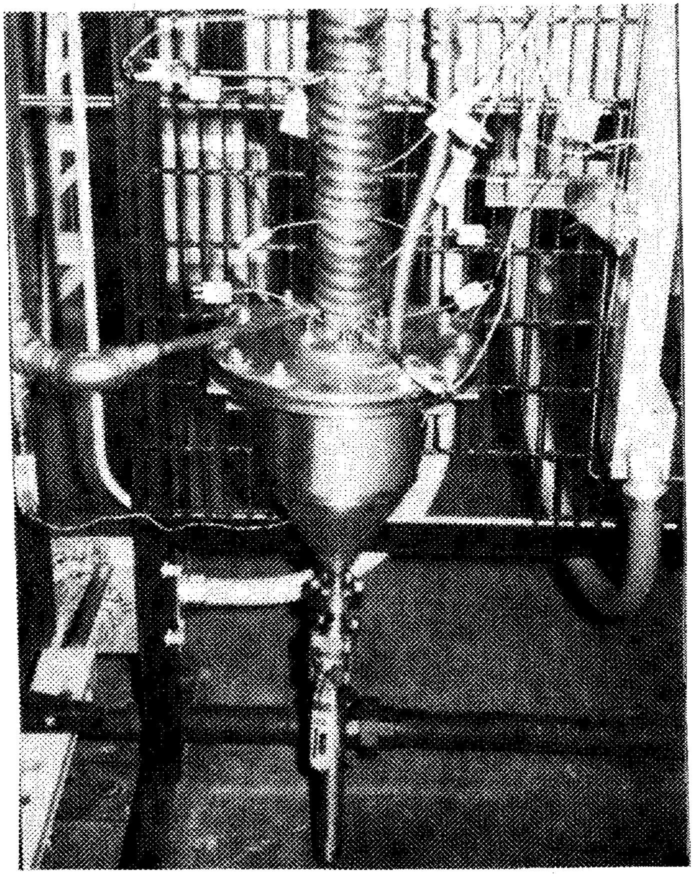

Figure 5. Exit End of Reactor with Simple Thimble Collector and Isolation Valve

Task 2. Development of a Theoretical Model

The development of a theoretical model is intended to correlate particle surface area with major operational parameters. An expansion of previous Carborundum sponsored work, this will develop a fundamental understanding of process reactions and assist in the extended parametric studies and scale-up tasks.

After consultation with the ORNL Technical Monitor, the modeling work was subcontracted to International Thermal Plasma Engineering, Inc. (Professor Boulous - University of Sherbrooke, Quebec, Canada, et al).

The model is being developed in stages:

1) Development of a model to describe the flow and temperature field in the reactor.
2) The calculation of thermodynamic equilibrium for the H_2-Ar-CH_4-$SiCl_4$ system and the study of the chemical kinetics of possible homogenous reactions occuring in the plasma process.
3) A literature review of nucleation and growth in an aerosol system which could be of relevance to this work.
4) Incorporation of all the above features in a comprehensive model.

The development of the model for calculating the velocity and temperature profile is complete. The standard k-ε model was used in describing the turbulent flow in conjunction with wall functions in the region close to solid boundaries. Preliminary calculations have been carried out with a pure Argon system and the model results seem to be consistent. The model will now be used for making calculations with the Ar/H_2 blend and for flows corresponding to what is presently used in the reactor.

Calculation of equilibrium composition for the H, Ar, C, Cl, Si system has been performed for temperatures ranging from 300°-6400°K. The method used consists of finding the values of N_i (the numerical density of each species) that satisfies the constraints of minimal Gibbs free energy while satisfying mass and electrical charge conservation. A total of 44 possible elements/compounds has been considered in making this calculation. The results of this study will be incorporated in the final comprehensive model for predicting conversion to silicon carbide.

Task 3. Baseline Characterization and Analytical Method Development

The objectives for this task include:

- .. Firmly establish the methodologies to be used for powder characterization.
- .. Define basic powder characteristics which may be utilized to assess property control and improvements as the program progresses.

Initially, two commercially produced SiC powders were to be characterized: H.C. Starck, Inc. (West Germany), A10 Grade; and Sohio-Carborundum submicron alpha SiC.

As both of the above powders are alpha phase, it was decided to characterize one beta phase powder in addition, Starck B-10 Grade.

The parameters characterized and the methodologies used include the following:

Characteristic	Methodology
..Pressureless sinterability	--Percentage of theoretical density achieved with and without sintering aids.
..Surface area	--B.E.T. surface analysis.
..Degree of agglomeration	--Tap density.
..Particle size distribution	--Horiba particle size analyzer.
..Bulk composition	--Wet chemistry
..Phase distribution	--X-ray diffraction.

The results of the baseline characterization of the three powders is as follows:

	Starck A10	Starck B10	Sohio-Carborundum
Pressureless Sinterability (percentage of theoretical density)			
- without sintering aids	63.6%	N/A	51.01%
- with sintering aids	96.2%	94.3%	99.88%
Surface Area	14.3m^2/g	15.35m^2/g	9.47m^2/g
Degree of Agglomeration			
- Tap density	0.847 g/cm^3	0.926 g/cm^3	0.962 g/cm^3

Particle Size Distribution

Size μm	Cumulative Percentage greater than the indicated particle size Starck A10	Starck B10	Sohio-Carborundum
>7	0	4.2	0
7-6	2.4	4.7	0.4
6-5	11.4	5.8	3.8
5-4	23.4	8.7	7.0
4-3	29.8	11.8	9.8
3-2	38.2	21.0	24.3
2.1.8	41.4	24.6	27.3
1.8-1.6	45.7	29.0	32.2
1.6-1.4	50.9	36.1	39.1
1.4-1.2	58.0	43.2	49.9
1.2-1.0	66.4	49.2	65.4
1.0-0.8	68.2	61.5	67.1
0.8-0.6	76.7	69.9	76.2
0.6-0.4	85.7	84.0	87.9
0.4-0.2	97.2	97.4	97.7
0.2-0	100.0	100.0	100.0
-Mean Particle Size (d_{50})	1.4μm	1.0μm	1.2μm

Bulk Composition	Starck A10	Starck B10	Sohio-Carborundum
Chemical Analysis (wt %)			
Total Carbon	30.3	30.49	29.95
Free Carbon (corrected for oxidation)	1.54	1.83	0.36
Total Oxygen	0.76	0.90	0.27
Free Silicon	0.29	0.40	0.09
Si + SiO$_2$	1.73	1.71	0.60
SiO$_2$ (calculated from O$_2$)	1.44	1.31	0.51
SiC (calculated)	96.10	95.70	98.80
Emission Spectroscopy (wt %)			
	Aluminum .01	Aluminum .07	Aluminum<.01
	Calcium<.01	Calcium<.01	Calcium<.01
	Iron 0.03	Iron .04	Iron<.01
	Magnesium<.01	Magnesium<.01	Magnesium<.01
	Titanium .01	Titanium<.01	Titanium<.01
		Vanadium<.01	Vanadium<.01
		Boron .02	

	Starck A10	Starck B10	Sohio/ Carborundum
Elements less than .005%	Boron		Boron
	Chromium	Chromium	Chromium
	Copper		Copper
	Manganese	Manganese	Manganese
	Nickel		Nickel
	Zirconium	Zirconium	Zirconium
	Cobalt		
	Molybdenum		Molybdenum
	Vanadium		
Phase Distribution			
Major	6H	3C	6H
Low Trace	15R/4H	6H	15R

Task 4. Screening Experiments

Task 4 was divided into subtasks for management and reporting purposes.

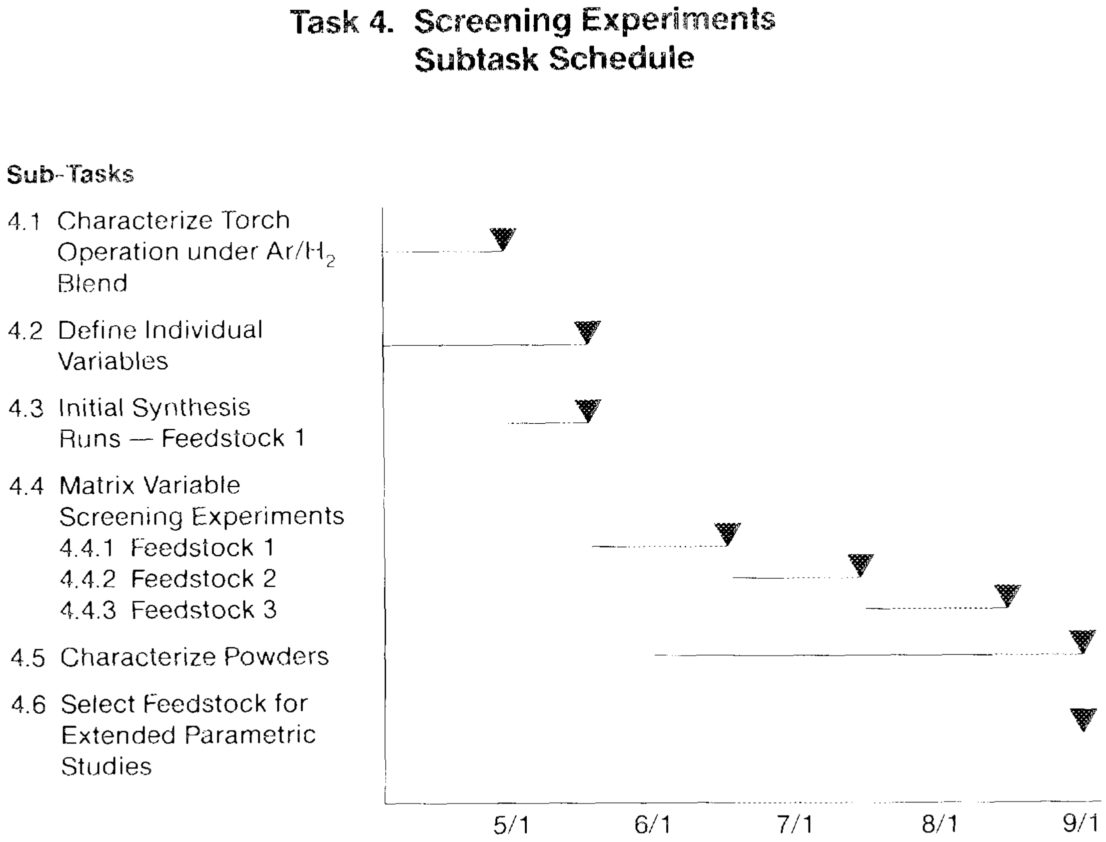

Figure 6. Subtask Schedule for Screening Experiments

The first subtask was to characterize the operating of the plasma torch using a Hydrogen/Argon blend. It should be noted that the original workscope included a short series of experiments to investigate the feasibility of using a hydrogen plasma in lieu of Argon. This could be advantageous as hydrogen is a reactant (to scavenge chlorine from the silicon source) and the argon (necessary only as a carrier of energy) could potentially be reduced or eliminated.

As both Sohio-Carborundum and the torch vendor, Plasma Materials, Inc. were confident that the torch would operate with a very rich Hydrogen to Argon blend, it was decided to accomplish this subtask first.

Concurrent with that subtask, careful consideration was given to the choice of the individual variables for the screening experiments. The candidate feedstocks were described in the statement of work, but the values (or range of values) for temperature, carbon/silicon ratio and reactant concentration had to be established.

A matrix of screening experiments depicted in Figure 7 was then developed. The candidate feedstocks are as follows:

Reactant 1: silicon tetrachloride ($SiCl_4$)
Reactant 2: dimethyl dichlorosilane [$(CH_3)_2SiCl_2$]
Reactant 3: methyl trichlorosilane (CH_3SiCl_3)

Proposed Test Matrix: Screening Experiments

Reactant	Temperature	Carbon/Silicon Ratio	Reactant Concentration
Reactant 1	Hi	Hi	Hi
			Lo
		Lo	Hi
			Lo
	Lo	Hi	Hi
			Lo
		Lo	Hi
			Lo
Reactant 2	Hi	Hi	Hi
			Lo
		Lo	Hi
			Lo
	Lo	Hi	Hi
			Lo
		Lo	Hi
			Lo
Reactant 3	Hi	Hi	Hi
			Lo
		Lo	Hi
			Lo
	Lo	Hi	Hi
			Lo
		Lo	Hi
			Lo

Figure 7. Screening Experiment Test Matrix

Once the plasma torch had been stabilized on a very rich H_2/Ar blend, silicon feedstock ($SiCl_4$) and methane were added to the system. Several short runs were made and powder was produced. Analysis later proved the powder to be beta silicon carbide.

Several debugging problems occurred which aborted many of the initial runs. Some of these problems included the silicon feed pump, the tail gas scrubber level transducer and a cooling water leak into the plasma torch. All items were satisfactorily resolved. The cooling water leak resulted in severe damage to the delrin housing, but prompt response by Sohio's plasma torch vendor (Plasma Materials, Inc.) resulted in very minimal downtime.

The torch and reactor system also experienced plugging problems which limited run times; some as short as 5 minutes. Minor anode configuration changes were made which has since allowed runs up to 3 hours in duration. Although this problem has not been completely solved, the present configuration is capable of running long enough to accomplish the tasks planned for Phase I. Runs of one hour duration will generate representative material in sufficient quantities for analysis.

At this point, the workplan called for the initiation of screening experiments; a matrix of 24 variations of temperature, carbon to silicon ratio and reactant concentration (defined as hydrogen to chlorine ratio). However, a priority was placed upon establishing the consistency and reproducibility of the process. The workplan was modified to first run four pre-screening experiments to establish a consistent baseline; then to prioritize the screening experiments (focusing primarily on feedstock one). Eight experiments (six of Feedstock 1 and two of Feedstock 2) will be run and the results analyzed. If there is any inconsistent data, those runs will be repeated.

A total of 24-28 screening experiment runs will be made in order to firmly identify the most promising feedstock for further evaluation in Task 5 Extended Parametric Studies.

The four pre-screening runs (two at 30 minutes and two at 60 minutes) were made with constant operating conditions and powder was collected from various points in the system. Each of these samples is being analyzed to check reproducibility and to obtain a rough material balance closure.

The screening experiments are now underway and should be concluded about November 15, 1985.

Analysis of Results

- Initial Synthesis Runs

Powder produced during the initial synthesis runs has been analyzed. Six samples, collected from either the reactor or the powder hopper at the base of the reactor, had SiC content ranging from 83.0% to 96.6% and surface areas from 11.3 to 28.4m^2/g.

As these were the very first runs of the reactor system with a silicon feedstock, the results are very encouraging. A typical photomicrograph appears below:

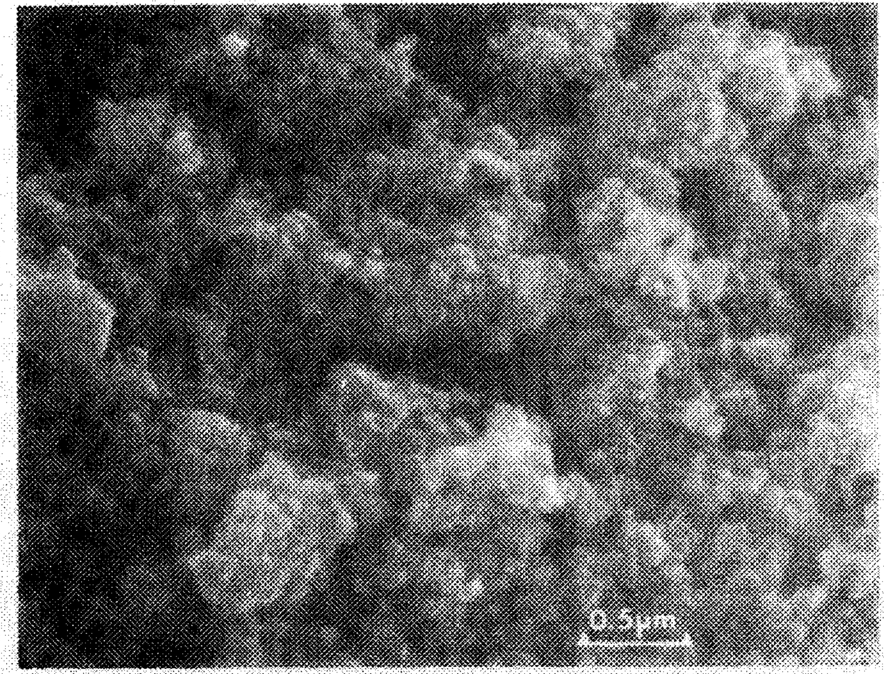

Figure 8. Photomicrograph of powder produced during one of the initial synthesis runs - 30,000x

Task 5. Extended Parametric Studies Status of Milestones

This task is intended to further evaluate the process parameters of the feedstock selected at the conclusion of the screening experiments. Among other parameters, gas flow rate will be varied in order to evaluate the effect of residence time and the best conditions for scaling up the selected process.

The structure of this task and the specific experiments will be developed at the conclusion of the screening experiments. It is anticipated that this task will get underway about December 1, 1985.

Status of Milestones

	Milestones	Status
Task 1.	Design, Construct and Test Laboratory Scale Equipment	- Complete
Task 2.	Develop Theoretical Model	- Initiated March 1; on schedule.
Task 3.	Baseline Characterization and Analytical Model Development	- Complete
Task 4.	Screening Experiments	- Initiated April 1; about two months behind schedule
	..Selection of Feedstock	- Scheduled for November 15
Task 5.	Extended Parametric Studies	- To be initiated December 1
	..Provide 200-500g Sample to ORNL	- Scheduled for - April 30, 1986
Task 6.	Reporting Requirements	- On schedule.
Task 7.	Quality Assurance	- Ongoing.

1.1.2 Silicon Nitride

Sintering of Silicon Nitride

G. E. Gazza (Army Materials Technology Laboratory)

Objective/Scope

The in-house program is concentrating on sintering compositions in the Si_3N_4 -$Y_2O_3SiO_2$ System using a two-step sintering method where the N_2 gas pressure is raised from 1-2 MPa during the densification process. During the sintering under high pressure nitrogen, the environment is extremely reducing and the oxygen content of the starting materials is significantly reduced by the formation of SiO. The use of cover powder over the samples reduces the oxygen loss. Milling time also influences "green" density and resultant sintered density by changing the particle size distribution of starting powders, reducing agglomeration and producing a more equiaxed particle morphology. Milling studies are being conducted with three different sources of starting Si_3N_4 powder.

Technical Highlights

A matrix of compositions in the Si_3N_4 - Si_2N_2O - $Y_2Si_2O_7$ and Si_3N_4 - Y_2/Si_2O_7 - $Y_5(SiO_4)_3N$ compatibility triangles have been densified by two-step, high gas pressure sintering. Temperatures in the range of 1900-2000°C are generally used. Nitrogen gas pressure in the first step is approximatly 1.5 MPa and is increased to either 5.5 MPa or 8.0 MPa in the second step. Higher sintered densities usually occur when 8.0 MPa pressure is used in the second step. Specimens are contained in a closed RBSN crucible when being sintered. Additionally, they are covered with Si_3N_4 powder containing appropriate additives and BN to restrict oxygen loss from the specimen via SiO. When the proper cover powder and sintering cycle is used, weight changes observed with specimens after densification are less than 1%. Of particular interest were specimens ranging in composition from Si_3N_4 - 3.5m/oY_2O_3(5.7w/o) - 11.9m/o SiO_2(5.4 w/o) to Si_3N_4 - 4.7m/o Y_2O_3(7.8w/o) - 9.5m/o SiO_2(4.2w/o).

These are compositions which approach the Si_3N_4 - $Y_2Si_2O_7$ join from the SiO_2 rich side. Also, for our sintering conditions, at least 10 volume percent of combined additive (Y_2O_3 + SiO_2), appears to be required to produce high sintered densities, i.e., >97%. X-ray diffraction analyses on these sintered specimens indicated that primarily two crystalline phases are present, β -Si_3N_4 and γ -$Y_2Si_2O_7$. As the compositons became more SiO_2 rich, some residual glassy phase remained in the specimen. Microstructural analysis by SEM revealed the presence of a duplex type microstructure with some elongated grains at least 15-20μ long in a finer grain matrix. This suggests the need for finer, uniform starting materials, developing a packing density with a fine, uniform pore distribution, lower sintering temperatures or the addition of grain growth inhibitors. Nevertheless, the room temperature MOR of specimens machined from the sintered bodies ranged between 585 MPa and 655 MPa. Preliminary oxidation studies with these specimens produced oxidation rate constants, kp, in the 10^{-12} range at 1200°C for 125 hours and 10^{-13} range at 1000° for 150 hours. Stress rupture data was obtained on a limited number of specimens with a compositional range as previously indicated. Specimens with compositions near the Si_3N_4 - $Y_2Si_2O_7$ join lasted 170 hours without failure under 300 MPa stress at 1200°C. Retained room temperature MOR on survivors was 480-550 MPa. More SiO_2 rich compositions lasted greater than 150 hours without failure under 300 MPa stress at 1000°C and 1100°C but failed in 1-2 hours at 1200°C.

Milestones:

Further sintering of specimens near the Si_3N_4 - $Y_2Si_2O_7$ join will continue with generation of MOR, oxidation and stress-rupture data. Crystallization treatments are also being studied to reduce residual glassy phase.

Other Si_3N_4 powders being studied as starting materials include UBE (SN-E-10), TSK (TS-7), and Siconide (P95).

A vibratory screening procedure is being used to produce powders with more uniformity.

Synthesis of High Purity Sinterable Si_3N_4 Powders

G. M. Crosbie (Ford Motor Company)

Objective/scope

The goal of this task is to achieve major improvements in the quantitative understanding of how to produce sinterable Si_3N_4 powders having highly controlled particle size, shape, surface area, impurity content and phase content. Through the availability of improved powders, new ceramic materials are expected to be developed to provide reliable and cost-effective structural ceramics for application in advanced heat engines.

Technical progress

This task was initiated February 1985. This is the first semiannual report for this task.

This process study for synthesis of alpha silicon nitride powder is directed towards a modification of the low temperature reaction of $SiCl_4$ with liquid NH_3. The modification is characterized 1) by absence of organics (a source of carbon contamination) and 2) by pressurization (for improved by-product extraction).

The pressurized apparatus for synthesis of silicon nitride has been designed and construction is underway.

In the first months of this task, the use of another liquid precursor for silicon, tetraethyl orthosilicate (TEOS), was investigated. Experimental results for this precursor are presented in the following paragraphs and Figure. Based on these results and discussions of the desirability of use of carbon-free reactants, technical emphasis was placed on the silicon tetrachloride-liquid ammonia process reported above.

Although equi-axed, alpha silicon nitride has been identified (by electron microprobe and x-ray diffraction) in powders formed from TEOS, a batch nitriding step is apparently required to convert the pyrolysis products. Assay of pyrolysis products from TEOS has shown that Si_3N_4 is not directly produced under a variety of conditions (Fig. 1). The pyrolysis product is primarily an intimate solid state mixture of amorphous silica and carbon black.

In view of interest in circumventing entrapped silica and carbon residuals (which are typical for carbothermal nitriding syntheses from powdered precursors), experimental emphasis was placed on tests of nitride-forming conditions in a single step pyrolysis. Actions included increased residence time and increased H_2/N_2 ratios in feed gases. These experiments typically yielded 0.1 to 0.2 wt% nitrogen (by Leco analysis) in the collected powders.

The highest value (1.03 wt%) for pyrolysis product nitrogen content (Fig. 1) was obtained with NH_3 as a carrier gas to sweep vaporizing TEOS fine droplets into a 1450^oC zone. Other constituents of solid products were 39.1% oxygen and 25.3% total carbon, by Leco analysis.

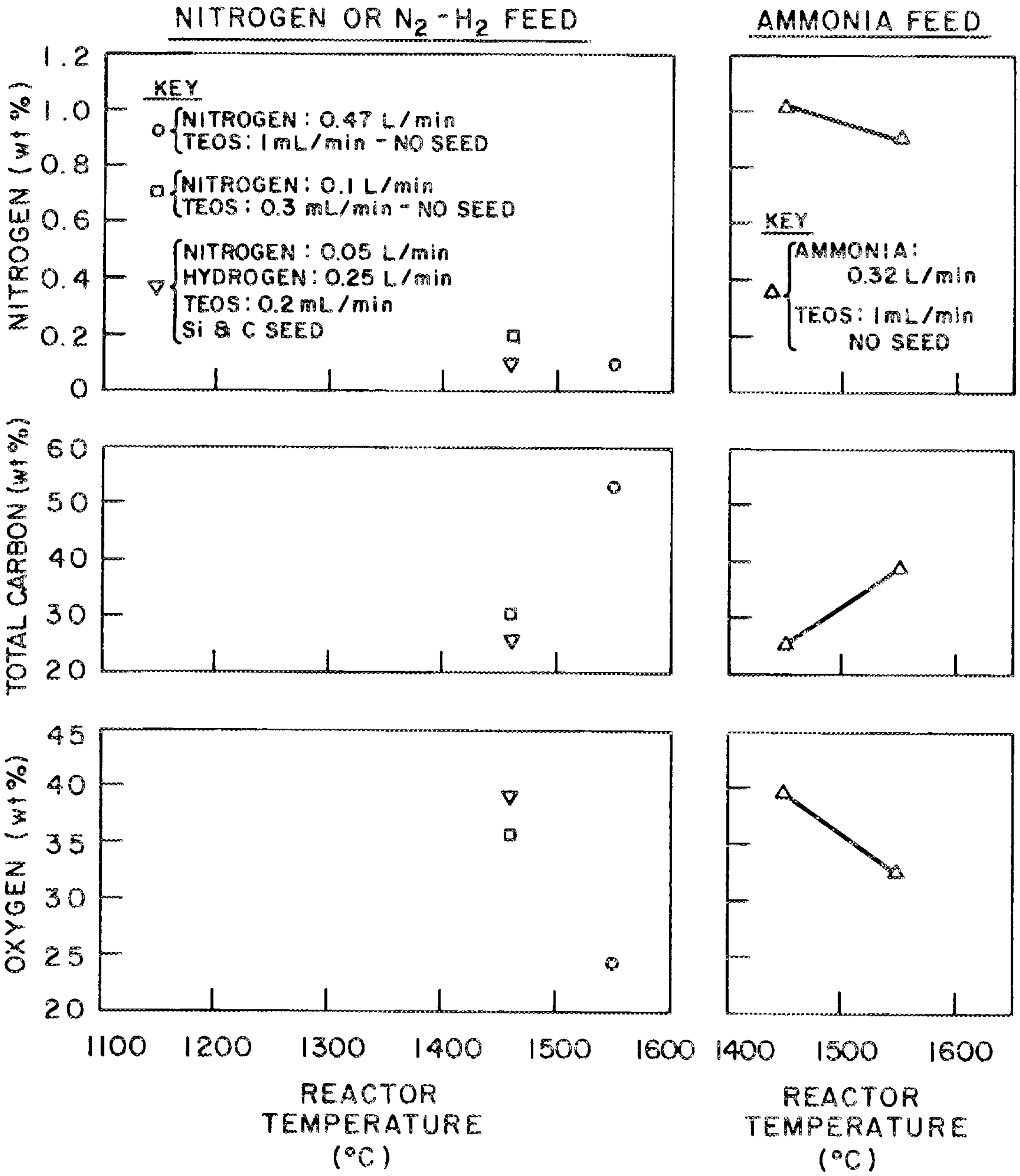

Fig. 1. Chemical analyses of powders formed by single step pyrolysis of tetraethyl orthosilicate.

Status of Milestones

There were no major milestones in this first contract period. Work is proceeding to meet the December 1985 milestone of construction and commissioning of the apparatus.

Publications

G. M. Crosbie, "Seeded Silicon Nitride Synthesis: A Progress Report," Paper No. 35-FII-85, presented at the Am. Ceram. Soc. Annual Meeting, Cincinnati, Ohio, May 8, 1985.

1.2 CERAMIC COMPOSITES

1.2.2 Silicon Nitride Matrix

Transformation Toughened Silicon Nitride

H. W. Carpenter (Rocketdyne Division, Rockwell International) and
F. F. Lange (Rockwell Science Center)

Objective/Scope

The objective of this program is to develop high toughness, high strength refractory ceramic matrix composites that can be made at low cost and to near net shape for heat engine applications. The composite system selected for development is based on a silicon nitride matrix toughened by dispersions of ZrO_2, HfO_2, or $(Hf,Zr)O_2$ modified with suitable additions of other refractory ceramics to control the physical behavior. The desired microstructure and optimum mechanical properties will be developed by expeditious laboratory methods including colloidal suspension, press forming, and sintering. Once the best composition and microstructure have been demonstrated, parameters will be optimized for producing samples by the injection molding process.

Technical Progress

Background - The intent of this initial study is to retain a transformable form of tetragonal ZrO_2 in the Si_3N_4 matrix that will significantly toughen the composite material by a martensitic transformation mechanism without decreasing strength. The problem experienced in the past is that Si_3N_4 and ZrO_2 react to form Zr-oxynitride, an undesirable compound as it depletes the ZrO_2 content without increasing toughness and it oxidizes at intermediate temperatures to monoclinic ZrO_2. The monoclinic ZrO_2, in turn, results in serious surface cracking. F. F. Lange (Ref. 1) has shown evidence that the formation of Zr-oxynitride can be prevented or retarded and that a transformable tetragonal ZrO_2 phase can be obtained by using ZrO_2 alloyed with Y_2O_3.

Four Y_2O_3-ZrO_2 alloys have been investigated, 13.7%, 12.0%, 8.0% and 4.5% (by wt.) Y_2O_3. The basic composite composition selected for evaluation was 30% by vol. ZrO_2 alloy plus 70% Si_3N_4. Two or 4% (by wt.) Al_2O_3 was also added as a sintering aid. Submicron powders were obtained by multiple sedimentation processes and they were mixed with ultrasonic energy while still suspended in water. Disc-shaped samples (3.8 cm dia.) were formed by pressure filtration, and the dried green density of these samples was 40% of theoretical. Severe cracking was experienced early in the program but this problem was eliminated by adding 2% (based on dry wt.) PVA to the slurry. Sintering was initially conducted in air at 1700C, but sintering in N_2 is now preferred because higher sintering temperatures can be easily obtained and because the $MoSi_2$ heating elements used for sintering in air often failed.

Results - Initial results (Table 1) of this program show that 70% Si_3N_4-30% ZrO_2 composites (1) can be sintered to near theoretical density using a small amount of sintering aid, (2) can be made to exhibit a fine, homogeneous microstructure (grain size is about 2 microns), and (3) exhibit a relatively high fracture toughness, 7.5 MPa $m^{1/2}$. Although these results are highly encouraging, the Y_2O_3 alloying content has not yet been optimized to obtain a transformable tetragonal phase of ZrO_2 in the Si_3N_4 matrix. The first compositions studied were 70% Si_3N_4 plus 30% ZrO_2 alloyed with 13.7% and 12% Y_2O_3. Although the ZrO_2 alloy was fully stabilized before sintering an appreciable amount of Y_2O_3 diffuses into the glassy grain boundaries during sintering. The ZrO_2 particles in the Si_3N_4 matrix retained the cubic structure after sintering in these samples and subsequent heat treatments, of 13.7% Y_2O_3 samples only, to 2200C did not initiate the formation of the tetragonal phase. Compositions containing 8.0% and 4.5% Y_2O_3 were evaluated next. These samples retained the tetragonal phase but examination of the microstructure of sintered samples showed poor mixing and the presence of ZrO_2 agglomerates (as large as 40 microns). Thus, the results of the 4.5% and 8.0% Y_2O_3 alloys reported in Table 1 are questionable and these experiments will be repeated. There may also be a compositional error in the 8.0% Y_2O_3 composite. This composition sintered to higher densities than any other composition, with either more or less Y_2O_3, and it sintered to densities higher than the calculated theoretical density. Chemical analyses are being performed to determine whether the composite contains the correct amount of ZrO_2 and Y_2O_3.

A parametric study showed that the ZrO_2 agglomerates and the poor mixing was due to the use of a small ultrasonic mixing chamber. Specimens without agglomerates and exhibiting good dispersion of ZrO_2 and Si_3N_4 particles were mixed manually with of an ultrasonic horn. Neither the use of PVA or the PVA burn out operation (800C, 1h) had any effect on the microstructure or on the high sintered densities.

According to theory, a divalent cation alloying agent in ZrO_2, such as MgO or CaO, may be more conducive to the formation of a transformable tetragonal phase than a trivalent cation, such as Y_2O_3. Compositions of 70% (by vol.) Si_3N_4 plus 30% ZrO_2 alloyed with MgO will be evaluated along with the Y_2O_3-ZrO_2 alloys during the next reporting period.

Status of Milestones

The first milestone was met on schedule and the next two, due 31 December 1985 and 30 June 1986, are on schedule.

References

1. F.F.Lange, L. K. L. Falk, and B.I. Davis, "Structural Ceramics Composites Based on Si_3N_4-ZrO_2(+Y_2O_3) Compositions", unpublished, October 1985.

TABLE 1
SUMMARY OF RESULTS

SLIP NO	ZrO_2 CONTENT (Vol. %)	Y_2O_3 CONTENT* (WT. %)	Al_2O_3 SINTER AID (WT %)	SINTERING TEMP (C) AND ATM, 1 HOUR	AVERAGE BULK DENSITY (g/cc)	% OF CALC'D THEO. DENSITY**	ZrO_2 PHASE	FRACTURE TOUGHNESS (MPa $m^{1/2}$)
S9	30	4.5	2	1800, N	3.69 (3)	91.3	ND	ND
S10	30	4.5	4	1800, N	4.00 (6)	99.0	Tetra	7.1 (1)
S14	30	8.0	2	1800, N	4.19 (6)	(103.7)	Tetra	6.3*** (1)
S15	30	8.0	4	1800, N	4.16 (5)	(103.0)	Tetra	
S16	30	8.0	4	1800, N	4.23 (8)	(104.7)	Tetra	6.3*** (1)
S5	30	13.7	0	1800, N	2.46 (1)	60.9	Cubic	ND
S6	30	13.7	2	1800, N	3.82 (1)	95.6	Cubic	ND
S7	30	13.7	4	1800, N	3.92 (3)	97.0	Cubic	7.5 (4)
S10	30	4.5	4	1750, N	3.90 (2)	96.5	ND	ND
S14	30	8.0	2	1750, N	4.04 (2)	(100.0)	Tetra	ND
S15	30	8.0	4	1750, N	4.17 (2)	(103.2)	ND	6.0 (1)
S16	30	8.0	4	1750, N	4.28 (1)	(105.9)	Tetra	ND
S6	30	13.7	2	1700, N	3.47 (1)	85.9	Cubic	ND
S7	30	13.7	4	1700, N	3.78 (1)	95.6	Cubic	7.5 (4)
S9	30	4.5	2	1700, Air	3.59 (5)	88.9	ND	ND
S10	30	4.5	4	1700, Air	3.93 (3)	97.3	Mono + Tetra	ND
BD	30	12.0	4	1700, Air	3.91 (2)	96.9	Cubic	
S5	30	13.7	0	1700, Air	3.07 (1)	76.0	ND	ND
S6	30	13.7	2	1700, Air	3.87 (2)	95.8	Cubic	6.4 (1)
S7	30	13.7	4	1700, Air	3.88 (2)	96.0	Cubic	5.9 (1)
S1	18	13.7	0	1700, Air	2.53 (1)	68.4	Cubic	ND
S2	18	13.7	2	1700, Air	3.18 (1)	85.9	Cubic	ND
S3	18	13.7	4	1700, Air	3.45 (1)	93.2	Cubic	7.2 (1)
S1	18	13.7	0	1700, Air (3h)	2.63 (1)	71.1	Cubic	ND
S2	18	13.7	2	1700, Air (3h)	3.43 (1)	92.7	Cubic	ND
S3	18	13.7	4	1700, Air (3h)	3.53 (1)	95.4	Cubic	6.9 (1)
S3	18	13.7	4	1750, N_2	3.32 (1)	89.1	Cubic	ND
S2	18	13.7	2	1800, N_2	3.15 (1)	85.1	Cubic	ND
S3	18	13.7	4	1800, N_2	3.54 (1)	95.7	Cubic	ND

* = All Compositions are 30% (by vol.) partially stabilized ZrO_2 + 70% Si_3N_4. The Y_2O_3 content is the amount of stabilizing agent in the ZrO_2.

** = Based on 4.04 g/cc for 30% ZrO_2 and 3.70 g/cc for 18% ZrO_2.

() = Number of samples

ND = Not determined

*** = Poor sample for diamond indention method because the surfaces were not parallel. However, the value is probably representative.

Silicon Nitride-Metal Carbide Composites

S. T. Buljan (GTE Laboratories Inc.)

Objective/scope

The objective of this program is to develop silicon nitride-based composites of improved toughness, utilizing SiC and TiC as particulate or whisker dispersoids, and to develop and demonstrate a process for near net shape part fabrication. Near net shape process development will explore forming by injection molding and consolidation by hot isostatic pressing or conventional sintering.

Technical progress

To date, most of the work has focussed on characterization of the raw materials used for this study and development of processing routes for incorporation of the whisker dispersoid into the Si_3N_4 matrix material. While Tateho SiC whiskers were not proposed for this study, they have been included and are considered a second source should the availability of the ARCO material become more limited. This material will also be used for process development and comparison with the ARCO whiskers.

Raw Materials Characterization

Previous work[1,2] has shown the importance of maintaining low impurity levels for control of interfacial reactions between the matrix material and dispersoid in Si_3N_4-TiC composites. The dispersoid material was identified as a major source of impurities.

The silicon nitride powder* used for current studies has an oxygen content of 1.5 wt. % with less than 700 ppm of other impurities. The powder consists of 94.1 wt. % α-Si_3N_4, 5.8 wt. % β-Si_3N_4 and 0.1 wt. % Si. The surface area of this powder** was determined to be 4.0 m^2/gm. Impurity levels, oxygen and carbon contents for the SiC and TiC dispersoid materials are given in Table 1. To determine if the impurities were surface contaminants or contained in the crystal structure, Secondary Ion Mass Spectrometry (SIMS) analysis was used. Surface layers of ARCO SiC whiskers were found to contain major concentrations of F, Al, and Mg, while the Tateho whiskers contain Mg and Al. The major impurities observed on the Cerac SiC particulate surfaces were F, Al, and Mg, while only Al was detected on the Lonza SiC particle surfaces. Reduction of some of the surface impurities, including oxygen, may be accomplished by acid leaching of the materials as observed by Tiegs, Becher and Wei at ORNL for ARCO whiskers. Based on the measured total carbon content,*** all potential dispersoids are between 95% and 100% of the stoichiometric compositions.

---

*GTE SN502

**Determined by BET

***Leco Technique

Table 1. Impurity levels detected in SiC and TiC raw materials

	Impurities[a] (PPM)												O (Wt %)	C Total (Wt %)
	Al	B	Ca	Cr	Fe	Mg	Mn	Na	Ni	Ti	V	Zr		
SiC Silar SC-9[b] Whiskers	800	-	1000	-	500	2000-3000	1000-2000	20	-	-	-	-	1.78	28.9
SiC SCW-1[c] Whiskers	2000	-	1900	-	200	800	400	-	-	-	-	-	1.70	-
SiC UF-15[d] Particulate	900	20	-	-	200	20	10	10	-	100	-	-	0.84	29.6
SiC L-3636[e] Particulate	2000-3000	10	-	-	2000-3000	100	80	20	600	900	1000	600	0.31	28.7
TiC[f] Whiskers	-	-	-	100-1000	100-1000	-	-	-	50-500	Major	-	-	-	19.7
TiC[g] Particulate	100	-	-	-	100	10	20	-	100	Major	-	-	0.58	19.3

[a] Measured by optical emission spectrography and inductively coupled plasma spectroscopy.

[b] ARCO Chemical Co., Greer, SC

[c] Tateho Chemical Ind. Co. Ltd., Hyogo-pre, Japan

[d] Lonza AG, CH-4002, Basel, Switzerland

[e] Cerac, Milwaukee, WI

[f] GTE Laboratories, Inc., Waltham, MA

[g] Hermann C. Starck, Inc. GmbH, Berlin

The average aspect ratio (l/d) of the ARCO SiC whiskers was calculated to be 33 with an average length of 17.5 μm and an average diameter of 0.53 μm. The aspect ratio of the GTE Labs' TiC whiskers was determined to be 53 with an average length of 275 μm and average diameter of 5.1 μm. Since a portion of these whiskers has extreme lengths (up to 1000 μm), development of a method to shorten these whiskers and separate them into narrower size fractions will be considered.

Crystal structure characterization of the TiC whiskers in the STEM (Figure 1) determined that the faceted whiskers were single crystals elongated in <110>, sometimes with polycrystalline terminal globes. To reduce the impurity level of the whiskers, leaching in a hot 1:1 HCl:water solution was implemented. Microprobe analysis of the whiskers after leaching indicated removal of iron and nickel with only a slight reduction in the chromium content. A second leaching of the same whiskers showed essentially no further removal of impurities. Examination of other leaching solutions to further reduce the impurity levels of the whiskers will be continued.

Powder Processing

Initial powder preparation was accomplished by simple dry mixing of pre-processed Si_3N_4+6 w/o Y_2O_3+1.5 w/o Al_2O_3 with the as-received SiC whiskers (ARCO and Tateho). Microstructural observation of polished sections from hot pressed samples showed poor dispersion of the whiskers. To obtain better whisker dispersion, a processing route using wet dispersion of the whiskers and mixing with the powders was developed. A flow chart for the wet processing procedure is given in Figure 2. The combined sonification and homogenization of the whiskers disperses greater than 98% of the whisker agglomerates as observed in the hot pressed composite (Figure 3).

Densification

Initial attempts to densify the Si_3N_4-SiC whisker composite materials used material processed by dry mixing the as-received whiskers with a previously prepared Si_3N_4-Y_2O_3-Al_2O_3 composition. Prepared powder mixtures were hot pressed at 1725°C and 34.5 MPa in an inert atmosphere. Table 2 shows the results for some of the hot pressing runs carried out with the two whisker materials and two processing techniques. Initially densification of the dry processed material using the ARCO whiskers showed that the poor whisker dispersion required increased time for densification and yielded a microstructure which contains voids associated with whisker agglomerates. For the Tateho whiskers processed in the same manner, a faster densification rate was achieved for both the 10 and 20 volume percent whisker loadings. The observed phases after hot pressing were β-Si_3N_4 and SiC. The material containing better whisker dispersion prepared by the wet processing route densified more rapidly than the dry processed material. These materials after hot pressing contained β-Si_3N_4, SiC and an additional phase Si_2ON_2 not previously observed in

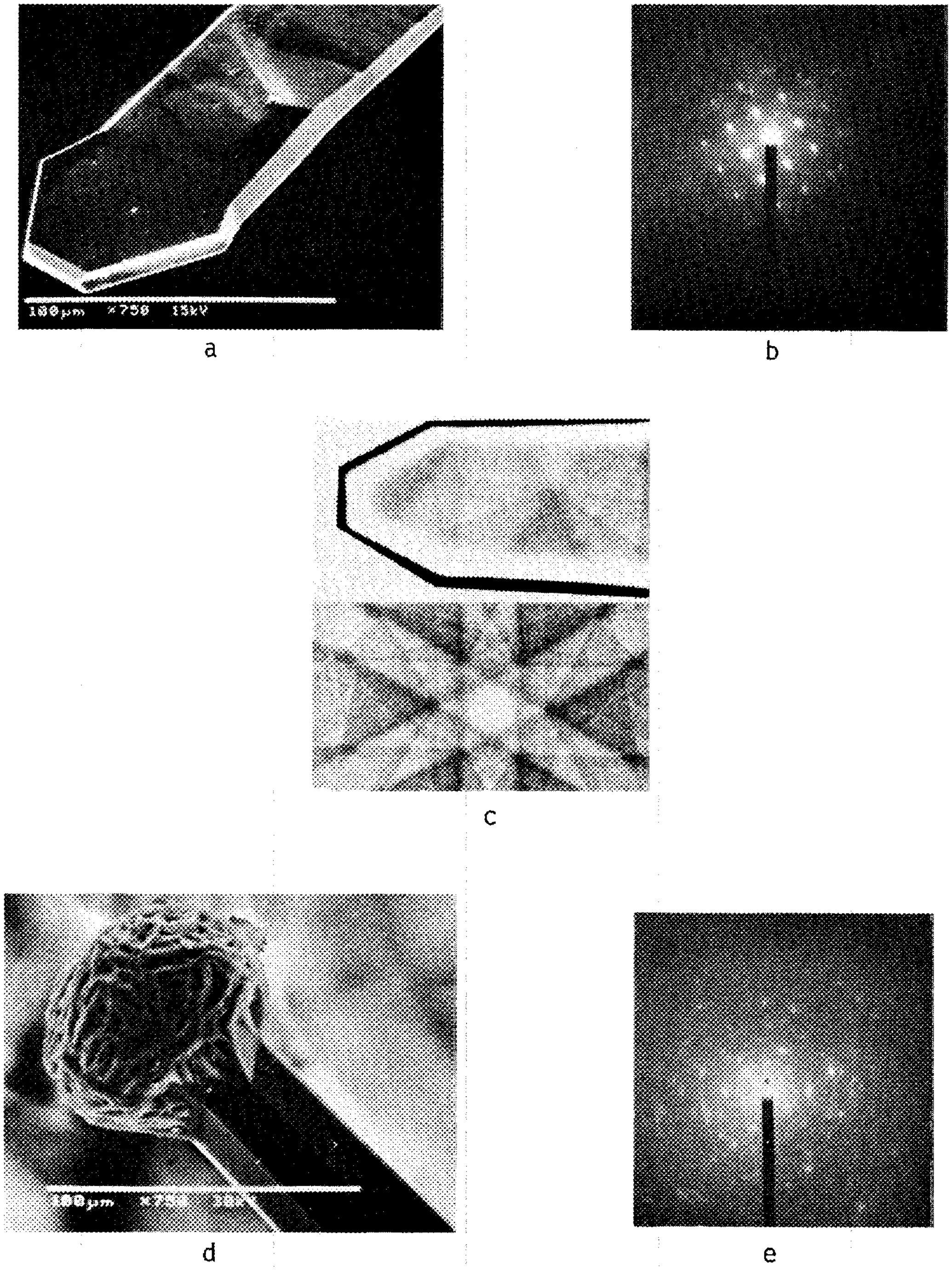

Fig. 1. Characterization of TiC whiskers: a) SEM photomicrograph of TiC whiskers with, b) single crystal electron diffraction pattern, and c) backscatter electron channeling pattern; d) illustrates polycrystalline globe sometimes observed at whisker tip and e) the associated diffraction pattern.

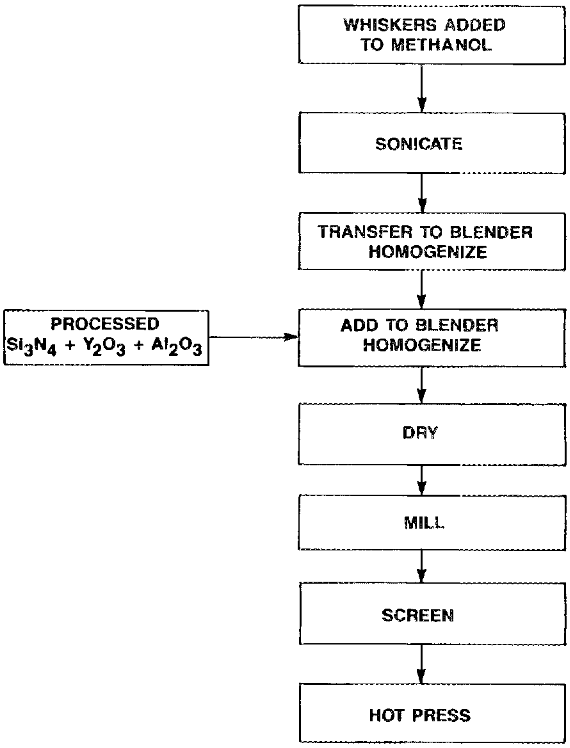

Fig. 2. Flow chart for wet processing of silicon nitride-silicon carbide whisker composites.

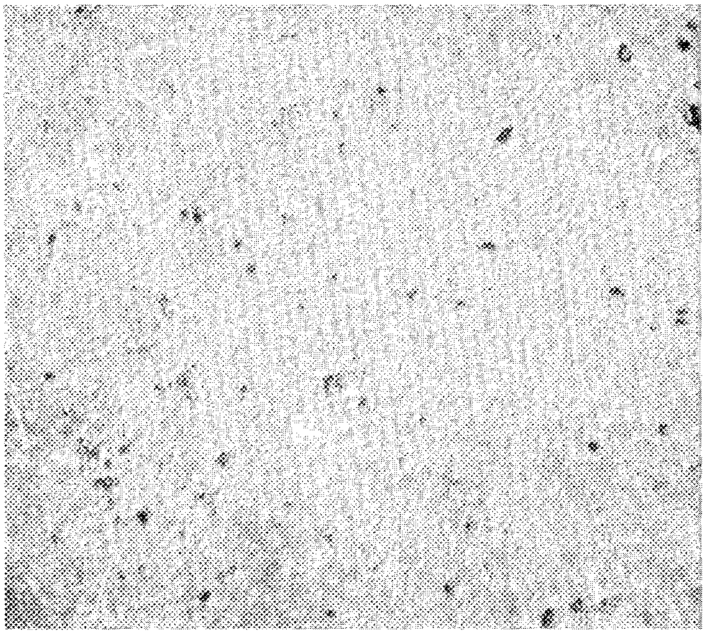

Fig. 3. Dispersion of silicon carbide whiskers in the silicon nitride matrix after hot pressing.

Table 2. Hot pressing results of SiC-whisker reinforced silicon nitride composites
(pressing conditions: 34.5 MPa at 1725°C)

Type	Whisker Content (Vol %)	Processing	Densification Time (min)	Density		Observed Phases
				(gm/cm^3)	(% Th)	XRD
ARCO	10	Dry	240	3.22	98.6	β-Si_3N_4, SiC
	20	Dry	90	2.86	88.0	↓
	20	Dry	310	3.17	96.4	
	20	Dry	480	3.20	98.3	
	20	Wet	200	3.21	98.8	β-Si_3N_4,SiC, Si_2ON_2
	20	Wet	200	3.21	98.8	↓
	20	Wet	140	3.20	98.3	
Tateho	10	Dry	130	3.21	98.6	β-Si_3N_4, SiC
	20	Dry	240	3.20	98.3	↓
	20	Wet	100	3.13	96.0	β-Si_3N_4, SiC, Si_2ON_2
	20	Wet	160	3.20	98.3	↓
	20	Wet	160	3.21	98.8	
	20	Wet	180	3.21	98.8	

the dry processed materials. The higher density materials have been fabricated into MOR bars for determination of mechanical properties.

A series of composites containing 10 v/o, 20 v/o and 30 v/o of fine (2 μm) particulate TiC in Si_3N_4 (6 w/o Y_2O_3 + 2 w/o Al_2O_3) matrix have been prepared and evaluated for their room temperature toughness using the indentation technique. Obtained K_{IC} values have been found to be statistically invariant with increased TiC content, and equivalent to that of matrix material. The absence of toughening may be attributed to antagonistic effects produced by the chemical interaction of the matrix and dispersoid as well as the textural complexity of the matrix phase, which may require considerably coarser dispersoids to obtain more effective crack-particle interaction. Preparation of initial specimens of the composites is expected to be completed by November, 1985, at which time work will focus on mechanical property determination and further microstructural tailoring.

References

1. G. Zilberstein and S.T. Buljan, "Characterization of Matrix-Dispersoid Reactions in Si_3N_4-TiC Composites," presented at Second Conference on Advances in Materials Characterization, Alfred Univ., Alfred, NY (1984).

2. S.T. Buljan and G. Zilberstein, "Effect of Impurities on Microstructure and Mechanical Properties of Si_3N_4-TiC Composites," presented at 21st University Conference on Ceramic Science, Penn. State Univ., University Park, PA (1985).

Status of milestones

No activity.

Publications

None.

SiC-Whisker-Toughened Silicon Nitride

K. Haynes, M. Martin and H. Yeh (AiResearch Casting Company)

Objective/Scope

The objective of this twenty-four month program is to develop the technology base for fabricating a ceramic composite consisting of silicon carbide whiskers dispersed in a dense silicon nitride matrix. This is to be accomplished by slip casting as the green shape forming method, and sintering or sinter/HIP as the densification method.

The recommended starting matrix composition is Si_3N_4 + 6% Y_2O_3 + 2% Al_2O_3 and four types of SiC whiskers are to be evaluated. Feasibility, as gauged by doubling the fracture toughness compared to the matrix Si_3N_4 containing no whiskers, will be demonstrated in Task 1. Once the feasibility has been demonstrated, systematic optimization studies will be conducted in Task 2 to develop optimum process parameters, microstructure, and mechanical properties. A full characterization of the optimized material will be carried out in Task 3.

Technical Highlights

Materials and Procedures

In Iteration 1, 10 volume percent loading of ARCO SC-9 SiC whiskers was used to determine suitable methods of incorporating the SiC whiskers into the Si_3N_4 matrix material as well as define HIP parameters. Uniform whisker dispersion was accomplished by milling followed with slip aging.

Iteration 2 was carried out using whisker incorporation and HIP parameters developed in Iteration 1. Three SiC whiskers were incorporated at 20 volume percent loading. The SiC whiskers used were ARCO SC-9, ARCO SC-9 coated by Naval Research Center, and Tateho SCW-1. Difficulty was experienced in preparing slips in this iteration due to the unexpected variation in GTE SN-502 Si_3N_4 powder which was used as the baseline as well as the matrix material. Solid contents had to be reduced and stronger defloculants used. In addition to this problem, the coated ARCO SC-9 (NRC) caused gelling problems not encountered with the standard ARCO SC-9. The solid content of this slip had to be reduced further. The slips were then cast into billets. A cracking problem developed which was attributed to the GTE powder variation. The billets in this case were 4" X 6" x ½" plates.

A new lot of GTE SN 502 Si_3N_4 powder was subsequently received which had improved properties. Iteration 2 samples were remade (identified as Iteration 2A) using this new powder, and crack free castings were obtained. Sample preparations for all other iterations continued with this new GTE powder.

The casting billet geometry, starting with Iteration 2A, was changed from the original plates (approximately 6" X 4" X ½") to cylinders (approximately 2" dia X 4" long). A cylindrical billet fits into a cylindrical quartz capsule with minimum gaps between the billet and the capsule. This was in an attempt to minimize capsule failure during HIP'ing. The cylindrical billets required longer casting time (7 days) versus the rectangular plates (2 days) because of the reduced casting surface.

An alumina free composition was investigated in Iteration 3. This composition was to minimize potential liquid phase reaction with SiC whiskers during densification. Four SiC whiskers have been incorporated, these being ARCO SC-9, ARCO SC-9 coated, Tateho SCW-1, and Tokai "Tokamax". Gelling problems with the coated ARCO whiskers were again encountered in this iteration. Even after solid content reduction, a usuable slip could not be prepared for casting. Castings were prepared from the three remaining slips.

In general, the Si_3N_4 slips containing SiC whiskers had a tendancy to gell, especially slips containing coated ARCO SC-9 SiC whiskers. Due to the problems associated with the coated ARCO SiC whiskers, further evaluation in Task 1 involving the coated ARCO SiC was discontinued. Although to a lesser degree, slips containing Tateho SCW #1 SiC whiskers and Tokai Carbon "Tokamax" SiC whiskers also showed gelling. This resulted in defective castings occasionally. The Si_3N_4 baseline material slips, and the Si_3N_4/SiC composite slips containing ARCO SC-9 SiC whiskers yielded good castings more consistently.

It was found that Tateho SCW #1 SiC whiskers exhibited the highest tendency to absorb moisture, ARCO SCW #1 SiC whisker second, and GTE Si_3N_4 the least. This was reflected in the weight loss values upon heating as shown in Table 1. This finding and the gelling phenomenon observed in slip containing Tateho SCW #1 versus SC-9 suggests that the Tateho SCW #1 SiC whiskers have undesirable whisker surface characteristics which resulted in difficulty of sample fabrication. Tokai Carbon SiC whiskers were not analysed due to exhausting the supply of these SiC whiskers. However, slip behavior using Tokai SiC is similar to Tateho SCW #1 SiC whisker behavior.

Specimens were prepared in Iteration 4 using ARCO SC-9 and Tateho SiC whiskers as well as baseline Si_3N_4. These cylindrical billets were pre-sintered and are awaiting encapsulation.

Powders were milled for Iteration 5 cold pressing evaluations. Again baseline, ARCO SC-9 and Tateho containing powders were prepared. Cold isostatic pressing at 60 ksi pressure was carried out using rubber cylindrical molds. The baseline material pressed very well. The composite materials containing SiC whiskers did not. Wafering was experienced as seen in Figure 2. Additional powders were prepared to which a 1 percent PVA binder addition was made. Pressings were made but the wafering problem remained.

Encapsulation and HIP

During the intial HIP studies with samples containing ARCO whiskers, specimens processed at 1750-1800°C without encapsulation showed severe whisker degradation. Quartz encapsulation and lower process temperatures were investigated. Composite samples up to 92% theoretical density were obtained.

Iterations 1, 2 and 3 samples were all encapsulated in quartz. HIP run conditions and results for the above iterations are summarized in Table 2. Most runs did not yield densified samples due to capsule failure during HIP'ing cycles. Based on observations after each HIP run, the failures were judged by one or a combination of more than one of the following reasons: 1) poor vacuum in the capsule, 2) gas formation between whiskers and the matrix material, 3) poor capsule seal and 4) variations in HIP cycle temperature and pressure profiles. In HIP run number 421 (Table 2) all billets except for billet 3B (ARCO SiC whisker) exhibited evidence suggesting explosion resulting from gaseous phase formation within the billets during HIP'ing. Fracture origins near the center of the billets were clearly visible in the exploded billets. These results and the gelling results discussed earlier indicate that ARCO SC-9 SiC whiskers seem to be the most stable and easiest to process among the four SiC whiskers evaluated in this program.

Due to the low success rate, quartz encapsulation was abandoned and the use of refractory metal cans was initiated. In the first attempts, molybdenum was used in preparing the cans. During the fabrication of the cans, problems developed in Electron Beam Welding causing brittle fracture of the can. The second group was formed from tantalum to avoid the problems encountered with the Mo cans.

Five specimens from Table 2 were encapsulated in the tantalum cans. In run 451, a single can containing a billet of Si_3N_4/ARCO SC-9 was processed to 1700°C and 27 ksi pressure argon. The collapsed can and specimen can be seen in Figures 3 and 4. Little if any densification occurred indicating a can failure. The can was very brittle.

To minimize the deformation during the brittle phase transformation, the remaining four cans were cold isostatically pressed at 60 ksi. This allowed the can to conform to the specimen while in a more ductile state.

Two specimens were processed in run 453. A baseline billet and a billet containing Tateho SiC whiskers were HIP'ed at 1700°C and 28 ksi. After HIP'ing the cans were again very brittle and can be seen in Figure 5. The baseline material densified very well but the Tateho sample did not. Examination of the can that contained the Tateho Sic whiskers revealed discoloration indicating some form of contamination and reaction. It appears from the yellow/bronze discoloration that a tantalum nitride compound might be formed. The processed specimens can be seen in Figure 6.

Further encapsulation studies will be carried out using niobium cans or tantalum cans. The one remaining tantalum encapsulated specimen is an ARCO sample and will be processed in the near future.

Evaluations

Three of the test bars that have been densified to 92% theoretical (3.03 g/cc, HIP run # 396, Table 2) were MOR tested in the as processed state. These test bars have rough surfaces and were slightly warped during HIP'ing. The MOR test results are 61.0, 53.3 and 38.9 ksi. Considering the conditions of the bars and the densities achieved, the maximum MOR value of 61 ksi suggests a high potential in property improvements.

Many whiskers were visible on the fracture surfaces of the MOR bars under SEM, indicating the whiskers were not severely degraded. These can be seen in Figure 7. No obvious whisker degradation was detected and whisker pullouts are evident. Additional test bars from run 396 were machined for fracture toughness testing. These bars (approximately 92% dense) were tested using single-notch techniques. These two bars yielded toughness values of 5.60 and 5.86 ksi-in$^{1/2}$ respectively. Two similiarly prepared baseline bars yielded values of 4.38 and 4.74 ksi-in$^{1/2}$. A comparison of the two would give an approximately 26 percent increase in fracture toughness. The composite specimens contained 10 percent loading of ARCO SC-9 SiC whiskers. Potentially higher values could be achieved with the current 20 percent loadings of SiC.

Status of Milestones

A revised milestone schedule has been submitted to ORNL for approval.

Publications

None.

TABLE 1

WEIGHT CHANGE OF MATERIALS UPON HEATING

AS RECEIVED MATERIALS	WEIGHT @ 25°C (g)	WEIGHT @ 300°C (g)	WEIGHT CHANGE (%)
GTE SN-502 (Lot SN-165)	0.159	0.156	-1.89
ARCO SC-9 SiC whiskers	0.144	0.137	-4.86
Tateho SCW #1 SiC whiskers	0.095	0.089	-6.32

TABLE 2

SUMMARY OF HIP EXPERIMENTS WITH QUARTZ ENCAPSULATION

							RESULTS				
DATE	HIP RUN #	PEAK TEMP (°C)	PEAK PRESSURE (ksi)	SAMPLE ITERATION	SAMPLE SHAPE	MATERIAL	ENCAPSULATION CONDITION	SAMPLE CONDITION	DENSITY (g/cc)	DENSITY INCREASE (%)	REMARKS
3/28/85	380	1750	15	1	B *	Baseline	---	W	2.88	37.1	See Note 1
				1	B	Baseline/ 10% ARCO	---	W	2.45	15.0	"
				1	B	Baseline/ 10% ARCO	---	W	2.47	16.0	"
				1	B	Baseline/ 10% ARCO	---	W	2.31	9.2	"
4/29/85	396	1700	15	1	B	Baseline/ 10% ARCO	CR/N	W	2.26	6.1	
				1	B	Baseline/ 10% ARCO	CL	G	3.03	43.3	
5/2/85	398	1750	25	1	B	Baseline	CR/N	W	2.54	21.0	
				1	B	Baseline/ 10% ARCO	CR/N	W	2.35	10.3	
5/21/85	401	1700	15	2	R	Baseline/ 20% ARCO	N	CR/W	2.24	6.2	
				2	R	Baseline/ 20% Coated ARCO	N	CR/W	1.72	14.7	
				2	R	Baseline/ 20% Tateho	N	CR/W	2.15	6.7	
				2	R	Baseline	N	CR/W	2.41	13.9	
5/28/85	405	1700	15	2	R	Baseline/ 20% ARCO	CR	W	NA	NA	
				2	R	Baseline/ 20% Tateho	CR	W	NA	NA	
				2	R	Baseline	CR	W	NA	NA	

TABLE 2
SUMMARY OF HIP EXPERIMENTS WITH QUARTZ ENCAPSULATION
(CONTINUED)

							RESULTS				
DATE	HIP RUN #	PEAK TEMP (°C)	PEAK PRESSURE (ksi)	SAMPLE ITERATION	SAMPLE SHAPE	MATERIAL	ENCAPSULATION CONDITION	SAMPLE CONDITION	DENSITY (g/cc)	DENSITY INCREASE (%)	REMARKS
7/9/85	417			2	R	Baseline/ 20% ARCO	N	NC	NA	NA	Aborted run; rerun as # 418
				2	R	Baseline/ 20% Tateho	N	NC	NA	NA	
				2	R	Baseline/ 20% Tokai	N	NC	NA	NA	
7/10/85	418	1700	28	2	R	Baseline/ 20% ARCO	CR	NC	NA	NA	
				2	R	Baseline/ 20% Tateho	CR	NC	NA	NA	
				2	R	Baseline/ 20% Tokai	CR	NC	NA	NA	
				3	CYL	Baseline/ 20% Tateho	S	BR	NA	NA	
7/11/85	419	1700	28.7	3	CYL	Baseline/ 20% ARCO	S	BR	2.07	8.9	
				3	CYL	Baseline/ 20% Tokai	CL	NC	2.02	6.9	
7/12/85	420	1300		3	CYL	Baseline/ 20% ARCO	N	NC	NA	NA	Aborted run; rerun as # 421
				3	CYL	Baseline/ 20% Tokai	W	NC	NA	NA	
				3	CYL	Baseline/ 20% Tateho	N	NC	NA	NA	
				3	CYL	Baseline/ 20% Tateho	N	NC	NA	NA	
7/15/85	421	1750	29	3B	CYL	Baseline/ 20% ARCO	s	NC	2.07	8.9	
				3D	CYL	Baseline/ 20% Tokai	S	E	1.98	4.8	
				3E	CYL	Baseline/ 20% Tateho	S	E	1.87	1.1	
				3E	CYL	Baseline/ 20% Tateho	S	E	1.99	7.6	

* EXPLANATION OF TABLE 2

BR - Broken

B - Test Bars (about 2" X 1/4" X 1/8")

R - Rectangular Plates (about 2" X 6" X 1/2")

CYL - Cylinders (about 2" dia. X 4" long)

CL - Collapsed

CR - Cracked

E - Exploded

G - Good - No Warpage/Distortion

N - No Collapse of Encapsulation Materials

NA - Not Available

NC - No Change

S - Shattered

U - Unencapsulated

W - Warpage

NOTE 1: Test bars were not encapsulated in an attempt to evaluate sinter/HIP possibilities.

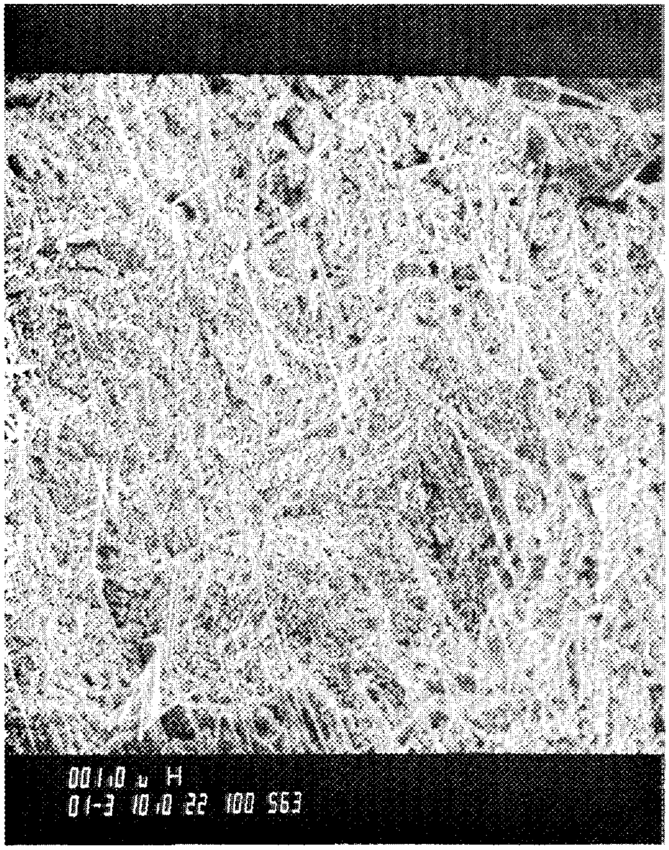

Figure 1: SEM micrograph showing fiber dispersion in a green compact (baseline + 20% ARCO SC-9 SiC_w)

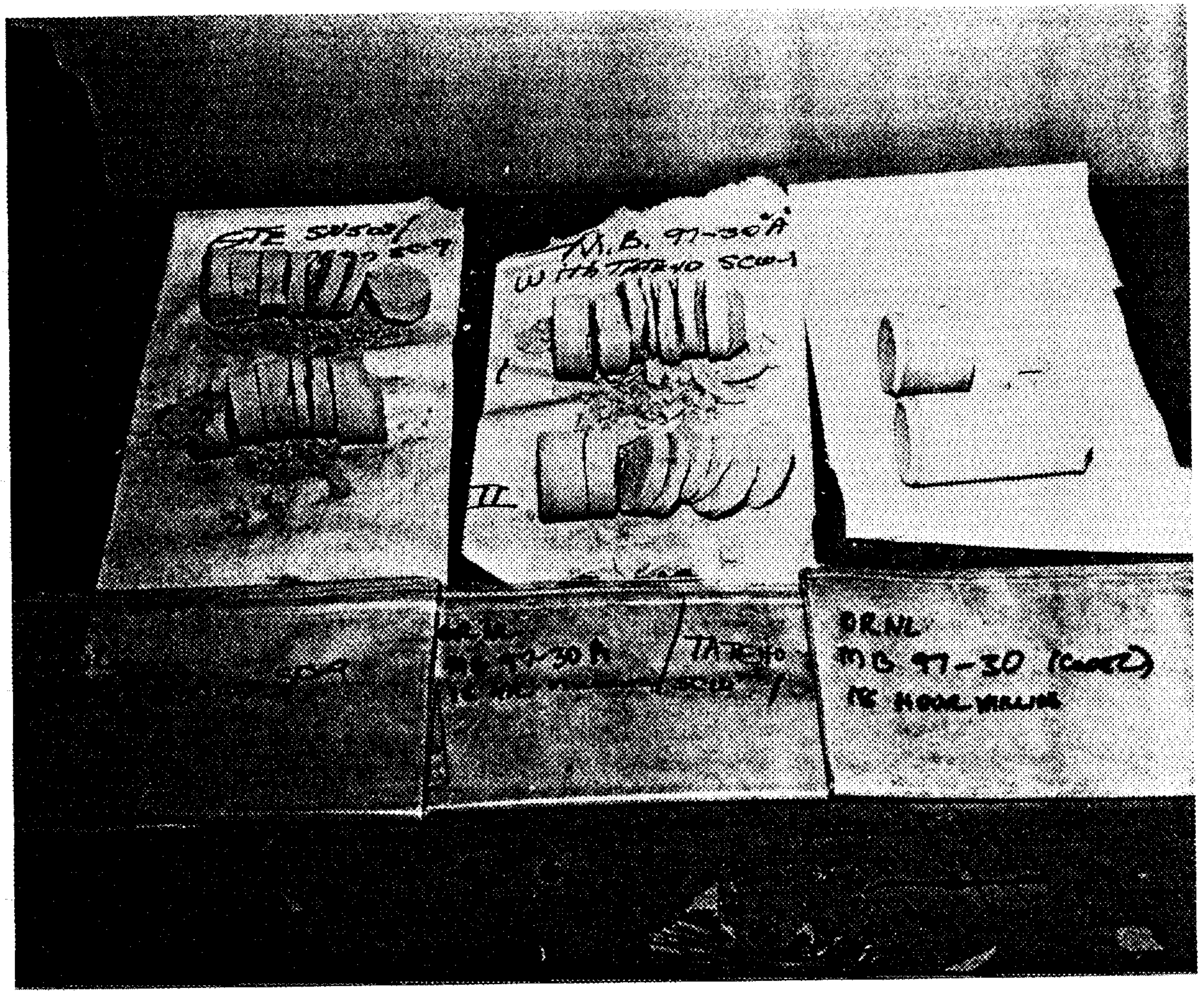

Figure 2: Results of cold pressing evaluations.
ARCO SC-9 Tateho SCW#1 GTE Baseline

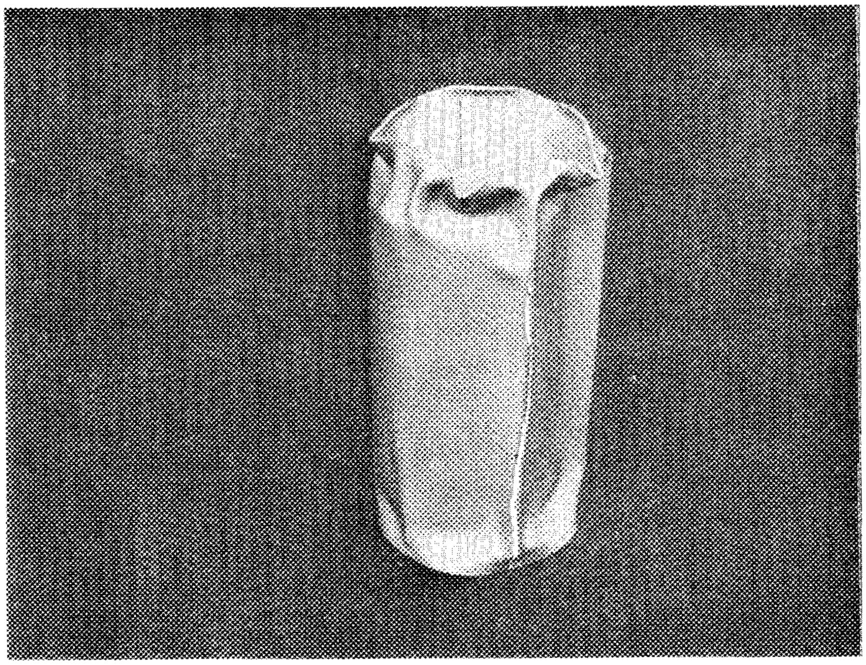

Figure 3: Collapsed can containing ARCO specimen.

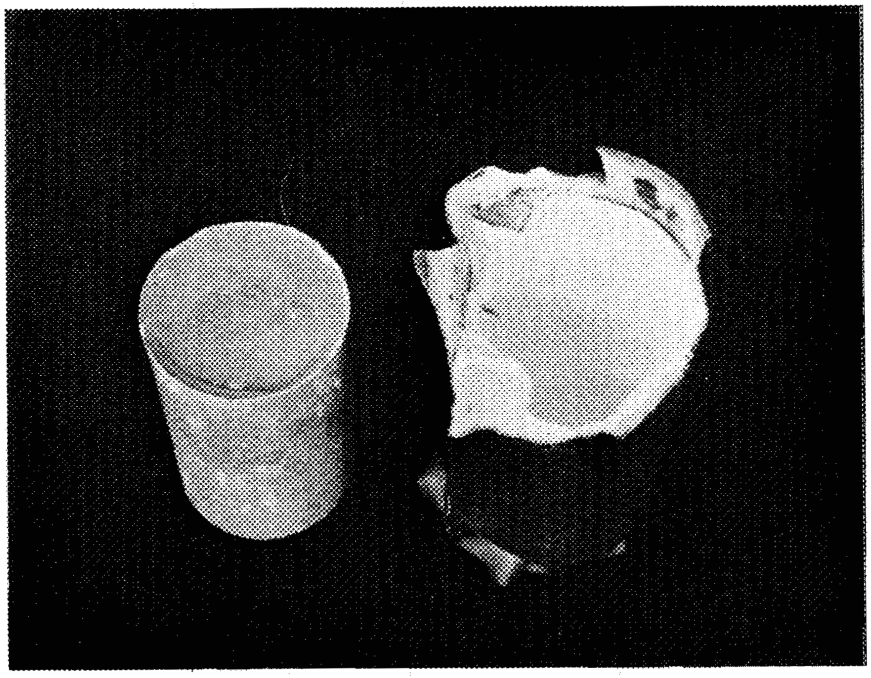

Figure 4: ARCO specimen from run 451.

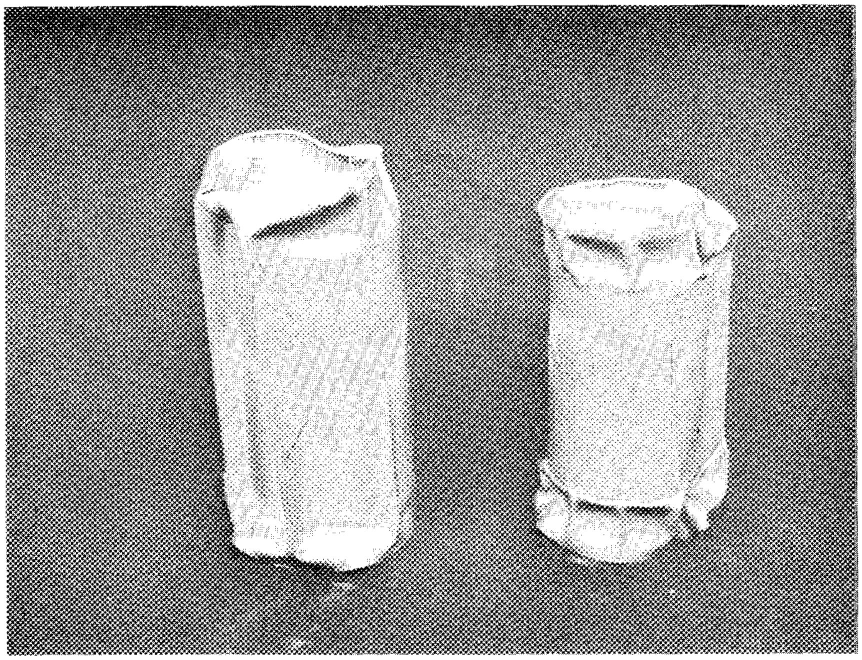

Figure 5: Collapsed cans from run 453.
Left: Tateho sample Right: Baseline sample

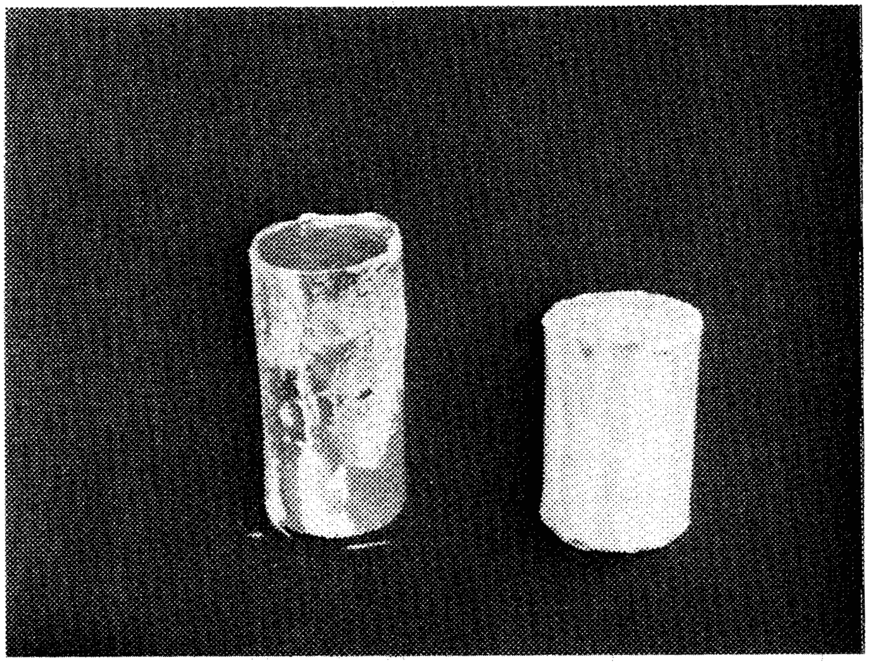

Figure 6: Specimens from run 453.
Left: Tateho Right: Baseline

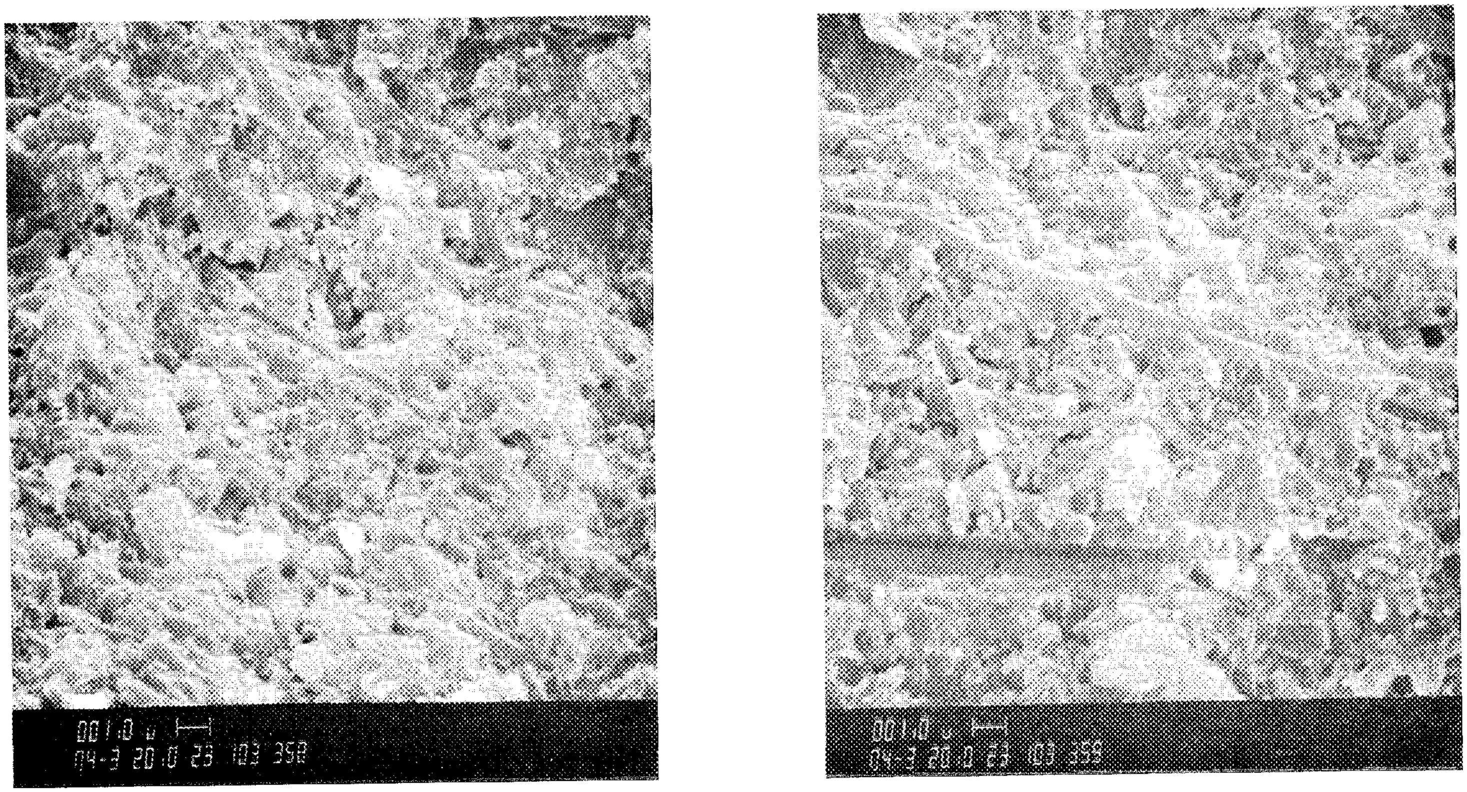

Figure 7: SEM fractographs of a 10% SiC_w (ARCO)/Si_3N_4 specimen HIP'ed at 1700°C - 15 ksi - 1 hr to 92% theoretical density.

1.2.3 Oxide Matrix

SiC-Whisker-Reinforced Ceramic Composites

T. N. Tiegs and P. F. Becher (Oak Ridge National Laboratory)

Objective/scope

This work involves development and characterization of SiC-whisker-reinforced oxide composites for improved mechanical performance. To date, most of the work has dealt with alumina as the matrix because it was deemed a promising material for an initial study. However, optimization of matrix materials is also being explored. The approach to fabrication is to first use hot pressing to identify compositions for toughening and then to develop pressureless sintering for fabrication of near-net-shape pieces. Initial work has been described in previous semiannual reports.

Technical progress

SiC whiskers

To date, essentially all composite work and process development have used SiC whiskers obtained from ARCO Chemical Company. Because alternate whisker sources are now available from both domestic and foreign sources, we made a series of Al_2O_3—20 vol % SiC whisker composites to determine the properties of composites using these alternate whiskers. The composites were hot pressed under conditions typically used for samples containing ARCO whiskers and subsequently machined into mechanical test specimens. The results of the mechanical property testing are summarized in Table 1. As shown, the mechanical properties were significantly lower for the composites containing the whiskers from other sources.

Under ceramographic examination of the composites made with the Tateho and Tokai Carbon whiskers, the SiC whiskers appeared to be intact. However, examination with a scanning electron microscope of a fracture surface revealed no SiC whiskers. This is in direct contrast to Al_2O_3-SiC whisker composites made with ARCO material, where the whiskers are easily visible on the fracture surface. Further examination with an electron microprobe suggests that at the hot-pressing temperature a reaction between the Al_2O_3 and the SiC whiskers occurred. This is also indicated by the high weight losses observed for the composites made with the Tateho and Tokai Carbon whiskers (Table 1). Although the composites made with the Versar whiskers have not been examined to date, similar degradation reactions are believed to be the cause of the poor mechanical properties.

To determine any possible cause for reactions between the alumina and the SiC whiskers, the various whiskers were analyzed for impurity levels (Table 2). As shown, the Tateho, Tokai Carbon, and Versar SiC whiskers had impurity levels not very much different from those of the ARCO product. Further examination of the whiskers to determine any differences is proceeding.

The composite made with the Los Alamos National Laboratory whiskers was examined further to determine the reason for the low flexural strength but good fracture toughness. Examination of fracture surfaces showed that the SiC whiskers were intact with no evidence of any

Table 1. Summary of mechanical testing of Al_2O_3–20 vol % SiC whisker composites from various whisker sources

SiC whisker source	Density (Mg/m^3)	Flexural strength (MPa)[a]	Fracture toughness ($MPa \cdot m^{1/2}$)[b]	Weight loss during hot pressing (%)
ARCO[c]	3.82	650	8.3	0.8
Tokai Carbon	3.79	270	7.2	5.17
Tateho	3.74	370	4.2	1.53
Versar	3.72	340	*d*	2.32
LANL[e]	3.83	430	9.1	4.85

[a] Four-point bend test.

[b] Multiple indent method.

[c] Typical values.

[d] Not determined.

[e] Los Alamos National Laboratory.

Table 2. Impurities in SiC whiskers

Whisker source	Impurities (ppm)									
	Na	Mg	Al	K	Ca	Cr	Mn	Fe	Co	Ni
ARCO	30	300	200	20	100	50	100	100	1	30
Tateho	5	30	30	30	300	30	50	50	1	10
Tokai Carbon	50	3	10	3	20	50	5	50	1000	10
Versar	5	50	30	30	300	30	50	50	>1	10

reactions. However, large flaws were observed that were rich in nickel and iron. Apparently, these result from some of the catalyst balls that were not removed during whisker cleaning procedures and caused the low observed flexural strengths.

Pressureless sintering

Several specimens of Al_2O_3-SiC whisker composites were fabricated by pressureless sintering and then machined into bars for flexural strength testing. Additional samples were subsequently hot isostatically pressed (HIP) to higher densities and their flexural strengths determined. The results are summarized in Table 3. As shown, strength reduction after the HIP processing was apparent although increases in density were observed. Examination of the tensile fracture surfaces with a scanning electron microscope showed degradation of the SiC whiskers within 0 to 50 μm of the specimen surfaces. The HIP procedures are being reexamined to determine the causes of the problems and means to alleviate them.

Thermal shock of alumina–SiC whisker composites

Another important consideration in the use of these SiC-whisker-reinforced alumina composites for structural applications is their thermal shock resistance. Because of the high fracture strength and toughness of these composites they would be expected to have good thermal shock resistance, but since this property is a complex function of several material properties, tests were conducted to determine if indeed these composites had good thermal shock resistance. An alumina–20 vol % SiC whisker composite hot pressed to full density was compared with a commercial alumina with no SiC whisker reinforcement.

The changes in flexural strength as a function of the temperature drop from the furnace to the boiling water bath are shown in Table 4. As shown the alumina–20 vol % SiC whisker composite shows virtually no decrease in flexural strength with temperature differences up to 900°C. Alumina, on the other hand, shows a significant decrease in flexural strength with a temperature change of 700°C. Other researchers have shown similar results from thermal shock tests on alumina.[1,2] Plans are to increase the temperature difference up to 1400°C to determine if any strength degradation occurs.

Because the thermal shock resistance was excellent for the single quench, some specimens were subjected to 10 quench cycles from 800°C into the boiling water bath. As shown in Table 4, some strength degradation was observed: an average strength of 540 MPa versus more than 610 MPa for the unshocked and singly shocked composites. While this indicated some fatigue effects, the thermal shock resistance of the alumina–20 vol % SiC whisker composite is considered to be excellent.

Oxidation of alumina–SiC whisker composites

A hot-pressed alumina–20 vol % SiC whisker composite was machined into bend bars, which were subjected to isothermal oxidation at elevated temperatures. The results are summarized in Table 5. As shown considerable oxidation of the composite material occurred. The oxidation rates up to 1000 h at 800 and 1000°C appear to be relatively linear, indicating oxygen transport through the alumina with no formation of a

Table 3. Summary of results for flexural strength of pressureless-sintered and hot-isostatically-pressed alumina—SiC whisker composites

Sample	Whisker content (vol %)	Pre-HIP properties: Density (% T.D.)	Pre-HIP properties: Flexural strength (MPa)	Post-HIP properties: Density (% T.D.)	Post-HIP properties: Flexural strength (MPa)
SCW-51-4	5	97.7	280	99.9	250
SCW-68-1	10	92.5	280	93.3	255
SCW-68-2	10	92.5	280	93.7	320
SCW-69-5	10	93.0	260	94.0	200
SCW-83-1A	10	92.6	275	94.2	245
SCW-83-60	10	96.0	310	97.5	285
SCW-90-60	10	94.8	310	96.5	230

Table 4. Results from thermal shock testing of alumina and alumina—20 vol % SiC whisker composite

Alumina—20 vol % SiC whiskers: Temperature change (°C)	Alumina—20 vol % SiC whiskers: Flexural strength (MPa)[a]	Alumina: Temperature change (°C)	Alumina: Flexural strength (MPa)[a]
0	620	0	305
300	630		
500	685		
700	610	700	120
700[b]	540		
900	710		

[a] Four-point bend test at room temperature.

[b] Bend bars subjected to 10 quench cycles.

Table 5. Results of isothermal oxidation of alumina—20 vol % SiC whisker composites

Oxidation temperature (°C)	Oxidation time (h)	Weight gain (g/m^2)	Room temperature flexural strength (MPa)
			510[a]
800	500	0.738	470
800	1000	1.772	410
1000	500	1.774	380
1000	1000	3.533	350
1200	100	3.933	460

[a] As fabricated.

protective layer at the surface. Although the oxidized sample had a rather low flexural strength initially, with oxidation further decreases in strength were observed. Longer-term oxidation studies are being planned.

Weibull modulus of hot-pressed composites

A hot-pressed alumina—20 vol % SiC whisker composite was machined into bend bars and mechanically tested to determine the Weibull modulus (Fig. 1). As shown, the Weibull modulus for the 20 bars tested was 12.2

ORNL-DWG 86-1816

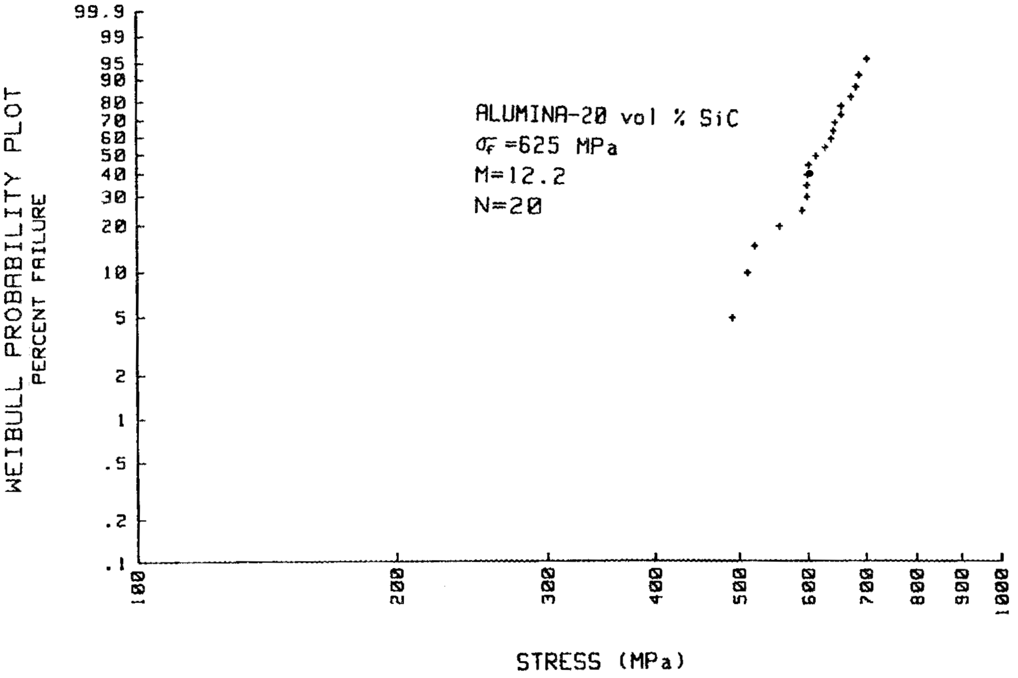

Fig. 1. Alumina—SiC whisker composites exhibit a good Weibull modulus.

with a mean flexural strength of 625 MPa. The flexural strength was slightly lower than that of previous samples with comparable whisker contents. Fractography of the specimens revealed numerous large defects (>100 μm), which were evidently introduced from the SiC whiskers. What is surprising is the relatively high mean strength and Weibull modulus in spite of the numerous defects.

Status of milestones

All milestones were on schedule.

Publications

T. N. Tiegs and P. F. Becher, "Whisker Reinforced Ceramic Composites," to be published by Plenum Press in their Materials Science Research Series.

References

1. P. F. Becher, "Transient Thermal Stress Behavior in ZrO_2-Toughened Al_2O_3," *J. Am. Ceram. Soc.* 64(1), 37–39 (1981).
2. H. P. Kirchner, *Strengthening of Ceramics*, Marcel Dekker, Inc., New York, 1979, pp. 63–65.

Sol-Gel Oxide Powder

W. D. Bond, P. F. Becher, and T. N. Tiegs (Oak Ridge National Laboratory)

Objective/scope

Sol-gel processes have the potential for the synthesis of materials that can be processed at modest temperatures while obtaining highly uniform composition in dense, fine-grain ceramics that incorporate dispersed second phases to increase fracture toughness. This research emphasizes the determination of the feasibility of sol-gel processes for (1) synthesizing powders of phase-stabilized zirconia and alumina and (2) coating whiskers to control the properties of their interface with matrix phases. Sol-gel processes take advantage of the high degree of homogeneity that can be achieved by mixing on the colloidal scale and the surface properties of the colloidal particles. The excellent bonding and sintering properties of colloids are a result of their very high specific surface energy.

Work conducted on sol-gel oxide powder synthesis and processing within this program is part of an integrated activity that is also supported by the U.S. Department of Energy (DOE) Materials Sciences Program at Oak Ridge National Laboratory (ORNL). The Materials Sciences Program supported research on ceramic composites derived from the sol-gel powders resulting from this work. The research on the coating of whiskers by sol-gel methods is a collaborative effort with research on SiC-whisker-reinforced composites under way at ORNL in the Ceramic Technology Project. The Ceramic Technology research includes the necessary research on the fabrication and properties of composites that are reinforced with the sol-gel-coated whiskers.

Technical progress

Studies in sol-gel synthesis included: (1) development of a method for preparing boehmite alumina gels that are seeded with colloidal particles of alpha alumina crystallites, (2) preparation of dispersible alumina powders by the thermal decomposition of alkoxide compounds in air, and (3) preparation of alumina powders reinforced with SiC whiskers. Studies supported by the DOE Material Sciences program were concerned with the sintering behavior of gel-derived powders and the properties of the resultant composites.

Sol-gel synthesis

The presence of seed crystals of alpha alumina (1 to 2 wt %) in boehmite alumina gels is reported to significantly lower the sintering temperature in the preparation of high-density alumina composites. Alpha alumina is the stable high-temperature form ($\geq$800°C) for Al_2O_3. We hope to improve sintering even further by using colloidal mixtures of both the alpha and boehmite crystal forms. A boehmite alumina gel powder seeded with 2 wt % alpha alumina was prepared by using the mixed sol approach. A hydrosol of alpha alumina was prepared by dispersing a high-purity commercial α-Al_2O_3 powder in nitric acid at 90°C, using 0.05 mole of HNO_3 per mole of Al_2O_3. Conductivity titrations indicated that this stoichiometry was about optimum for a stable dispersion of the powder. The boehmite alumina sol was prepared by the usual precipitation-peptization method.

Colloidally dispersible alumina powders were prepared from aluminum isopropoxide by using decomposition temperatures as high as 550°C. Although the Al_2O_3 powders are agglomerated, colloidal dispersions were prepared by heating an aqueous slurry of the powder in dilute nitric acid (~0.2 mole HNO_3/mole Al_2O_3) at 85°C. The dispersion process is relatively slow; about 24 h was required for complete dispersion. This preparation method is an attractive route to the synthesis of sols and gels of gamma-alumina. Conventional sol-gel methods produce aluminas that have the boehmite structure.

A 100-g batch of 20 vol % SiC whiskers in Al_2O_3 was prepared for composite evaluation studies. The SiC whiskers were dispersed into a boehmite alumina sol (3 wt % Al_2O_3) at a pH of 3.5 by using ultrasonic mixing, and then gelation was rapidly effected by adjusting the pH to 6 with dilute ammonium hydroxide. After drying at 110°C, a uniform dispersion of SiC whiskers in alumina was obtained.

Sintering and composite property studies

Hot-pressing and sintering studies with gel-derived powders continued to show that high densities are obtained with gel powders prepared by mixed oxide sols and by the rapid and direct precipitation of gels (Table 1). However, problems are still encountered with regard to obtaining uniformity of Y_2O_3 in the zirconia phase, which was determined by electron microprobe analysis of two of the composites in Table 1. The Y_2O_3 content in the zirconia phase of the composite derived from the ZrO_2 — 3 mol % Y_2O_3 powder (Run 207) ranged from 2 to 5 mol %. The compound from sintering the Al_2O_3 — (20 vol % ZrO_2 • 1 mol % Y_2O_3) powder (Run 208) had somewhat less variability, 1.34 ± 0.34 mol %. Because these gel powders were prepared by a rapid transition from sol to gel (flash evaporation of sol droplets), the homogeneity of the mixed sols employed is suspect. We plan to reexamine the mixing methods to determine if significant variations in the ratios of yttrium to zirconium occur in the mixed sols.

Status of Milestones

The chemical synthesis parameter study of sol-gel-derived powders (milestone 123301) is progressing well. The draft technical report on the status of these studies was completed as scheduled by September 30, 1985. In-house review of the draft is in progress.

Publications

None.

Table 1. Density of composites prepared by hot pressing gel powders

Powder preparation run number	Composition	Gel preparation		Sintering conditions		Density of composite
		Gel precursor	Gelation method[a]	Temp. (°C)	Time (min)	(% theor.)
240	Al_2O_3 — 14 vol % (ZrO_2 · 3 mol % Y_2O_3)	Metal salts	RGP	1450	95	96
241	Al_2O_3 — 19 vol % (ZrO_2 · 1 mol % Y_2O_3)	Metal oxide sols	RGP	1450	120	92
207	ZrO_2 — 3 mol % Y_2O_3	Mixed oxide sols	FED	1500	55	95
208	Al_2O_3 — 20 vol % (ZrO_2 · 1 mol % Y_2O_3)	Metal oxide sols	FED	1410	60	97
230	ZrO_2 — 10 mol % HfO_2	Metal salts	RGP	1450	65	95
231	ZrO_2 — 10 vol % HfO_2	Metal oxide sols	SEW	1450	30	95
232	ZrO_2 — 5 mol % HfO_2	Metal salts	RGP	1450	30	98
233	ZrO_2 — 5 mol % HfO_2	Mixed oxide sols	SEW	1450	30	96

[a] RGP = rapid gel precipitation.
FED = flash evaporation of droplets.
SEW = slow evaporation of water.

Advanced Transformation-Toughened Oxides

T. K. Brog, J. S. Wallace, and T. Y. Tien (University of Michigan)

ABSTRACT

The fracture toughness, strength, and modulus of Al_2O_3-Cr_2O_3(matrix)/ZrO_2-HfO_2(dispersed phase) composites were measured. The fracture toughness increased with increasing volume fraction dispersed phase whereas the strength and modulus remained nearly constant up to 10v/o dispersed phase and then decreased for larger volume fractions. Multiple toughening mechanisms are apparently active in this system, with microcrack nucleation/growth dominating at high monoclinic contents.

INTRODUCTION

Zirconia toughened alumina (ZTA) has received considerable interest in recent years due to the enhancement in fracture toughness (1-5). The improvement in fracture toughness and strength of zirconia containing materials, as well as the long-term stability, has made possible the prospect of using some of these materials for high temperature structural applications such as for adiabatic engine components.

A modification of ZTA was investigated here to evaluate this material as a preliminary candidate material for engine applications. The matrix consists of an Al_2O_3-Cr_2O_3 solid solution. Additions of Cr_2O_3 were made to both lower the thermal conductivity and to modify the matrix properties, fracture toughness and modulus. Previous work has shown that Cr_2O_3 additions lowers the thermal conductivity (6) and increases the hardness (7). Slight increases in the bulk modulus with Cr_2O_3 additions (0-15m/o) have also been reported (8).

The dispersed phase consists of a ZrO_2-HfO_2 solid solution. Hafnia additions were made to zirconia to increase the tetragonal-to-monoclinic transformation temperature, thus increasing the temperature at which the transformation can be a viable toughening mechanism (9,10). The critical particle size for the transformation, however, decreases with increasing hafnia content. In order to retain a reasonable fraction of the zirconia-hafnia particles in the tetragonal symmetry using conventional processing methods, the maximum hafnia concentration was small, 10m/o.

The present study was undertaken to try to experimentally distinguish the various toughening mechanisms in this system by measuring the fracture toughness, strength, and modulus as a function of zirconia-hafnia volume fraction.

EXPERIMENTAL PROCEDURE

Al_2O_3-5m/oCr_2O_3 and ZrO_2-10m/oHfO_2 solid solutions were made by mixing appropriate amounts of the single oxides and solution annealing at 1350°C for 24 hrs. These solid solutions were attrition-milled in isopropanol for 4 and 8 h respectively. The solid solutions were mixed in a ball-mill, dried, sieved and isostatically pressed (170 MPa). The samples were then sintered at 1550°C for 2 h in a graphite induction furnace (argon atmosphere) and nearly theoretical density (>98%TD) was achieved.

Phase determination was performed on as-sintered surfaces. Integrated intensities of the $(11\underline{1})$ monoclinic peak (28.5°, Cu $K\alpha$) and the (111) tetragonal peak (30.5°) were measured and the tetragonal phase content was calculated using the method of Porter and Heuer (11). The pellets were then prepared for microstructural examination using standard metallographic techniques. The mean linear intercept length was measured using a digitizing tablet and encircling the ZrO_2-HfO_2 particles on SEM micrographs.

Machined bars (50mm x 3mm x 2mm) were annealed at 1550°C (well above the A_F temperature) to relieve residual stress from the machining process thus eliminating the effect of machining on the fracture toughness measurement. The fracture toughness was measured using the ISB (12) technique using single indents (20, 40kg) and fracture toughness values were calculated using the equation from Chantikul et al (12),

$$K_C = \eta(E/H)^{.125}(\sigma P^{.33})^{.75}.$$

Unindented bars (ground, annealed) were broken to measure the strength. All measurements were performed in 4 point bending with spans of 9.5 and 19.0mm.

Modulus measurements were made by measuring the sample thickness, density, and the propagation time for longitudnal and shear waves. The sonic elastic modulus and Poissons' ratio were calculated using

$$E = 3\rho[V_L^2 - 4V_S^2/3](1-2\nu)$$

$$\nu = (1-2x^2)/(2-2x^2),$$

where x is the ratio of the longitudinal wave velocity, V_L, to the shear wave velocity, V_S.

RESULTS AND DISCUSSION

The dispersed phase mean linear intercept length increased with increasing volume fraction dispersed phase, as would be expected, due to particle coarsening (Fig. 1). As would be expected for increasing mean particle size, the tetragonal fraction, X_t, decreases with increasing volume fraction dispersed phase, V_v, (Fig. 2). This, however, has also been attributed to loss-of-matrix constraint (4) as V_v is increased.

Measurements of the fracture toughness (Fig. 3) show a monotonic increase with increasing V_v, similar to that reported by Swain and Claussen (13) and Hori et al (14) on annealed ZTA samples. While this trend is similar to that expected from crack deflection models (15) there may be contributory mechanisms such as stress induced transformation (SIT) toughening (16,17) and/or microcrack nucleation/growth toughening (3,4,18).

SIT toughening can only occur when tetragonal zirconia particles transform to the monoclinic symmetry in the crack tip stress field. Toughness enhancement has been proposed to occur due to a crack shielding mechanism (19) in which a large compressive zone exists in the region surrounding the crack tip, effectively shielding the crack tip from the applied stress field.

The large volume increase associated with the t-m transformation may cause nucleation and growth of microcracks in the matrix surrounding monoclinic zirconia particles either occurring spontaneously upon cooling from the fabrication temperature or when an external stress field is applied. The nucleation and propagation of these microcracks increases the fracture surface, thus, absorbs energy.

Crack deflection can increase the fracture toughness by deflecting the crack out of the plane normal to the applied stress, thereby reducing the stress intensity applied to the crack tip. Crack deflection appears to be insensitive to stress state and magnitude in a glass-alumina system (20). The theoretical model proposed by Faber et al (15) suggests that the relative toughness enhancement is a function of the volume fraction dispersed phase, the size distribution, and morphology of the dispersed phase.

There is poor correlation between the fracture toughness and the total tetragonal volume. The fracture toughness does, however, increase with both increasing monoclinic volume and volume fraction dispersed phase. For low volume fractions of ZrO_2 the tetragonal fraction is high and the toughness enhancement is small due to the low tetragonal volume. In this regime SIT toughening and crack deflection are responsible for toughness improvement. For high volume fractions of ZrO_2 the tetragonal fraction is quite low, thus SIT contributions must be small. This suggests that crack deflection and/or microcrack nucleation/growth are the primary toughening mechanisms. As the volume fraction dispersed phase is increased, the contributions via SIT and microcrack nucleation/growth varies due to the change in tetragonal fraction and volume, and these contributions are superimposed on the enhancement due to crack deflection.

It is difficult to evaluate the effectiveness of each particular toughening mechanism on the basis of fracture toughness measurements alone. Strength and modulus measurements combined with fracture toughness data can be used to identify or detect the presence of SIT and microcrack nucleation/growth toughening.

Measurements of the strength as a function of V_v (Fig. 4) indicate that the strength remains approximately constant with increasing V_v up to 10v/o dispersed phase, above which the strength decreases slightly at 12.5v/o then precipitously at 15v/o. This behavior can be attributed to the existence of microcracks in the samples with high monoclinic contents. These results are similar to those reported by Claussen et al (3) but are not in good agreement with those reported by Hori et al (14) and Becher (5). The strength would be expected to decrease when microcrack nucleation/growth occurs due to the presence of microcracked domains, resulting in a larger critical flaw. Therefore, the strength degradation and the toughness enhancement for large zirconia contents can be attributed to microcrack nucleation/growth. Any toughness enhancement at low zirconia contents can in part be attributed to SIT toughening. SIT toughening may increase the strength by the creation of large compressive zones.

Elastic modulus measurements of composite materials which deviate from the rule of mixtures of the components are evidence for microcracking. Green (4) reported a large deviation from the rule of mixtures for Al_2O_3-ZrO_2 composites which contained high monoclinic fractions and attributed this to microcracking.

Sonic modulus measurements were made on the annealed bars (Fig. 5). The modulus shows a linear decrease with increasing V_v up to 10v/o dispersed phase and a large decrease for the the 15v/o material. One shortcoming of this technique (wave propagation as opposed to dynamic modulus measurements) is that it is impossible to detect microcracking in a sample which occurs when an external stress field is applied.

The degradation in both the strength and modulus occurs at the same composition, such that a nearly linear relationship exists between the strength and modulus in this material (Fig. 6). Thus, the presence of microcracks in this system contributes to a degradation in both the strength and modulus and an enhancement in the fracture toughness.

CONCLUSIONS

1. The dispersed phase particle size increases with increasing volume fraction dispersed phase, resulting in a decrease in the tetragonal phase content.
2. Multiple toughening mechanisms are apparently active in the system.
3. Evidence of microcrack nucleation/growth as a toughening mechanism is substantiated by a decrease in both the strength and modulus at high monoclinic contents.

ACKNOWLEDGEMENT

We would like to thank Dr. Lisa Schioler (AMMRC) for modulus measurements.

This work was supported by the Army Materials and Mechanics Research Center and the DOE Office of Vehicle and Engine Research and Development Ceramics Technology for Advanced Heat Engine Program.

REFERENCES

1. F.F. Lange, "Transformation Toughening Part 4 - Fabrication, Fracture Toughness, and Strength of Al_2O_3-ZrO_2 Composites", J. Mat. Sci., 17 247-54 (1982).

2. N. Claussen, "Fracture Toughness of Al_2O_3 with an Unstabilized ZrO_2 Dispersed Phase", J. Am. Ceram. Soc., 59 [1-2] 49-51 (1976).

3. N. Claussen, J. Steeb, and W. Pabst, "Effect of Induced Microcracking on the Fracture Toughness of Ceramics", Ceram.. Bull., 56 [6] 559-562 (1977).

4. D.J. Green, "Critical Microstructures for Microcracking in Al_2O_3-ZrO_2 Composites", J. Am. Ceram. Soc., 65 [12] 610-614 (1982).

5. P.F. Becher, "Transient Thermal Stress Behavior in ZrO_2 Toughened Al_2O_3", J. Am. Ceram. Soc., 64 [1] 37-39 (1981).

6. D.P.H. Hasselman, R. Syed, and T.Y. Tien, "The Thermal Diffusivity and Conductivity of Transformation-Toughened Solid Solutions of Alumina and Chromia", J. Mat. Sci., 20 2549-2556 (1985).

7. R.C. Bradt, "Cr_2O_3 Solid Solution Hardening of Al_2O_3", J. Am. Ceram. Soc., 50 [1] 54-55 (1967).

8. L.R. Rossi and W.G. Lawrence, "Elastic Properties of Oxide Solid Solutions: The System Al_2O_3-Cr_2O_3", J. Am. Ceram. Soc., 53 [11] 604-608 (1970).

9. N. Claussen, F. Sigulinski, and M. Ruhle, "Phase Transformations of Solid Solutions of ZrO_2 and HfO_2 in an Al_2O_3 Matrix", in Advances in Ceramics, (ed. A.H. Heuer and L.W. Hobbs), The American Ceramic Society, Cols., Ohio, 1981.

10. R. Ruh, H.J. Garrett, R.F. Domagala, and N.M. Tallan, "The System Zirconia-Hafnia", J. Am. Ceram. Soc., 51 [1] 23-27 (1968).

11. D.L. Porter and A.H. Heuer, "Microstructural Development in MgO Partially Stabilized Zirconia (Mg-PSZ)", J. Am. Ceram. Soc., 62 [5-6] 298-305 (1979).

12. P. Chantikul, G.R. Anstis, B.R. Lawn, and D.B. Marshall, "A Critical Evaluation of Indentation Techniques for Measuring Fracture Toughness: II, Strength Method", J. Am. Ceram. Soc., 64 [9] 539-543 (1981).

13. M.V. Swain and H. Claussen, "Comparison of K_{IC} Values for Al_2O_3/ZrO_2 Composites Obtained from Notched-Beam and Indentation Strength Techniques", J. Am. Ceram. Soc., 66 [2] C27-C29 (1983).

14. S. Hori, M. Yoshimura, and S. Somiya, "Mechanical Properties of ZrO_2-Toughened Al_2O_3 Ceramics from CVD Powders", J. Mat. Sci. Letters, 4 413-416 (1985).

15. K.T. Faber, A.G. Evans, and M.D. Drory, Fracture Mechanics of Ceramics, (ed. R.C. Bradt, A.G. Evans, D.P.H. Hasselman, and F.F. Lange), Vol. 6, 77-91, Plenum Press, New York, 1983.

16. F.F. Lange, "Transformation Toughening Parts 1-5" J. Mat. Sci., 17 225-254 (1982).

17. N. Claussen, "Stress-Induced Transformation of Tetragonal ZrO_2 Particles in Ceramic Matrices", J. Am. Ceram. Soc., 61 [1-2] 85-86 (1978).

18. N. Claussen, R.L. Cox, and J.S. Wallace, "Slow Growth of Microcracks: Evidence for One Type of ZrO_2 Toughening", J. Am. Ceram. Soc., 65 [11] C190-C191 (1982).

19. A.G. Evans, "Toughening Mechanisms in Zirconia Alloys", in Advances in Ceramics, (ed. N. Claussen, M. Ruhle, and A.H. Heuer), Vol. 12, 193-212, The American Ceramic Society, Cols., Ohio, 1984.

20. J.C. Swearengen, E.K. Beauchamp, and J.R. Eagen, Fracture Mechanics of Ceramics, (ed. R.C. Bradt, D.P.H. Hasselman, and F.F. Lange), Vol. 4, p. 973, Plenum Press, New York, 1978.

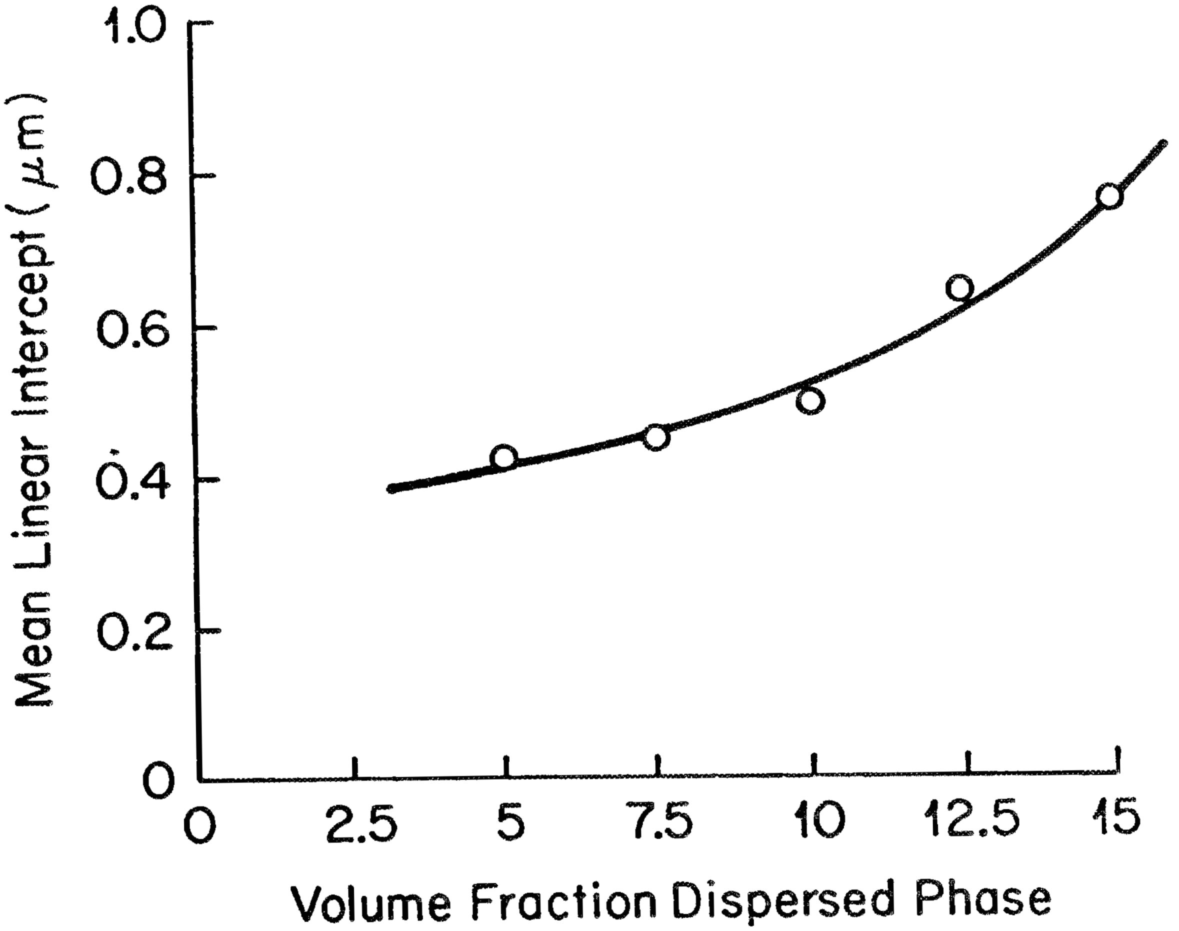

Figure 1. Mean linear intercept length of ZrO_2-$10^{m}/0HfO_2$ particles as a function of ZrO_2-HfO_2 content.

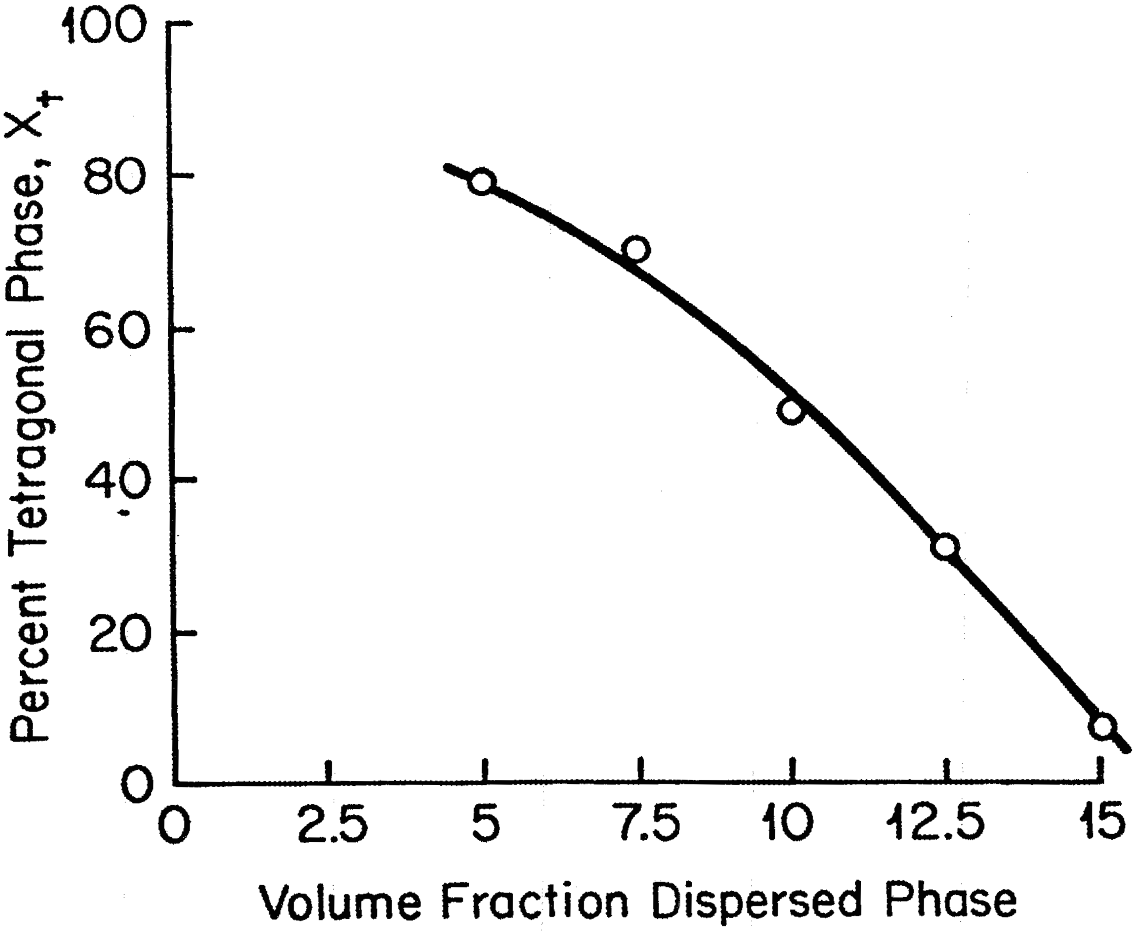

Figure 2. Tetragonal phase fraction of ZrO_2-10^{m}/0HfO_2 particles as a function of ZrO_2-HfO_2 content.

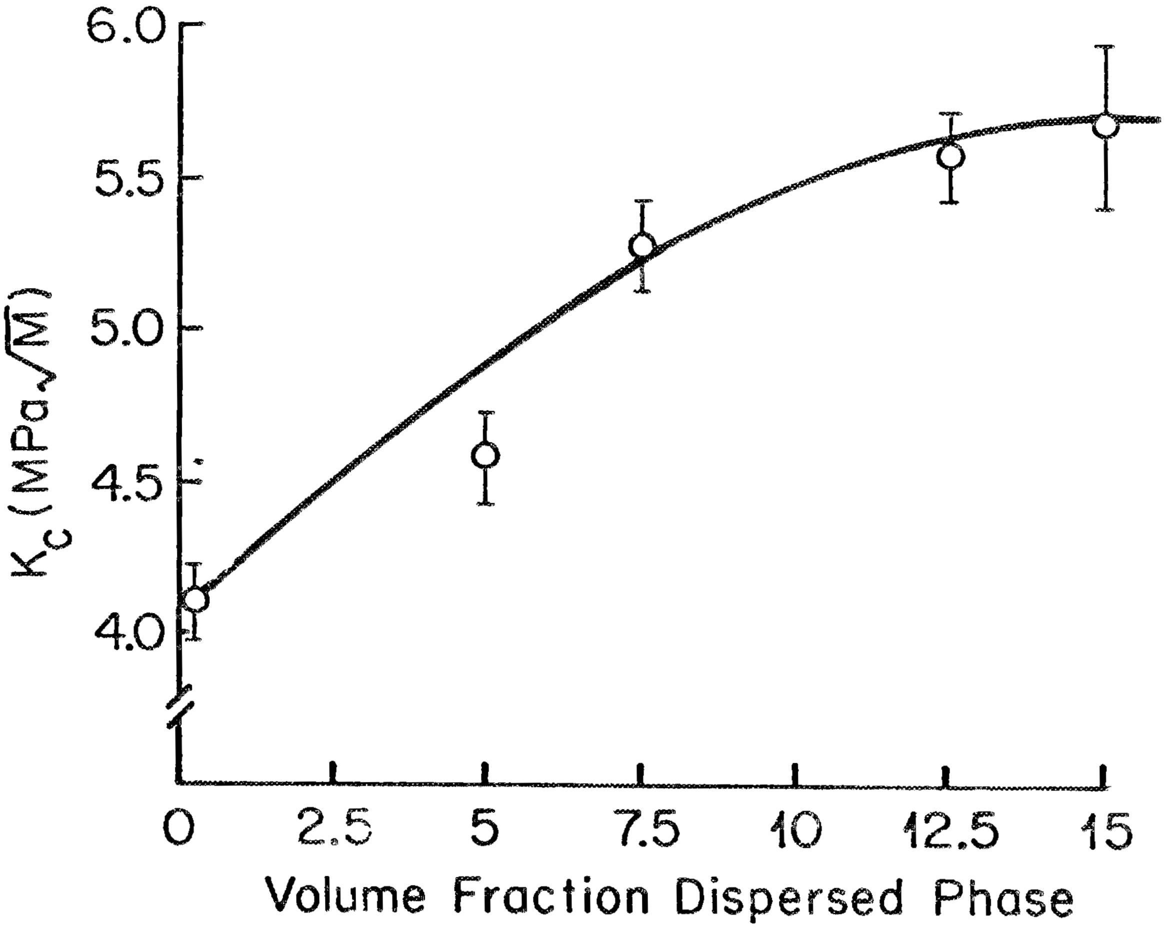

Figure 3. Fracture toughness as a function of ZrO_2-HfO_2 content measured using the ISB (12) method.

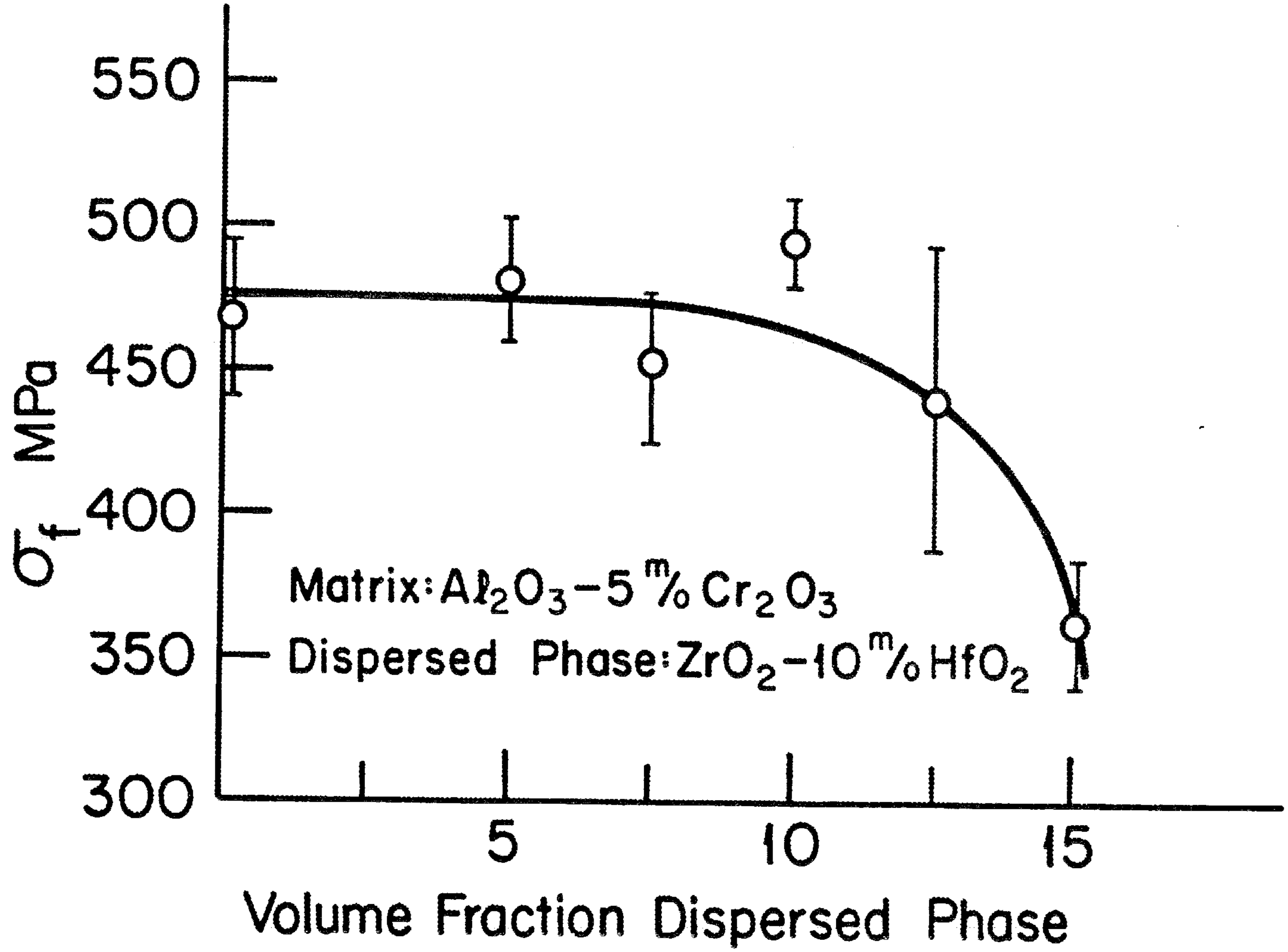

Figure 4. Strength as a function of ZrO_2-HfO_2 content showing the degradation in strength at high ZrO_2-HfO_2 volume fractions.

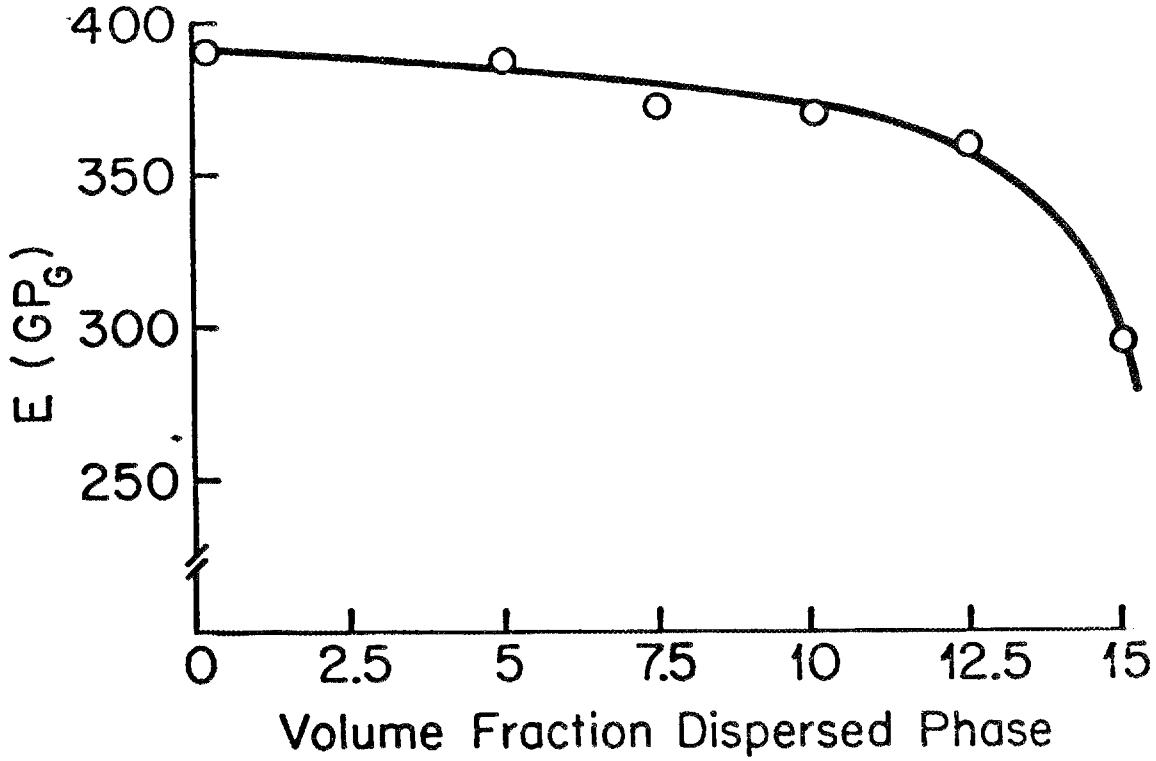

Figure 5. Elastic modulus as a function of ZrO_2-HfO_2 content showing the degradation in the modulus with increasing ZrO_2-HfO_2 content due to microcracking.

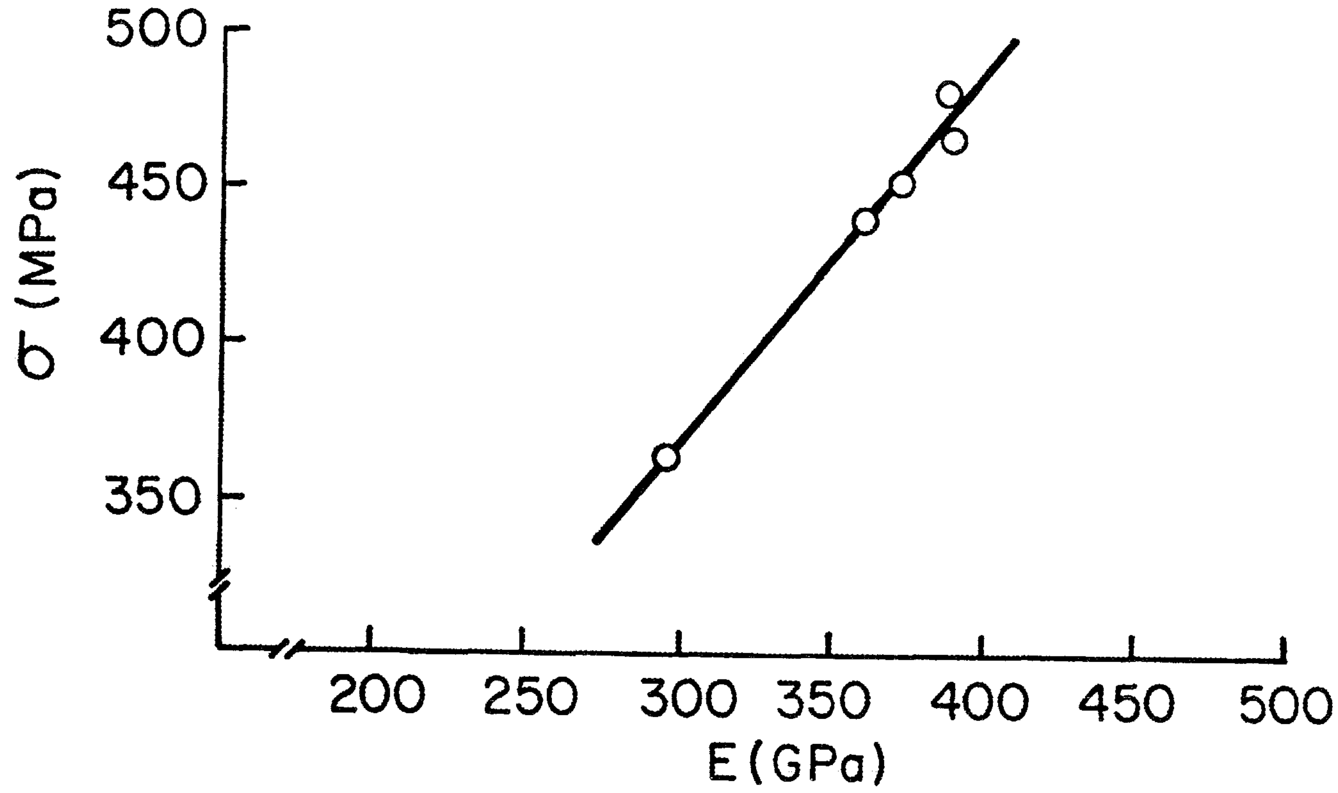

Figure 6. Strength vs. elastic modulus showing the degradation of both the strength and modulus for high ZrO_2-HfO_2 contents due to microcracking.

Injection Molded Composites

M. A. Janney (Oak Ridge National Laboratory)

Objective/scope

The goals of this activity are twofold: (1) to evaluate the ability of advanced ceramic-ceramic composites to be injection molded and processed by using standard wax- and/or polymer-based binder systems and (2) to develop advanced complex-shape forming technologies that will eliminate some of the problems associated with wax- and polymer-based binder systems such as long binder removal times, cracking, and low green strength.

Technical progress

Work this period focused on two major efforts: (1) rheology of SiC whisker—alumina slurries and (2) establishing the Ceramic Technology Powder Characterization Laboratory.

The ability to make whisker-reinforced ceramics (such as SiC-whisker-reinforced alumina) by wet forming methods (such as injection molding, slip casting, or extrusion) depends critically on the flow properties of the liquid-solid system. It has been demonstrated that slurries of SiC whiskers and alumina in water, which have properties similar to conventional ceramic slurries, can be made. However, it has also been shown that the rheology of these slurries is highly sensitive to processing conditions such as milling and pH. Our goal during this past reporting period was to begin characterizing the alumina—SiC whisker slurries currently in use at Oak Ridge National Laboratory and to document their sensitivity to a variety of processing condition changes.

The following procedure was used to make the slurries. The starting materials are listed in Table 1.

Two sets of alumina—SiC whisker slurries were prepared for rheological analysis. Both sets were prepared according to the same procedure except that Set 1 used whiskers in the as-received condition and Set 2 used whiskers after they were rod milled in water for 1 h. The basic composition of the mixes was:

Solid phase — 10 wt % whiskers
90 wt % A16SG

Fluid phase — 0.2 wt % (dwb) Darvan 7
0.07 wt % (dwb) citric acid
2.5 wt % (dwb) PEG 4000
NH_4OH to adjust to pH 11
balance water to give solids loadings of 25, 30, 35, and 40 vol %

Table 1. Raw materials for Al_2O_3—SiC whisker slurries

Material	Designation or product code	Role	Supplier
Alumina	A16SG	Ceramic matrix	Alcoa, Pittsburgh, Pa.
SiC whisker	SC9	Reinforcing phase	ARCO Chem. Co., Greer, S.C.
Darvan No. 7		Dispersant	RT Vanderbilt, Norwalk, Conn.
Citric acid		Dispersant	Fisher, Pittsburgh, Pa.
Polyethylene glycol	PEG4000	Binder	Union Carbide, Danbury, Conn.
NH_4OH solution		pH adjustment	Fisher, Pittsburgh, Pa.

The solid and fluid phases were mixed together in a beaker and sonicated for about 3 min to effect homogeneous mixing. The slurries were aged for 24 h (with continuous agitation to prevent segregation) prior to rheological characterization. Flow curves were determined with a Rheometrics RFS 8400 fluids spectrometer; a parallel-plate test geometry was used with a gap between plates of about 1.5 mm.

The slurries made with the milled whiskers exhibited rheology consistent with standard ceramic particulate slurries; an example for a 30 vol % slurry is shown in Fig. 1. The viscosities and yield points of the slurries increased with increasing solids loading, Table 2. The general shapes of the curves are also consistent with standard particulate slurries. Furthermore, the tendency toward thixotropic behavior, i.e., hysteresis in the flow curves between the UP (or accelerating) and the DOWN (or decelerating) behavior, increases with solids loading, which is typical of many standard ceramic materials. Such behavior is highly encouraging as it suggests that these whisker-reinforced composite materials might be processable according to procedures similar to standard ceramic practice; i.e., they may be spray dried, slip cast, etc.

In contrast to the milled-whisker-containing slurries, the unmilled-whisker-containing slurries exhibited anamolous rheological behavior as compared with standard ceramic particulate slurries. Figure 2 shows the behavior of a 30 vol % slurry for a standard thixotropic loop analysis in which the sample is sheared from 0.0 sec^{-1} strain rate to 10.0 sec^{-1} strain rate and back to 0.0 sec^{-1}. Notice that the UP curve lies below the DOWN curve, which is in marked contrast to the standard thixotropic behavior exhibited by the milled-whisker slurries, Fig. 1. Such behavior is termed anti-thixotropic, or reverse-thixotropic. Also, notice that the shear stresses generated in this material are approximately an order of magnitude

ORNL-DWG 86-1803

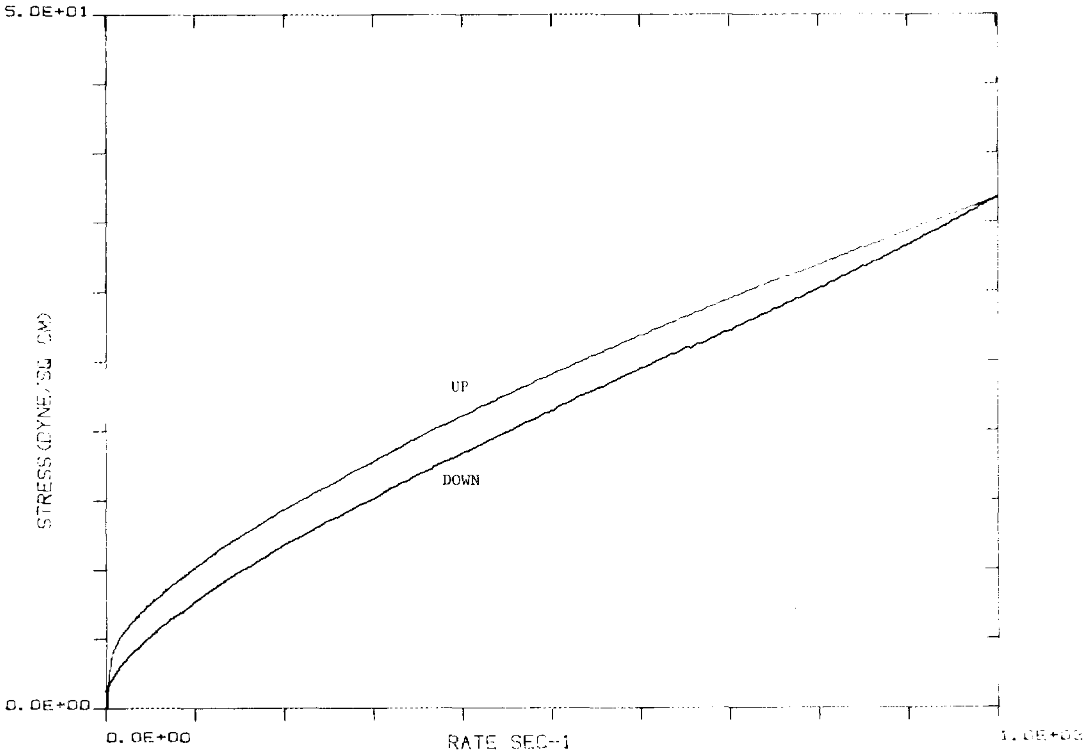

Fig. 1. A 30 vol % solids slurry made with milled ARCO SiC whiskers and A16SG alumina (10/90 weight ratio) exhibited flow behavior consistent with standard ceramic slurries.

Table 2. Rheological summary of slurries made with milled whiskers

Vol % solids	Yield point (dyne/cm^2)	Viscosity @ 100 s^{-1}	Thixotropy
25	0.56	0.29	None
30	3.1	0.39	Weak
35	32	0.96	Strong
40	99	2.8	Strong

higher than those generated in the milled-whisker slurry of the same solids loading. The shape of the flow curves for this sample can be significantly altered by reversing the thixotropic loop analysis, i.e., by starting at 10.0 sec^{-1}, decellerating to 0.0 sec^{-1}, and accelerating back to 10.0 sec^{-1}. Such a procedure brings the UP and DOWN curves more nearly into coincidence; however, the UP curve still lies below the DOWN curve, even though the hysteresis has been markedly decreased. This behavior

ORNL-DWG 86-2804

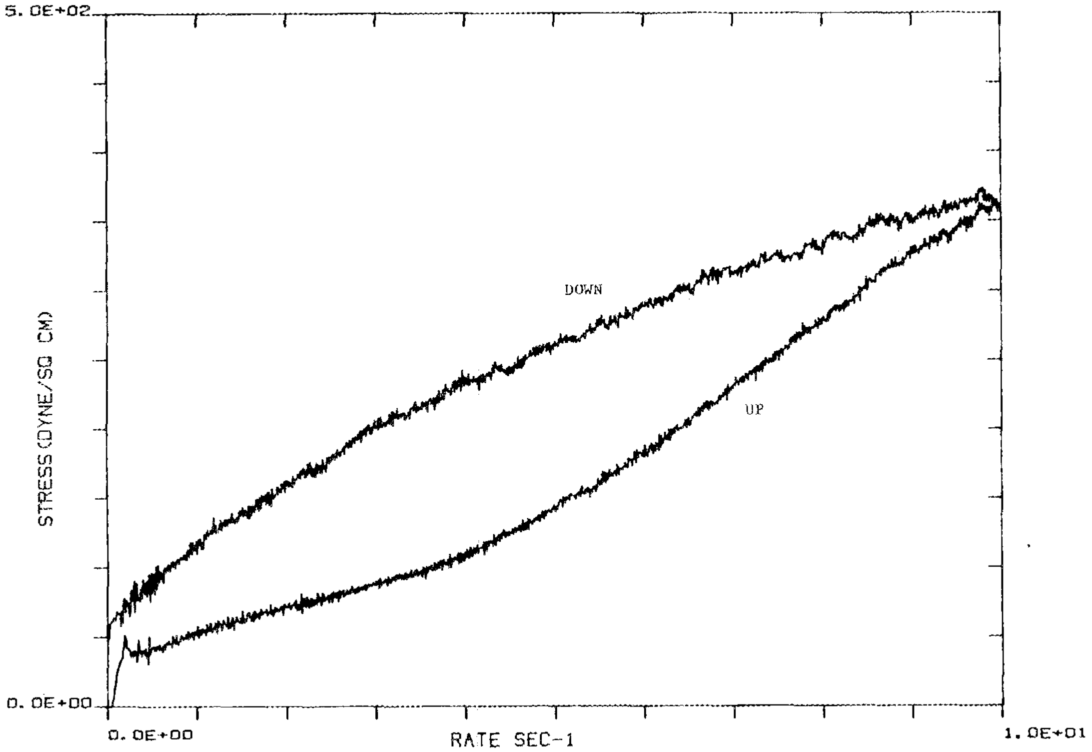

Fig. 2. A 30 vol % solids slurry made with unmilled ARCO whiskers and A16SG alumina (10/90 weight ratio) exhibited anomalous flow behavior, which was anti-thixotropic.

suggests that a form of "phase separation" may be occurring in the slurry, resulting in the formation of a thin, fluid layer between the bulk of the slurry and the face of the rheometer test probes (i.e., the parallel plates). Such phase separation has been observed in slurries made at lower solids content (~10 vol % solids) in which the solids sedimented out of the slurry. Experiments are under way to determine the nature of this phase separation. They include rheometric evaluations and also compaction and permeability tests, which will provide information concerning the agglomerate and pore geometries of these slurries.

A Powder Characterization Laboratory is being established. When finished, it will be one of the most complete ceramic powder characterization facilities in the United States. The following capabilities will be included in the facility:

1. Particle electrophoresis (zeta potential).

A Pen Kem 3000 particle electrophoresis analyzer has been acquired. Its measurement capabilities include electrophoretic mobility and distribution, specific conductance, pH, and turbidity, determined sequentially on one sample. It will also measure particle diffusion constant (i.e., Brownian motion) from which a median particle size can be determined.

Status: Operational.

2. Rheometry.

A Rheometrics RFS 8400 fluids spectrometer has been acquired. Its capabilities are the most extensive of any viscometer for slurry and polymer solution characterization. In the steady-state mode, the instrument will perform step scan (i.e., hold at a series of given rates), thixotropic loop scan, time scan to examine shear degradation, and stress-relaxation analyses. In the dynamic (oscillatory) mode, it will perform frequency, strain, and time sweeps. All of these measurements are performed under full programmatic control.

Furthermore, the unit is equipped with an environmental chamber to allow testing over the temperature range 5 to 90°C.

Status: Operational.

3. Gas adsorption (BET surface area).

A Quantachrome Quantasorb gas adsorption unit is included in the laboratory (previously purchased with other programmatic funds). It operates on the dynamic flow adsorption principle. Its capabilities include single- and multi-point BET surface area analysis, complete adsorption and desorption isotherms, micropore analysis, and chemisorption studies.

Status: Operational.

4. Gas permeability.

A PMI, Inc., gas permeability analyzer is included in the laboratory (purchased with other programmatic funds). It is capable of measuring powder and solid body permeabilities at pressure differentials from 0.7 to 410 kPa (0.1–60 psi) and flow rates from 0.02 to 12,000 ml/min.

Status: Operational.

5. Light scattering particle size analyzer.

A Microtrac particle size analyzer is included and is being upgraded to increase its performance. After upgrading, the unit will have an analysis range of 0.12 to 300 μm, will require only about 0.01 g of sample for analysis, and will be capable of running organic solvents, in addition to water, as the dispersing medium.

Status: Ordered.

6. Centrifugal sedimentation particle size analyzer.

   A Horiba centrifugal sedimentation instrument will be included in the laboratory. It is capable of determining particle size and distribution between 0.02 and 200 μm in both aqueous and nonaqueous solvents with a sample cell volume of 2 cm^3.

   Status: Ordered.

7. Mercury porosimeter.

   A mercury porosimeter for determining pore size distribution in powders, compacts, and sintered bodies is to be included in the laboratory. Pore sizes from about 300 μm to 0.003 μm can be analyzed. The combination of data from the porosimeter, the BET gas adsorption unit, and the gas permeability unit will give a good description of the pore geometry in a porous material.

   Status: Specification in preparation.

8. Fourier transform infrared spectrometer (FTIR).

   An FTIR for examining the chemistry of powder surfaces and their interactions with solvents, dispersants, binders, and other processing aids is to be included in the laboratory.

   Status: Specification in preparation.

9. Soil mechanics triaxial test cell.

   A triaxial test cell, which can impose an arbitrary stress state or stress history on a powder compact and measure the response of the compact in terms of compaction/dilation, extension, and pore pressure, is to be included in the laboratory. It will be useful in characterizing both raw and prepared (e.g., spray dried) powders in terms of compaction, shear strength, and internal friction. It will also be useful in exploring powder forming processes such as die pressing and extrusion because arbitrary stress histories can be imposed by it.

   Status: Specification in preparation.

Status of milestones

No activity.

Publications

No activity.

1.2.4 Silicate Matrix

Mullite SiC Whisker Composites

S. Musikant and S. Samanta (General Electric Company)

OBJECTIVE/SCOPE

The objective of this program is to develop high toughness, high strength, refractory ceramic matrix composites which are amenable to low cost, near net shape forming for application to automotive engines.

In this program, the General Electric Company, Space Systems Division, is pursuing the development of SiC whisker reinforced mullite ($3\ Al_2O_3\ 2\ SiO_2$) matrix ceramic composite. In addition, the enhancement of the mullite matrix fracture toughness by the incorporation of transformation toughening by additions of $Zr_{0.5}Hf_{0.5}O_2$ is proposed. This mullite matrix composite can meet a very significant need in the ceramic heat engine technology. That specific need is for a low thermal conductivity, high strength, tough, hard and wear resistant ceramic with intrinsically good thermal shock resistance. The intrinsically good thermal shock resistance is due to mullite's moderately low modulus of elasticity, $\sim 30 \times 10^6$ psi (207 GPa), and relatively low coefficient of thermal expansion (CTE), $5 \times 10^{-6}/°C$, as well as good levels of strength. The thermal conductivity is low, being approximately equal to that of ZrO_2. Since the coefficient of thermal expansion (CTE) is about half that of ZrO_2, mullite experiences far lower thermal stresses than ZrO_2 when exposed to the same thermal gradient.

Similarly, in comparison to alumina, mullite is intrinsically superior with respect to thermal shock because of mullite's lower CTE and lower modulus of elasticity. Any matrix with a high CTE tends to have lower resistance to thermal shock.

The initial aim of the investigation is to prepare a composite with fracture toughness of $\geq 4.0\ MPa\sqrt{m}$.

In order to achieve this goal, we have initiated investigation of the mullite-SiC whiskers compositions with varying parameters. The major steps in this investigation are as follows:

1. Prepare mullite/SiC whisker compositions using fine particle size mullite powder. Whisker compositions may range between 15 and 30 wt %. Whiskers may be milled for size reduction before incorporating into a batch composition.

2. Investigate sintering aids which will assist in composite consolidation.

3. Investigate the addition of a transformation toughening agent, $Zr_{0.5}Hf_{0.5}O_2$, to mullite/SiC compositions to enhance the fracture toughness of the matrix material.

4. Consolidation methods include:

   (a) Cold isostatic pressing and sintering.
   (b) Hot isostatic pressing (HIP).
   (c) Cold isostatic pressing (CIP), sintering, and hot isostatic pressing (HIP).

5. Explore the application of coating materials to whiskers to control the bonding strength of whisker to matrix; incorporate diffusion barriers at the whisker/matrix interface to minimize chemical reactions between the matrix and whisker.

6. Characterize the composites for mechanical, physical, chemical and thermal properties at room temperature and at elevated temperatures.

TECHNICAL HIGHLIGHTS

MATERIALS AND PROCEDURES

During this initial phase of the investigation, experimental data on our hot pressed mullite-SiC whisker composites from an earlier IR&D program were reviewed. Table I lists the flexural strength or modulus of rapture (MOR), percent strain at failure and density of a few of such hot pressed composites. Based on these data, it appeared that a hot pressed (1700°C, 6200 psi, 1 hour) mullite-SiC whisker (SILAR SC-9 ARCO METALS) composite in 70/30 weight ratio yielded the highest MOR of about 56,000 psi at room temperature in three point flexure.

The primary objective of the current program is to develop a high density ($\geq$95%) composite without resorting to hot pressing. Thus, we have conducted a series of sintering experiments with several mullite-SiC whisker compositions (Table II) with and without a sintering aids. Two high-SiO_2 glasses in the SiO_2-Al_2O_3 system and niobium pentoxide, Nb_2O_5, were used as liquid phase sintering aids in order to enhance further densification during sintering. The SiO_2/Al_2O_3 glasses contain 95/5 and 85/15 mole % ratios of SiO_2/Al_2O_3. They are shown in the SiO_2-Al_2O_3 phase diagram in Figure 1. In some compositions, requisite amounts of Al_2O_3 were added so that the SiO_2/Al_2O_3 glasses would react with Al_2O_3 and would be converted into mullite phase during the final stage of sintering. In case of Nb_2O_5, it acts as a good liquid phase sintering aid and also it has a potential to form a carbide (NbC) diffusion barrier on the SiC whisker. A few compositions were also prepared, where the mullite matrix contained 10 vol % of $Zr_{0.5}Hf_{0.5}O_2$ used as a toughening phase.

SiC whiskers (SILAR SC-9) from ARCO Metals Co. have been used as the reinforcing phase. Initially, these whiskers were used in the as-received condition. Later on, they have been washed and cleaned by slurrying them in deionized water and thus getting rid of the floatable organic matters and fine particulate impurities. A series of experiments have also been performed using SC-9 whiskers, which have been planetary ball milled, dry or wet, for various periods of time (10 mins to 2 hrs). Milling of SiC whiskers is to reduce the L/d ratio and thus enhance ability to densify on sintering.

The baseline mullite (Baikowski mullite Ref. 193, planetary ball milled 1-½ hours), Baikowski mullite ball milled for 48 hours, and a newly available, deagglomerated, finer particle size variety of mullite (Ref. 193CR) also from Baikowski Corp. were investigated as the starting matrix material. Table III describes some characteristics of Baikowski Mullite 193CR and SC-9 whisker raw materials.

Various mullite-SiC whisker mix compositions were prepared. Their processing methods and densities (measured by water immersion-Archemedi's method) of the sintered composites have been summarized in Table II. In general, SiC whiskers and mullite matrix powder (with or without other powder additive materials) are blended together in a planetary mill for 15 minutes in order to achieve a homogeneous dispersion of whiskers in the matrix. Powder batches containing the whiskers were then pressed into a billet form (up to approx. 2.5" X 1" X 1") in a cold isostatic press (CIP) at 40,000 - 55,000 psi. Pressed billets were then sintered in air at 1650 - 1670°C for 3-3½ hours. Sintered composite billets exhibited a thin oxidized layer on the surface. A small piece (without the skin) was saw cut from each billet and the density was determined by immersion in water. Sintered composites have a greenish color, except those containing Nb_2O_5, which are blackish probably due to formation of a niobium carbide, NbC.

RESULTS AND DISCUSSIONS

Based on the data shown in Table II, it was observed that the use of slightly milled SiC whiskers improves the composite density (compositions Nos. 14-16). Milling the as-received whiskers (10-80 µm) for about ½ hour, wet or dry, in a planetary ball mill (PBM) broke down the major fraction of the fibers to $\leq$10-12 µm in length. Figures 2 and 3 show scanning electron microscope (SEM) photomicrograph of SiC whiskers in batch composition No. 14 (whiskers wet milled in PBM for ½ hour, dried and then PBM dry, 15 minutes) and after ½ hour PBM dry (whiskers used in compsitions Nos. 17 and 18). Figures 4 and 5 show fiber structures in powder batches of compositions Nos. 15 and 16 (whiskers wet PBM for 1 hour and 2 hours respectively). Figure 6 shows the presence of much longer whiskers in a batch of composition No. 19 prepared by wet dispersion and with unmilled whiskers.

Addition of ZrO_2-HfO_2 toughening agent (compositions Nos. 3, 4 6 and 13) did not exhibit any retained tetragonal in the system, probably because of high porosity in the sintered composites.

It was also observed that the new, finer, deagglomerated Baikowski mullite (Ref. 193CR) is superior to the earlier Baikowski mullite (Ref. 193) and thus the new mullite powder has been used in the latest batch compositions and will be used in future.

Also, as shown in Table II, density of the sintered composites ranged between approx. 80-91% theoretical. The highest density of about 91.1% theoretical was obtained with the composition No. 20 containing mullite/SiC whiskers/Nb_2O_5 in 70/30/10 weight ratio. The addition of two SiO_2-Al_2O_3 glasses as a sintering aid in the same proportion (10 wt. ratio) produced about 87-88% dense material (compositions Nos. 22 and 23).

It was interesting to note, however, that it was possible to achieve approximately 90-91% density (compositions Nos. 24 and 25) even without adding any sintering aid. The use of new, finer mullite matrix powder as well as milled (½ hour PBM), purer (washed and cleaned) SiC whiskers probably contributed to such improved densification on sintering.

Microstructures of the polished sections of a few sintered composites examined by SEM are shown in Figures 7 to 10 (compositions Nos. 20, 22, 24 and 25 respectively). In general, they exhibit random but rather uniform distribution of whiskers in the matrix. The whisker lengths are usually seen to be ≤ 5 μm.

CONCLUSIONS

Mullite/SiC whisker composites (70/30 wt %), prepared by cold isostatic pressing followed by sintering, yielded approximately 91% dense material with or without a sintering aid. It is believed that sintered material should be improved to $\geq 95\%$ density (no open porosity) in order to densify it further by hot isostatic pressing (HIP'ing), without containerization). For a net shape process, sintering followed by a containerless HIP'ing is the preferred route. For a low density sintered material, canning or encapsulation of the material followed by HIP'ing will be needed to achieve high density (>95% theoretical).

FUTURE WORK

As mentioned earlier, the primary objective at the current stage of investigation is to achieve a high density composite without resorting to hot pressing. In order to be able to HIP a material directly (containerless) it is necessary to achieve at least 95% dense material after sintering. Otherwise, it is imperative that a lower density, sintered material needs to be canned or encapsulated first so that it can be HIP'ed and densified further. Thus, the future work is planned as follows:

(1) Continue to investigate the use of Nb_2O_5, a glass or other sintering aid(s) (possibly in larger proportions) to achieve further densification during sintering of mullite-SiC whiskers composites. If such a composite material having $\geq 95\%$ density is achieved after sintering, it will be further densified by containerless (no encapsulation) HIP'ing.

(2) Investigate HIP'ing of sintered composites after they are encapsulated or canned in a refractory metal (like, molybdenum,tantalum, or niobium) or silica glass to produce denser composites.

(3) Further investigate the wet dispersion technique to produce more homogeneous batch compositions of mullite and milled SiC whiskers.

(4) Measure mechanical properties (MOR and K_{IC} at room as well as elevated temperatures) and determine microstructures of sintered and HIP'ed, dense, composites prepared.

Table I

Hot Pressed Compositions (1700°C, 1 Hour, 6200 psi)

No.	Composition, Parts by Weight					Modulus of Rupture		Maximum Strain (%)	Density (g/cm^3)	(% Theoretical)
	Mullite	SiC Whisker	Eutectic Glass	Al_2O_3	Nb_2O_5	(KSI)	(MPa)			
CCHP841	70	30	5	11.4	-	42.35	292	0.112	3.05	97.1
CCHP842	70	30	-	-	5	37.73	260	0.105	3.19	98.5
CCHP843	60	40	-	-	-	36.05	249	0.108	3.00	94.1
CCHP844	85	15	-	-	-	43.21	298	0.113	3.07	96.8
CCHP845	70	30	-	-	-	48.88	337	0.169	2.92	92.0
CCHP6	70	30	-	-	-	56.05	386	0.15	3.05	95.9
CCHP7	100	-	-	-	-	27.02	186	0.08	3.14	99.0

NOTE: 3 Point bend bars, 0.750" X 0.125" X 0.050", 0.50" span

Raw Materials:

Mullite - As received Baikowski Mullite , Ref 193
SiC Whisker - ARCO Metals SILAR SC-9 in CCHP841-4 and CCHP6
Tateho Chemical SCW #1 in CCHP845 only.
Eutectic Glass - 95 m% SiO_2/5 m% Al_2O_3
AL_2O_3 - calcined catapal SB (Conoco Chemicals)
Nb_2O_5 - Kenametal Corp.

TABLE II

MULLITE-SiC WHISKER COMPOSITES

NO.	COMPOSITION, PARTS BY WEIGHT						PROCESSING CONDITIONS	(% THEORETICAL)
	MULLITE	SiC WHISKERS	Nb_2O_5	GLASS I	GLASS II	AL_2O_3		
1	70 (1)	30 (1)					Blended in planetary mill for 15 minutes, isostatically pressed at 40,000 psi and sintered at 1650°C in air for 3-3½ hours. Sintered billets ~ 2.5" X 1.0" X 1.0"	83.7
2	80 (1)	20 (1)					"	80.6
3	70 (2)	30 (1)					"	84.6
4	80 (2)	20 (1)					"	80.9
5	70 93)	30 (1)					"	84.6
6	70 (4)	30 (1)					"	84.5
7	70 (5)	30 (1)					"	85.5
8	70 (5)	30 91)		10		24	Same as above, except the powder batch was CIP-ed at 55,000 psi.	82.6
9	70 (5)	30 (1)		30		72	"	80.0
10	70 (5)	30 (1)			10	18.5	Same as above, except sintered at 1670°C/3 Hrs	81.4

TABLE II (CONTINUED)

NO.	COMPOSITION, PARTS BY WEIGHT						PROCESSING CONDITIONS	DENSITY (% THEORETICAL)
	MULLITE	SiC WHISKER	Nb_2O_5	GLASS I	GLASS II	Al_2O_3		
11	70 (5)	30 (1)			30	55.5	Same as above, except sintered at 1670°C/3 Hrs	81.3
12	70 (1)	30 (2)					Same as above, except sintered at 1650°C/3 Hrs. Sintered billets ~ 1.0" X 0.6" X 0.6".	83.6
13	70 (2)	30 (2)					"	85.4
14	70 (1)	30 (3)					Same as above, except sintered at 1670°C/3 Hrs	88.0
15	70 (1)	30 (4)					"	87.7
16	70 (1)	30 (5)					"	86.0
17	70 (1)	30 (6)	5				"	86.6
18	70 (1)	30 (6)	10				"	90.8

TABLE II (CONTINUED)

NO.	COMPOSITION, PARTS BY WEIGHT						PROCESSING CONDITIONS	DENSITY (% THEORETICAL)
	MULLITE	SiC WHISKERS	Nb_2O_5	GLASS I	GLASS II	AL_2O_3		
19	70(1)	30 (1)					Prepared by wet dispersion mixing in a Waring blender at PH 11.0, re-adjusted the PH to 7.0, concentrated the slurry by boiling off water and then dried. Dry batch powder CIP-ed at 55,000 psi, and sintered at 1670°C/3 Hrs	84.6
20	70 (5)	30 (7)	10				Mullite and Nb_2O_5 first blended in a planetary mill for 15 minutes, dry; whiskers added and then blended for another 15 mins: the batch material then CIP-ed at 55 KSI and sintered at 1670°C for 3 hours; sintered billets $\simeq$ 2¼" X 1" X 1"	91.1
21	85 (5)	15 (7)	10				"	Did not sinter well; seems quite porous.
22	70 (5)	30 (7)		10			Mullite and glass powders first blended together in planetary mill for 15 minutes and then blended for another 15 mins with whiskers added. The batch is then CIP-ed at 55 KSI and sintered at 1670°C/3 Hrs	87.7

TABLE II (CONTINUED)

NO.	COMPOSITION, PARTS BY WEIGHT						PROCESSING CONDITIONS	DENSITY (% THEORETICAL)
	MULLITE	SiC WHISKERS	Nb_2O_5	GLASS I	GLASS II	AL_2O_3		
23	70 (5)	30 (7)			10		"	87.1
24	70 (5)	30(7)					Blended together in a planetary mill for 15 mins, CIP-ed at 55 KSI and sintered at 1670°C/3 Hrs	90.9
25	70 (5)	30 (7)					Same as for composition #19	90.9

TABLE II (CONTINUED)

NOTE: Raw Materials

- Mullite (1) - Baikowski mullite (Ref. 193), planetary ball milled (PBM), wet, 1-1½ hours, dried and planetary ball milled, dry, 15 minutes
- SiC Whiskers (1) - SILAR SC-9 from ARCO Metals Co.
- Mullite (2) - Mullite (1) and 1:1 molar ZrO_2-HfO_2 in 90/10 V% ratio, planetary ball milled, dry, 15 minutes
- 1:1 molar ZrP_2-HfO_2 - Prepared by sol-gel method, dried, calcined 750°C /2 hours, wet planetary ball milled 8 hours, dried and then planetary ball milled for 15 minutes.
- Mullite (3) - Baikowski mullite, ball milled, wet, 48 hours, dried and planetary ball milled, dry, 15 minutes
- Mullite (4) - Mullite (3) and 1:1m ZrO_2-HfO_2 in 90/10 V% ratio, planetary ball milled, dry, 15 minutes
- Mullite (5) - New, deagglomerated, as-received Baikowski mullite (Ref: 193CR)
- SiC Whiskers (2) - Whisker (1) PBM, dry, 10 minutes
- SiC Whisker (3) - Whisker (1) PBM, wet, ½ hour, dried and PBM, dry, 15 minutes
- SiC Whisker (4) - Same as whisker (3), except PBM, wet, 1 hour
- SiC Whisker (5) - Same as whisker (3), except PBM, wet, 2 hours
- SiC Whisker (6) - Same as whisker (2), except PBM, dry, ½ hour
- SiC Whiskers (7) - SILAR SC-9 from ARCO Metals Co. (Whisker #1)
  Washed and cleaned by suspending the whiskers in deionized water and separating the blackish floatables and fine particles in the top aqueous layer; good whiskers, settled at the bottom, were then dried, and planetary ball milled for ½ hour.
- Nb_2O_5--325 mesh, Kenametals Co.
- Glass I - SiO_2/Al_2O_3, 95/5 mole %, melted and ground, -325 mesh
- Glass II - SiO_2/Al_2O_3, 85/15 mole %, melted and ground, -325 mesh

TABLE III

STARTING MATERIALS

- BAIKOWSKI MULLITE (193 CR) ($3\ Al_2O_3 \cdot 2\ SiO_2$)

  MINIMUM PURITY: >99.2%
  >98% CONVERTED TO MULLITE PHASE

  AGGLOMERATE SIZE DISTRIBUTION

CUMULATIVE	WEIGHT	PERCENT
<1.0	μm	24
<1.5	μm	34
<3.0	μm	85
<6.0	μm	100

- ARCO METALS SiC WHISKER (SILAR SC-9)

  WHISKER CONTENT: 80 - 90%
  DIAMETER: 0.6 μm
  LENGTH : 10-80 μm
  TENSILE STRENGTH $\simeq 1 \times 10^6$ PSI

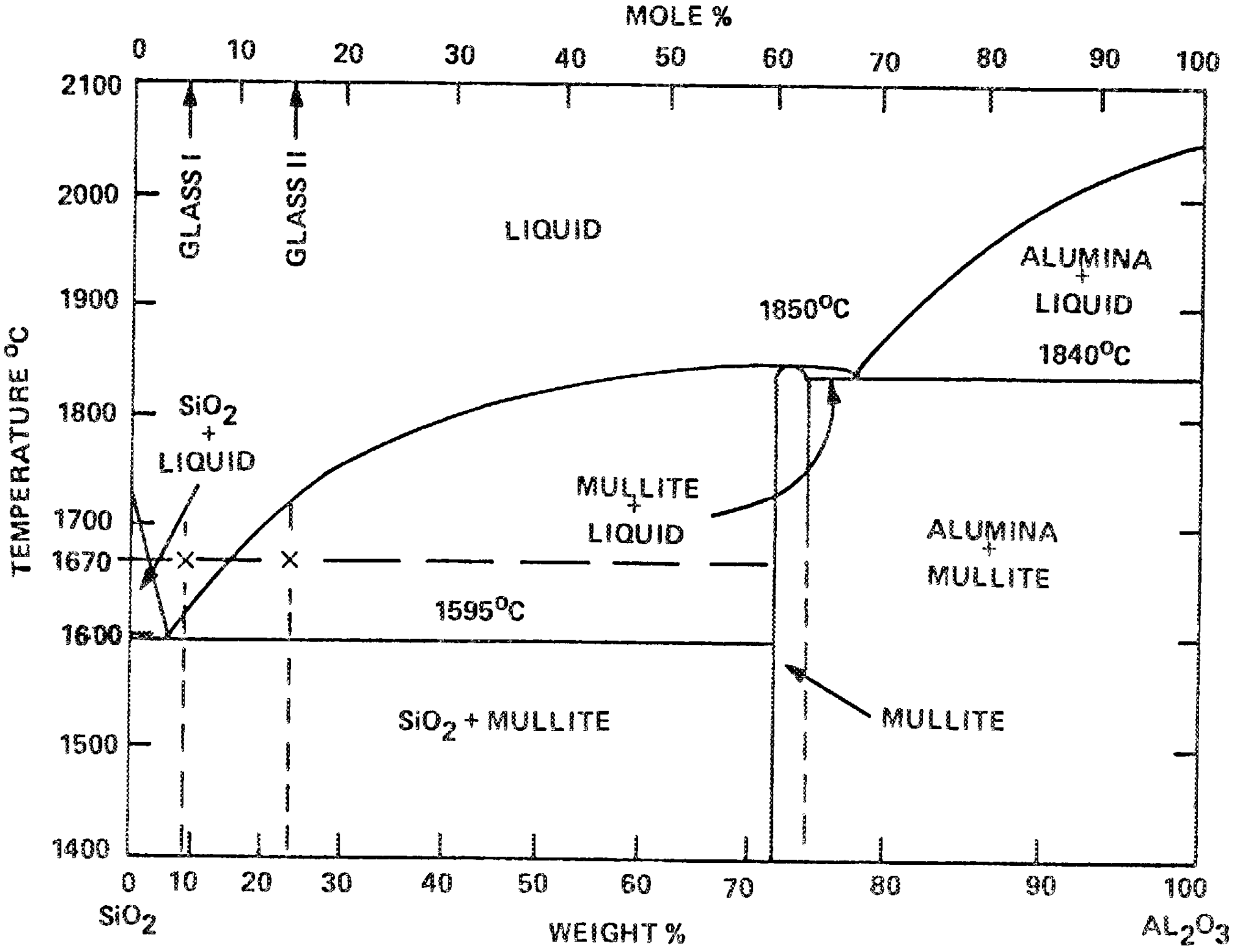

Figure 1 SiO_2-Al_2O_3 Phase Diagram (Aramaki & Roy 1962) - Glass I & Glass II Sintering Aids

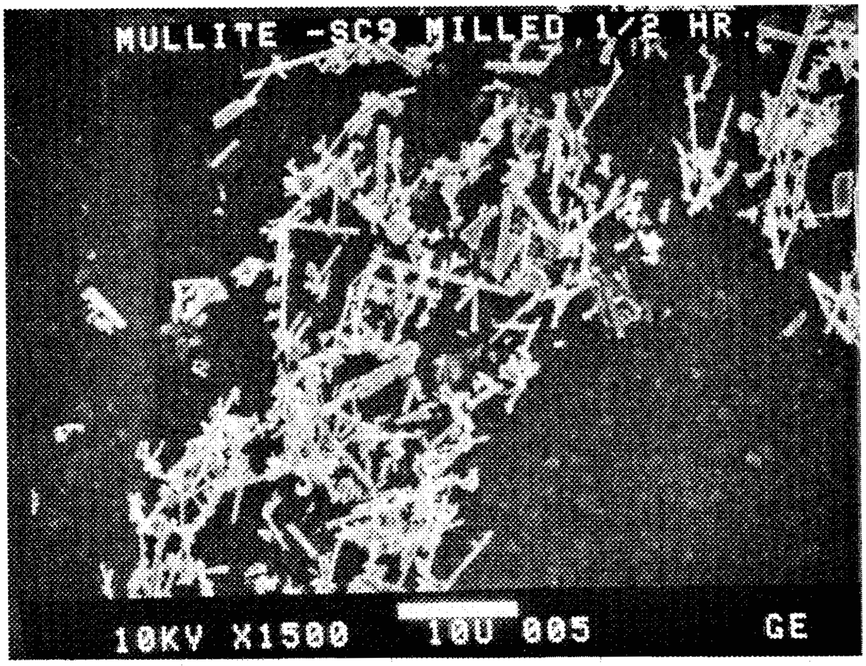

Figure 2: 1/2 hour PBM, wet, SiC whiskers in composition #14 batch

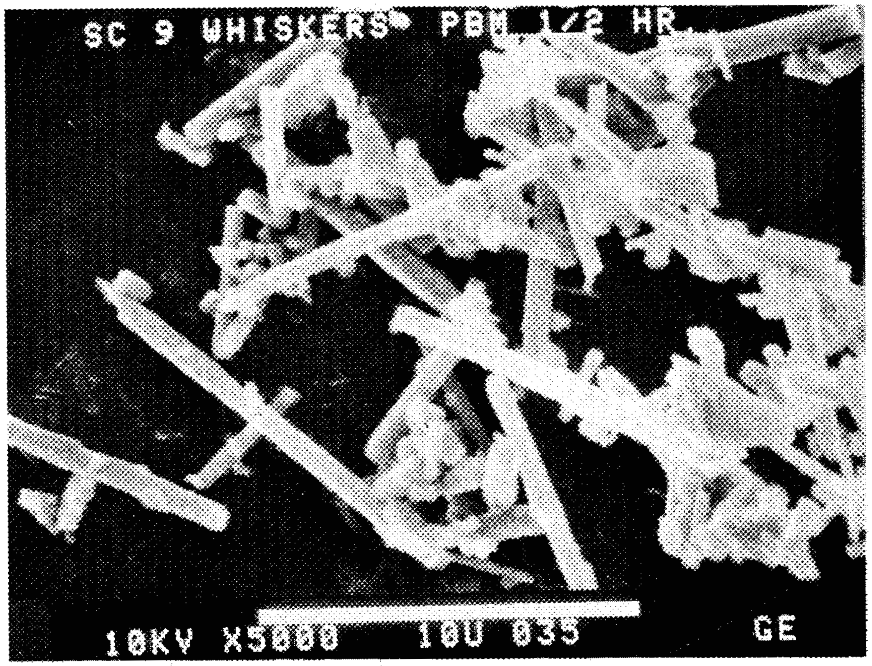

Figure 3: 1/2 hour PBM, dry, SiC whiskers

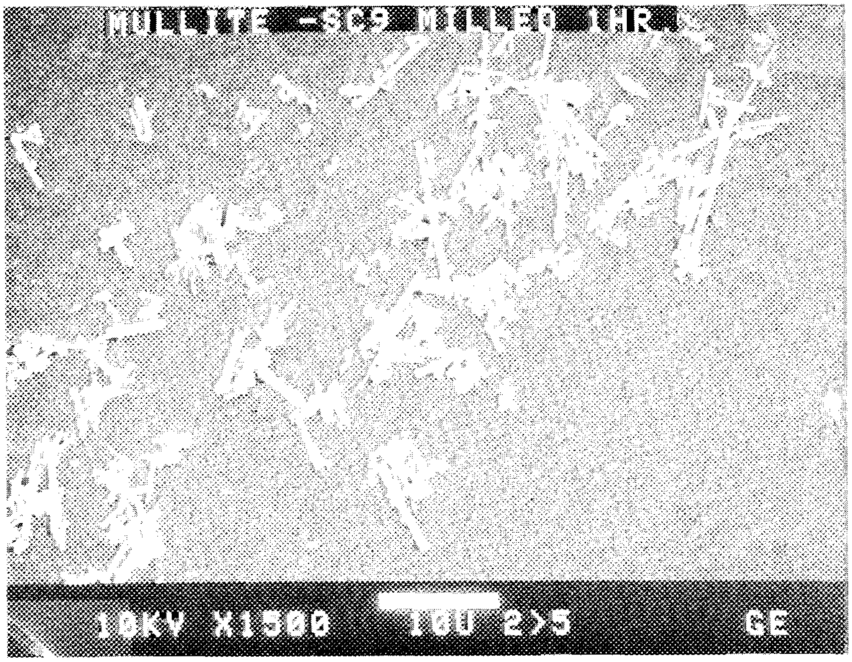

Figure 4: 1 hour PBM, wet, SiC whiskers in composition #15 batch

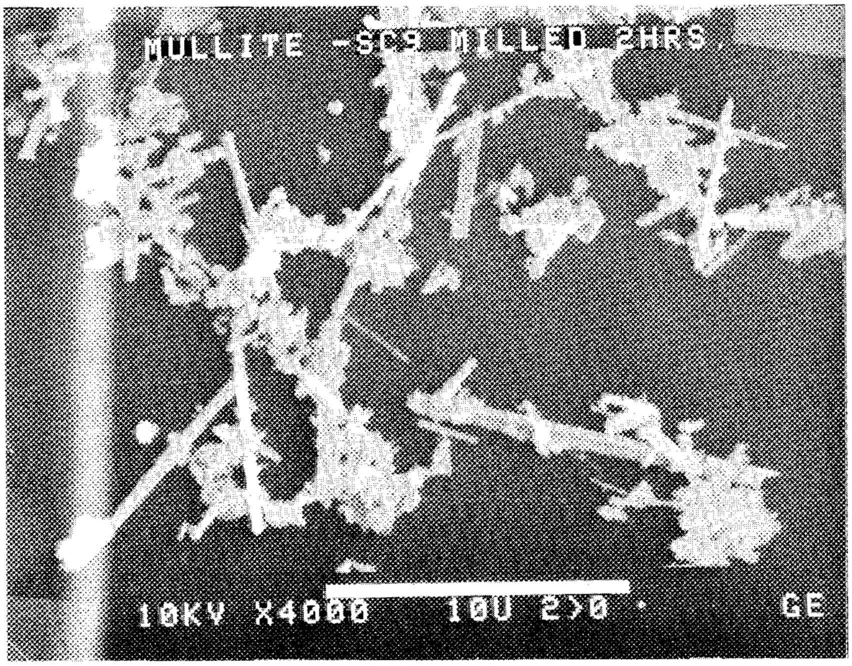

Figure 5: 2 hours PBM, wet, siC whiskers in composition #16 batch

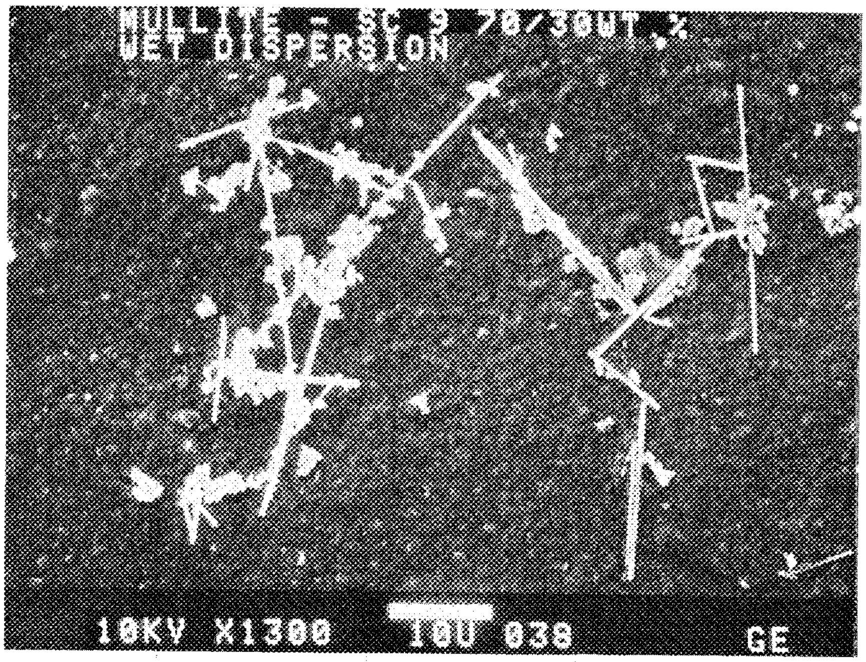

Figure 6: Unmilled SiC whiskers in batch composition #19

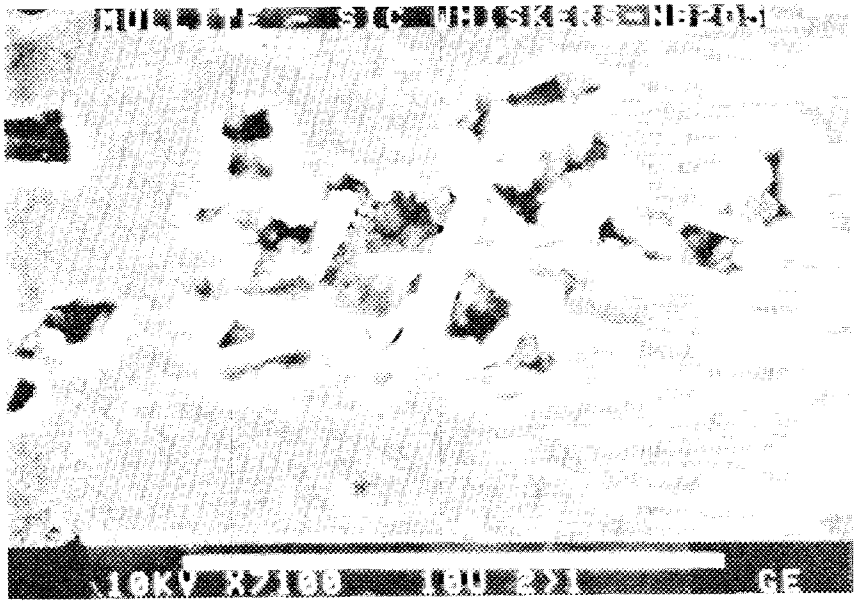

Figure 7 Mullite/SiC Whiskers Composite with Nb_2O_5 Sintering Aid

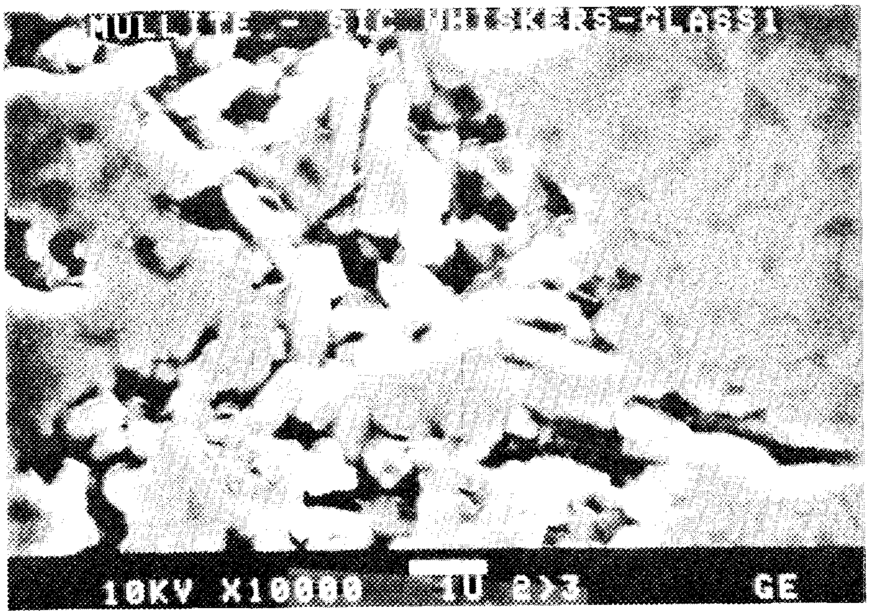

Figure 8 Mullite/SiC Whiskers Composite With Glass I Sintering Aid

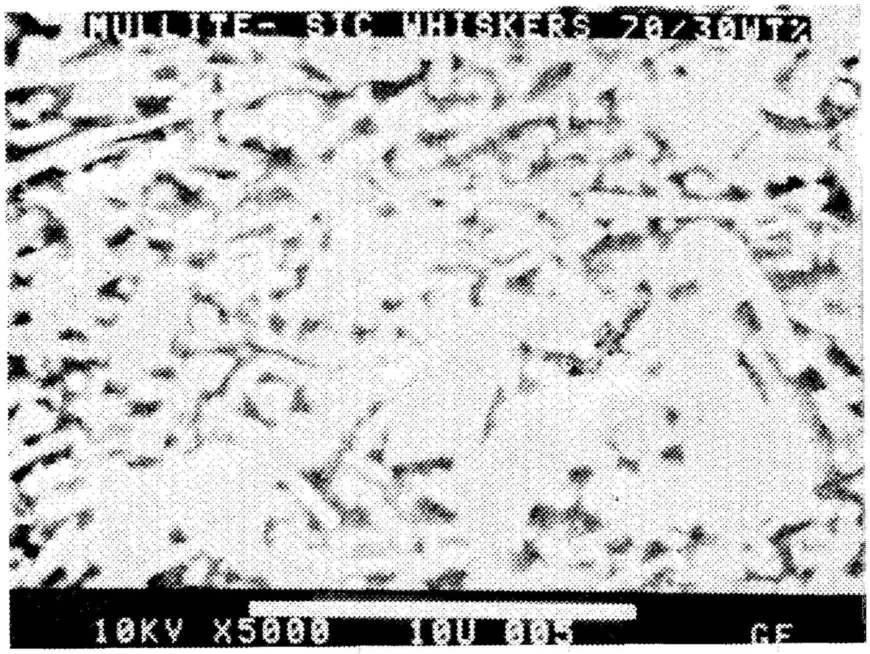

Figure 9 Mullite/SiC Whiskers Composite 70/30 Wt % - Dry Blended

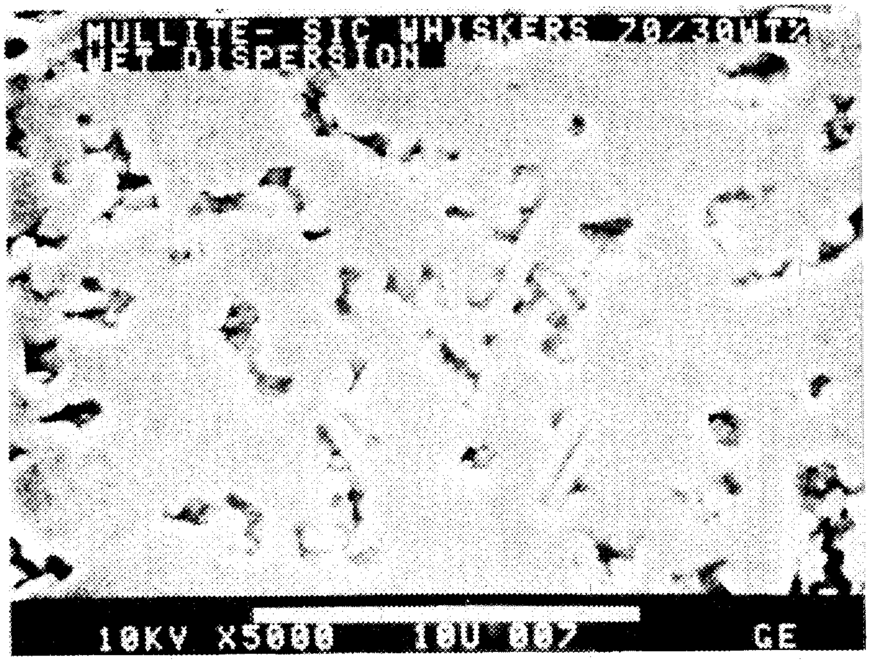

Figure 10 Mullite/SiC Whiskers Composite 70/30 Wt % - Wet Dispersion

1.3 THERMAL AND WEAR COATINGS

ZrO_2-Cr_2O_3 Coating Evaluation

T. M. Yonushonis (Cummins Engine Company, Inc.)

Objective/scope

The objective of this program is to improve the understanding of the processing-microstructure-property relationships of chrome oxide based coatings and chrome oxide infiltrated plasma sprayed zirconia. The chrome oxide wear coatings have been applied to cylinder liners for wear protection, while plasma sprayed zirconia has been used for thermal protection of piston crowns in advanced adiabatic engines.

Technical progress

The abstract of the final report for this program follows:

CHARACTERIZATION OF CHROMIUM OXIDE BASED CERAMIC COATINGS FOR ADVANCED HEAT ENGINES

T. M. Yonushonis

ABSTRACT

The purpose of this investigation was to improve the understanding of the protective chromium oxide based coatings used as critical wear surfaces and zirconia coatings used as insulation for metal components in advanced diesel engines.

This investigation focused on the coatings developed by Kaman Sciences Corporation which were chromium oxide based coatings. A limited portion of this program concentrated on plasma sprayed zirconia coatings which have been infiltrated with the chromium oxide coatings after the plasma spray process. The zirconia coatings were supplied by Plasma Technics. The baseline substrate materials were gray cast iron and ductile iron.

The program consisted of three major tasks:

Task 1 — Microstructural and Property Characterization
Task 2 — Friction and Wear Characterization
Task 3 — Post-Engine Test Coating Characterization

The Task 1 investigation on chromium oxide ceramic coatings confirmed that optical and electron beam microscopy techniques are well developed for microstructural and chemical characterization. The Kaman SCA coating consists of alpha-quartz, chromium oxide and alumina. An interfacial layer was detected between the coating and the iron substrate which consisted of an iron-chromium solid solution.

The techniques for measuring physical properties of thin coatings, properties such as density, adherence, fracture toughness, and elastic modulus are not well defined for heterogeneous coatings. Serious gaps exist in the technology to determine these properties which are necessary for structural analysis and eventually performance prediction of ceramic coatings on metallic substrates. Therefore, the development of ceramic protective coatings will continue to rely on empirical rig and engine tests to define coating performance.

Task 2, Friction and Wear Characterization, was conducted using a block-on-ring test machine, ASTM Practice G77-83. A 2^4 factorial experimental design was used to minimize the number of tests and assist in the interpretation of the results. The coefficients of friction and wear volumes were analyzed by regression analysis procedures. Major conclusions from friction and wear tests pointed out potential problem areas (increased ring wear anticipated with harder liner coatings), detected interactions between the lubricant/load combinations (SE/CD 15W-30 lubricant at low load had a significantly higher coefficient of friction than any other combination of variables evaluated), and lubricant/line interactions (gray iron blocks tested with SE/CD 15W-30 lubricant had higher average wear volumes).

The Task 3, Post-Engine Test Coating Characterization was conducted on cylinder liners and turbocharger housings coated with Kaman SCA. Evaluation of the liners revealed that the coatings performed satisfactorily. However, some coating removal has been observed during engine testing.

Key areas that must continue to be addressed include coating reliability, durability, cost reduction, and measuring techniques for quantifying the properties of thin coatings.

1.4 JOINING

1.4.1 Ceramic-Metal Joints

Active-Metal Brazing of PSZ to Iron

M. L. Santella, J. P. Hammond, and S. A. David (Oak Ridge National Laboratory)

Objective/scope

The purpose of this work is to develop brazing processes for joining ceramic insulation components to nodular cast iron (NCI) for adiabatic diesel engine applications. Foremost of these applications is the attachment of the ceramic piston cap. Presently, the lead candidate material for the ceramic piston cap is partially stabilized zirconia (PSZ), Nilsen grade MS, with dispersion toughened alumina (DTA) as an alternate. Promising brazing methods and the mechanical properties of prototypical brazements are evaluated so that reliable joining processes may be transferred to industry.

Technical progress

During the last reporting period, important observations and accomplishments were made in the areas of mechanical testing, microstructural characterization of braze joints, and scale-up of the active substrate process. The enlarged shear testing apparatus was used to test several braze joints at 400°C. These results, along with previously obtained room-temperature results, are presented in Table 1. The ZrO_2/Ti interface was evaluated by using titanium-sputter-coated Nilsen MS zirconia pads and pure titanium bars. The Fe/Ti interface was evaluated with grade 8003 nodular cast iron pads and pure titanium bars. The interfaces were vacuum brazed with 604 filler metal at 735°C. Three of the ZrO_2/Ti joints and one of the Fe/Ti joints were tested. As Table 1 shows, the shear strength

Table 1. Shear strength data on the active substrate process interfaces tested at 25 and 400°C

Interface	Test temperature (°C)	Shear strength (MPa)
ZrO_2/Fe	25	137
ZrO_2/Ti	25	140
ZrO_2/Ti	400	28
Fe/Ti	25	253
Fe/Ti	400	150

of the ZrO_2/Ti interface at 400°C was only 20 to 25% of its typical room-temperature value. The shear strength of the Fe/Ti interface was about 60% of its room-temperature value. While a reduction in shear strength at elevated temperature was expected, the low strength of the ZrO_2/Ti interface prompted a careful microstructural evaluation of these joints.

All of the ZrO_2/Ti specimens, whether tested at 25 or 400°C, fractured at the zirconia—braze filler metal interface, so it was decided to examine these surfaces in detail in the scanning electron microscope (SEM). Figure 1(*a*) shows the typical appearance of a zirconia surface. Small braze filler metal fragments remain stuck to the zirconia, but the surface appears to have been relatively unaffected by brazing and shear testing. Figure 1(*b*) shows the typical appearance of a braze filler metal surface at the zirconia interface. This surface mates directly to that shown in Fig. 1(*a*). It is obvious from Fig. 1(*b*) that a considerable amount of porosity was formed at the zirconia—braze filler metal interface. This condition was observed over the entire area of contact for all of the ZrO_2/604 interfaces examined. In some instances the contact area of the braze alloy on the zirconia was reduced by as much as 60%. This situation would be expected to degrade mechanical properties at room temperature as well as at 400°C.

A major effort is being directed toward elimination of the type of porosity described above. Many variations of the original active-substrate brazing process have been tried, and it now appears that modification of the coating process can produce braze joints that are free of porosity. A comparison of braze joints made by the standard and modified methods is shown in Fig. 2. Once it is well established that the porosity can be eliminated, mechanical testing will continue.

In the scale-up effort the active substrate process was used to braze 11.5-cm discs of titanium-sputter-coated zirconia (furnished by Coors) to cast iron with a titanium transition piece. This demonstration braze is shown in Fig. 3. After brazing, the diameter of the assembly was dressed by surface grinding to a final dimension of 11.2 cm. The appearance of the braze was excellent. However, ultrasonic examination indicated that several unbonded areas existed around the circumference of the assembly and near its center as shown in Fig. 4. The circumferential defects are due in part to splices that were made in the braze foil, and they probably can be eliminated with refinements to our assembly techniques. The central unbonded region was shown by analysis of ultrasonic rf waveforms to be located at the zirconia—braze alloy interface. Subsequent sectioning and metallographic analysis indicated that this unbonded area resulted from coalescence of the type of porosity shown in Fig. 1.

Status of milestones

On schedule.

Publications

None.

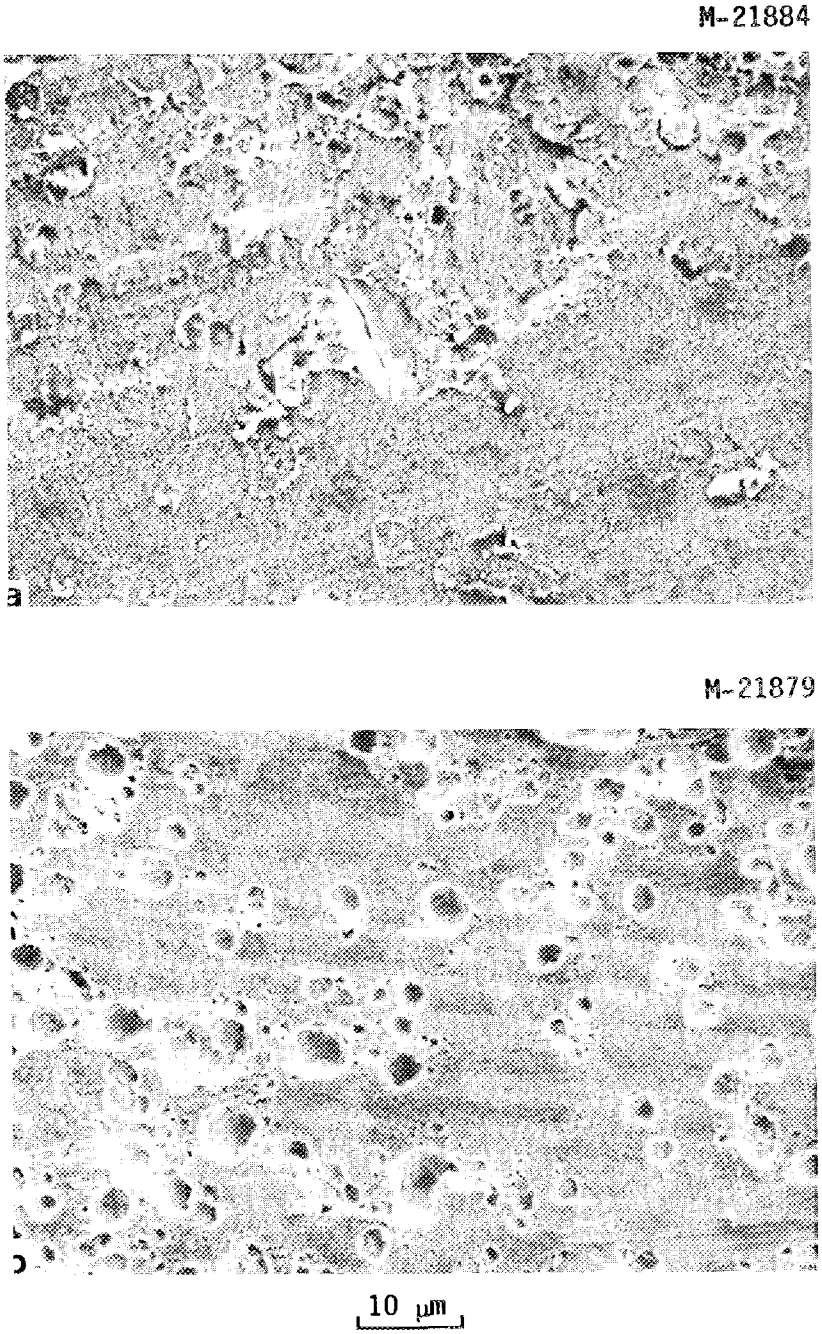

Fig. 1. Scanning electron micrographs of ZrO_2/Ti braze shear test specimen. (*a*) Zirconia fracture surface. (*b*) Braze alloy fracture surface.

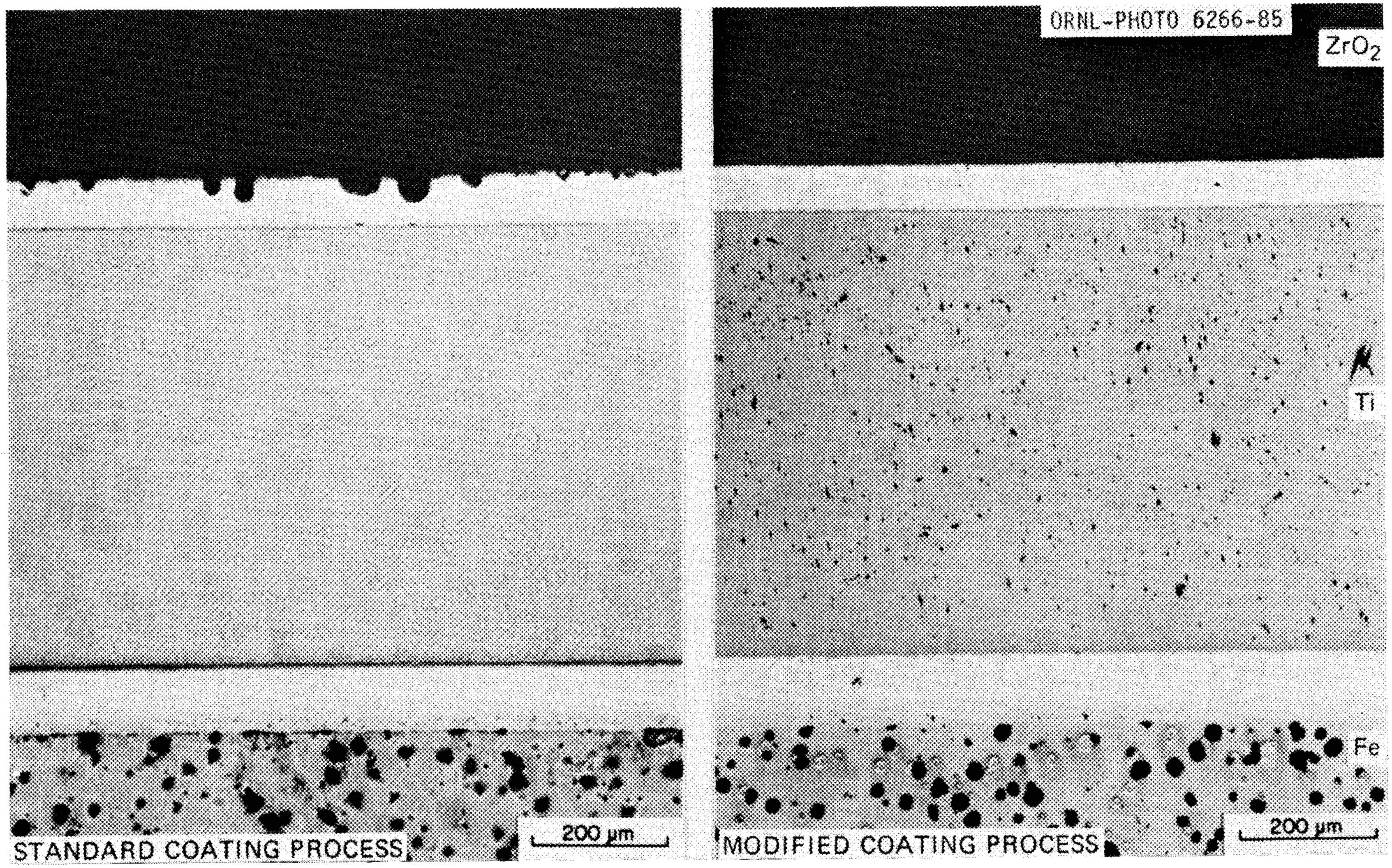

Fig. 2. Comparison of active substrate braze joints showing that modification of the sputter coating process can eliminate porosity at the zirconia surface.

YP419

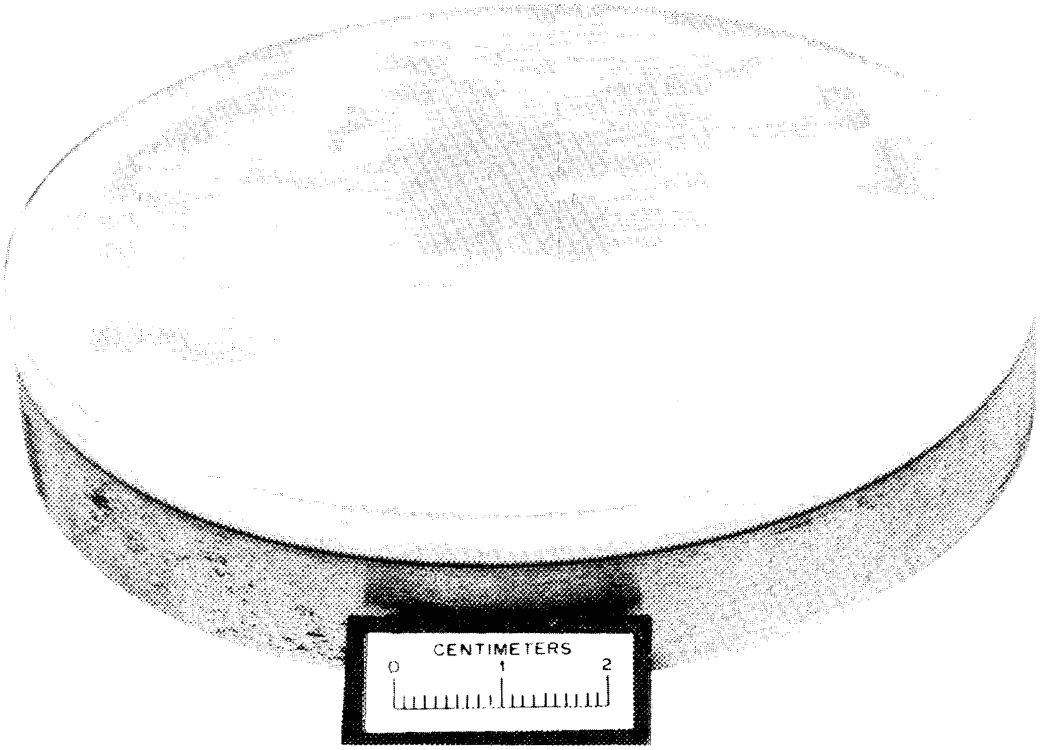

Fig. 3. Piston cap demonstration brazed by the active substrate method.

ORNL PHOTO 6269-85

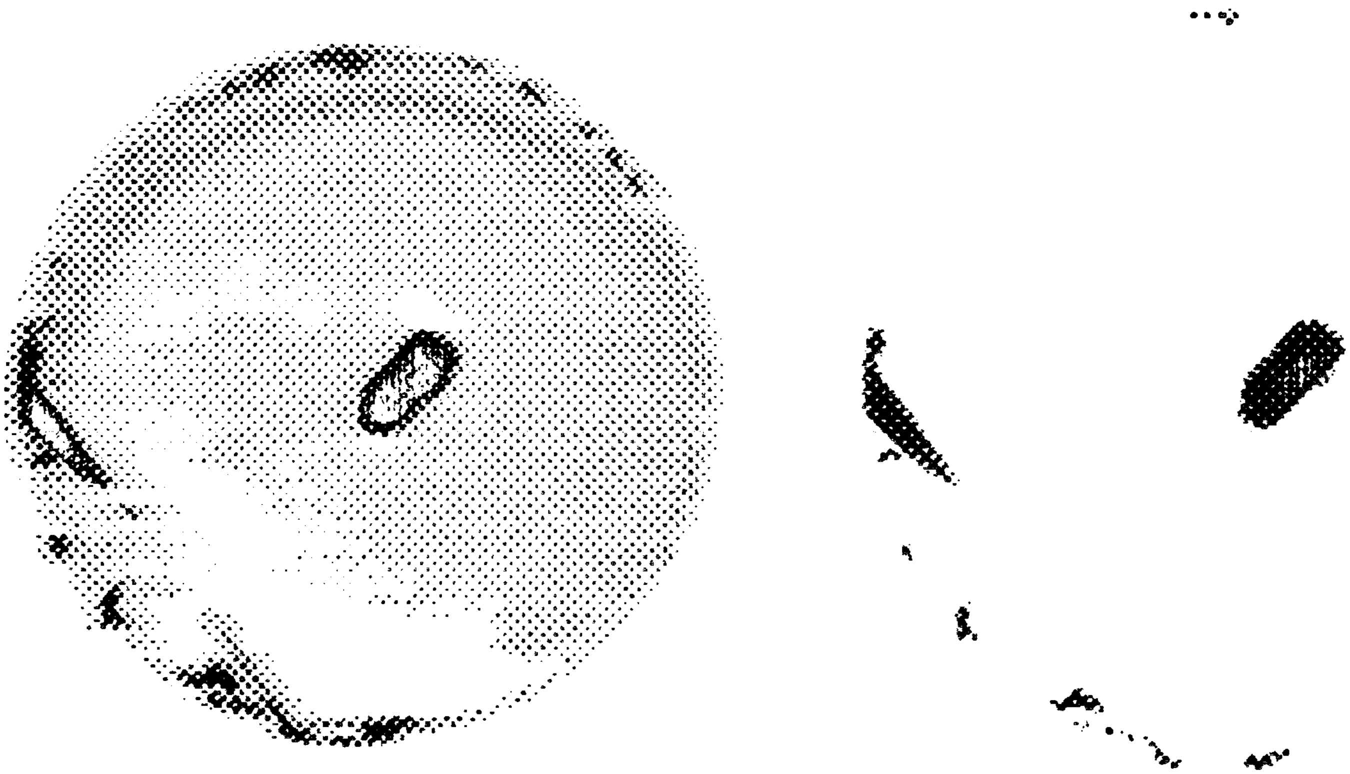

EXPANDED GRAY SCALE

COMPRESSED GRAY SCALE

Fig. 4. Ultrasonic scan of piston cap demonstration braze showing unbonded areas. The raw pixel data have been enhanced by computer processing.

2.0 MATERIALS DESIGN METHODOLOGY

INTRODUCTION

This portion of the project is identified as project element 2 within the work breakdown structure (WBS). It contains three subelements: (1) Three-Dimensional Modeling, (2) Contact Interfaces, and (3) New Concepts. The subelements include macromodeling and micromodeling of ceramic microstructures, properties of static and dynamic interfaces between ceramics and between ceramics and alloys, and advanced statistical and design approaches for describing mechanical behavior and for employing ceramics in structural design.

The major objectives of research in Materials Design Methodology elements include determining analytical techniques for predicting structural ceramic mechanical behavior from mechanical properties and microstructure, tribological behavior at high temperatures, and improved methods for describing the fracture statistics of structural ceramics. Success in meeting these objectives will provide U.S. companies with methods for optimizing mechanical properties through microstructural control, for predicting and controlling interfacial bonding and minimizing interfacial friction, and for developing a properly descriptive statistical data base for their structural ceramics.

2.2 CONTACT INTERFACES

2.2.1 Static Interfaces

High Temperature Coating Study to Reduce Contact Stress Damage of Ceramics

J. L. Schienle (Garrett Turbine Engine Company)

Objectives/scope

The objective of this research program is to develop coating compositions and procedures that will yield long term adherence and reduce or eliminate contact-stress damage to silicon nitride (Si_3N_4) and silicon carbide (SiC) ceramics. Prior studies[1-3] have determined that Si_3N_4 and SiC ceramics are susceptible to contact stress damage at ceramic-ceramic and ceramic-metal interfaces in heat engines. Subsequent studies have demonstrated a reduction or elimination of contact-stress damage to these ceramics using plasma-sprayed oxide coatings, but the coating adherence was not adequate for long term use.

This program utilizes an alternate coating method, electron beam physical vapor deposition (EB-PVD), as the coating process because of high control of composition, thickness, and morphology. Three substrate materials were selected for this study: reaction-bonded Si_3N_4 (RBSN), sintered Si_3N_4 (SSN), and sintered SiC (SSC).

The present program scope consists of four technical tasks to be conducted over 31 months:

- Task 1 - Coating Adherence and Characteristics Investigation
- Task 2 - Advanced Pretreatment and Coating Studies
- Task 3 - Contact Stress Testing and Friction Measurements
- Task 4 - Post-Contact Strength Measurements

Technical progress

During this reporting period, Task 2 (Advanced Pretreatment and Coating Studies) was completed. The emphasis of Task 2 was to evaluate the coating adherence of several systems, and to select the best of these for evaluation in Task 3. Task 2 consisted of seven subtasks:

Subtask 1: Oxidation. This subtask studied oxidation-adherence relationships in baseline specimens (the baseline zirconia coating on as-machined substrates). The objective of this subtask was to achieve a better understanding of the oxidation-degradation of baseline coating adherence observed in Task 1 of the program.

Subtask 2: Oxygen Diffusion Barrier. Under this subtask, efforts were made to avoid or minimize coating adherence degradation due to substrate oxidation (identified as a primary source of reduced adherence during Task 1) by depositing an oxygen diffusion barrier between the substrate and the coating. A secondary objective was to select an interlayer which has increased chemical adherence to both the substrate and the coating.

The candidate interlayers were chemical vapor deposited (CVD) alumina, CVD AlN, EB-PVD alumina, EB-PVD mullite, and sol-gel alumina.

Subtask 3: High Purity Interlayer. This subtask evaluated the potential of using high purity CVD SiC as an interlayer between the substrate and standard zirconia coating to improve coating adherence.

Subtask 4: Diffusion/Gradation Zone. The objective of this subtask was to explore techniques that might chemically root the zirconia coating to the substrates. Candidate techniques were ion implantation and ion mixing.

Subtask 5: Coating Variations. Studies with metal substrates have determined that coating adherence can be increased by increasing coating temperature. Prior plasma spray studies suggest a similar condition for ceramic substrates. This subtask evaluated the effect of coating at temperatures 56C higher than used in Task 1.

Subtask 6: Surface Preparation. Adherence of Task 1 specimens was strongly influenced by surface topography of the original substrate. This subtask explored techniques of roughening the surface. Candidates included 150-grit machining (compared to 320 grit), HF etching, and laser machining.

Subtask 7: Mullite Coating. The objective of this substask was to determine if columnar mullite could be deposited by EB-PVD on RBSN, SSN, and SSC. Mullite is a better oxygen barrier than zirconia and has a closer thermal expansion match to the SiC and Si_3N_4 substrate materials.

Experimental procedures

Materials. Three substrate materials were selected for this investigation: (1) reaction-bonded silicon nitride (RBSN), (2) sintered silicon nitride (SSN), and (3) sintered silicon carbide (SSC). The RBSN and SSC were selected because substantial baseline strength and contact damage data were available. The SSN was selected to provide a nonporous Si_3N_4 to compare with the porous RBSN. Billets of RBSN and SSN were obtained from the AiResearch Casting Company, Torrance, California, and SSC billets were obtained from the Carborundum Company, Niagara Falls, New York. The billets were longitudinally ground with a 320-grit diamond wheel into 2 x 0.250 x 0.125 inch test bars, which were subsequently subjected to different pretreatments under the various subtasks of Task 2 (the various pretreatment procedures are described in the Results section under their respective subtasks). Following pretreatment, all specimens (except those under subtasks 5 and 7) were coated at Temescal with the baseline EB-PVD zirconia coating. The baseline coating is zirconia stabilized with 20-percent yttria applied at 982C and is approximately 75 to 125 μm in thickness. A typical coating microstructure resulting from baseline processing procedures is illustrated in Figure 1.

Characterization. Three techniques were utilized for coating adherence evaluations: flexural testing, indentation testing, and line contact testing.

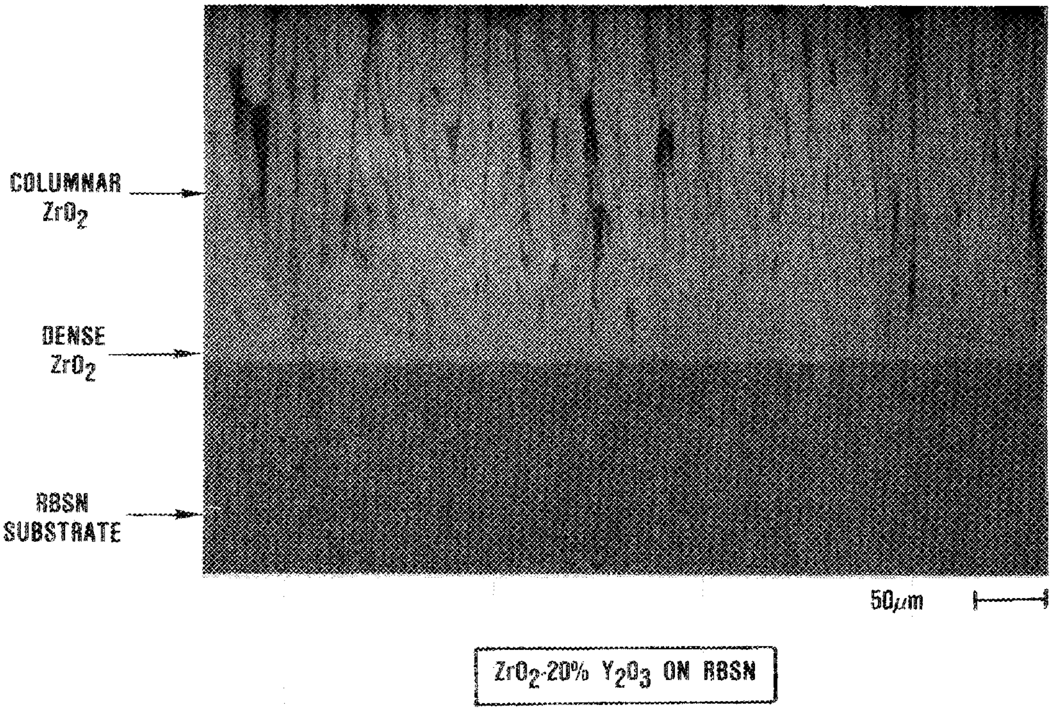

Figure 1. The baseline coating is graded from dense at the interface to columnar.

Flexural testing was conducted at room temperature in four-point bending with the coated side of the specimen in tension. The purpose of this test was to determine the effect of a mechanical shock (from fracture) on the coating adherence. Observation of coating integrity in the contact area under the flexural load pins also was utilized to assess adherence.

Indentation testing consisted of applying a Vickers' indentation normal to the coating. Four tests are conducted per specimen at loads of 5, 10, 20, and 30 kg. The radius of coating uplift or debond area is used to assess coating adherence. Typical examples of indented specimens are illustrated in Figure 2.

Line contact testing involved sliding a line contact load across the coating. The contact rig utilized in this program is illustrated in Figure 3. With this apparatus, a normal force is applied to the specimen through a dead weight load system while a tangential force is applied through displacement of the crosshead. Prior studies identified the criticality of this loading mode in assessing contact stress damage[1-3]. Four tests were conducted per specimen with loads of 9.1, 13.6, 18.2, and 22.7 kg. The crosshead displacement was 1.52 mm. Visual observations were used to qualitatively assess coating adherence. Typical line contact tested specimens are illustrated in Figure 4.

Specimens were tested for coating adherence in both the as-coated condition and after static air oxidation exposures. In the selection of coating/interlayer/substrate systems recommended for evaluation in Tasks

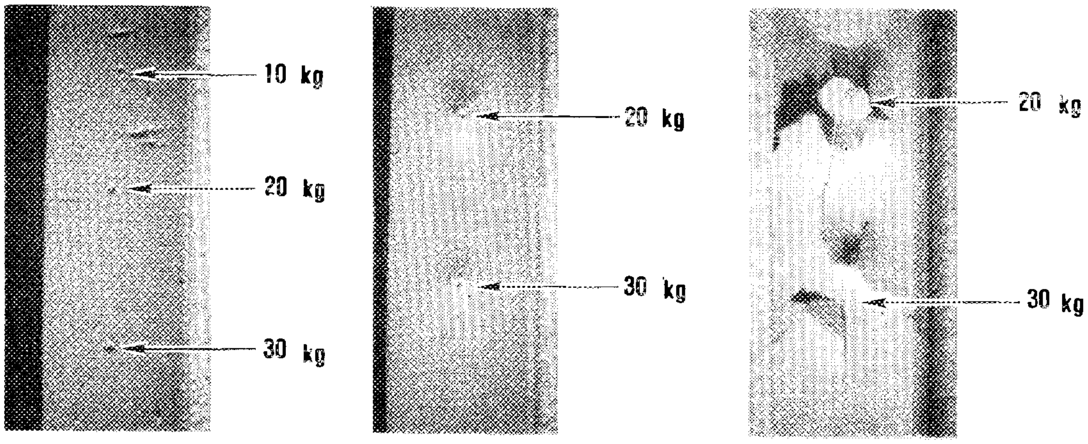

EXCELLENT ADHERENCE

FAIR ADHERENCE

POOR ADHERENCE

Figure 2. A Vickers' indentation was applied normal to the coating for coating adherence assessment.

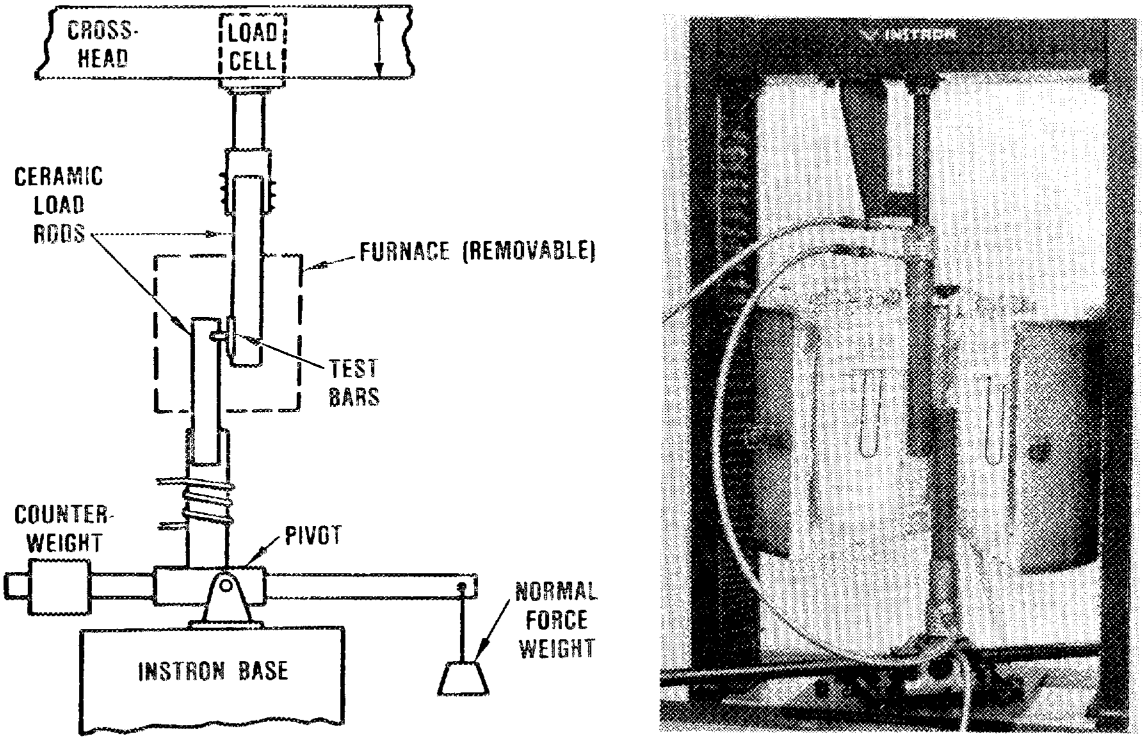

Figure 3. Garrett's line contact rig was used to assess coating adherences.

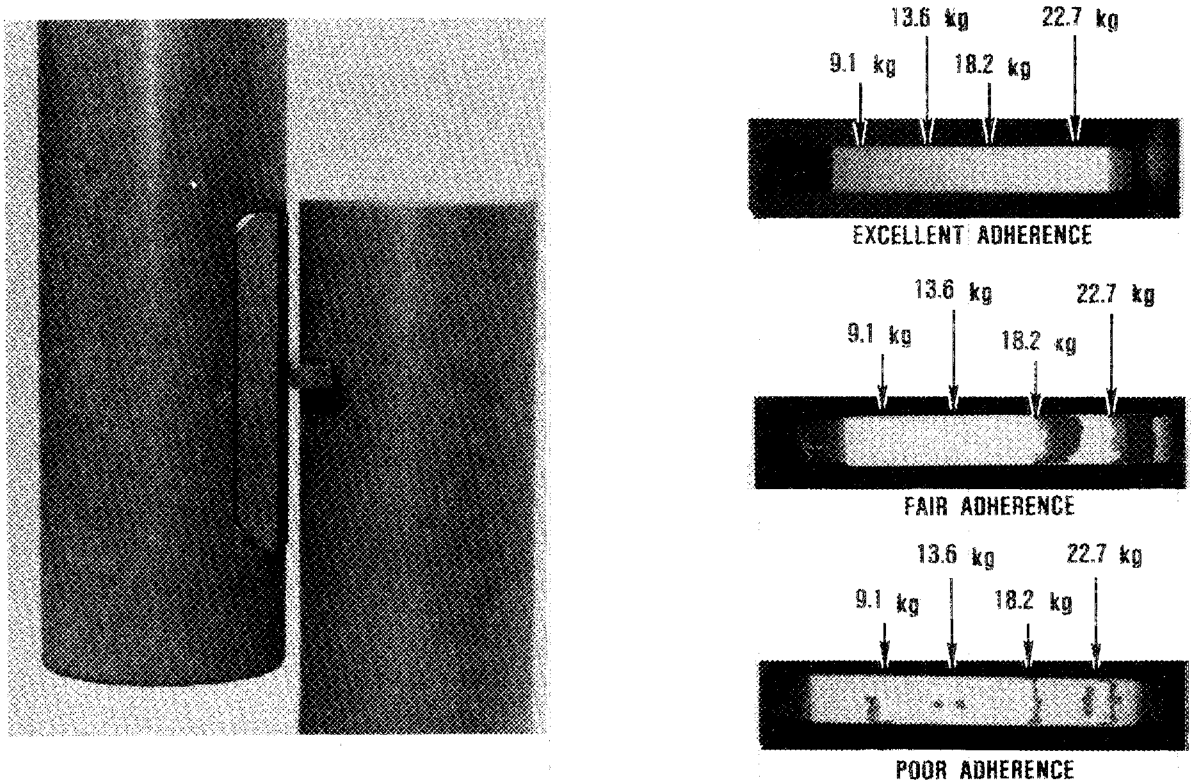

Figure 4. A line contact under a normal load is slid across the coating surface to produce a biaxial load. Visual observations are used to assess coating adherences.

3 and 4, decisions were biased towards adherence results after oxidation exposures since these coatings are intended for use in heat engine applications.

Results

Subtask 1: Oxidation. Baseline specimens were subjected to various static air oxidation heat treatments and adherence was assessed by flexure testing. Based on visual examination of the coating/substrate systems after flexure testing, adherence was judged to be good to excellent for as-coated specimens. However, the adherence degraded significantly for all substrates after 100-hour/1200C static air exposures. This degradation was similar to that observed after 24-hour/1200C exposures in Task I evaluations. Longer duration heat treatments (200 hours versus 100 hours at 1200C) did not result in any additional degradation in adherence, suggesting stabilization of the interface. However, higher temperature exposures (1400C versus 1200C for 200 hours) resulted in decreased adherence for the RBSN and SSN substrates but not for the SSC substrates suggesting that the ZrO_2/substrate interface is more stable for SSC than for RBSN and SSN at higher temperatures.

Subtask 2: Oxygen Diffusion Barrier. CVD alumina coatings 2 to 2.5-μm thick were applied at 920C to the three substrate materials at Kennametal's Philip M. McKenna Laboratory. The as-coated alumina was a mixture of alpha and kappa phase Al_2O_3. The specimens were heat treated in air at 1200C for 20 hours to convert the kappa-alumina to the alpha phase. X-ray diffraction after heat treatment indicated complete conversion.

CVD AlN coatings approximately 2 to 3-μm thick were deposited at G.A. Technologies using a fluidized bed.

EB-PVD alumina coatings approximately 1 μm in thickness were applied by Temescal. The oxygen partial pressure in the coating chamber was adjusted to give two variations of coating: stoichiometric Al_2O_3 and non-stoichiometric (Al-rich) Al_2O_3.

EB-PVD mullite coatings were attempted by Temescal. However, mullite could not be successfully applied by EB-PVD techniques. The silica in the mullite material source tends to evaporate more easily than the alumina, resulting in silica rich coating.

Sol-gel alumina coatings were applied by Signal UOP Research Center. The specimens were dipped in alumina sol, air dried, then calcined in air for 2 hours at 1200C. The resulting coating was approximately 0.5-μm thick.

Zirconia coated specimens containing an oxygen diffusion barrier interlayer were evaluated for coating adherence. The results are summarized in Table 1. CVD Al_2O_3 and CVD AlN yielded the best adherence for RBSN substrates. The CVD Al_2O_3/RBSN system resulted in excellent as-coated adherence of the zirconia coating with essentially no decrease in adherence after a 100-hour/1200C oxidation exposure. This result

Table 1. Subtask 2 (oxygen diffusion barriers) adherence results.

Substrate	Interlayer	Flexure	Indentation		Contact
RBSN	CVD Al_2O_3	-*	3*	3**	3**
	CVD AlN	0	1	3	3
	PVD Al_2O_3 (stoich.)	2	2	0	2
	PVD Al_2O_3 (non-stoich.)	0	0	0	0
	Sol-gel Al_2O_3	3	1	0	2
SSN	CVD Al_2O_3	-	1	0	1
	CVD AlN	0	1	1	0
	PVD Al_2O_3 (stoich.)	1	1	0	1
	PVD Al_2O_3 (non-stoich.)	0	0	0	0
	Sol-gel Al_2O_3	3	1	1	2
SSC	CVD Al_2O_3	-	2	0	1
	CVD AlN	0	0	1	1
	PVD Al_2O_3 (stoich.)	1	1	0	2
	PVD Al_2O_3 (non-stoich.)	0	0	0	0
	Sol-gel Al_2O_3	1	2	1	2

0 = Poor, 3 = Excellent

*Results in column are for as-coated specimens

**Results in column are for specimens with post-coat heat treatments suggests that the CVD alumina oxidation diffusion barrier is preventing degradation of the interface during oxidation exposure. The CVD AlN/RBSN system resulted in relatively poor adherence of the zirconia coating in the as-coated condition, but excellent adherence after oxidation exposure. EDX analysis of a spalled surface on an as-coated flexure tested specimen detected only Al and no Si. This suggests that the PVD zirconia spalled from the AlN interlayer but the AlN interlayer remained adherent on the substrate. The increased adherence of the zirconia coating observed after oxidation exposure suggests chemical interaction between the zirconia coating and AlN interlayer. Optical and SEM analysis of the interface before and after oxidation exposure also suggests a change in interfacial characteristics (Figure 5).

CVD Al_2O_3 and CVD AlN resulted in only poor to fair adherence of the zirconia coating on SSN and SSC substrates. For SSN and SSC, sol-gel Al_2O_3 resulted in the best adherence. Zirconia coating adherence was fair both before and after an oxidation exposure of 100 hours at 1200C suggesting that the alumina interlayer is protecting the interface from degradation. The adherence for SSC was slightly better than SSN. The remaining oxygen diffusion barriers resulted in relatively poor adherence for SSN and SSC substrates.

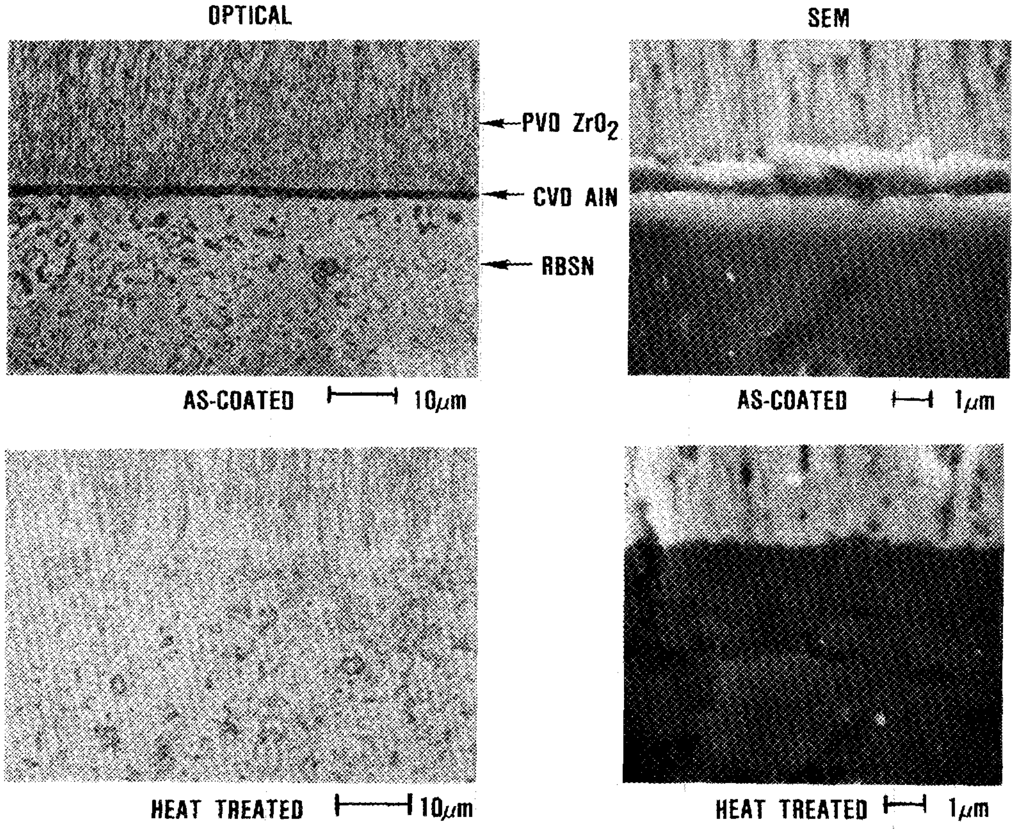

Figure 5. Optical and SEM analysis of the ZrO_2/AlN/RBSN interface before and after oxidation exposure suggests a change in interfacial characteristics.

Subtask 3: High Purity Interlayer. In-house specimens of SSC having CVD SiC coatings applied by San Fernando Laboratories were used in this evaluation. EB-PVD zirconia was applied over the CVD SiC interlayer. The specimens were tested both as-coated and after 100-hour/1200C heat treatments using indentation and line contact techniques. Both as-coated and oxidation exposed specimens exhibited poor coating adherence in all cases. Based on these preliminary results, efforts were not extended to the RBSN and SSN substrates.

Subtask 4: Diffusion/Gradation Zone. Substrates of each material were sputtered with an aluminum overlay then ion implanted with nitrogen at ORNL. These specimens were then heat treated 8 hours at 1200C in air in an effort to form an Al_2O_3 layer and were subsequently zirconia coated. Preliminary analysis using contact testing to evaluate oxidation exposed specimens suggested poor adherence for all three substrates. Other candidate approaches included ion implanting the substrates with aluminum and zirconium. However, the program scheduling did not permit analysis of these systems.

Subtask 5: Coating Variation. As-machined specimens of all three substrate materials were EB-PVD zirconia coated at 1038C(1800F) instead of at the standard temperature of 982C (1900F). Visually, these coatings seemed as clean and as adherent as the 982C coatings. The specimens were subjected to various static air heat treatments (24 hours/1200C, 100 hours/1200C, 24 hours/1400C, and no heat treatment), and then evaluated for coating adherence using flexure testing and indentation testing. Adherence was good to excellent for as-coated specimens, however, coating adherence degraded significantly after a 24-hour/1200C heat treatment. Longer duration heat treatments (100 hours) did not result in further degradation of adherence. Higher temperature exposures (1400C for 24 hours) resulted in additional adherence degradation for RBSN and SSN substrates but not for SSC. These results reflect the general poor adherence characteristics observed for baseline coatings evaluated in Task 1 of the program.

Subtask 6: Surface Preparation. Surface roughening techniques were evaluated for their effect on surface topography and potential to improve mechanical adherence of the baseline ZrO_2 coating. Three techniques were evaluated: 150-grit machining (versus 320 grit), HF etching, and laser machining.

150-Grit Machining. Baseline substrates (320-grit finish) were machined on one face using a 150-grit diamond wheel. The roughened faces were subsequently coated with EB-PVD zirconia. These specimens were evaluated for coating adherence before and after 100-hour/1200C oxidation exposures. Adherence was good to excellent in the as-coated condition and poor after oxidation. These results suggest 150-grit machining does not have a significant effect on coating adherence relative to 320-grit machining.

HF Etching. An HF etch study was conducted to determine the effect of etch treatments on the surface topography of as-machined and oxidized substrates. The surface topography was characterized using SEM and the results are shown in Figure 6. The SEM results suggest that HF etching

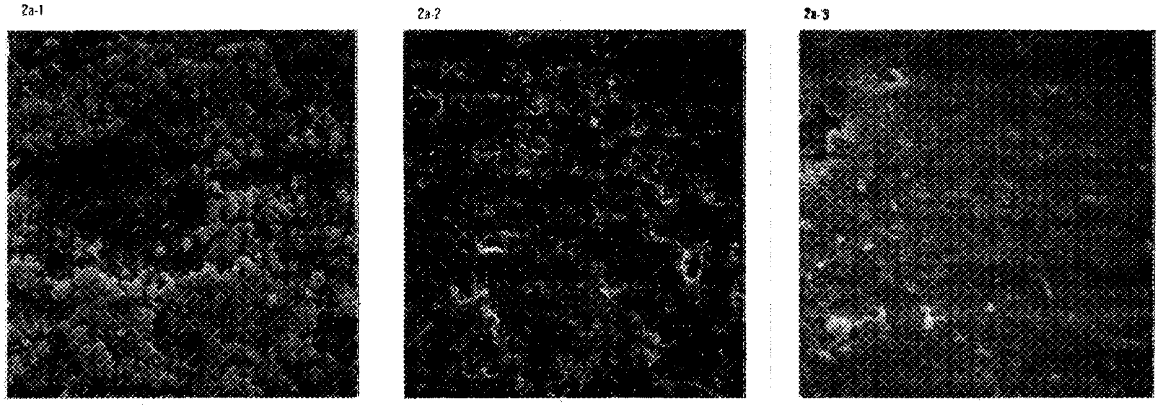

BASELINE RBSN

BASELINE RBSN WITH
10-MINUTE HF ETCH

OXIDIZED RBSN WITH
10-MINUTE ETCH

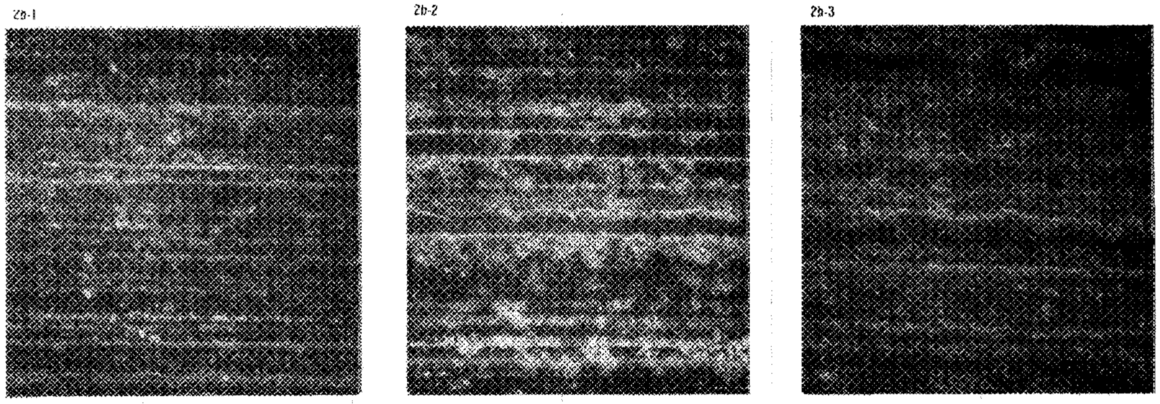

BASELINE SSN

BASELINE SSN WITH
10-MINUTE HF ETCH

OXIDIZED SSN WITH
10-MINUTE HF ETCH

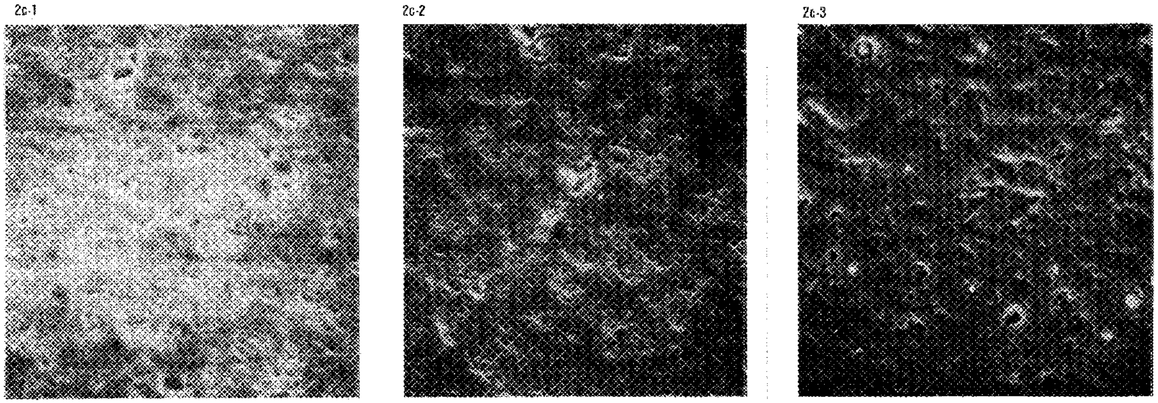

BASELINE SSC

BASELINE SSC WITH
10-MINUTE HF ETCH

OXIDIZED SSC WITH
10-MINUTE HF ETCH

Figure 6. SEM micrographs showing the surface topography of baseline and oxidized substrates after HF etching suggest HF etching would not improve mechanical adherence.

produces a surface topography that would not significantly enhance mechanical interlocking with the zirconia coating, and therefore should not significantly improve coating adherence. In addition, the etch treatments reduced substrate strength in most cases. Therefore, this study was not extended to include the evaluation of zirconia coating adherence.

Laser Machining. Substrates of RBSN, SSN, and SSC were texturized using a 1.2-kw CO_2 laser. The laser was operated in a pulsed mode at 20 to 30 percent of the rated power to produce a matrix of dots with approximately one diameter spacing. Currents of 200, 150, and 300 amps were used for RBSN, SSN, and SSC, respectively. Preliminary studies showed a strength reduction of about 20 percent for the substrate materials. However, the pits produced by the laser were very acicular, measuring approximately 0.1-mm in diameter and 0.3-mm deep. The current was subsequently reduced to 125, 100, and 200 amps for RBSN, SSN, and SSC, respectively in an attempt to reduce cavity depth. The resulting decrease in cavity depth was significant for SSC (cavities were approximately 0.1-mm deep). However, RBSN and SSN exhibited little change in cavity depth. Laser machined specimens were EB-PVD coated with zirconia and evaluated for coating adherence using indentation and contact testing. Evaluation of SSC by indentation showed excellent adherence for both as-coated and heat treated specimens. Good adherence was observed for both as-coated and heat treated RBSN and SSN specimens. Contact testing was conducted on heat treated specimens only. The results are shown in Figure 7. In contrast to the indentation results, poor adherence was observed for RBSN and SSN while SSC exhibited good adherence. The results for SSC were encouraging because good adherence was achieved without having an oxygen diffusion barrier to prevent oxidation of the substrate. SSC's better adherence is believed to be due to the surface topography and not the substrate material. RBSN and SSN had very deep surface cavities, which were not successfully penetrated by the PVD ZrO_2 as observed on the spalled test surfaces. SSC had much smaller cavities, which were successfully penetrated. ZrO_2 was still adherent inside the surface cavities after the coatings had spalled for all three substrates. Only the walls of the cavities appeared coated for RBSN and SSN, but the surface cavities were completely filled for SSC. Therefore, the adherence of the RBSN and SSN substrates may be improved to the degree observed for laser machined SSC substrates by reproducing SSC's surface topography on RBSN and SSN.

Subtask 7: Mullite Coating. Mullite could not be applied to the substrates by EB-PVD techniques at Temescal. The silica in the mullite material source tends to evaporate more easily than the alumina resulting in a silica rich coating. These efforts paralleled those under Subtask 2 for EB-PVD mullite oxygen diffusion barriers. Efforts under both subtasks were terminated.

Conclusions

Task 2 adherence assessment results for all specimens with post-coating static air heat treatments are summarized in Tables 2 and 3. This

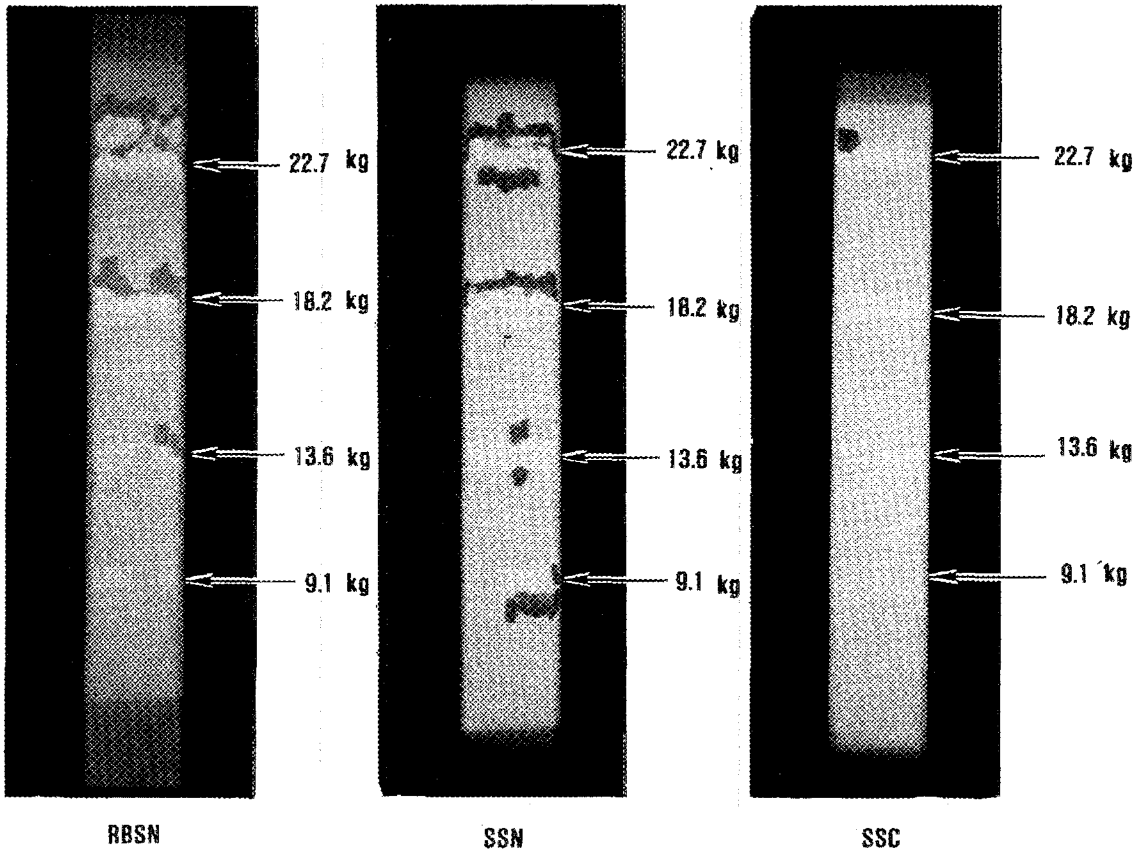

Figure 7. Laser machining substrates resulted in power adherence for RBSN and SSN and good adherence for SSC.

information was used to select systems recommended for evaluation in Task 3. Task 2 efforts did not result in a single pretreatment that yielded adequate adherence for all three substrate materials. Therefore, two pretreatments were selected for each substrate material (the Revised Scope of Work, ID 86K/48271 dated February 13, 1985, defined that only two pretreatments could be selected for Task 3 investigations). Table 4 summarizes the ranking of the systems based on the information in Tables 2 and 3. Based on these results, the pretreatments listed in Table 5 appear to be the best for their respective substrate materials and are recommended for evaluation in Task 3.

Table 2. Indentation results.

Pretreatment	RBSN	SSN	SSC
150-grit machined	Poor	Poor	Poor
Laser machined	Good	Good	Excellent
CVD Al_2O_3	Excellent	Poor	Poor
Sol-gel Al_2O_3	Poor	Fair	Fair
PVD Al_2O_3 (stoich.)	Poor	Poor	Poor
PVD Al_2O_3 (non-stoich.)	Poor	Poor	Poor
CVD AlN	Excellent	Fair	Fair
CVD SiC	--	--	Poor

Table 3. Line contact testing results.

Pretreatment	RBSN	SSN	SSC
150-grit machined	Good	Good	Fair
Laser machined	Poor	Poor	Good
CVD Al_2O_3	Excellent	Fair	Fair
Sol-gel Al_2O_3	Good*	Good*	Good*
PVD Al_2O_3 (stoich.)	Good*	Fair*	Good*
PVD Al_2O_3 (non-stoich.)	Poor	Poor	Poor
CVD AlN	Excellent**	Poor	Fair
CVD SiC	--	--	Poor

*Lower than typical coefficient of friction
**Not tested in rig, but manually scraped

Table 4. Task 2 adherence ranking.

Pretreatment	RBSN	SSN	SSC
150-grit machined	2	2	1
Laser machined	2	2**	5
CVD Al_2O_3	6	1	1
Sol-gel Al_2O_3	2	3	3
PVD Al_2O_3 (stoich.)	2	1	2
PVD Al_2O_3 (non-stoich.)	0	0	0
CVD AlN	6	1	2
CVD SiC	--	--	0

*Rankings assigned to pretreatment/substrate combinations by giving numerical values to qualitative results in Tables 2 and 3 (poor = 0, fair = 1, good = 2, excellent = 3) then adding Tables 2 and 3 together (0 = worst, 6 = best)

**Chosen over 150 grit machining because potential for improvement exists.

Table 5. Coating systems suggested for task 3.

RBSN	SSN	SSC
CVD alumina CVD AlN	Sol-gel alumina Laser machining	Sol-gel alumina Laser machining

Status of Milestones

Task 2 was completed during this reporting period. Task 3 will be initiated as soon as ORNL concurrence is obtained on the selection of coatings for investigation.

Publications

No publicatons were prepared beyond the Bi-monthly Technical Progress and Contract Management Summary Reports which were submitted in April, June, and August 1985.

References

1. D.W. Richerson and K.M. Johansen, "Ceramic Gas Turbine Engine Demonstration Program", Final Report, DARPA Contract N00024-76-C-5352, Garrett Report 21-4410, May 1982
2. D.W. Richerson, W.D. Carruthers, and L.J. Lindberg, "Contact Stress and Coefficient of Friction Effects on Ceramic Interfaces", Surfaces and Interfaces in Ceramic and Ceramic Metal System, Berkeley, CA, July 29-30, 1980
3. J.R. Smyth and D.W. Richerson, "High Temperature Dynamic-Contact Behavior of Sintered Alpha Silicon Carbide", Ceramic Engineering and Science Proceedings, Vol. 4, No. 7-8, 1983, pp. 663-673

2.2.2 Dynamic Interfaces

Studies of Dynamic Contact of Ceramics and Alloys for Advanced Heat Engines

K. F. Dufrane, W. A. Glaeser, and A. L. Rosenfield (Battelle Columbus Laboratories)

Objective/Scope

The objective of the study is to develop mathematical models of the friction and wear processes of ceramic interfaces based on experimental data. The supporting experiments are to be conducted at temperatures to 1200 F under reciprocating sliding conditions reproducing the loads, speeds, and environment of the ring/cylinder interface of advanced engines. The test specimens are to be carefully characterized before and after testing to provide detailed input to the model. The results are intended to provide the basis for identifying solutions to the tribology problems limiting the development of these engines.

Technical Progress

Literature Review. To provide a basis for the wear modeling efforts, a review was made of the literature regarding wear of ceramics. The following is a summary of the review.

Introduction. A computer search has been made of technical literature using Dialog Information Services Inc. covering the period 1970 to 1984. The following sources were searched:

- Chemical Abstracts
- EI Engineering Meetings Database
- Patent Abstracts
- Engineering Index

Key words included wear, high temperature, diesel, and ceramic. Approximately 500 abstracts were obtained and reviewed. From these, complete copies of about 100 documents were obtained. Information was often redundant in these final 100 documents.

A search was also made of the five International Conferences on Wear of Materials 1977-1985, since each conference proceedings contained at least one session on Friction and Wear of Ceramics. Information from some of these original sources also lead to other documents having useful information not necessarily directly related to wear of ceramics.

Literature dealing with actual wear testing seemed to fall roughly into two categories: bench tests (pin on disk, block on ring) and cutting tests (tool bits for metal cutting, bits for rock drilling). The bench test research involved operating conditions in which loads were relatively high and velocities moderate to slow. Loads used in the bench test comprised an exponential distribution with much of the data falling in the range 0.1 to 3 N. Velocities covered the range 0.0002 m/sec to 5.4 m/sec. Most of the velocities fell between 0.0002 m/sec to 0.05 m/sec. Therefore much of the ceramic bench type wear experiments have been conducted at low loads and velocities. Cutting tests involved much higher loads (ranging between 100 and 350 N) and higher velocities (100 m/sec). It is not surprising, therefore, that the wear mechanisms described in the cutting tests were much different from the mechanisms described in the bench tests. In the bench test grouping, there were some high velocity experiments reported and the wear mechanisms in these experiments were related to thermal shock effects.

Even with these two sets of test conditions considered, wear mechanisms reported contained considerable variety. This was partly a result of different material specimens, different environments, elevated temperature versus room temperature, and the effect of various lubricants.

Mechanisms reported included surface microfracture, adhesive transfer, plastic deformation, surface fatigue, and oxidation. Lateral fracture was not reported in tests run in the load range 0.1 - 10 N. Thermal shock surface fracture resulting from thermal mechanical instability was reported in some high sliding velocity testing. The range of wear mechanisms reported appears to relate to environmental and surface chemical phenomena extant in each test condition.

Ceramic Deformation Mechanisms. It takes five separate active slip systems to make a material ductile. Most metals behave this way. In BCC metals a transition to nonductile behavior occurs at a critical temperature or range of temperatures. As the temperature is reduced, stacking fault energy decreases, limiting cross slip and increasing the tendency for limiting slip systems. This concentrates slip on planes that intersect and cause dislocation pile-ups, stress concentrations, and the formation of voids. Depending on the state of stress, critical temperature is acheived when pile-up and void formation leads to fracture and apparent brittle behavior. Ceramic materials behave much like BCC metals below the critical temperature. However, increasing the temperature of a ceramic to about 0.6 Tm (Tm = melting temperature) increases the probability of climb and break-through in dislocation pile-ups allowing more plastic flow and reduction in the brittle behavior. Of course, strength reduction and creep are also encountered with elevated temperature. The resemblance to BCC metals ends here. Although ceramics exhibit more plastic deformation and creep at elevated temperatures, they do not exhibit the ductility common to metals. The number of operative slip systems is still limited and brittle or semi-brittle behavior prevails. Under contact conditions existing during sliding contact, plastic deformation will occur locally and to shallow depths owing to the hydrostatic component of the state of stress. Ceramics are much more sensitive to strain rate than metals and, therefore, high sliding velocity will be more likely to produce microfracture. In addition, the thermal properties of ceramics (low thermal diffusivity) will promote thermal shock or thermal fatigue type fracture. The above characteristics of ceramic mechanical behavior make it necessary to consider different parameters from those used for metals when modeling wear processes.

Lateral Cracking. One of the consequences of the brittle character of ceramics is the tendency to crack under contact stress. Once a critical load is exceeded such that the tensile component of the contact stress state initiates cracks, the wear rate jumps significantly and visible surface damage occurs. Evans and Wilshaw (1) have shown that a sphere pressed into a brittle solid will initially produce radial cracks, then with further load increase, produce lateral cracks--or cracks running parallel with the surface. This process is shown in Figure 1. The consequence of this process is a propagation and joining up of cracks and the release of chips. Thus, the ceramic material has a critical load capacity, P^*, above which lateral cracking will occur. This, obviously, is a load barrier above which one does not wish to go. Sliding contact will modify this process and Lawn (2) has demonstrated the consequence of friction levels on the lateral crack initiation and propagation during sliding of a spherical contact over a brittle material. When two ceramic surfaces contact, one may find a combination of plastic deformation and plowing together with lateral cracking as shown in Figure 2. The asperity carrying the larger percent of the load will produce a groove with "chevron" cracks from friction forces and subsurface lateral cracks. Spalls and break-out occur where cracks meet the surface. As friction increases, Lawn (2) shows that the surface-crack and subsurface-crack orientations change resulting in longer chevron cracks and deeper penetration of lateral cracks--hence, larger volume removal of material when chips form.

There are other factors which influence lateral cracking. For instance, the size of defects in the material. The larger the defect, the lower the critical load, P^*. For defect-initiated cracks, the critical load decreases with increasing grain size. This is shown in Figure 3.

Hardness will influence lateral fracture initiation. The harder ceramic will generally exhibit a higher sensitivity to lateral cracking. Figure 4 shows an example of the wear resistant very hard material having a low fracture threshold such that under a given load range it would be into lateral fracture and chipping wear while a softer ceramic would still be in the plastic deformation wear regime (3).

Fracture toughness also influences the critical load for lateral fracture. An equation has been proposed by Evans (3) relating critical load and mechanical properties:

$$P^* \approx \frac{K_c}{H^3} f(E/H)$$

where

K_c = Fracture toughness
H = Hardness
E = Elastic Modulus.

P^* covers a wide range of values for commercial ceramics. The list below presents three common ceramics for comparison:

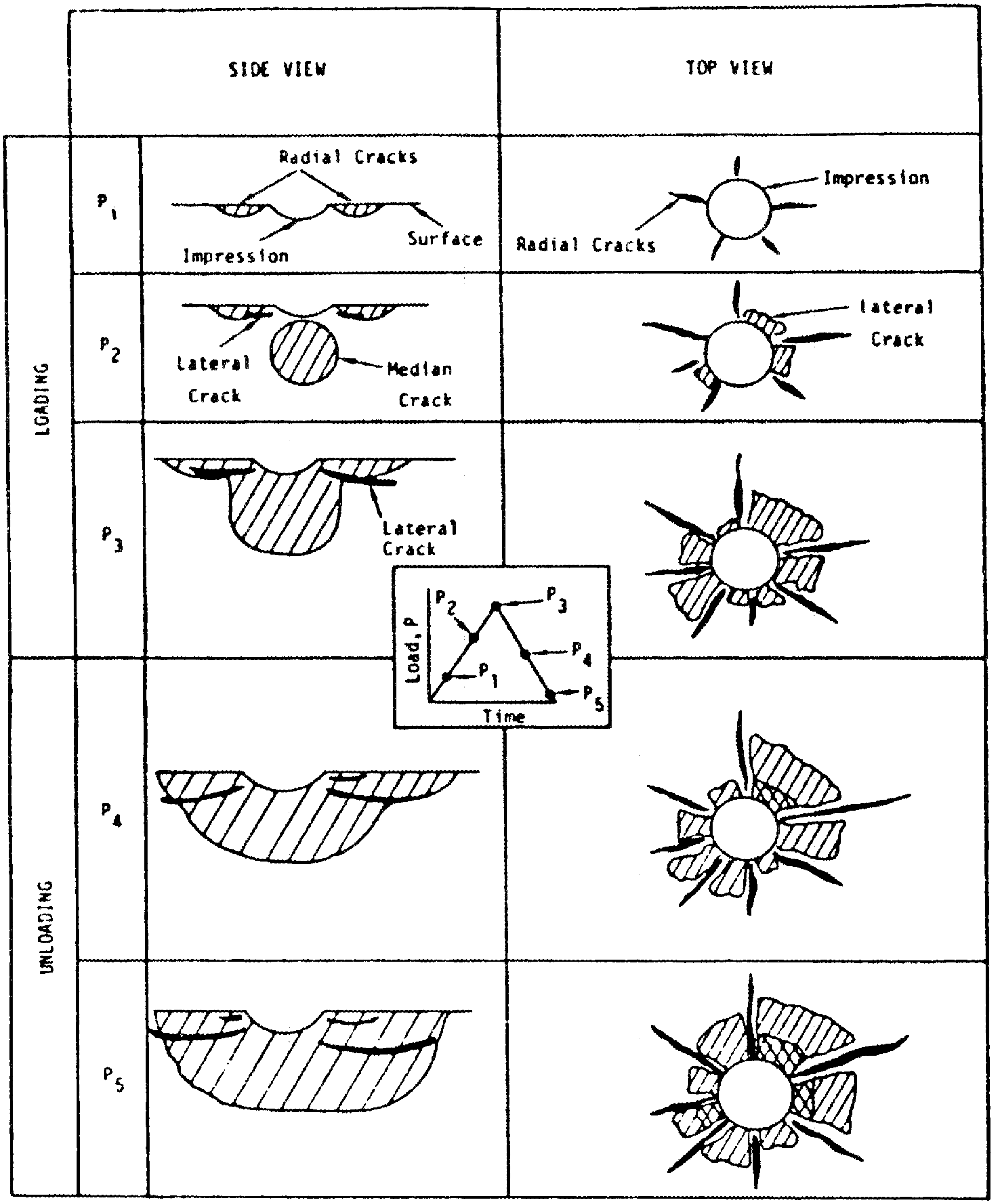

FIGURE 1. STATIC INDENTATION FORMATION OF LATERAL CRACKS IN GLASS (FROM EVANS & WILSHAW)

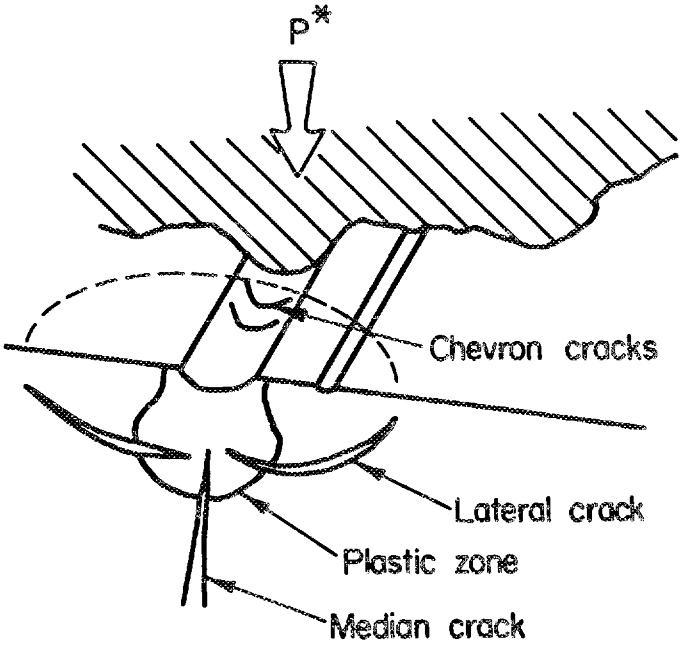

FIGURE 2. CRACKING MECHANISMS DURING HARD ASPERITY PENETRATION

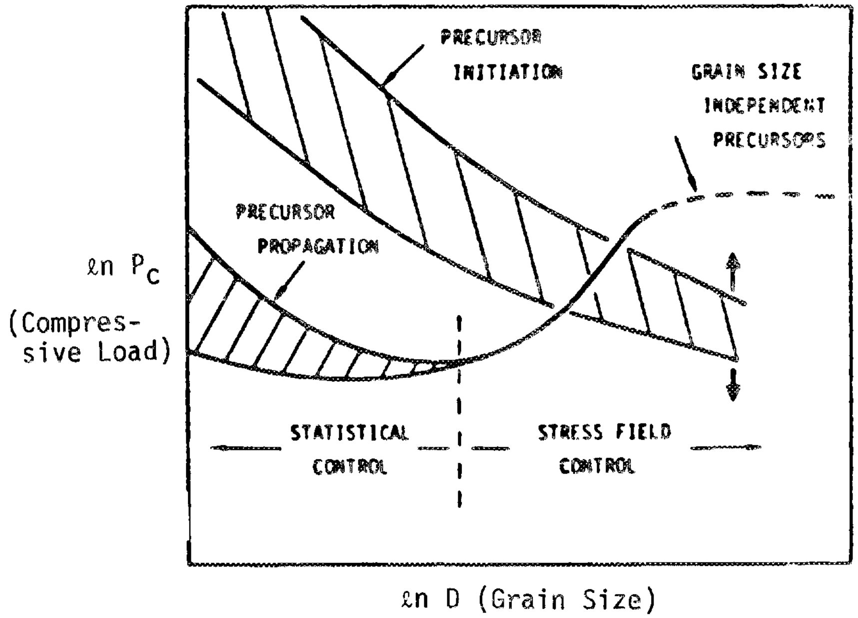

FIGURE 3. EFFECT OF GRAIN SIZE ON INITIATION AND PROPAGATION OF CRACKS IN CERAMICS (LAWN)

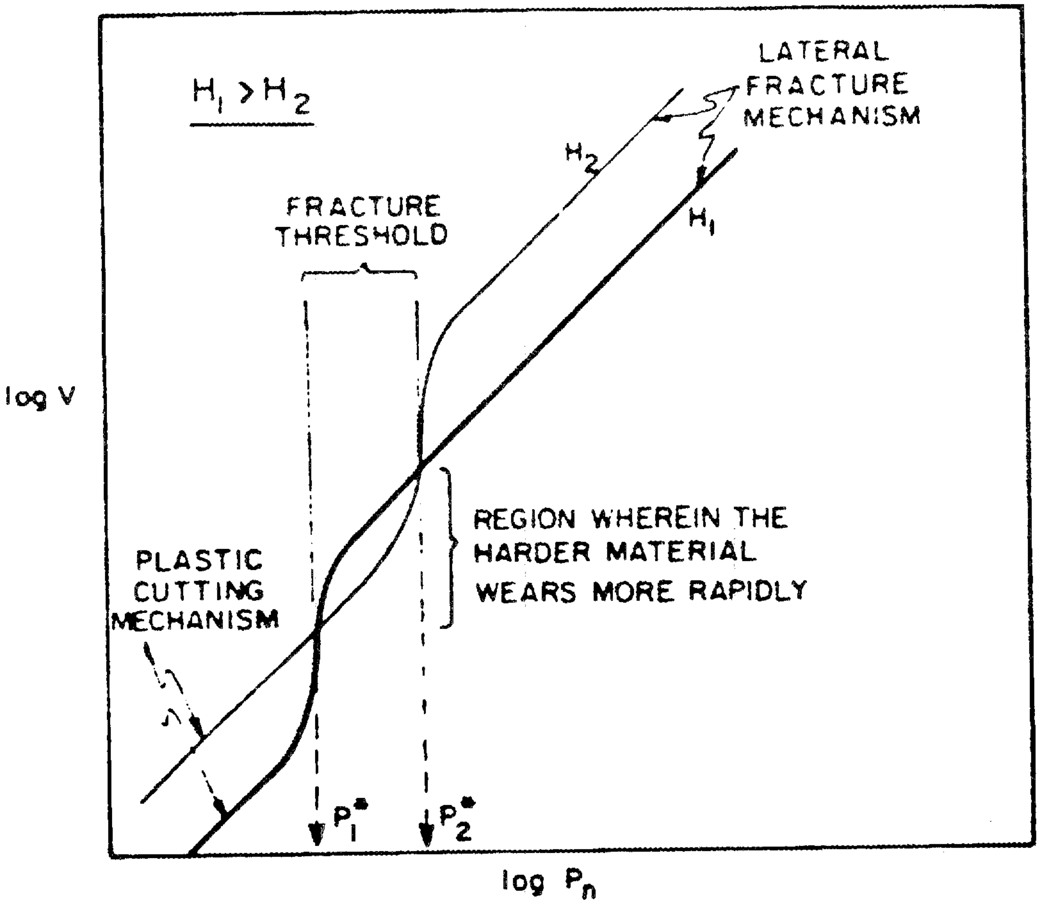

FIGURE 4. EFFECT OF HARDNESS ON THE THRESHOLD FOR LATERAL FRACTURE AND CHIPPING WEAR

Ceramic	P*
Alumina	0.4
Magnesia	0.9
Silicon Nitride	31.0

Little is known about the effect of elevated temperature on lateral cracking. Presumably, it might change the coefficients shown in Equation (1). Certainly, the hardness will be reduced and Kc may increase somewhat so that P* might increase somewhat until a temperature is reached at which plastic deformation may take over.

Thermal Effects. Increasing sliding velocity produces localized frictional heating in ceramic materials owing to their relatively low thermal diffusivity. One phenomenon that results from frictional heating is thermal mechanical instability (TMI) (4,5). Both metals and ceramics are subject to it, but ceramics have a much lower threshold for TMI. There has been a significant amount of study directed toward the TMI phenomenon and a number of mathematical models have been proposed and have been verified by experiment. It is possible to estimate a critical sliding velocity above which TMI phenomena will occur. The observed presence of TMI is the development of widely spaced localized hot spots that move about the surface. A well developed TMI condition on ceramics will produce flashes of light which rapidly change location--often in a periodic manner. Wear rates of ceramics tend to increase when the TMI threshold is crossed (6). The wear mechanism for ceramics involves a micro-thermal shock process which occurs at each local hot spot. Several mathematical models have been developed to predict the onset of TMI. A typical relation for predicting V* or the critical velocity above which instability takes over is shown below (7):

$$V^* = \frac{\kappa^2 J^2}{(\mu E \alpha)^2} \frac{1}{D},$$

where

J = Mechanical equivalent of heat
κ = Thermal conductivity
μ = Friction coefficient
α = Coefficient of thermal expansion
E = Elastic modulus
D = Thermal diffusivity, or $\kappa/\rho c$.

Depending on the friction level in the sliding contact, then, a critical velocity can be predicted from the thermal properties of the ceramic. Some typical velocities for sliding pairs are shown in the list below.

Material	μ	V*
Aluminum Oxide	1.0	5.0
Silicon Carbide	1.0	20.4
Aluminum	0.5	125.0
Cast Iron	0.23	155.0

This shows the possible range of V* among various materials. Under conditions which produce thermal shock, a model for wear rate has been developed from empirical methods (6):

$$w \approx \frac{\mu}{R^a D^b} ,$$

where

a & b = Constants
μ = Coefficient of friction
R = Thermal stress resistance factor, $s(1-)/E$
  s = Short time tensile strength
  ν = Poisson's ratio
  E = Elastic modulus
  α = Coefficient of expansion
D = Thermal diffusivity, $\kappa/\rho c$
  ρ = Density
  c = Heat capacity
  κ = Thermal conductivity.

Creep. Since the number of operative slip systems in ceramics is limited owing to their ionic and/or covalent structure, the pile-up of edge dislocations and generation of voids and cracks under applied shear stresses is very probable. The critical stress required to initiate a crack is a function of surface energy, modulus, and embrio crack length:

$$\sigma_c = (2ES/\pi c)^{1/2}$$

where

σ_c = Critical stress
c = Crack length
S = Surface energy
E = Elastic modulus.

When stress is applied to a ceramic, the shear stress component acts to pile up edge dislocations against an obstacle while the tensile component is the crack propagater. In sliding contact, therefore, the cracking is either generated at the edges of the contact or, if the contact stress is high enough, below the surface as a lateral crack. Thick glide bands with high dislocation density promote crack generation. Ceramics with high covalent bonding like alumina have high Peierls stress and inherent resistance to dislocation motion. However, by raising the temperature, dislocation bands can be broadened and their dislocation density decreased. When the temperature approaches T/Tm = 0.6, climb and breakdown of dislocation obstacles allow greater plastic deformation and ductility in ceramics. At this point, creep becomes a significant operator in the mechanical behavior (8).

The classic creep curve is shown in Figure 5. Both metals and ceramics follow this creep characteristic. In wear processes at elevated temperature, the linear portion of the curve should be inconsequential. The last stage of creep where deformation accelerates to rupture is the damage stage for ceramics. Therefore, the time it takes to reach the stage III creep is important to the life of a part. Creep can become a component of the high temperature wear process on parts which see a heavy contact stress located in one spot (the contact zone on a non-rotating cam follower, for instance). In polycrystalline ceramics, creep can occur as grain boundary void growth (diffusion creep) or as void growth within the grains. A glassy phase at the grain boundaries can exacerbate void growth along grain boundaries.

The rate of damage accumulation varies depending on the type of creep occurring in the ceramic. Figure 6 shows the effect of two types of creep -- diffusion creep and power law creep. As the applied stress is increased on a body the creep mode changes from diffusion to power law. Note the significant increase in damage rate as the power rate creep regime is entered.

Some estimate of creep damage potential in a high temperature system can be obtained by referring to deformation maps. One for copper is shown in Figure 7. As the temperature increases one can move from diffusional flow to power law creep. The same happens as shear stress is increased. At a shear stress of 10 the material flows with full plasticity -- creep no longer prevails. In the breakdown zone, a transition from creep to full plastic flow occurs. The same type of diagram has been developed for void formation and for fracture of ceramics (9).

Phase Change. Some ceramics considered for wear control in engines are rather complex in structure. The structures have been modified in attempts to improve toughness while still maintaining chemical inertness and wear resistance. Examples include alumina-zirconia, silicon nitride-zirconia, zirconia-magnesia, and zirconia-yttria. The more popular modified ceramics are PSZ and TTZ (partially stabilized zirconia and transformation toughened zirconia). As an example of the possible effects on wear mechanisms, partially stabilized zirconia (zirconia-magnesia) will be considered.

When heat treated, PSZ consists of a stabilized cubic matrix containing monoclinic precipitates transformed from the tetragonal during aging. The precipitation results in a volume expansion and compressive residual stresses result. These residual stresses presumably inhibit propagation of crack fronts and therefore improve the apparent toughness. At the same time, wear resistance is reported acceptable (10).

Studies have been made on the effect of temperature on the deformation of PSZ. An Arrhenius plot of ln (hardness) versus 1/T for PSZ shows a discontinuity at about 400 C. The straight line curve takes the form Hardness $\approx \exp^{(Q/mRT)}$ (11). The activation energy, Q, estimated from the slope of the curve beyond 400 C is about 40 kcal/mol. If the change in hardness with temperature can be attributed to creep, the activation energy for the slowest moving ion, Zr, would have to be considered. The approximate value of Q for zirconium ions is

OA – Instantaneous (elastic) deformation at room temperature
OB – Instantaneous (elastic and plastic) deformation at an elevat temperature
OBDEF – Creep – Rupture curve
BD – First stage (primary or transient creep)
DE – Second stage (secondary or linear creep)
EF – Third stage (tertiary or accelerating creep)

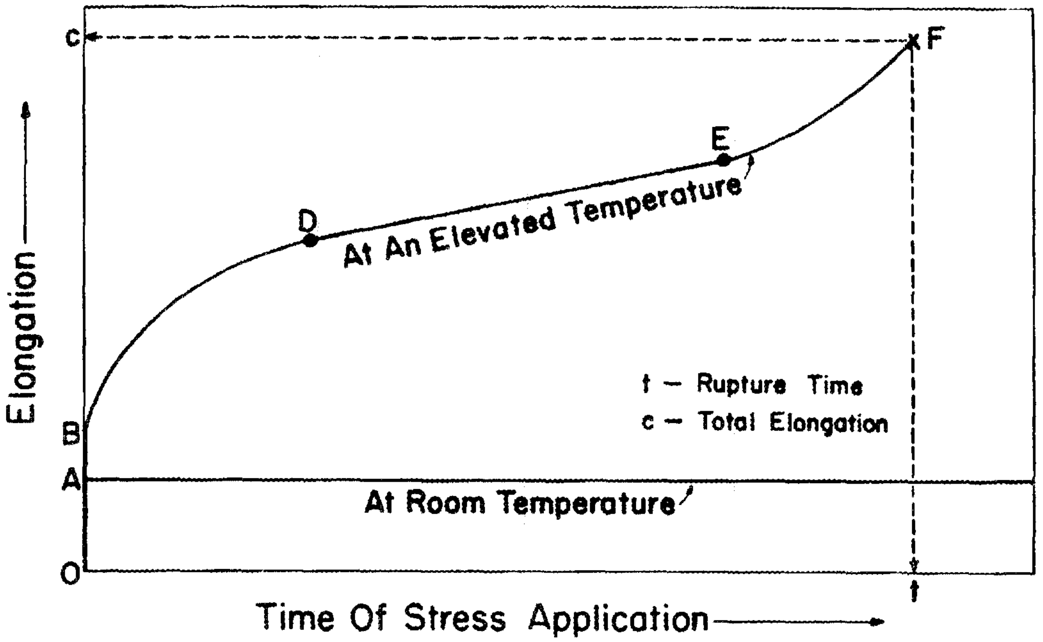

FIGURE 5. CREEP-RUPTURE CURVE

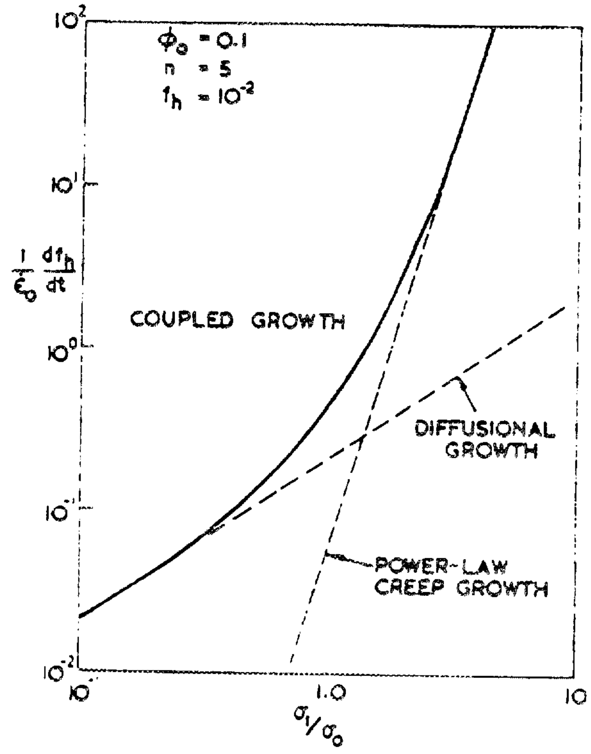

FIGURE 6. THE EFFECT ON CREEP RATE IN GOING FROM DIFFERENT DIFFUSIONAL TO POWER LAW CREEP MODE (FROM A.C.F COCKS)

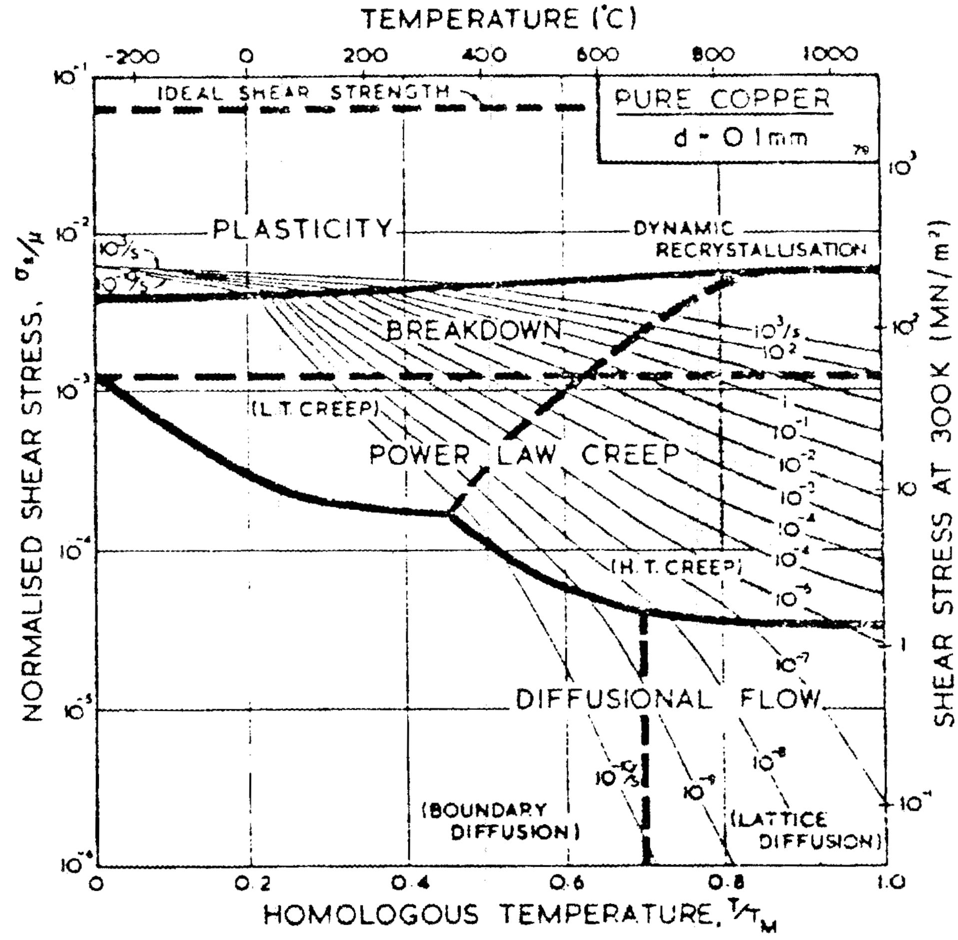

FIGURE 7. DEFORMATION MAP FOR COPPER (FROM ASHBY)

80 kcal/mol at 1300 C (11). The deformation behavior (at least under conditions of the indentation test) of PSZ at these temperature levels does not appear to be related to creep. It is conjectured that the change in slope of the hot hardness curve may indicate activation of another slip system or climb. This effect at 400 C, however, may be an important one to consider when selecting operating temperatures for contact wear conditions involving PSZ.

As temperature is increased further, the effect of the second phase in PSZ in resisting deformation begins to fade. Strain induced precipitation allows accommodation of strains in adjacent grains and deformation increases. As temperature increases further, this effect is lessened and probability of crack propagation increases. It is possible that new slip systems may begin to operate at elevated temperatures under the hydrostatic state of stress occasioned by sliding contact. There is no evidence of this effect as yet and the effect of strain rate is not known.

At 950 C and above, overaging occurs in PSZ and the transformation toughening characteristic no longer operates. On cooling back to room temperature, the resulting structure is a cubic matrix enriched in magnesia. At this point, the toughness of the alloy has been permanently diminished. Studies on loss of strength over 250 hours have shown the effect at 800 C and is more prevalent in yttria-stabilized zirconia (12).

Holding PSZ at elevated temperatures can coarsen the precipitates. Once the precipitates reach a critical size, cooling to room temperature results in transformation to the monoclinic phase. Deformation caused by grinding during finishing operations can also cause transformation of tetragonal precipitates to monoclinic with subsequent formation of residual compressive stresses at transformation sites.

The above various structural changes in PSZ occasioned by elevated temperature and deformation are difficult to relate to wear mechanisms because of an overwhelming unknown--that of the effect of contact-stress-induced structural changes such as observed in metals and in limited information available for ceramics (13, 14, 15). The radical changes in near-surface structures (dislocation cell formation, deformation twinning and subgrain formation) that are possible during wear are much different from conventional PSZ structures described above. It is likely that wear-induced phase changes could be accompanied by a microfracture wear mechanism.

High Temperature Reactions. Ceramic materials are generally considered inert. However, at elevated temperature some of the silicon-containing ceramics (SiC, Si_3N_4) will react with oxygen in the atmosphere to form silica. Although silica melts at 1720 C, glassy films are often found on silicon-containing materials after wear at elevated temperatures. These films look as if they had been molten at some time. Examination of ceramic phase diagrams reveals eutectics in a number of oxide solutions. Furthermore, silicon often acts as a vitrifier for other materials making possible relatively low-melting-point glasses. The formation of a glassy phase on silicon containing materials is often accompanied by a reduction in friction and less wear (16). Thus, one must consider what other species ceramics may contact during sliding at elevated temperature. If the formation of a glassy film results from "contamination" of a silicon-containing ceramic, its presence will significantly alter wear mechanisms.

Most ceramics contain a small amount of glassy phase as a binder. The glassy phase is found at grain boundaries. If temperatures become high enough to melt the glassy binder, it can exude on the rubbing surface. In addition, grain boundary weakening will occur if the glassy phase in the boundary softens.

Some ceramic materials have been found to be very sensitive to humidity during sliding contact. This appears to be the result of surface reactions producing protective amorphous surface films. Studies of Si_3Ni_4 and Al_2O_3 (17) have shown that wear of Si_3N_4 slows in water vapor while wear of Al_2O_3 increases in water vapor. These observations have been made at room temperature--therefore tribochemical reactions should be expected on ceramics at elevated temperatures.

Conclusions Regarding Literature Review. The results of the survey have emphasized the need for research to better define high temperature wear mechanisms in ceramics. A number of different mechanisms or combinations of mechanisms have been reported. For instance, Sutor (18) recently reported friction values for hot pressed Si_3N_4 ranged from 0.70 to 0.15; Fischer reports similar findings (17). Some researchers found that Si_3N_4 sliding against itself showed a decrease in friction with increasingly fine finish while others found the opposite effect. Sutor's own wear experiments on silicon nitride indicated several wear mechanisms operating at the same time.

The reason for the great variation in ceramic wear data becomes clear when one examines known mechanical properties and surface chemical characteristics of ceramics. There are three areas of concern when attempting to predict wear processes in ceramics:

(1) Definition of threshold parameters which signal a change of mechanical or chemical behavior.

For wear model development, the thresholds for lateral cracking, thermal mechanical instability, thermal shock, glassy phase film formation and alloy phase transformations must be defined initially. A wear model may be required for each condition encountered when a threshold has been passed. In some instances there may be thresholds one does not want to cross, notably lateral cracking and thermal mechanical instability. Avoiding these conditions may require adjustments to operating conditions for wear experiments depending on the material combinations under evaluation.

(2) The significance of fracture toughness and surface energy to the wear process in ceramics, once a specific wear mode has been established. The wear rate and extent of surface damage may differ from one operating condition to another,

but the brittle behavior of ceramics will still dominate the wear process.

(3) There are important gaps in the understanding of ceramic wear processes that have to be filled before reliable models can be developed.

Limited information has been developed on the wear surface structure in ceramics resulting from the rubbing-contact state of stress. It is suspected that some of the wear-induced high strain microstructures found in metals may prevail to some extent in ceramics. If they do, how do they influence deformation and fracture behavior? How do they relate to phase transformations defined for unstrained ceramic alloys? Because of these unknowns, TEM work on ion-thinned wear specimens is needed, much like Hockey did in the early 1970's (19).

The effect of high temperature and contact stress on the surface chemistry of ceramics is also limited. Since ionic materials are more influenced by surface double layers, the nature of the bonding of absorbed species requires examination. The chemical composition and structure of surface layers formed during high temperature wear need to be defined. Surface chemistry <u>before</u> wear is also essential.

<u>Specimen Procurement</u>. Monolithic cylinder specimens were received from three different suppliers. Included were eleven specimens each of TS grade magnesia partially stabilized zirconia, Z-191 grade yttria partially stabilized zirconia, and Hexoloy sintered alpha silicon carbide. Production difficulties with five specimens of 2Y20A HIP-processed transformation - toughened alumina have delayed their delivery. Four cylinder specimens were also obtained with coatings of SCA-1000 on mild steel from the Kaman Sciences Corporation.

Because of repeated delays in obtaining coated ring specimens from the commercial ring supplier, ring specimens were fabricated by Battelle's thermal spray group. Table 1 presents the coating materials applied to AISI 410 stainless steel specimens. A concave profile was machined at the edge of the ring specimens with a 1-in. radius milling tool to provide edge support for the coatings. After spraying, the coatings were finished by grinding with a crown radius of 1.25 in.

<u>Specimen Characterization</u>. The fracture properties of sintered monolithic α - SiC were measured as part of the specimen characterization efforts.

Fracture strength was assessed in four-point bend tests at room temperature (20 C). Bend tests on 18 specimens, 2.5 x 5.0 x 38 mm in dimensions, loaded with a 32 mm support span and 19 mm loading span were as follows:

$$\text{Mean Fracture Stress, } \bar{\sigma}_f = 360 \text{ MPa}$$
$$\text{Std. Dev.} = 47 \text{ MPa}$$

TABLE 1. COMPOSITION OF PLASMA-SPRAYED COATINGS FOR RING SPECIMENS

Identification	Composition
Metco 130	0.13 titanium dioxide 0.87 aluminum oxide
Metco 501	0.30 molybdenum 0.12 chromium 0.025 boron 0.0275 iron 0.0075 carbon bal nickel
Plasmalloy 312 M	molybdenum disilicide
Metco 63/G234 basecoat with Metco 130 topcoat	0.99 molybdenum basecoat with topcoat of 0.13 titanium dioxide 0.87 aluminum oxide

TABLE 2. SHORT-BAR FRACTURE TOUGHNESS OF SINTERED α - SiC

Specimen Number		K_{Ic} (MPam$^{1/2}$)
1T	:	2.74
2T	:	2.74
3T	:	2.80
4P	:	2.73
5P	:	2.71
6P	:	2.85
Mean	:	2.76 MPam$^{1/2}$
Std. Dev.	:	0.05 MPam$^{1/2}$

Figure 8 shows the fracture-stress distribution and a two-parameter Weibull distribution function fitted to the data. The fracture probability for the bend specimens was calculated from the relation, $F = (i - 0.5)/N$, where i is the ranking number of a specimen in the order increasing strengths and N is the total number of specimens. The following Weibull parameters were calculated by linear regression on a linearized form of the Weibull relation given in Figure 8:

Weibull modulus, $m = 8.5$
Scale Parameter, $\sigma_0 = 380$ MPa

Fracture surfaces of three specimens selected arbitrarily were examined in a scanning electron microscope. Two bend specimens failed from surface flaws without evidence of any obvious microstructural inhomogeneity at the fracture origin. These surface flaws were likely produced in surface grinding. The fracture in the third specimen originated from a microstructural defect located close to the tension surface of the specimen. An inclusion-like feature had the same composition as the matrix. This suggested that it was probably an agglomerate in the starting powder which caused nonuniform sintering and a crack-like flaw at its periphery.

The fracture toughness (K_{Ic}) of α - SiC was measured in short-bar tests. Results are summarized in Table 2. In specimens 1T, 2T, and 3T the chevron-notch plane was oriented perpendicular to the large (15 x 5 cm) faces of the billet (transverse orientation), while in specimens 4P, 5P, and 6P the notch planes were parallel to the large faces of the billet (parallel orientation). There was no apparent difference in the fracture toughness in the two orientations. The average K_{Ic} for all the specimens was 2.76 $MPam^{1/2}$.

Experimental Apparatus. The experimental apparatus was completed and demonstrated during the report period. The apparatus provides the following capabilities.

Cylinder Specimens: 1.25 x 5 x 0.5 in. flats

Ring Specimens: 0.75 x 0.75 x 0.125 in. flats

Motion: Reciprocating, 4.25 in. stroke

Speed: Variable, 500 to 2200 rpm

Temperature: to 1200 F

Applied Load: to 200 lbs (continuous)

Contact Pressure: to 2100 psi

Atmosphere: Diesel exhaust or other controlled gas, as desired

Output data: Wear at intervals, friction from drive torque

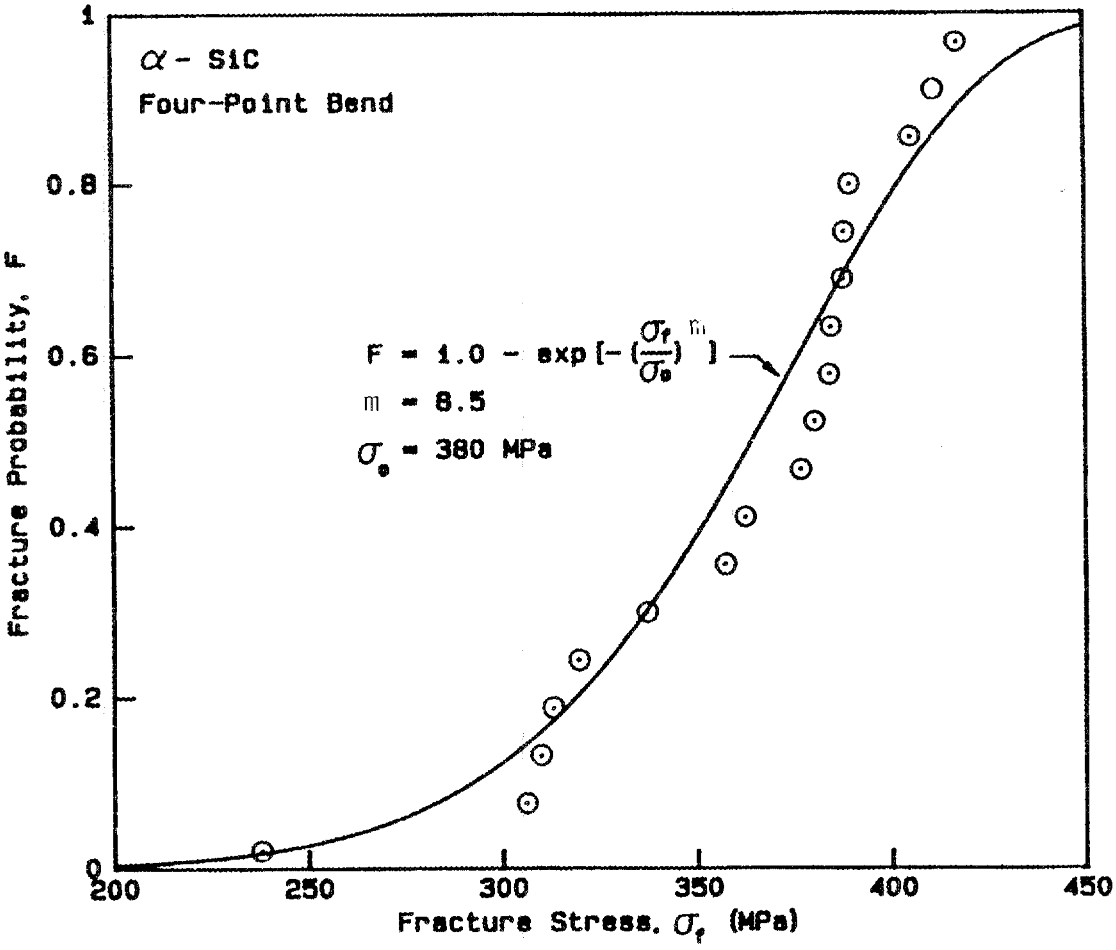

FIGURE 8. DISTRIBUTION OF FRACTURE STRESSES AND TWO-PARAMETER WEIBULL FIT FOR α - SiC IN FOUR-POINT BEND TESTS

Since most of the experiments are planned to be conducted in diesel exhaust atmosphere, an analysis was made of the composition of the exhaust being supplied to the specimen chamber. The results are presented in Table 3.

Wear Experiments. Wear experiments were performed on four ring materials sliding against α-SiC cylinder specimens. Table 4 summarizes the results of these initial experiments. The Metco 130 (alumina-titania), which is referred to in Table 4 as M-130, spalled off the ring specimens at light load at very short times, Experiments 7 and 8. While no reliable friction coefficients could be measured in the short time period, very loud squealing suggested high readings. The Metco 501 coating, Experiment 9, performed the best to date. The friction decreased during the 20 minute run from 0.6 to 0.3, and the coating remained largely intact after the experiment. While these results are encouraging, a relatively high wear of 0.006 in. was measured. The P-312M (molybdenum disilicide), Experiment 10, worn and/or spalled off in 15 minutes of running. The M-130 with a molybdenum basecoat, Experiment 12, appeared to wear rapidly, but the experiment had to be terminated when one cylinder specimen fractured. The fracture was caused by a warpage of the pedestal on which it was mounted. The experiments proved the apparatus able to run specimens for extended times at elevated temperatures. However, the high wear and bonding problems on the ring specimens have prevented wear rate measurements for times exceeding 20 minutes.

Status of Milestones

With the receipt of most of the monolithic specimens and the fabrication of the coated ring specimens at Battelle, the experimental program has been initiated in accordance with the schedule. Examination of the wear specimens has been initated to form the basis of the wear modeling to be performed in the remainder of the study.

Publications

None.

References

1. Evans, A. G., and Wilshaw, T. R., "Quasi-Static Solid Particle Damage in Brittle Solids - I. Observations and Implications", Acta Metallurgica, 24, pp 939-956, 1976.

2. Lawn, B. R., "Partial Cone Crack Formation in a Brittle Material Loaded with a Sliding Spherical Indenter", Proceedings Royal Society, 299A, pp 307-316, 1967.

3. Evans, A. G., and Marshall, D. B., "Wear Mechanisms in Ceramics, Fundamentals of Friction and Wear of Materials", Edited by D. A. Rigney, AMS, pp 439-452, 1981.

TABLE 3. SUMMARY OF EXHAUST GAS MEASUREMENTS ON 6.5 HORSEPOWER LOMBARDINI ENGINE

Load Press, psig	NO_x ppm	NO ppm	O_2 Percent	CO_2 Percent	CO ppm	Particulates mg/m^3	H_2O Percent	Excess Air Percent	Exhaust Temp. F
80	385	335	13.4	6.2	560	26.3	7.66	70	579
100	450	400	12.9	5.6	580	27.9	7.29	48	590
120	540	500	12.1	5.2	608	27.7	7.30	31	632

TABLE 4. RESULTS OF INITIAL EXPERIMENTS WITH PLASMA-SPRAYED RING SPECIMENS SLIDING AGAINST α-SiC CYLINDER SPECIMENS IN DIESEL EXHAUST ATMOSPHERE

Experiment Number	Ring Specimens	Applied Load, lbs.	Projected Area Contact Pressure psi	Testing Temperature F	Speed, rpm	Running Time, Minutes	Coefficient of Friction	Average Ring Wear, Inch	Comments
7	M-130	9	96	1000	1000	<1	--	--	coating spalled off
8	M-130	9	96	600	1000	<1	--	--	coating spalled off
9	M-501	44	470	700	1000	20	0.6 to 0.3	0.006	coating intact
10	P-312M	44	470	750	1000	15	0.2	>0.008	coating worn off
12	M-63/130	44	470	550	1000	2	--	0.003	cylinder specimen fractured

4. Dow, T. A., and Burton, R. A., "The Role of Wear in the Initiation of Thermoelastic Instabilities of Rubbing Contact", ASME JOLT pp 72-75, Jan 1973.

5. "Thermomechanical Effects in Wear", Edited by T. A. Dow, Elsevier Sequoia, 1981.

6. Sibley, L. B. Mace, A. F., Grieser, D. R., and Allen, C. M., "Characteristics Governing the Friction and Wear Behavior of Refractory Materials for High Temperature Seals and Bearings", WADD TR 60-54, Dec. 1959.

7. Dow, T. A., and Burton, R. A., "Thermoelastic Instability of Sliding in the Absence of Wear", Wear, 19, 1972, pp 315-328.

8. Cocks, A.C.F., and Ashby, M. F., "On Creep Fracture by Void Growth", Progress in Materials Science, 27, 1982, pp 189-244.

9. Gandha, C., and Ashby, M. F., "Fracture-Mechanism Maps for Materials Which Cleave: FCC, BCC, and HCP Metals and Ceramics", Acta Metallurgica 27, 1979, pp 1565-1602.

10. Hannink, R.H.J., and Swain, M. V., Induced Plastic Deformation of Zirconia, Pamphlet, 14 pp.

11. Hannink, R.H.J., Murray, M. J., and Marmach, M., "Magnesia - Partially Stabilized Zirconia (Mg-Psz) as Wear Resistant Materials", Proceedings International Conference on Wear of Materials, ASM, 1983, pp 181-186.

12. Schiloer, L. V., Guinn, G. D., and Katz, R. N., "Time-Temperature Dependence of the Strength of Commercial Zirconia Ceramics", Report AMMRC TR 84-16, Army Materials and Mechanics Research Center, Watertown, Mass., April 1984.

13. Heilmann, P., Don, J., Sun, T. C., Rigney, D. A., and Glaeser, W. A., "Sliding Wear and Transfer", Wear 91, 1983, pp 171-190.

14. Yust, C. S., "Low Speed Sliding Damage in TiB_2-Ni Composites", Proceedings International Conference on Wear of Materials, 1983, pp 167-173.

15. Dufrane, K. F., and Glaeser, W. A., "Rolling Contact Deformation of MgO Single Crystals", Wear 37, 1976, pp 21-32.

16. Stogg, F. H., Stevenson, C. W., and Wood, G. C., "Friction and Wear Properties of Stellite 31 at Temperatures from 293 to 1073K", Metals Technology, Feb. 1977, pp 66-74.

17. Fischer, T. E., and Tomizawa, H., "Interaction of Tribochemistry and Microfracture in the Friction and Wear of Silicon Nitride", Proceedings Inte

17. Fischer, T. E., and Tomizawa, H., "Interaction of Tribochemistry and Microfracture in the Friction and Wear of Silicon Nitride", Proceedings International Conference on Wear of Materials, 1985, pp 22-32.

18. Sutor, P., "Tribology of Silicon Nitride and Silicon Nitride-Steel Sliding Parts", Proceedings 8th Annual Conference on Composites and Advanced Ceramic Materials, ACS 1984, pp 460-469.

19. Hockey, B., "Observations by Transmission Electron Microscopy on the Subsurface Damage Produced in Aluminum Oxide by Mechanical Polishing and Grinding", Presented at London, England Symposium Textrural Studies on Ceramics, Dec. 1970.

2.3 NEW CONCEPTS

Advanced Statistics[*]

W. P. Eatherly (Oak Ridge National Laboratory)

Objective/scope

The existence of flaw fields involving large flaws occurring at relatively rare sites cannot in principle be treated by Weibull statistics. The present effort is aimed at developing failure criteria involving a finite cell size describing the occurrence of flaws.

Technical progress

The model being considered initiates with the definition of a finite cell (volume element) in the material chosen large enough to completely contain any flaw in question, but small enough to contain not more than one flaw. This last premise is for counting purposes only. Any material under stress then contains some countable number of these cells, and the occurrence of flaws within the stressed volume becomes simply a binomial distribution over the number of cells in question.

The flaw sizes are assumed to be normally distributed or, more exactly, the strengths arising from them are assumed to be normal. The weakest-link argument is now introduced as being the first order statistic for a sampling of size n, the n being the number of flaws expected in the totality of cells representing the stressed volume. In this manner a strength-volume dependence arises similarly to that of a Weibull statistic.

This model is independent of cell size in that any choice of cell size over several decades leads experimentally to the same observable results. In other words, the premise that a cell not contain more than one flaw is for convenience only, and the observer cannot detect whether the premise is satisfied or not. His experimental results are insensitive to the cell size as long as the probability per cell is adjusted accordingly.

The resulting statistic, a product of binomial by normal order statistics, does not lead to the ordinary Weibull volume sensitivity; the strength at large stress volumes falls off more rapidly than the Weibull case. Presumably, a skewed strength distribution could compensate for this. The simplest and somewhat trivial candidate distribution would be the log normal. This case is currently being examined.

It is too early to say whether the model and mathematical formalism described above is of practical significance. We are encouraged that the model is tractable, is capable of experimental verification, and possesses the essential features of a Weibull distribution.

Status of milestones

None.

Publications

None.

---

[*] These studies supported jointly by the Ceramic Technology for Advanced Heat Engines Program and the HTGR Technology Program.

Advanced Statistical Concepts of Fracture in Brittle Materials

C. A. Johnson and W. T. Tucker (General Electric Corporate R&D)

Objective/Scope

The design and application of reliable load-bearing structural components from ceramic materials requires a detailed understanding of the statistical nature of fracture in brittle materials. The overall objective of this program is to advance the current understanding of fracture statistics, especially in the following three areas:

- Optimum testing plans and data analysis techniques.
- Confidence and tolerance bounds on predictions for non-normal distributions, in particular, the Weibull distribution.
- Consequences of time dependent crack growth on the evolution of initial flaw distributions.

The studies are being carried out largely by analytical and computer simulation techniques. Actual fracture data are then used as appropriate to confirm and demonstrate the resulting data analysis techniques.

Technical Highlights

One of the milestones for the first year of this program involves the development of procedures for estimation of the Weibull modulus from the locations of fracture origins. The most likely position of fracture initiation in a structure with a macroscopic stress gradient is the position of maximum stress. Because the most severe flaw (in terms of size, shape, orientation and position) may not be present in that location, failure may instead originate at a position stressed at lower than the maximum stress. The probability of the origin occurring in any given location can be predicted if the strength distribution is known for that material. Conversely, if the positions of the fracture origins are measured in a number of nominally identical test specimens or components, then information can be derived about the strength distribution. More specifically, for the case of the Weibull distribution, the Weibull modulus can be estimated from the positions of fracture origins in bodies that contain stress gradients.

To illustrate the concept, consider a stressed body such as that illustrated schematically in Figure 1 where the body is composed of two sections, A and B. The material in section A is identical to that in B but is at a different stress and may or may not have the same volume. Upon loading to failure, the body will either fail from a flaw located in A or from one in B. For the case of the Weibull distribution function, we have shown that the conditional probability of the strength controlling defect occurring in section A, given a failure, is equal to the effective volume (or effective surface area, if appropriate) of A divided by the effective volume (or area) of the entire component. This results for the Weibull distribution since the conditional probability is actually a norming constant. We believe that only the Weibull distribution has this property.

The simple relationship involving effective volumes can be extended to any stressed body that is conceptually subdivided into two sections at any arbitrary boundary and is subject only to the following assumptions: fracture strengths of the material are properly described by the two-parameter Weibull distribution; the flaw distribution is homogeneous throughout the component; and the strengths of sections A and B are independent of each other. The resulting probabilities are then conditional upon failure.

Most structures have continuous gradients in stress rather than the step change of the structure in Figure 1. As an example of a structure with a more conventional stress gradient, consider a three-point bend specimen. The most statistically efficient boundaries to separate such a structure into regions A and B are boundaries of constant stress such as those shown on Figure 2. The stress at a boundary divided by the maximum stress in the beam will be referred to as the relative stress, R, for that boundary. The relative stress is only a function of position within the structure, and interestingly, is not a function of the actual maximum stress. To draw an analogy with Figure 1, one could consider region A of the three-point bend specimen to consist of that portion of the specimen with a relative stress, R, greater than some value, say 0.5 for the moment, and region B to be the remainder. When failure occurs, the origin will be located either in region A or in region B. The expected fraction of origins with a relative stress greater than or equal to R will be defined as F_R and is equal to the effective volume of the higher stressed region divided by the effective volume of the entire specimen. For three-point bend specimens with rectangular cross sections and with volume distributed defects, this ratio of effective volumes is:

$$F_R = 1 - R^{m+1} + R^{m+1} \ln R^{m+1} \quad (1)$$

Therefore, if a series of three-point bend specimens of a material with a Weibull modulus, m, are tested to failure, Equation 1 can be used to predict the expected fraction of origins that will occur inside any given stress contour, R. The same information can be expressed graphically as shown on Figure 3 where F_R is plotted as a function of R for the same bend specimen geometry. The family of curves on Figure 3 represents the behavior of materials with various Weibull moduli.

The following procedure can be used to estimate the Weibull modulus of a material from the fracture origin sites in a set of three-point bend specimens: the location of the fracture initiating defect must be determined in each specimen; an R value is calculated for each specimen using the coordinates of the origin; the R values are ordered from highest to lowest, ranked and assigned an estimated F_R using a relationship such as

$$F_R = (n - 0.5)/N \quad (2)$$

where n is the ranking number and N is the total number of specimens; and finally, one data point for each specimen is plotted on Figure 3 using the calculated R and F_R values. If the fracture strength of the material is properly described by a two parameter Weibull distribution, then the points should fall on a curve that is similar in shape and position to one of the family of curves drawn on Figure 3. The estimate of m can then be done by visual inspection and interpolation or by more reproducible methods such as iteratively searching for the m with the maximum likelihood or with the minimum sum of squared error between measured and predicted behavior.

Relationships similar to Equation 1 have been derived for other bend geometries allowing analysis of fracture origin positions in the following test specimens:

Three-point bend, rectangular cross sections, surface defects
Three-point bend, circular cross sections, surface defects
Four-point bend, rectangular cross sections, volume defects
Four-point bend, rectangular cross sections, surface defects

In each case, the distribution of origins can be expressed in the form:

$$F_R = f(R,m) \qquad (3)$$

where m is the Weibull modulus, R is a relative stress contour separating the specimen into two regions, and F_R is the fraction of origins expected in the higher stressed region.

Status of Milestones

The two milestones due to be completed at the end of the first year of the program are on schedule.

Publications

None.

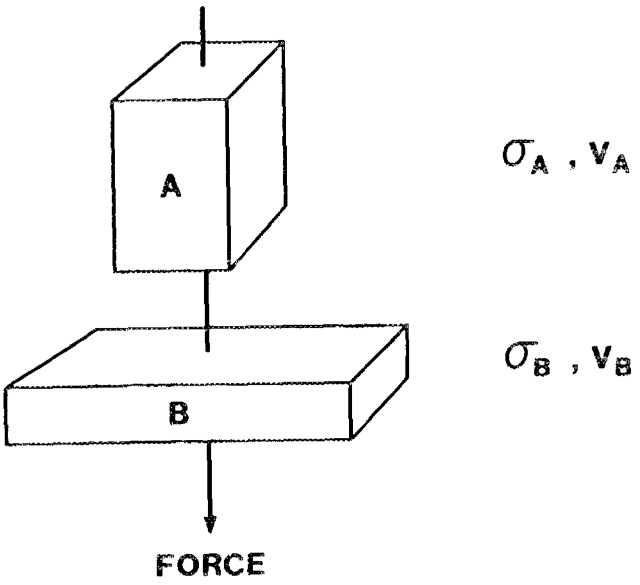

Figure 1: Schematic of a body composed of two sections, A and B, at different stresses.

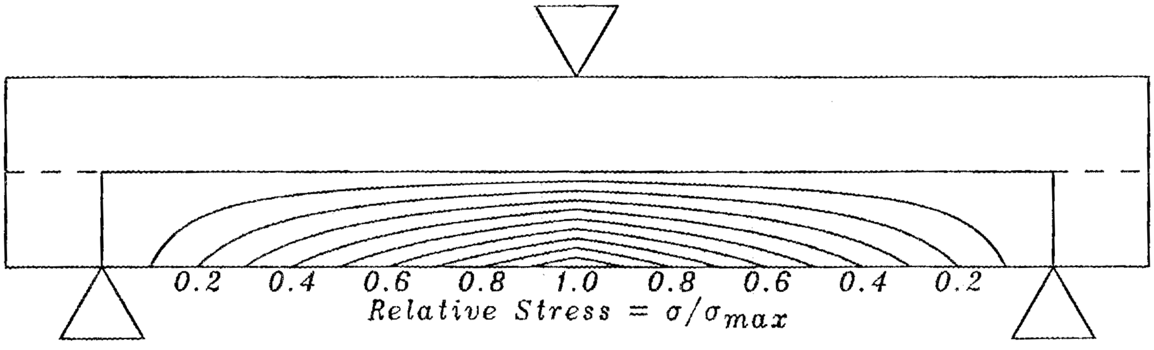

Figure 2: Side view of a three-point bend specimen showing contours of constant stress.

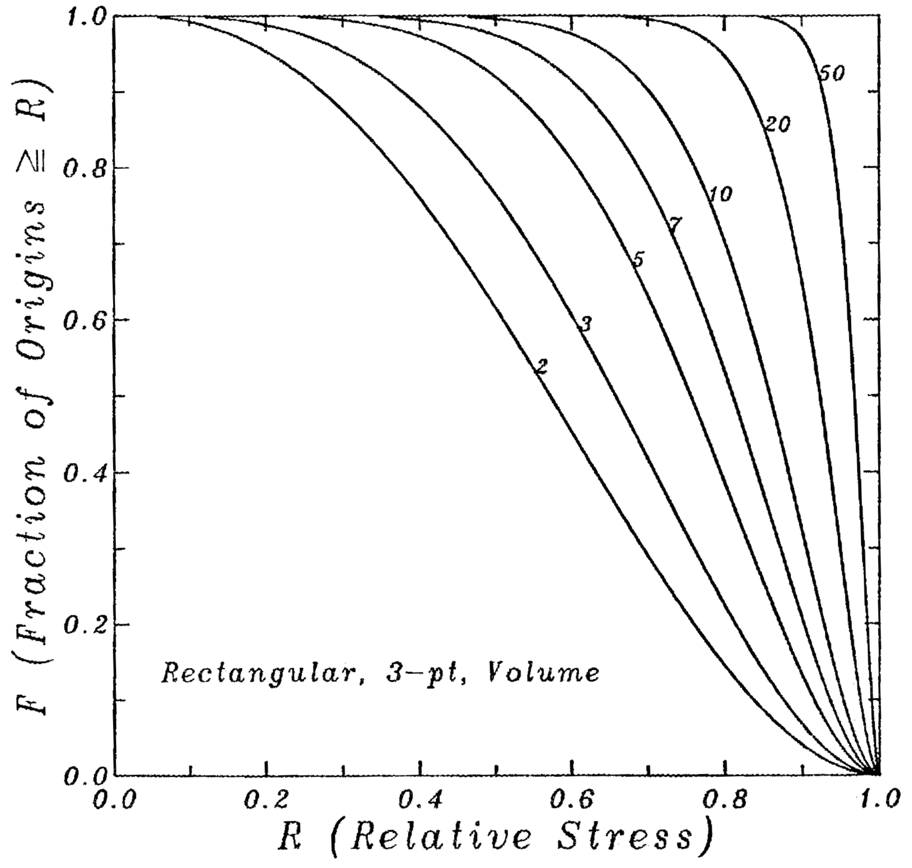

Figure 3: Plot of F vs R for three-point bend specimens with rectangular cross sections that contain defects distributed through the volume.

3.0 DATA BASE AND LIFE PREDICTION

INTRODUCTION

This portion of the project is identified as project element 3 within the work breakdown structure (WBS). It contains five subelements, including (1) Structural Qualification, (2) Time-Dependent Behavior, (3) Environmental Effects, (4) Fracture Mechanics, and (5) Nondestructive Evaluation (NDE) Development. Research conducted during this period includes activities in subelements (1), (2), and (3). Work in the Structural Qualification subelement includes proof testing, correlations with NDE results and microstructure, and application to components. Work in the Time-Dependent Behavior subelement includes studies of fatigue and creep in structural ceramics at high temperatures. Research in the Environmental Effects subelement includes study of the long-term effects of oxidation, corrosion, and erosion on the mechanical properties and microstructures of structural ceramics.

The research content of the Data Base and Life Prediction project element includes (1) experimental life testing and microstructural analysis of Si_3N_4 and SiC ceramics, (2) time-temperature strength dependence of Si_3N_4 ceramics, and (3) static fatigue behavior of PSZ ceramics.

Major objectives of research in the Data Base and Life Prediction project element are understanding and application of predictive models for structural ceramic mechanical reliability, measurement techniques for long-term mechanical property behavior in structural ceramics, and physical understanding of time-dependent mechanical failure. Success in meeting these objectives will provide U.S. companies with the tools needed for accurately predicting the mechanical reliability of ceramic heat engine components, including the effects of applied stress, time, temperature, and atmosphere on the critical ceramic properties.

3.2 TIME-DEPENDENT BEHAVIOR

Characterization of Transformation-Toughened Ceramics

L. J. Schioler, J. J. Swab, and R. N. Katz
(Army Materials Technology Laboratory)

Objectives/Scope:

Because of their unusual combination of properties, transformation toughened zirconias (TTZ) are leading candidates for cylinder liners, piston caps, head plates, valve seats, and other components for the adiabatic diesel engine. These materials are age-hardened ceramic alloy systems and as such they are likely to be susceptible to overaging and loss of strength at long times at high temperatures (i.e., close to the age hardening temperatures). The possibility of overaging with its likely negative impact on materials performance was identified as a critical area of ignorance in the preliminary technology assessment on ceramics for diesel engines previously prepared by AMMRC/MTL. Accordingly, a task was initiated to: (a) define the extent of magnitude of the overaging (if any), and (b) develop toughened ceramic alloy systems which would not be susceptible to overaging at temperatures which may be encountered in advanced diesels (1000-1200°).

The first subtask is being carried out at MTL while the second subtask is to be completed by Professor T. Y. Tien at the University of Michigan on contract from MTL.

Technical Progress

MATERIALS TECHNOLOGY LAB

During this period the analysis of the "second generation" zirconias was completed. All room and high temperature properties of these materials have been completed. The next phase of this project, the evaluation of Japanese zirconia materials was initiated. Eight different materials have been identified and have been ordered, three high temperature heat treatment furnaces have been constructed and heat treatment fixtures have been made.

The second draft of the final report covering the analysis of the "second generation" zirconias has been completed.

Because funds for 1985 were late in arriving no other technical work was completed.

UNIVERSITY OF MICHIGAN (CONTRACT)

Composites of Al_2O_3: Cr_2O_3 solid solution matrix with ZrO_2://HfO_2 solid solution dispersed particles were prepared and the modulus of elasticity, bend strength and fracture toughness were studied. The results showed that all three properties strongly depended on the size and volume fraction of the dispersed zirconia solid solution particles. The optimum composite should contain a high volume fraction of dispersed zirconia particles with approximately a 1:1 ratio of tetragonal to monoclinic. The strength degradation of a composite with high amounts of dispersed zirconia particles can be reduced by introducing hafnia in solid solution with zirconia.

Composites containing more than 20 mole % Cr_2O_3 in solid solution in the alumina matrix had a lower thermal conductivity than partially stabilized zirconia at temperatures above 300°C. Composites were annealed at 1000°C and 1200°C for more than 300 hours and no mechanical property degradation was observed. These studies suggest that these composites are a potential candidate for heat engine applications.

Status of Milestones

Because funds for 1985 were late in coming many of the milestones were pushed back. However, for the next phase of the work to be done at MTL the procurement of the Japanese zirconia materials and the construction of three heat treatment furnaces has been completed. Due to problems encountered in obtaining the Japanese zirconia from the manufacturer the materials will not be completely machined by the end of calendar year 1985.

Publications

Second draft of the final report for the past three years has been completed.

Future Plans

This DOE project is being co-funded by the Army. Funding from DOE ($68K, expiring December 1986) have arrived. FY86 Army funds ($10K) have been used on a machining contract. $75K of Army funds are planned for FY86.

The DOE funds will cover the heat treatment of all the specimens and the initial stages of the mechanical properties testing. The mechanical properties testing to be started during this time include room temperature, fracture strength, and fracture toughness tests, and some of the stress rupture and stepped temperature stress rupture tests. The Army funds will be used for materials acquisition and machining, plus materials characterization involving microhardness, density, chemical and X-ray phase analysis, optical and SEM microscopy

The joint funding of this project will enhance the quality of the data base that will be obtained from this work.

Time-Temperature Dependence of the Strength of New High-Performance Ceramics

G. D. Quinn (Army Materials Technology Laboratory)

Objective/Scope:

Stepped temperature stress rupture and standard stress rupture testing are performed to obtain a preliminary evaluation of strength retention with time under load at various temperatures for new high performance ceramics.

Technical Progress:

In this 6 month period, Lucas Syalon grade 201 was evaluated. The 201 grade is the high temperature engine grade, whereas the 101 grade is for lower temperature applications including tool bits. The Syalon 201 materials exhibited the highest strength, creep and stress rupture resistances yet measured for a commercial material in the sintered silicon family, (comparable results were obtained previously on a General Electric sintered silicon nitride with $BeSiN_2$ additions, but only on a laboratory batch of material). Figure 1 presents STSR results which indicates static fatigue and creep phenomenon became problems at 1300°C or above. This is remarkably close to a lowest eutectic temperature of 1350° in the Si_3N_4 SiO_2 AlN Y_2O_3 system. The average room temperature strength was 569 MPa with a Weibull modulus of 9. The few stress rupture failures at 1200° were at stresses 80% or greater of the room temperatures average strength (Figure 2). The grain boundary phase of this material appeared to be fully crystalline and is principally YAG with some $YSiO_2N$. Further analysis and fractography is ongoing.

Status of Milestones:

This task is terminating because a program reevaluation at MTL. Preliminary results and all specimens of Kyocera sintered silicon nitride grade SN220 have been turned over to ORNL. GTE Wesgo SNW-1000 will be evaluated as part of an ongoing internal MTL program.

Publications:

A summary of current results was presented at the CCM meeting in October 1985. Data was presented for GE Beta silicon carbide, University of Michigan SiC and Lucas Syalon 201. A brief review of the entire workscope and accomplishments done under this task since 1976 was presented along with a complete bibliography.

Outstanding reports include:

"Static Fatigue of a Siliconized SiC" to be published as an MTL TR.

"Mechanical Property Evaluation at Elevated Temperatures for Beta Silicon Cabide" to be published as an MTL TR and also submitted to International Journal of High Technology Ceramics.

"Static Fatigue of a Commercial Sialon" to be submitted to J. Mat. Science.

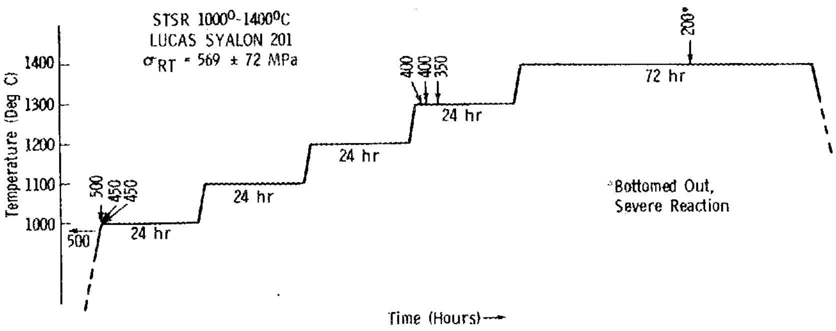

Figure 1. STSR Results for Syalon 201 in Air.

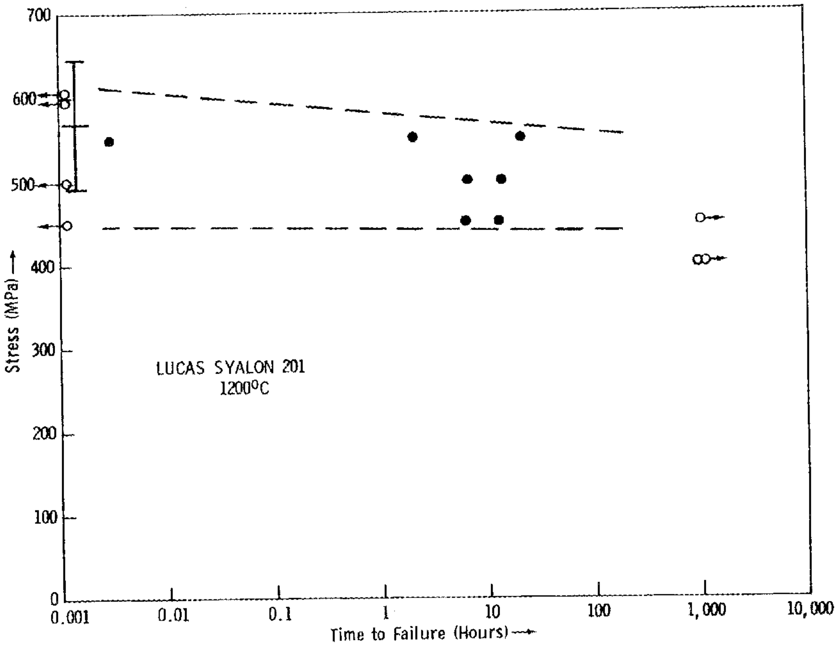

Figure 2. Flexural Stress Rupture at $1200^{\circ}C$ in Air. The Room Temperature Average Strength and Standard Deviations are shown next to the ordinate axis.

Fracture Behavior of Toughened Ceramics

P. F. Becher, T. N. Tiegs, and W. H. Warwick (Oak Ridge National Laboratory)

Objective/scope

Because of their excellent toughness, oxide ceramics such as partially stabilized zirconia (PSZ), dispersion-toughened alumina (DTA) and whisker-reinforced ceramics are prime candidates for many diesel engine components. The enhanced toughness of the PSZ and DTA materials is thought to be due to a stress-induced transformation (of the dispersed phase) which requires additional energy in order for catastrophic fracture to occur. However, these materials are still susceptible to slow crack growth and thus strength degradation. Also there is limited evidence that, at temperatures above 700°C, time-dependent aging effects can reduce the concentration of the phase involved in the transformation process, leading to significant losses in toughness and strength. Again it is essential that mechanisms responsible for both the slow crack growth and aging behavior be well understood. Similarly the toughening behavior in whisker-reinforced ceramics and the high-temperature performance of those ceramics must be evaluated in order to develop materials for particular applications.

In response to this need, studies have been initiated to examine toughening and fatigue properties of PSZ, DTA, and whisker-reinforced materials. Particular emphasis has been placed on understanding the effect of microstructure upon processes responsible for time-dependent variations in toughness and high-temperature strength. In addition, fundamental insight into the slow crack growth behavior associated with these materials is being obtained.

Technical progress

In the the case of ZrO_2, the tetragonal to monoclinic transformation involves a volume increase as well as a shear strain. Thus under conditions where the sample is stressed, the transformation occurs in a tensile strain field (e.g., that surrounding a crack tip) which allows the volume to expand. Observations reveal that the shear (shape change) strain is often minimized by the generation of twins within the monoclinic phase. When they transform and expand, the ZrO_2 particles introduce radial compressive strains in the surrounding matrix. Because the volume increase is 5 to 6%, the linear compressive strains in the matrix are quite large (1–2%). In this case the associated local compressive stresses are very high (0.01–0.02 times the Young's modulus of the matrix) and modify (decrease) any nearby crack tip tensile stress fields. When tetragonal ZrO_2 particles transform in the tensile stress field of a crack tip, the crack tip tensile stress is decreased and the external tensile stress must be increased to generate sufficient tensile stress to continue to propagate the crack. This is clearly why this type transformation is so attractive in ceramics, where cracks normally grow quite easily when subjected to very modest tensile stress conditions.

In studies[1] supported by the Office of Basic Energy Science Materials Sciences Program, it has been shown that the tetragonal to monoclinic phase transformation in ZrO_2 can be characterized by the temperatures at which the forward (M_s) and reverse (A_s) transformations are initiated during decreasing and increasing temperature cycles, respectively (Fig. 1). At $T = M_s$, a portion of the tetragonal precipitates/particles spontaneously transforms to the monoclinic phase so that the total chemical free energy change, ΔG_T^{t-m}, must be zero. When $T > M_s$, $\Delta G_T^{t-m} > 0$ and additional energy must be supplied to initiate the transformation. This can be derived from the strain energy introduced from an externally applied tensile stress. When ΔG_T^{t-m} is still positive but is decreased toward zero, the amount of externally supplied strain energy, ΔU_{se}, required is likewise decreased.

In the case of transformation-toughened materials, determination of the M_s temperatures for different compositions and microstructures (e.g., precipitate size) should be useful in describing the stability of the tetragonal phase and hence should provide an indication of the toughness of each material. Again when $T = M_s$, ΔG^{t-m} is zero and the transformation initiated spontaneously as seen by

$$\Delta G_T^{t-m} = (T - M_s)\Delta S \quad , \tag{1}$$

where T represents the temperature of interest and ΔS is the entropy difference between the two phases. Thus when $T > M_s$, the tetragonal phase is stable, and some external energy must be supplied to transform it. This is, of course, the case of interest in transformation-toughened systems where the strain energy supplied by an external tensile stress triggers the transformation.

The critical stress (σ_c^T) required to transform tetragonal precipitate/particle is related to the external applied strain energy required ($\Delta U_{se} = \Delta G_T^{t-m}$) to initiate the transformation.

$$\Delta U_{se} = \sigma_c^T \, e^T \quad , \tag{2}$$

so that

$$\sigma_c^T = (\Delta G^{t-m})/e^T \quad , \tag{3}$$

where e^T is the volume expansion strain associated with the transformation.

The incremental increase in the fracture toughness due to the transformation (ΔK_{IC}^T) is related to the half width of the transformed zone surrounding the crack (r):

$$\Delta K_{IC}^T = A e^T \, V_f \, E^c \, r^{1/2} \quad , \tag{4}$$

where A is a function of the form of the transformation stress ($A = 0.22$ for transformations triggered by the principle stress, and $A = 0.50$ for those initiated by shear stress), V_f is the volume fraction of transformable ZrO_2, and E^c is the Young's modulus of the system. Analogous to the plastic zone size in metals, the transformation zone size is a function of the critical transformation stress (σ_c^T)

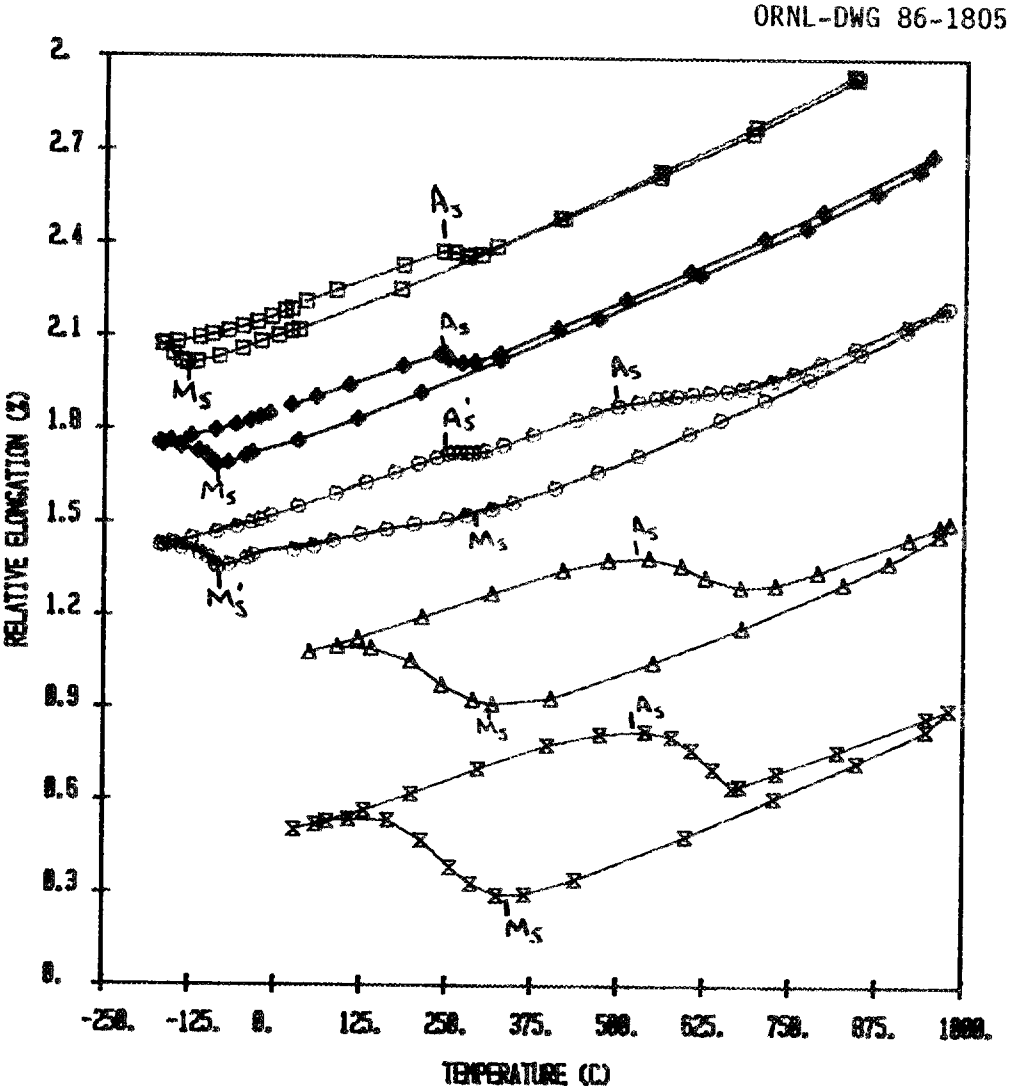

Fig. 1. Thermal expansion hysteresis of PSZ ceramics generated by tetragonal ⇄ mononoclinic transformation. At $T \leqslant M_s$, tetragonal precipitates transform to monoclinic phase during cooling. During heating cycle, monoclinic phase transforms to tetragonal at $T \geqslant A_s$. The M_s temperature is a measure of the tetragonal phase stability at a given test temperature (T) where $T > M_s$. Note for those PSZ ceramics where $M_s < 20°C$ (top two curves), heating cycles which start and end at 20°C will yield no hysteresis but will give linear expansion-contraction versus temperature plots. Only when first cooled below M_s will such samples exhibit any expansion hysteresis. When $M_s \geqslant 20°C$, the transformation expansion hysteresis will be initiated when the maximum $T > A_s$. These are important considerations when concerned with heating-cooling strains, e.g., brazing materials and interfaces between components.

$$r = B\ (K_{IC}^{M}/\sigma_{c}^{T})^{2}\ , \tag{5}$$

where K_{IC}^{M} is the fracture toughness of the matrix and $B = [2(1 + v)^2/9\pi]$ accounts for the geometry of the crack tip stress field. By combining Eqs. 3, 4, and 5, we find that

$$\Delta K_{IC}^{T} = AB^{1/2}\ (e^{T})^{2}\ V_{f}E^{c}K_{IC}^{M}\ /(\Delta G_{T}^{t-m})\ , \tag{6}$$

and by substitution of Eq. 1 we obtain

$$\Delta K_{IC}^{T} = AB^{1/2}\ (e^{T})^{2}\ V_{f}\ E^{c}\ K_{IC}^{M}/\Delta S(T - M_{s}) \tag{7}$$

and the dependence of the toughness on the transformation temperature of the material and the test temperature, Fig. 2.

As one expects, the above relationship predicts that the fracture toughness due to the transformation decreases as the reciprocal of the increase in the test temperature for a given material. This is consistent with the increase in stability of the transforming tetragonal phase with increase in test temperature and also predicts that the critical transformation stress increases (Eqs. 1 and 3) and the zone size decreases (Eqs. 1, 3, and 5) as either the test temperature increases or M_s decreases. A similar increase in toughness is predicted as the M_s approaches T for the case of $T > M_s$. Thus, a maximum in toughness can be achieved by increasing the M_s temperature of the ZrO_2 until it is nearly equal to the temperature of interest. Likewise, the toughness of a given ZrO_2 will reach a maximum as the test temperature is lowered to its M_s temperature.

The M_s temperature thus gives a measure of tetragonal phase stability and toughness of the PSZ ceramics. The feature that controls the M_s values in MgO-PSZ is the size of the tetragonal precipitates achieved during heat treatment (Fig. 3). With increasing size of the precipitates there is a corresponding increase in M_s.

Through the preceeding analysis, esp. Eq. 7, one can describe the transformation toughening contribution obtained in MgO-PSZ ceramics. Values of A, ΔS, and K_{IC}^{M} were obtained experimentally and, when incorporated into Eq. 7, yield

$$\Delta K_{IC}^{T} \simeq 2V_{f}(\mathrm{GPa}\ K)/(195K - M_{s})\ , \tag{8}$$

which is consistent with the experimental data for the MgO-PSZ samples.

In additional studies by one of the authors[2] on ceramic matrix composites toughened by the incorporation of zirconia particles sponsored by the Materials Sciences Program, the critical fracture toughness of zirconia-toughened composites is described by

$$K_{IC}{}^{C} = K_{IC}{}^{M} + \Delta K_{IC}{}^{T}\ , \tag{9}$$

where the contribution $\Delta K_{IC}{}^{T}$ associated with the transformation of tetragonal ZrO_2 particles is described by Eq. 4. Referring to Eqs. 5 and 4 we can see that

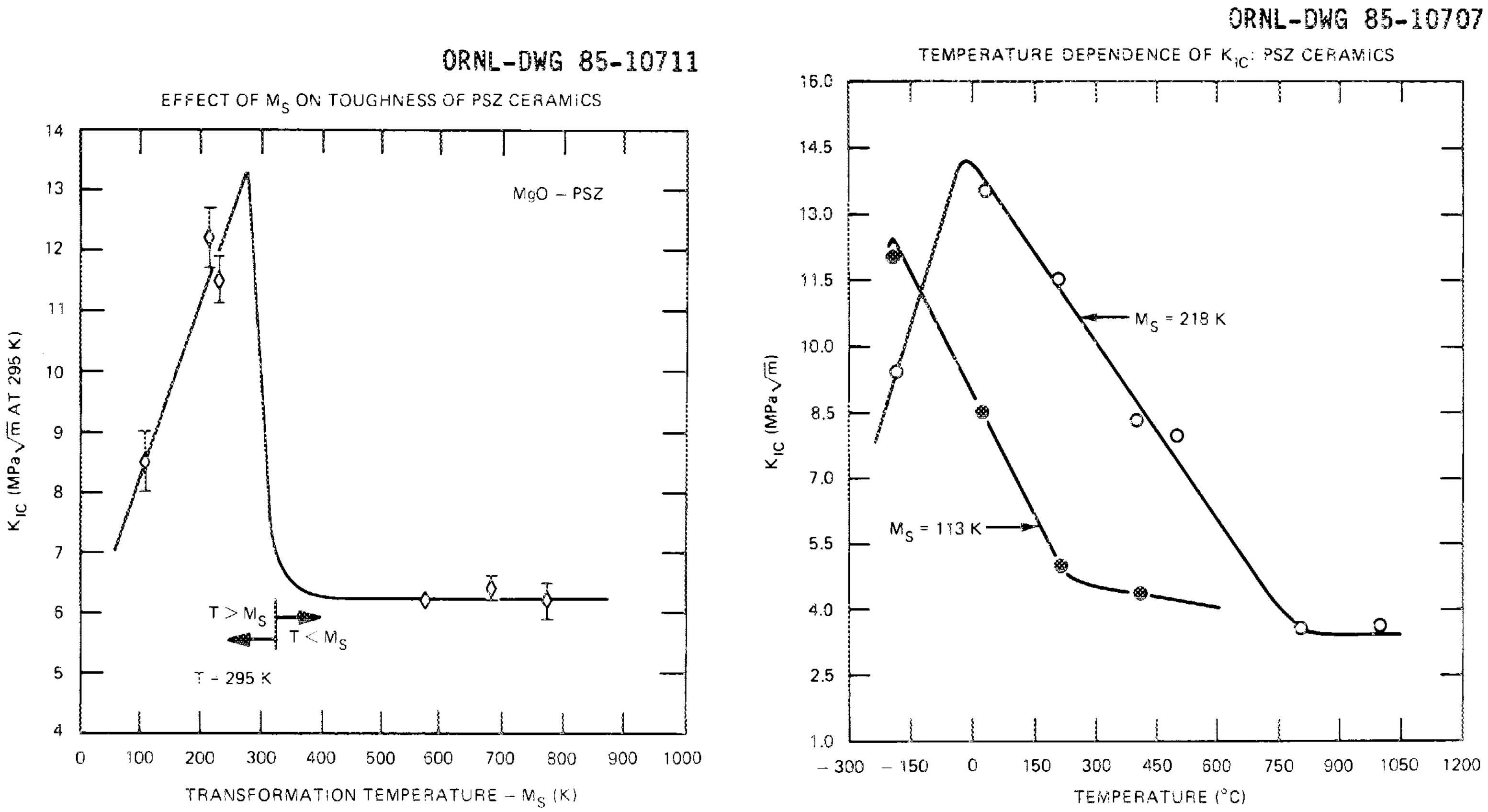

Fig. 2. For the case $T > M_s$, transformation toughening occurs and K_{IC} is a function of M_s. For the case $T < M_s$, crack deflection and branching occur and K_{IC} is essentially independent of M_s. (*a*) As expected, toughness is a function of M_s temperature of PSZ. (*b*) Similarly for $T > M_s$, ΔK_{IC}^{T} for a given PSZ (M_s is constant) will be a unique function of the test temperature, T.

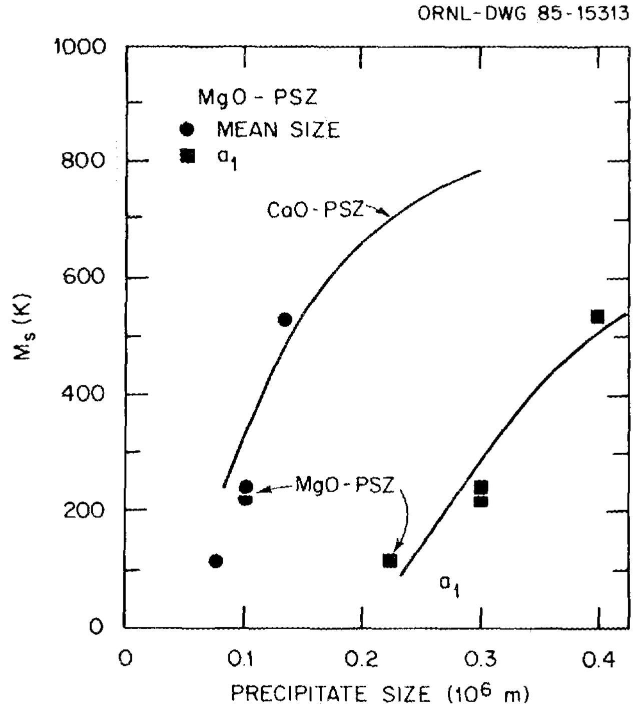

Fig. 3. In MgO-PSZ and CaO-PSZ ceramics, M_s temperatures are a function of precipitate size. Increasing size of tetragonal precipitates in large-grained cubic ZrO_2 increases the M_s temperature. Precipitate size is controlled by heat treatment temperature and time at temperature.

$$K_{IC}^{C} = K_{IC}^{M} + AB^{1/2}V_f E_c e^T (K_{IC}^{M}/\sigma_C^T) \ , \tag{10}$$

which indicates the dependence of the composite toughness on the matrix toughness.

Equation 10 states that the composite toughness significantly increases with increase in matrix toughness as both toughness components on the right-hand side of Eq. 10 increase. What these studies show then is that the toughness of ZrO_2-toughened composites can be increased further by increasing K_{IC}^{M}. The studies next assumed that K_{IC}^{M} could be defined as the toughness of a matrix which was a composite and not a single-phase material. The matrix composite of two or more phases would not contain transformable ZrO_2 as that case is already addressed in Eq. 10. These studies thus show that multiple toughening mechanisms introduced by the use of multiple toughening agents should give a combined toughness that is greater than that achieved with a single toughening agent.

Our previous results in the Ceramic Technology for Advanced Heat Engines Program show that polycrystalline oxides can be toughened by incorporating SiC whiskers. It was thus logical to test the above analysis by using a SiC-whisker-reinforced oxide as a matrix to which ZrO_2

particles were added. Note that we assume that K_{IC}^M is the toughness of the SiC-whisker-reinforced oxide matrix and is the value of K_{IC}^M in Eq. 10. The experimental data obtained for mullite (1) with SiC whiskers, (2) with ZrO_2 particles, and (3) with SiC whiskers plus ZrO_2 particles are shown in Fig. 4. The data confirm the above predictions that the use of multiple toughening mechanisms indeed results in a greater increase in toughness than a single mechanism. The use of such an approach thus offers a means for obtaining significant additional toughening in ceramic composites.

ORNL-DWG 86-1806

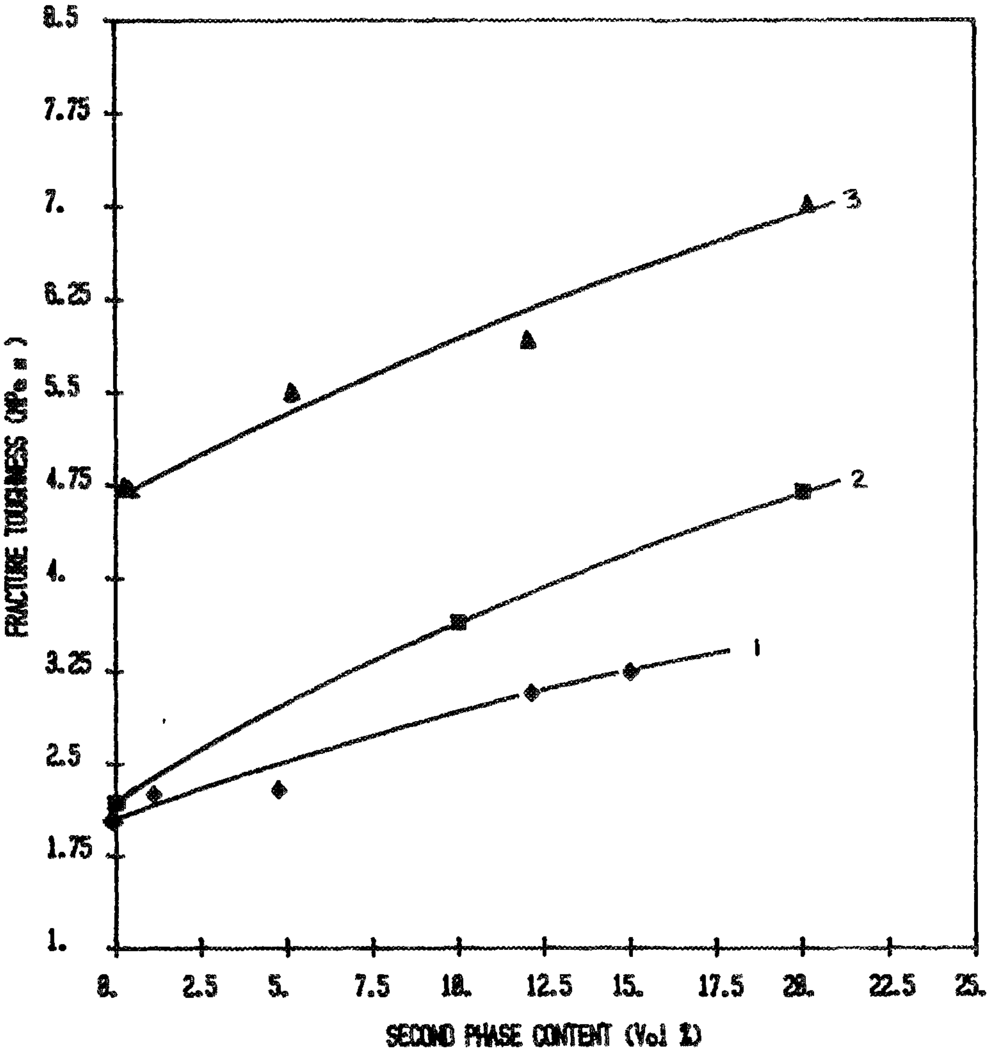

Fig. 4. Studies of the critical fracture toughness of mullite-based composites reveal that multiple toughening mechanisms (i.e., incorporating SiC whiskers and ZrO_2 particles, curve 3) result in greater toughness than either mechanism by itself (i.e., just SiC whiskers, curve 1, or ZrO_2 particles, curve 2). Data for mullite-zirconia composites from Refs. 3 and 4.

Status of milestones

On schedule.

Publications

None.

References

1. P. F. Becher, M. V. Swain, and M. K. Ferber, "The Relation of Transformation Temperature to the Fracture Toughness of Transformation Toughened Ceramics," to be published.

2. P. F. Becher, "Toughening Behavior in Ceramics Associated with the Transformation of Tetragonal ZrO_2," to be published.

3. J. S. Wallace, N. Claussen, and S. Prochaska, "Properties of Mullite-Zirconia Composites Prepared by Different Processing Routes," pp. 642–9 in *Proceedings of the 1st International Symposium on Ceramics Components for Engines*, ed. S. Somiya, E. Kanai, and K. Ando, KTK Scientific Publishers, Tokyo, 1984.

4. P. F. Becher, unpublished results.

Cyclic Fatigue of Toughened Ceramics

K. C. Liu and C. R. Brinkman (Oak Ridge National Laboratory)

Objective/scope

The objective of this task activity is to develop, design, fabricate, and demonstrate the capability of performing tension-tension dynamic fatigue testing on a uniaxially loaded ceramic specimen at elevated temperatures.

Three areas of research have been identified as the main thrust of this task: (1) design, fabrication, and demonstration of a load train column that truly aligns with the line of specimen loading; (2) development of a simple specimen grip that can effectively link the load train and test specimen without complicating the specimen geometry and, hence, minimize the cost of the test specimen; and (3) design and analysis of a specimen for tensile cyclic fatigue testing.

Technical progress

A major milestone has been successfully completed — the development of a capability for room-temperature testing. This progress report describes the development effort and successful testing of a self-aligning grip system for tensile cyclic fatigue testing of advanced ceramic materials.

The ORNL grip system is a unique device capable of carrying out uniaxial tensile testing with specimen stress uniformity superior to that of other methods. Simple concepts of hydrostatics and mechanics were used in the grip design. The grip system consists basically of two major components: a hydraulic housing assembly and a pull rod assembly. A cutaway view of the grip system is illustrated in Fig. 1. Inside the housing block (1) are eight built-in miniature hydraulic piston assemblies equally spaced on a circle. An exploded view of the hydraulic piston assembly shows an O-ring seal (5) and a piston (6) with a long stem guided by a ball-bearing bushing (7). Directly beneath the oil chambers (4) is a circular fluid channel (2). The passage of hydraulic fluid between the oil chambers is accomplished through a vertical needle hole drilled from the bottom of the oil chamber to the fluid channel (2). The piston assembly is secured in place by a snap ring (8). An assembled piston is shown near the lower left end of the specimen (16). An overhead view of the grip housing (components 1–6) is shown in Fig. 2.

For room-temperature testing, the button-head fatigue specimen (16) is directly connected to the metal pull rod (10) with a tapered split collar (14) and a matching metal plug (15). This is a highly reliable gripping technique used previously by many investigators. Good concentricity between the pull rod and specimen and dependable gripping are its features. For high-temperature testing, the pull rod is extended with a ceramic pull rod and cooled by water through the cooling channel (13) built into the rod stem. A concentrically grooved circular flat ring (12) made of tempered steel is bolted on the bottom side of the disc head (10) by eight small screws (11).

YP-729

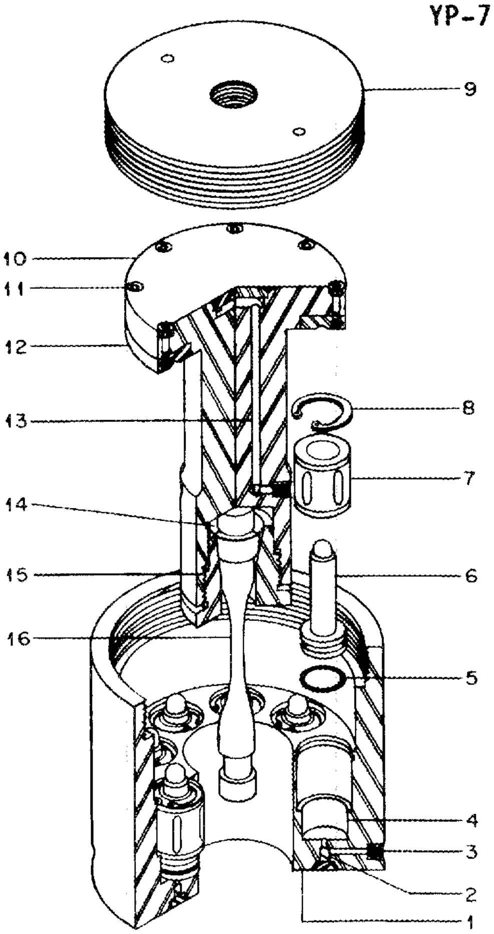

Fig. 1. Cutaway view of Oak Ridge National Laboratory self-aligning grip system.

YP-689A

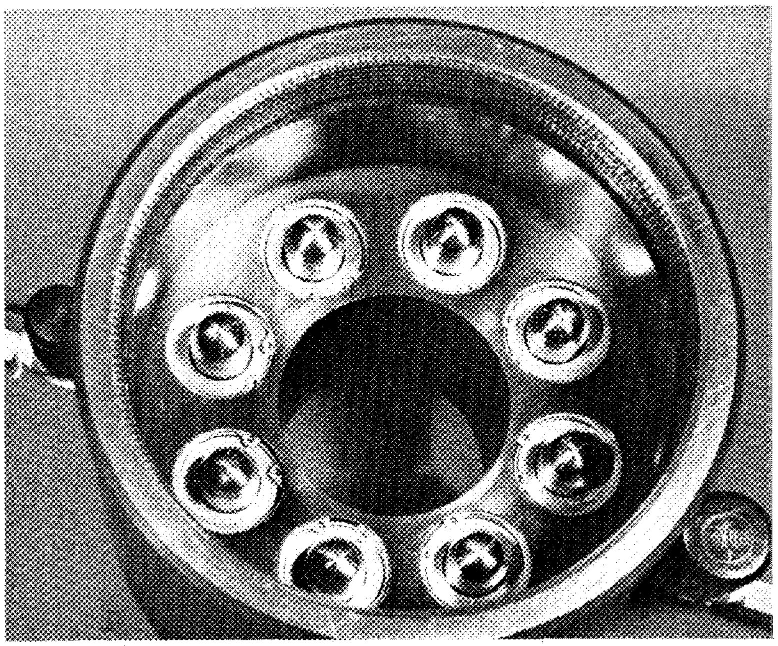

Fig. 2. Overhead view of grip housing with cover plate removed.

The grip is assembled by slipping the pull rod into the center hole of the housing and placing the large disc head on the hydraulic piston heads. The cover plate (9) completes the assembly. Figure 3 shows the arrangement of load train, load frame assembly, and control electronics.

YP-682

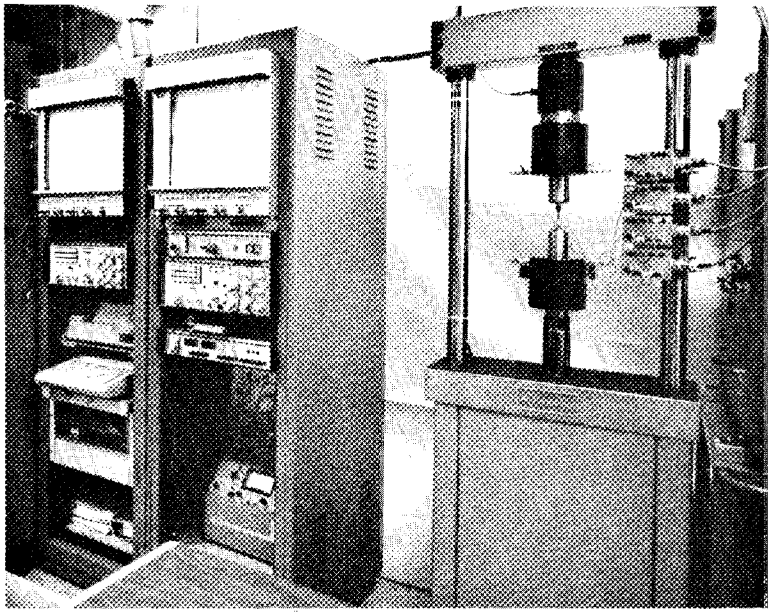

Fig. 3. Testing apparatus, showing the arrangement of load train with self-aligning grips.

The operational principle of the self-aligning grip system can be described best by using the schematic diagram shown in Fig. 4. The center arrow "p" represents the specimen load. This load is balanced by a circular array of reacting forces generated from the eight piston assemblies. Two conditions must be met in order to achieve perfect concentric loading (i.e., zero eccentricity $\delta_x = \delta_y = 0$). The first condition requires that all the reacting forces must be equal. The next requires that the reactive forces must be equally spaced on a circle. Any deviations from ideal conditions will result in some eccentricity.

Proof of the concepts was performed with a special load applicator instrumented with strain gages as shown in Fig. 5. Four sets of strain gage full bridges were bonded on the radial cantilever arms to monitor the distribution of the reactive loads. Eight tests were performed. For each test, the load applicator was rotated one-eighth of a turn so that the reactive forces were measured by a different bridge circuit. The outputs of load and strains were monitored continuously by a data acquisition system while cyclic loading was imposed to the grip housing. The maximum deviation from the load-strain response was less than 0.5% of the full-scale load equal to 22.2 kN (5000 lb). The maximum load deviation from

ORNL DWG 85-15846

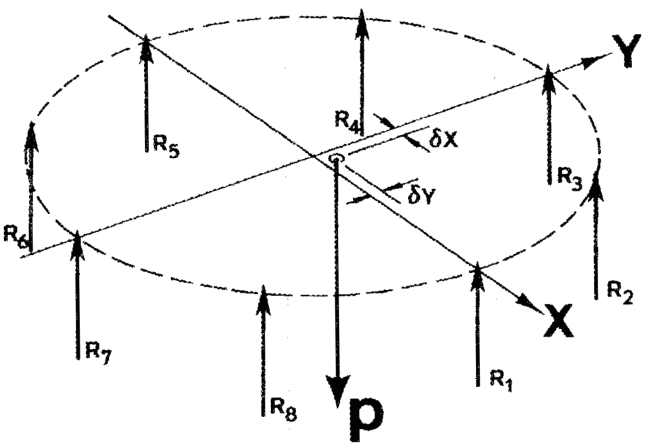

Fig. 4. Schematic diagram showing the design concepts of the self-aligning grip system.

YP-668

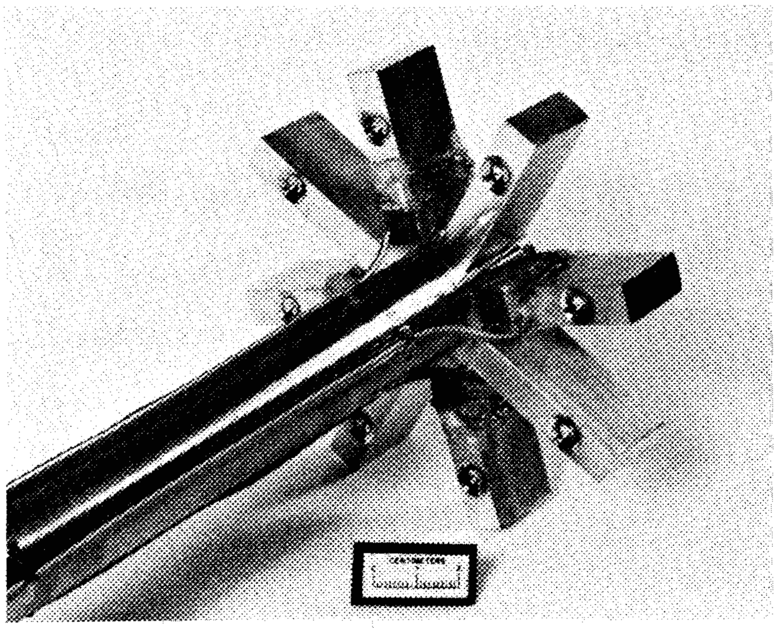

Fig. 5. Strain-gaged load applicator used to measure the piston reacting forces.

the average value was 0.46% of the full load. The average deviation of the reactive loads that occurred in the piston systems was >0.08%. On the basis of these test data, the eccentricity of the resultant load was calculated to be less than 2.54×10^{-2} mm (0.001 in.). The eccentricity improved to less than 1.52×10^{-2} mm (0.0006 in.) in a subsequent test.

To complete system alignment evaluation, a 6-mm-diam (1/4-in.) dummy specimen made of high-strength aluminum alloy was used as shown in Fig. 6. This specimen was instrumented with strain gages to measure bending at the midlength of the gage section and shank sections. At each of the three positions, four strain gages were spaced equally on the circumference so that the strain gages were paired diametrically. To limit the loading within the elastic range, the specimen was cycled only to 907 kg (2000 lb) giving a tensile strength of about 276 MPa (40 ksi) and a maximum strain of about 0.4%. To further ensure that the test results were not biased, the dummy specimen was rotated successively from the previous test position by 90° for each test performed. Results show that the percentage of bending stress at the midlength of the uniform gage section was less than 0.5% of the average tensile stress measured by the strain gages.

A final check-out test was then performed with a buttonhead fatigue specimen made of MACOR, which is the trade name of Corning machinable glass-ceramic. Four strain gages were bonded on the midlength of the uniform gage section as shown in Fig. 7. Because the proportional limit stress of MACOR was not known, the specimen was cycled initially to 222 N (50 lbf). To avoid overstressing, the cyclic load was incrementally increased in three steps to 666 N (150 lbf). This produced a tensile

YP-683

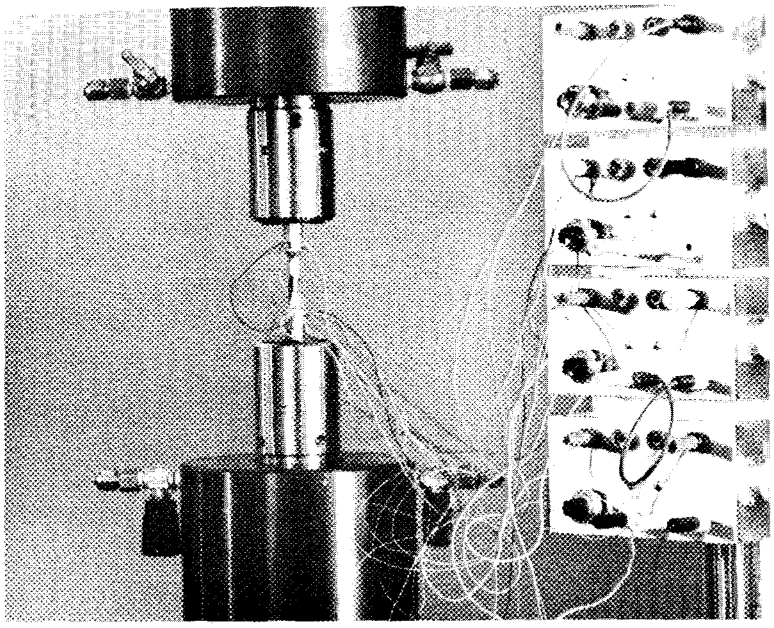

Fig. 6. Close-up view of the load train with a heavily strain-gaged aluminum specimen mounted on the self-aligning grips.

YP-688

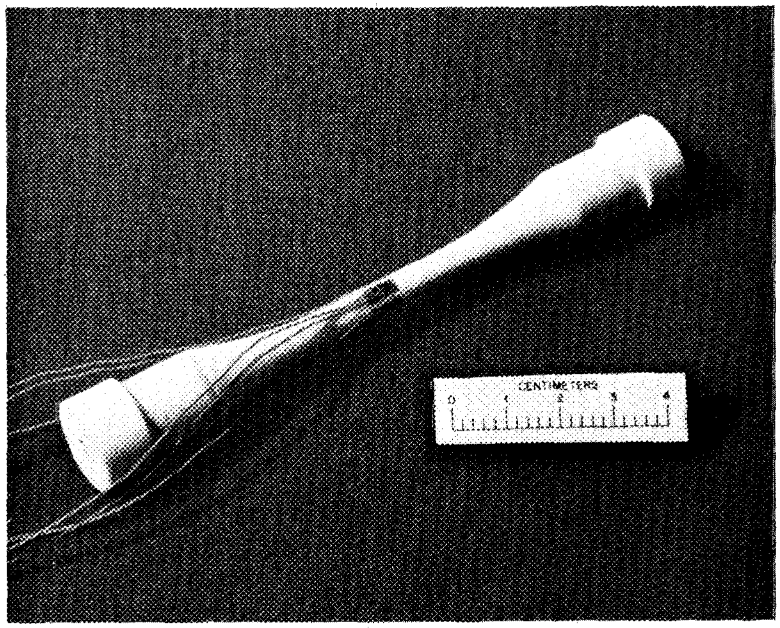

Fig. 7. Fatigue specimen, made of MACOR machinable glass-ceramic, instrumented with strain gages.

stress of 21 MPa (3000 psi) and a total strain of 0.03%. The test was repeated four times with the specimen rotated a quarter turn each time. Results show that the bending was about 2.5% of the average tensile stress. For most testing systems, the percentage of bending stress at this low load level would be at least 20% or higher. The percentage of bending stress usually decreases as the load increases. By the rule of linear extrapolation, we believe that the bending stress will decrease to about 0.5% level as the tensile load increases to 6.66 kN (1500 lb) for the ceramic specimen, as was the case reported for the aluminum specimen.

Summary

1. Laboratory room-temperature testing to date indicates that the self-aligning grip system is capable of concentric load transfer between the grip and specimen with negligible eccentricity.
2. The specimen alignment provided by the grips appears to be superior to that of other gripping methods.[1,2]
3. Measurements taken from strain gages indicate that the grip system can perform tension-tension cyclic fatigue testing with a minimal bending stress below 0.5% of the maximum tensile stress.
4. The grip system is now available for room-temperature testing.

Status of milestones

Completed design, fabrication, installation, and initial phase of evaluation of tension-tension fatigue grips for room-temperature testing of advanced ceramic materials, September 30, 1985.

Publications

"Tensile Cyclic Fatigue of Structural Ceramics," to be presented at, and published in the proceedings of, the 23rd Automotive Technology Development Contractors' Coordination Meeting, Dearborn, Michigan, Oct. 21–24, 1985.

References

1. B. W. Christ and S. R. Swanson, "Alignment Problems in Tensile Testing," *J. Testing and Evaluation* 4(6), 405–17 (Nov. 1976).

2. F. F. Lange and E. S. Diaz, "Powder-Cushion Gripping to Promote Good Alignment in Tensile Testing," *J. Testing and Evaluation* 6(5), 320–23 (Sept. 1978).

3.3 ENVIRONMENTAL EFFECTS

Static Behavior of Toughened Ceramics

M. K. Ferber (University of Illinois)

Objective/Scope

The objective of this program is to study the long-term mechanical stability of toughened ceramics for diesel engine applications. The work is divided into the two tasks. The first involves the measurement of the time-dependent strength behavior of ceramic bend-bar samples as a function of temperature and applied stress using the Interrupted Fatigue (I.F.) method. Although a variety of candidate engine materials will be examined, current studies are focusing upon commercially available partially stabilized zirconia (PSZ). In the second task, the microstructures of selected I.F. specimens will be characterized using SEM and TEM. In addition, x-ray diffraction and dilatometry studies will be conducted to examine changes in the transformation behavior of the PSZ ceramics resulting from the high-temperature exposure.

Technical Progress

Two commercial Mg-PSZ ceramics* designated TS PSZ (thermal shock grade) and MS PSZ (maximum strength grade) were chosen for initial testing since both are prime candidates for use as prototype diesel engine components.[1] These materials were obtained in the form of circular discs 100 mm in diameter and 7.6 mm thick. Rectangular bend specimens (25.4 X 2.82 X 2.5 mm) were then machined from the discs for subsequent mechanical property studies. The tensile surface of each sample was polished to a 0.25 μm finish and the edges beveled using a 6μm diamond wheel.

The fatigue behavior was determined using an interrupted fatigue (I.F.) technique in which the four-point bend strength S_f was measured as a function of time (t), temperature (T), and applied stress (σ_a). This method has several advantages over conventional static fatigue testing. First, since time is a controllable quantity, problems associated with an unpredictable fatigue life (as in the case of static fatigue) are avoided. In the present study, this feature allowed for periodic examination of test specimens so that changes in both phase composition and transformation characteristics could be

---

*Manufactured by Nilcra Ceramics, USA Office, Glendale Heights, Illinois.

ascertained. A second advantage is that processes responsible for both strength degradation and strength enhancement can be readily distinguished.[2]

I.F. studies involving both materials were conducted at temperatures of 500, 800, and 1000°C for exposure times ranging from 1 to 1008 h. The baseline data were established using specimens subjected to a zero stress level. Subsequent tests were then performed with σ_a equal to 60% of the fast fracture strength (i.e. 60% of S_f value measured at the same T for t=1 h and $\sigma_a = 0$). For each test condition, S_f was determined at temperature by fracturing three or more samples.

All testing was conducted in a specially designed Flexure Test System (F.T.S.) capable of holding up to three bend samples.* The general layout of the F.T.S. is shown in Fig. 1. The Test Frame contains the hardware for applying mechanical forces to each of three samples which are supported by Al_2O_3 four-point bend fixtures. The loads are generated by pneumatically driven air cylinders located at the top of the support frame. These loads are transmitted into the hot zone of the furnace through aluminum oxide (Al_2O_3) rods. Each of the bottom three Al_2O_3 rods are also attached to a load cell which monitors the applied force as a function of time. Water-cooled adapters are used to connect the aluminum oxide rams to both the load cells and the air cylinders. The computer monitors the load on each specimen and provides necessary adjustments in the air pressure (via the electro-pnuematic transducer) such that the desired stress level is maintained. Following the designated exposure time, the samples are fractured using a prescribed loading rate (345 KPa/s in the present study).

Several techniques were used to characterize both the as-received and tested I.F. samples. For example, the microstructures were examined using both standard ceramographic methods and SEM. The latter technique allowed for characterization of fracture surfaces. The volume fractions of the cubic (c), tetragonal (t), and monoclinic (m) phases were also determined from x-ray diffraction and Raman spectroscopy studies.

The microstructures of the TS and MS PSZ ceramics generally consisted of 30-50 μm grains containing fine (<0.1 X 0.4 μm) (t) precipitates. The precipitate structure in the vicinity of a three-grain region is illustrated for the TS PSZ in Fig. 2. The larger grain boundary precipitates (possibly monoclinic) were characteristic of both materials. Although not shown in this figure, considerable

---

*The F.T.S. design is based on a similar system originally developed by S. M. Wiederhorn and N. J. Tighe of the National Bureau of Standards.

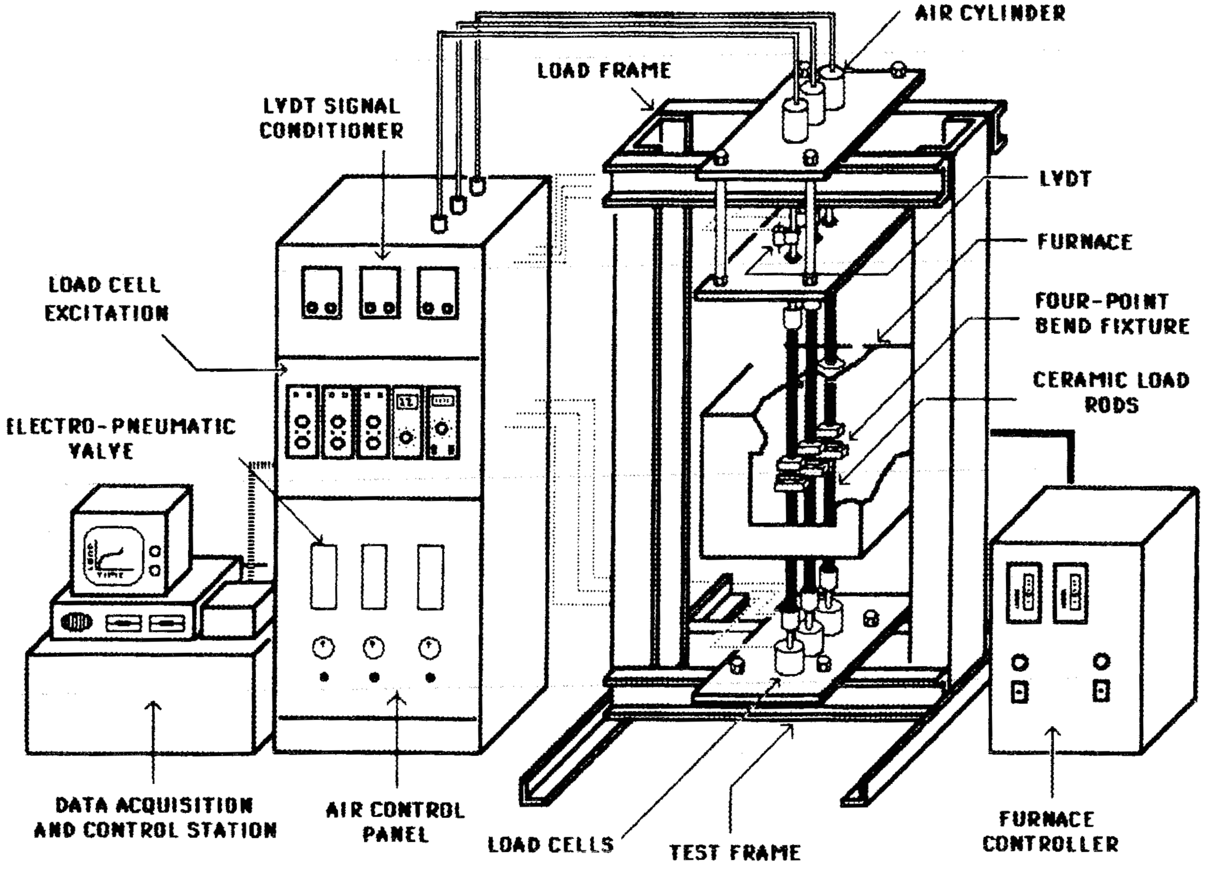

Figure 1. In Flexure Test System, the required mechanical loads are applied pnuematically (with air cylinders) to each of three alumina bend fixtures.

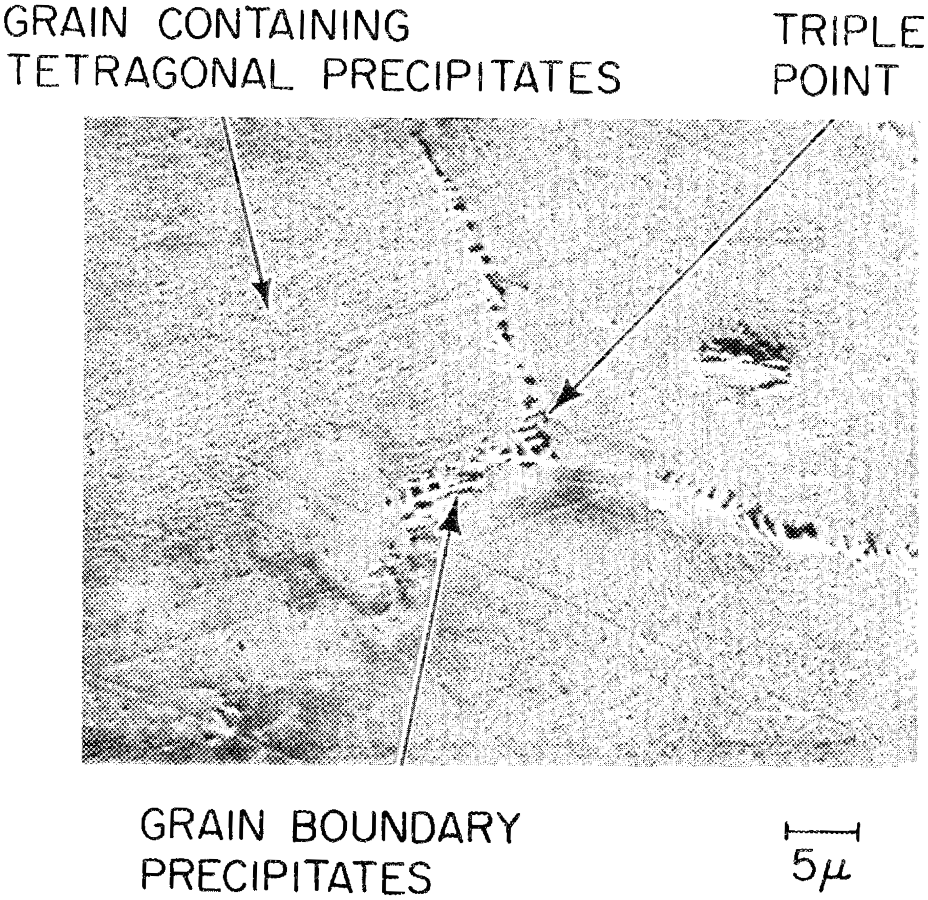

Figure 2. Microstructure of MgO partially stabilized zirconia contains dense array of submicron tetragonal precipitates.

porosity was also observed in both microstructures. Finally, a microprobe analysis indicated that the two PSZ ceramics contained MgO and HfO_2 at concentrations of 8.4 and 1.0 mole %, respectively.

An x-ray analysis of the polished surfaces of the as-received MS and TS PSZ materials revealed (m) volume fractions (V_f^m) of 0.9 and 0.16, respectively. The calculations were based on equations given in Ref. 3. Unfortunately the volume fractions for the (c) and (t) phases (V_f^c and V_f^t) could not be determined using this technique because of overlapping of the cubic (111) tetragonal (101) peaks. However, additional Raman spectrographic studies provided independent estimates of the V_f^t/V_f^m ratios. These numbers were then used in conjunction with the x-ray data to yield the approximate phase analysis:

$$\text{TS PSZ:}\quad V_f^c = 0.64;\ V_f^t = 0.20;\ V_f^m = 0.16$$

$$\text{MS PSZ:}\quad V_f^c = 0.65;\ V_f^t = 0.26;\ V_f^m = 0.09$$

These results agree favorably with those reported by the vendor and determined in independent investigations.[4]

Preliminary results from the I.F. measurements for the TS PSZ are shown in Fig. 3. At 500°C (σ_a = 248 MPa) the strength did not change appreciably for exposure times up to 1008 h (Fig. 3(a)). However, when the temperature was raised to 800°C (σ_a = 207 MPa), S_f increased significantly for t< 200 h. Although not illustrated in Fig. 3(a), recent measurements have shown that after 1008 h, S_f (for T = 800°C and σ_a = 207 MPa) decreases to 373 $\pm$ 56 MPa, which is comparable to the value obtained after 24 h. Therefore S_f exhibits a definite maximum with increasing exposure time.

Similar behavior was observed when the TS samples were stressed (σ_a = 172 MPa) at 1000°C (Fig. 3(b)). However, the average strength after 1008 h was only 85% of it's initial short-term value (t = 24 h). A few I.F. measurements at 1000°C were also conducted using σ_a = 241 MPa. In this case all samples fractured prematurely within ~ 5h (300 s). When no stress was applied, the strength did not change significantly, at least to 360 h, the extent of present data. These results suggest that for T $\geq$ 800°C, the applied stress level can have a dramatic affect upon the long-term mechanical behavior.

The preliminary I.F. data for the MS PSZ samples tested at 800 and 1000°C are illustrated in Figs. 4(a) and (b), repectively. At 800°C, S_f was relatively independent of time and only marginally dependent upon the stress level; the strength being slightly greater for the stressed samples (σ_a = 207 MPa) at all values of t. Although limited, the I.F. data at 1000°C gave evidence of an enhanced rate of strength degradation for t> 200 h when the 172 MPa stress was applied. Results of ongoing studies will confirm this possible trend.

X-ray analyses of the polished surfaces of fractured MS and TS specimens were used to determine the volume fraction of (m). Preliminary results for tests conducted at 1000°C are summarized in Table 1. In general V_f^m increased significantly with increasing

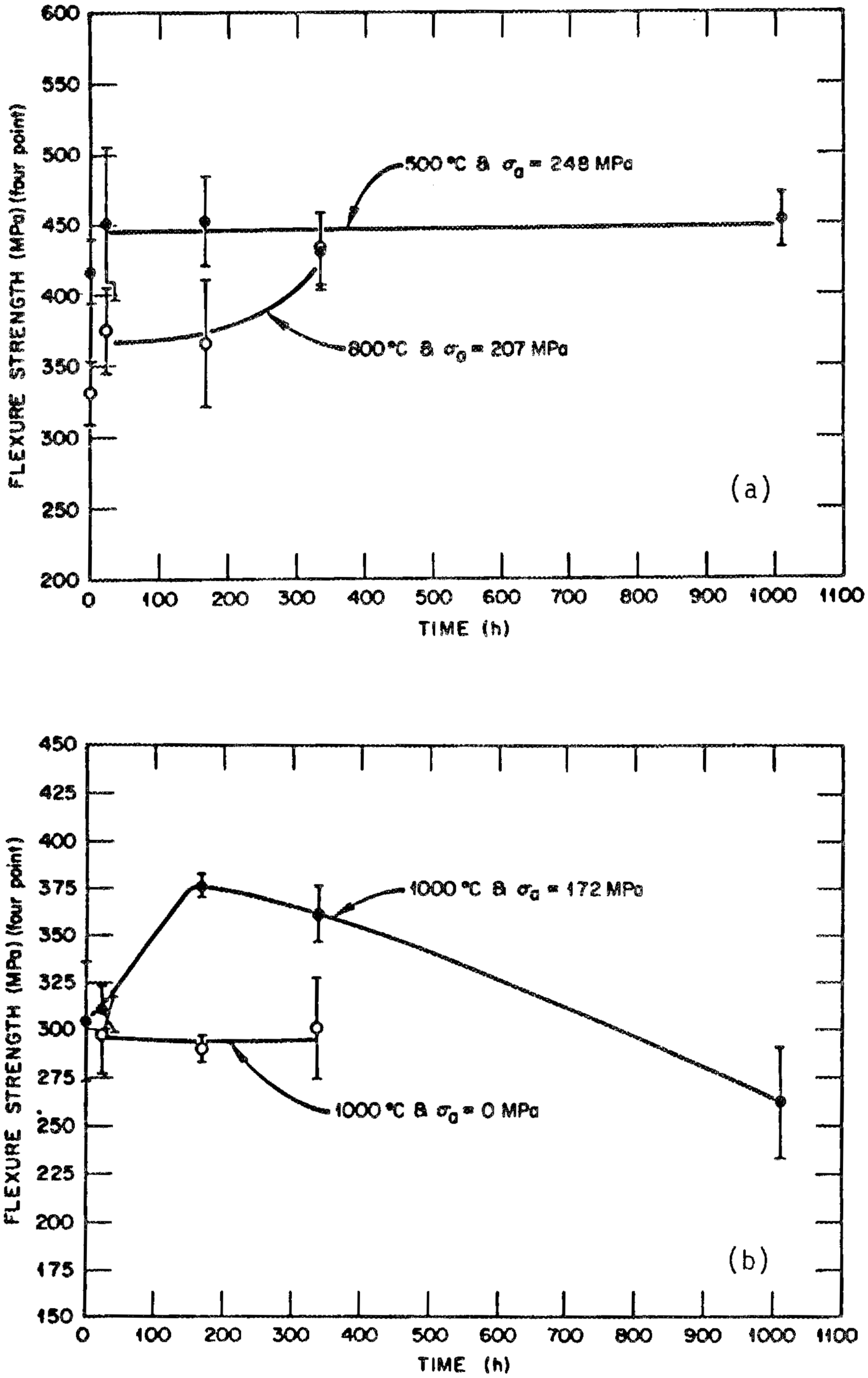

Figure 3. Strength data for TS PSZ obtained at 800°C (a) and 1000°C (b) exhibits strong stress dependency.

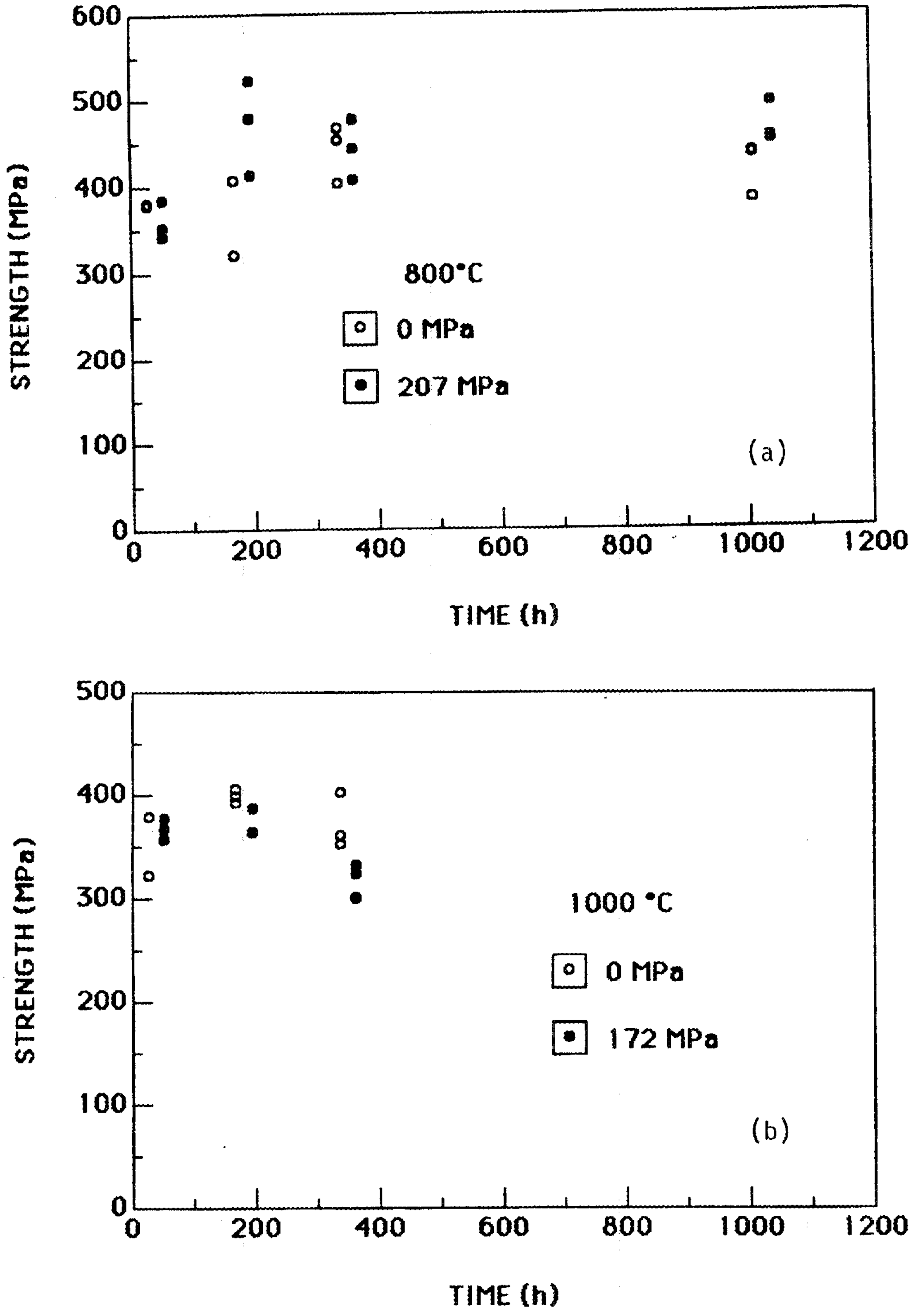

Figure 4. Strength of MS PSZ tested at 800°C (a) does not vary appreciably with time or applied stress. The results for tests conducted at 1000°C (b) are still inconclusive.

exposure time. Futhermore, the data for the TS material suggest that the magnitude of V_f^m for a given t was significantly greater when a stress was applied. However, the stress dependency for (m) formation in the MS PSZ was minimal. The reasons for these differences are unclear.

The fact that V_f^m values often exceeded the V_f^t for the as-received ceramics indicates that both the (c) and (t) phases were involved in the (m) formation. Recent aging studies conducted at 1100°C[5-8] have shown that at least two types of reactions can lead to the generation of the (m) phase. The first is the eutectoid decomposition of the MgO-stabilized (c) matrix;

$$Mg\text{-}ZrO_2\ (c) \longrightarrow ZrO_2\ (m) + MgO. \qquad (1)$$

This reaction generally initiates along grain boundaries and then slowly consumes the (c) phase within grain interiors. The resulting (m) phase has a typical grain size of 1-5 um.[7,8] The thermal expansion anisotropy associated with these (m) grains can promote extensive microcracking upon cooling. This microcracking is also facilitated by thermal expansion differences between the (m) and surrounding matrix.

Table 1. Values of V_f^m for selected MS and TS samples fractured in I.F. tests conducted at 1000°C

Sample	Time (h)	Stress	V_f^m
TS	24	0	0.39
TS	336	0	0.49
TS	336	172	0.85
TS	1000	172	1.0
MS	168	0	0.81
MS	168	172	0.87

The second type of reaction involves the formation of an ordered anion vacancy δ-phase ($Mg_2Zr_5O_{12}$)within the region between adjacent (t) precipitates.[5-8] The δ-phase nucleates at the (t) - (c) interface and then grows into the (c) matrix due to short-range diffusion of Mg. The interfacial strains which accompany this δ-phase reaction can destroy the precipitate coherency and thus promote the (t) to (m) transition upon cooling. This results in an increase in the M_s temperature. The presence of these destabilized precipitates at relatively low concentration levels can lead to improved thermal shock resistance without significantly sacrificing strength and toughness.[5-7]

The SEM examination of the polished (tensile) surfaces of several fractured TS samples (tested at 1000°C) gave additional evidence for the eutectoid decomposition reaction. As shown in Fig. 5, extensive formation of the (m) phase occurred in the specimen exposed for 1008 h at the 60% stress level. The (m) grain size was in the 1-5 um range in agreement with previous studies.[5-7] Numerous microcracks were also observed particularly in regions containing a high density of (m) grains. In general, the concentration of this (m) phase diminished as the exposure time decreased. In addition, no microcracking was observed for $t \leq 168$ h. Differences in microstructure between stressed and unstressed samples are currently being investigated.

In addition to I.F. studies, considerable emphasis is being placed on developing suitable models capable of describing the time-dependence of fracture strength and toughness. The results of this modeling effort will be discussed in future progress reports.

Status of Milestones

No milestones for this reporting period.

Publications

Work was initiated on a publication for the 23rd Automotive Technology Development Contractor's Coordination Meeting to be held in Dearborn, Michigan on October 21-24, 1985.

References

1. R. Kamo and W. Bryzik, "Cummins/TACOM Advanced Adiabadic Engine," pp. 121-134 in *Proceedings of the Twenty-First Automotive Technology Development Contractors' Coordination Meeting* P-138, Society of Automotive Engineers, Warrendale, PA, March 1984.

2. S. M. Wiederhorn, "A Probabilistic Framework for Structural Ceramics," pp. 197-226 in *Fracture Mechanics of Ceramics,* Vol 5., eds. R. C. Bradt, A. G. Evans, D. P. H. Hasselman, and F. F. Lange. Plenum, New York, 1983.

3. D. L. Porter and A. H. Heuer, "Microstructural Development in MgO-Partially Stabilized Zirconia (Mg-PSZ)," *J. Am. Ceram. Soc.,* **62** (5-6), pp. 298-305 (1979).

4. D. C. Larsen and J. W. Adams, "Long-Tern Stability and Properties of Partially Stabilized Zirconia," pp. 399-407 in *Proceedings of the Twenty-Second Automotive Technology Development Contractors' Coordination Meeting* P-155, Society of Automotive Engineers, Warrendale, PA, March 1985.

5. R. Hannink and M. Swain, "Magnesia-Partially Stabilized Zirconia: The Influence of Heat Treatment on Thermomechanical

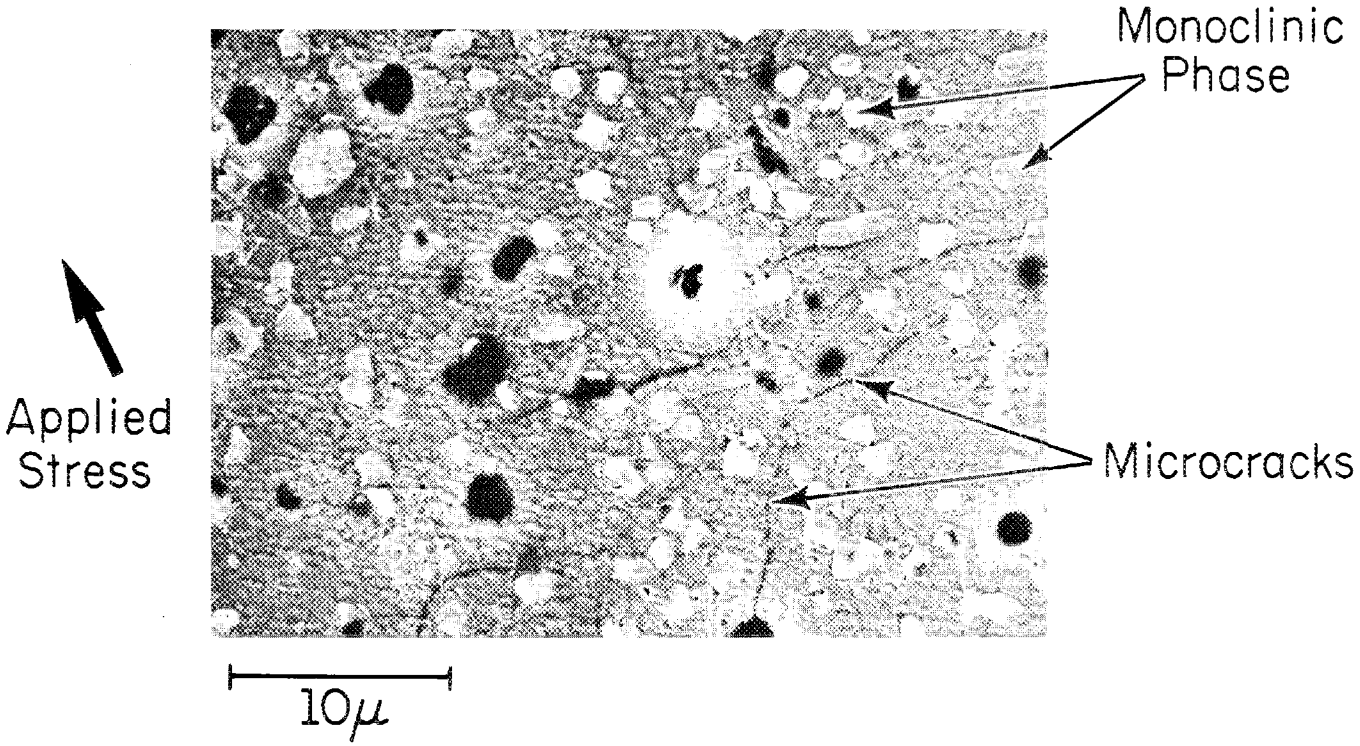

Figure 5. Eutectoid decomposition of stabilized cubic ZrO_2 leads to extensive microcracking in TS PSZ samples exposed for 1000 h at 1000°C and subjected to a 60% stress level.

Properties," *J. Aust. Ceram. Soc.* **18** (2), pp. 53-62 (1983).

6. R. Hannink and R. Garvie, "Sub-eutectoid Aged Mg-PSZ Alloy with Enhanced Thermal Upshock Resistance," *J. Mater. Sci.* **17**, pp. 1637-1643 (1982).

7. R. Hannink, "Microstructural Development of Sub-eutectoid Aged Mg-ZrO_2 Alloys," *J. Mater. Sci.* **18**, pp. 457-470 (1982).

8. M. V. Swain, R. C. Garvie, R. H. J. Hannink, "Influence of Thermal Decomposition on the Mechanical Properties of Magnesia-Stabilized Cubic Zirconia," *J. Am. Ceram. Soc.* **66** (5), pp. 358-362 (1983).

Environmental Effects in Toughened Ceramics

N. L. Hecht (University of Dayton)

Objective/scope

The University of Dayton has initiated a contract from the U.S. Department of Energy (DOE) through a subcontract with Martin Marietta Energy Systems Inc., Oak Ridge, Tennessee, to study the "Effect of Environment Upon the Mechanical Behavior of Structural Ceramics for Application in the DOE Ceramic Technology for Advanced Heat Engines Program." The primary goal of this program is to determine the effect of environment upon toughening and strength in commercially available transformation toughened ceramics (TTC) [partially stabilized zirconia (PSZ) and dispersion toughened alumina (DTA)]. Emphasis will be focused on understanding the mechanism(s) responsible for environmentally induced strength degradation in the temperature range of 25°C to 1050°C. It is anticipated that the information and insights obtained from this program can be used to determine the long-term applicability of toughened ceramics for use as diesel engine components.

Dynamic fatigue test methods (4 point bend strength measurements as a function of stressing rate) will be used to investigate slow crack growth in environments containing controlled amounts of water vapor at temperatures from 25°C to 1050°C. Similar tests will also be conducted in inert atmospheres to distinguish intrinsic effects from environmentally induced fatigue.

In the first phase of the program, all commercially available materials will be considered for evaluation. In this phase of the program, manufacturers' data and preliminary characterization studies conducted at the University will be utilized to screen candidate PSZ and DTA materials. It is anticipated that from these candidate materials six materials will be selected for the study. In the second phase of the program, the dynamic fatigue tests will be carried out on the six materials selected. From these studies, two materials will be selected for more intense evaluation. A description of the activities pursued and the results obtained are presented in this expanded semiannual report.

Technical progress

A detailed work plan was developed to effectively accomplish the stated program goal. This plan is outlined in Table 1.1.1. As shown in Table 1.1.1, Task 1 is primarily concerned with the identification of commercial sources for transformation toughened ceramics (TTC) and the acquisition of available TTC for evaluation. In Task 1 all commercially available materials are screened in order to select the six most promising candidate ceramic materials for more detailed evaluations. The list of commercial suppliers for TTC and the materials available from each supplier is tabulated in Table 1.1.2. As shown in Table 1.1.2, nine different TTC materials have been identified for characterization and screening. The characterization protocol for screening 20 specimens of each potential candidate material is outlined in Table 1.1.3.

Task 2 of this program is directed toward an evaluation of the six candidate materials in order to select the best two materials for a more extensive evaluation. Phase 1 of this task concentrates on the development of test procedures, the test facility, and the mini-matrix test plan for the six candidate TTC materials. The development of the mini-matrix test plan and the construction of the dynamic fatigue test facility are carried out concurrent with the activities outlined for Task 1.

Table 1.1.1. Proposed work plan.

I. Task 1 - Candidate Materials Acquisition, Characterization, & Screening

  A. Identification of Material Suppliers & Review of Manufacturers' Data

  B. Acquisition of Commercially Available Transformation Toughened Ceramics for Screening

  C. Characterization & Screening Studies (based on an analysis of 20 samples of each material)

    1. Microstructure analysis
    2. Chemical analysis/density measurements
    3. Crystallographic analysis
    4. Fracture toughness measurements/hardness calculations
    5. Flexure strength measurements (fast & slow loading rates)
    6. Effects of aging on flexure strength and crystal structure

II. Task 2 - Investigation of Candidate Materials

  A. Phase 1 - Investigation of Six Candidate Materials

    1. Mini-matrix test plan development
       a) selection of test variables for the dynamic fatigue test studies
       b) finalize mini-matrix test plan
    2. Establish dynamic fatigue test facility & verify test procedures
       a) test sample configuration
       b) test chamber design & operation
       c) trial run for procedure verification
    3. Selection of the six candidate materials for further evaluation
    4. Implementation of the mini-matrix test plan (80 samples for each candidate material)
    5. Analysis of test specimen microstructure, chemistry, & fracture surface (Raman microprobe, x-ray, SEM, EDAX, & optical microscopy)
    6. Review of test results & selection of the two most promising materials for expanded test matrix analysis

  B. Phase 2 - Investigation of Two Finalist Materials

    1. Approval & implementation of an expanded matrix test plan
    2. Analysis of test data
    3. Analysis of test specimen microstructure, chemistry, & fracture surface
    4. Review of results
    5. Conclusions & Development of a test matrix plan for advanced studies (static/cyclic fatigue)

III. Task 3

  A. Reporting

IV. Task 4

  A. Quality Assurance Requirements

Table 1.1.2. Transformation toughened ceramic materials commercially available for evaluation.

No.	Material Supplier	Material Designation	Material Description
1	Coors Porcelain	TTZ	3-3.5 wt. % MgO Stabilized ZrO_2
2	NGK Locke Inc.	Z191	5 wt. % Y_2O_3 Stabilized ZrO_2
3	Nilcra Ceramic (USA) Inc.	MS-PSZ	3 wt. % MgO Stabilized ZrO_2 (heat treated for high strength)
		TS-PSZ	3 wt. % MgO Stabilized ZrO_2 (heat treated for high thermal shock resistance)
4	Kyocera International	DTA-AZ301	Dispersion Toughened Al_2O_3 (19% ZrO)
		PSZ-Z201	5.4 wt. % Y_2O_3 Stabilized ZrO_2
5	Ceramatec Inc.	ZTA-XS121	ZrO_2 Dispersion Toughened Al_2O_3
		YTZP-XS241	5 wt. % Y_2O_3 Stabilized ZrO_2 (with 10% Al_2O_3 addition)
		CTZP	CeO_2 Stabilized ZrO_2 (with 10% Al_2O_3 addition)

Table 1.1.3. Characterization plan for candidate systems.

SAMPLE NO.	VISUAL INSPECTION	SURFACE AND DENSITY FINISH MEASUREMENT	XRD	RMS	SEM EDAX	OPTICAL MICROSCOPY	AGING	MOR* $\dot{\sigma}_1/\dot{\sigma}_4$	K_{IC} MEASUREMENT	POST+ FRACTURE ANALYSIS
1	X	X	X	X	X	X				
2	x	x	x	x		x	x	$\dot{\sigma}_4$		
3	x	x	x	x		x	x	$\dot{\sigma}_4$		
4	X	X					X	$\dot{\sigma}_4$		
5	X	X					X	$\dot{\sigma}_4$		X
6	X	X					X	$\dot{\sigma}_4$		X
7	X	X						$\dot{\sigma}_4$		
8	X	X						$\dot{\sigma}_4$		
9	X	X						$\dot{\sigma}_4$		
10	X	X						$\dot{\sigma}_4$		X
11	X	X						$\dot{\sigma}_4$		x
12	X	X							X	
13	X	X							X	
14	X	X							X	
15	X	X							X	X
16	X	X							X	X
17	X	X						$\dot{\sigma}_1$		
18	X	X						$\dot{\sigma}_1$		
19	X	X						$\dot{\sigma}_1$		X
20	X	X						$\dot{\sigma}_1$		X
TAB	X		X	X	X					

+POST FRACTURE ANALYSIS INCLUDES XRD, RMS, SEM, AND OPTICAL MICROSCOPY

The initial months of the program focus on developing the mini-matrix test plan, determining specimen configuration, and designing and building the dynamic fatigue test facility to be used to study the TTC candidate materials. The test facility to be used is shown in Figure 1.1.1, and the test fixture and specimen configuration is presented in Figure 1.1.2. The mini-matrix test plan is presented in Table 1.1.4. Ten test samples will be used for evaluating each of the eight different test conditions selected for the mini-matrix plan investigation (for a total of 80 test specimens). The results of these studies will be used for selecting the two finalist TTC materials to be evaluated in the second phase of Task 2. The results of Phase 1 will also be used to develop the expanded test protocol to be used in evaluating the two finalist materials. It is anticipated that the results obtained from the expanded evaluation of the two finalist materials will provide the information needed to develop a data base for the utilization of TTC in advanced engine designs with a high degree of confidence.

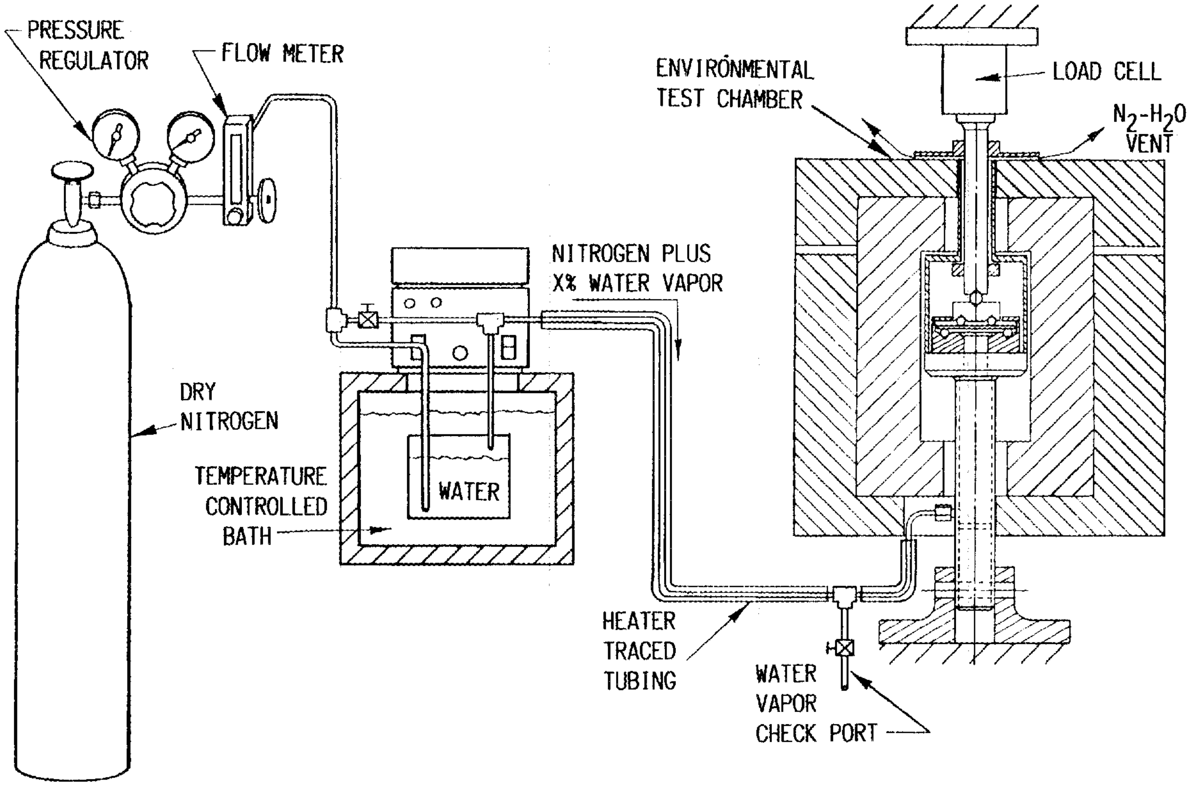

Fig. 1.1.1. Test facility.

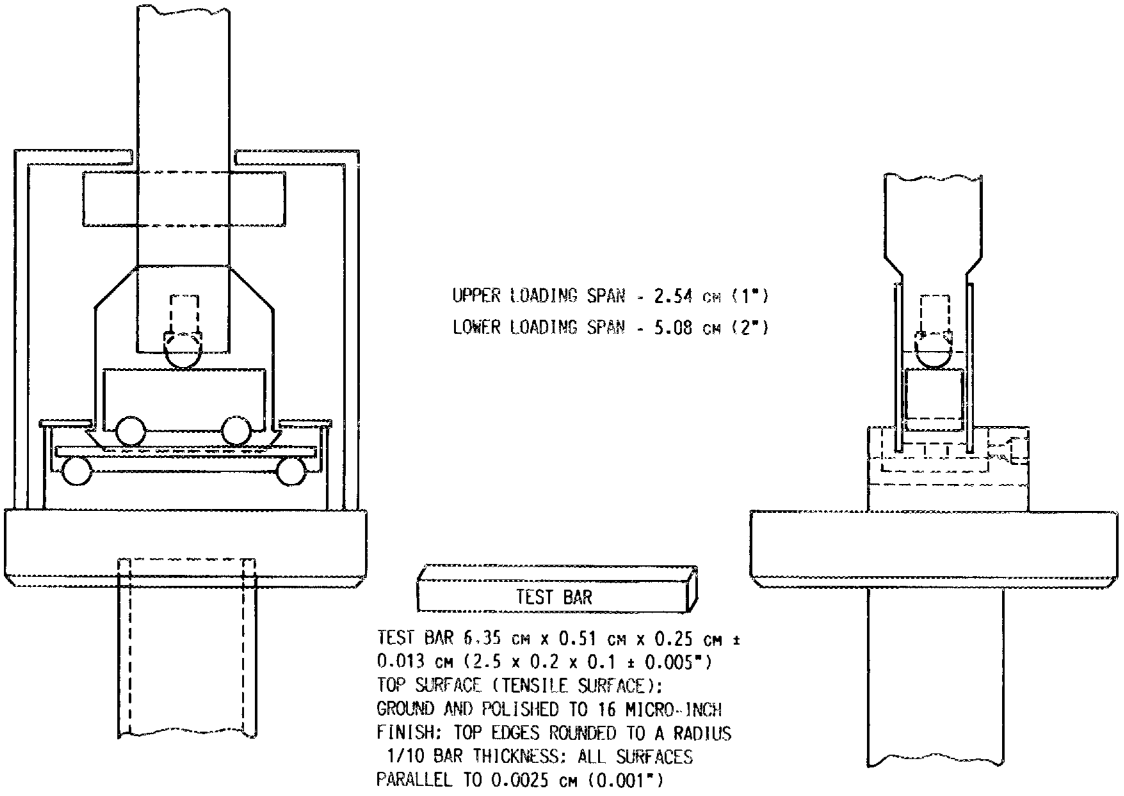

Fig. 1.1.2. MOR test fixture and specimen configuration.

Table 1.1.4. Mini-matrix test plan.

Temperature	Environment	Stress Rates $\dot{\sigma}_1$	 $\dot{\sigma}_2$	 $\dot{\sigma}_3$	 $\dot{\sigma}_4$
T_1	Atm_1	β			β*
T_2	Atm_1	X			X*
T_2	Atm_3	X			X
T_4	Atm_1	X			X
T_4	Atm_3	X			X

*β = baseline characterization measured during screening; X = mini-matrix measurement.

Table 1.1.4. (Concluded)

Variable values to be investigated in the evaluation program.

Test Variable	Proposed Variable Levels
Stress Rate:	*Stress rate/crosshead speed
σ_1	0.5 MPa/s (74 psi/s) - .0025 cm/min (.001 in/min)
σ_2	2.6 MPa/s (370 psi/s) - .0125 cm/min (.005 in/min)
σ_3	26 MPa/s (3700 psi/s) - .125 cm/min (.05 in/min)
σ_4	77 MPa/s (11060 psi/s) - .375 cm/min (.15 in/min)
Temperature	Temperature
T_1	25°C (77°F)
T_2	300°C (572°F)
T_3	850°C (1562°F)
T_4	1050°C (1922°F)
Environmental Conditions	Environmental Conditions
Atm_1	Dry Nitrogen
Atm_2	95% Nitrogen/5% Water
Atm_3	90% Nitrogen/10% Water

*Stress rates are approximate values based on average room temperature elastic modulus data for the designated crosshead speeds.

1.2 RESULTS

Test specimens of the nine commercially available TTC materials (see Table 1.1.2) were ordered for characterization and screening evaluations. In addition, property data for these nine materials was requested from the suppliers and sought from the published literature. All of the data obtained was reviewed and categorized in order to develop an initial insight into the nature of these materials. A compilation of the data collected is presented in Table 1.2.1.

During this reporting period, the three TTC materials ordered from Ceramatec Inc., the two materials ordered from Kyocera Intl., the material ordered from NGK Locke Inc., and the two materials ordered from Nilcra Ceramic Inc. were received. However, the Nilcra materials were received late (end of August), and some post-test evaluations are still in progress. These eight materials were evaluated according to the procedures described in the Materials Characterization and Screening Protocol and enumerated in Table 1.1.3.

Table 1.2.1. Composite of available property data for transformation toughened ceramics to be evaluated.

MATERIAL DESIGNATION	STABILIZER	SOURCE	DENSITY (G/CC)	α^+ (x 10^{-6}/°C)	TEMP (°C)	MOR (MPA)	E (GPA)	K_{IC} MPA$\sqrt{M}$
TTZ	3-3.5WT%MgO	COORS	5.74	10.1*	R.T.	(650-950)	191	(8-12)
				10.2*	R.T.	490	200*	-
					R.T.	446*	-	-
					R.T.	634*	-	-
					500	414*	-	-
					760	200*	-	-
					1000	143*	-	-
					1000	290*	-	-
TS-PSZ	3WT%MgO	NILCRA	5.78	9.0	R.T.	650	205	8.0
				8.3*	R.T.	604*	-	-
					500	472	169	5.75
					760	368*	-	-
					800	400	-	-
					1000	288	165	5.25
MS-PSZ	3WT%MgO	NILCRA	5.69	10.6	R.T.	800	205	10.0
				9.9*	R.T.			
					500	495	169	6.75
					1000	400	165	5.25
Z191	5WT%Y_2O_3	NGK	5.91	10.6	R.T.	1020	205	8.5
				10.6*	R.T.	944*	-	-
					500	640	-	-
					760	428	-	-
					1000	330	-	-
						301*	-	-
PSZ-Z201	5.4WT%Y_2O_3	KYOCERA	5.9	11.3	R.T.	980	210	5.4
DTA-AZ301 ZrO_2 DISPERSION TOUGHENED Al_2O_3(81%)	-	KYOCERA	-	8.2	R.T.	1150	370	6.0
ZTA-XS121 ZrO_2 DISPERSION TOUGHENED Al_2O_3	-	CERAMATEC	4.2	-	R.T.	700	-	5.0
YTZP-XS241	3MOLE%Y_2O_3	CERAMATEC	5.56	-	R.T.	750	-	6.6
CTZP	CeO_2	CERAMATEC	-	-	R.T.	250-700*	192*	4-7*
					R.T.	450-700	-	8-16

+ R.T. TO 1000°C

* PUBLISHED LITERATURE/UNSTARRED DATA FROM MFG.

α COEFFICIENT OF THERMAL EXPANSION

MOR BEND STRENGTH

E YOUNGS MODULUS

K_{IC} FRACTURE TOUGHNESS

When received, all of the materials obtained were visually inspected, and the surface finish for each test sample was measured (see Table 1.2.2). Samples were then characterized using optical microscopy (OM), x-ray diffraction (XRD), scanning electron microscopy (SEM), and energy dispersive x-ray analysis (EDAX). In addition, Raman microprobe spectroscopy (RMS) of the samples was initiated. Fracture toughness (controlled surface flaw method) and modulus of rupture (MOR) were determined for each of the materials supplied. Both fast (77 MPa/s) and slow (0.5 MPa/s) loading rates were used in performing the MOR measurements. In addition, five samples from all but the Nilcra materials were aged at 300°C for 25 hours in a moisture laden N_2 (10% H_2O) atmosphere. Five samples from the two Nilcra materials were aged in the 10% H_2O nitrogen environment at 800°C for 200 hours. After aging, the samples were tested in flexure (MOR) at the rapid loading rate. Representative specimens from each test batch were evaluated after failure to determine fracture origin and mode.

Table 1.2.2. Surface finish measurements.

No.	Material Designation	Average Surface Finish (μ in)	Range (μ in)	Comments
1	TZP-XS241	8	5-10	—
2	ZTA-XS121	3.1	2-10	—
3	CTZP	3.1	2-6	—
4	PSZ-Z201	6.1	4-8	—
5	DTA-AZ301	2.8	2-4	—
6	Z191	6.9	4-16	About 20% were above 16 μ in
7	MS-PSZ	—	∿16	} Preliminary Values +
8	TS-PSZ	—	∿16	

+The Nilcra MS & TS materials are still being evaluated. It should be noted that these preliminary evaluations indicate that the Nilcra materials contain an extensive quantity of surface scratches.

1.2.1 Density Determinations

Three samples from each of the eight candidate materials were used for density determinations by the immersion method. The data from these measurements are tabulated in Table 1.2.3.

Table 1.2.3. Density Measurements

Manufacturer	Material Designation	Average Density (g/cc)
Ceramatec	TZP-XS241	5.4
	ZTA-XS121	4.4
	CTZP	5.7
Kyocera	PSZ-Z201	5.9
	DTA-AZ301	4.2
NGK-LOCKE	Z191	5.9
Nilcra	MS-PSZ	5.7
	TS-PSZ	5.7

1.2.2 Microstructure Evaluations

To better characterize the microstructure of the eight different TTC materials, both optical and scanning electron microscopes were used to examine sections of selected samples from each test group. Representative photomicrographs obtained from each group of materials are presented in Figures 1.2.1 to 1.2.16. A summary of the major microstructural features observed for each material is presented in Table 1.2.4.

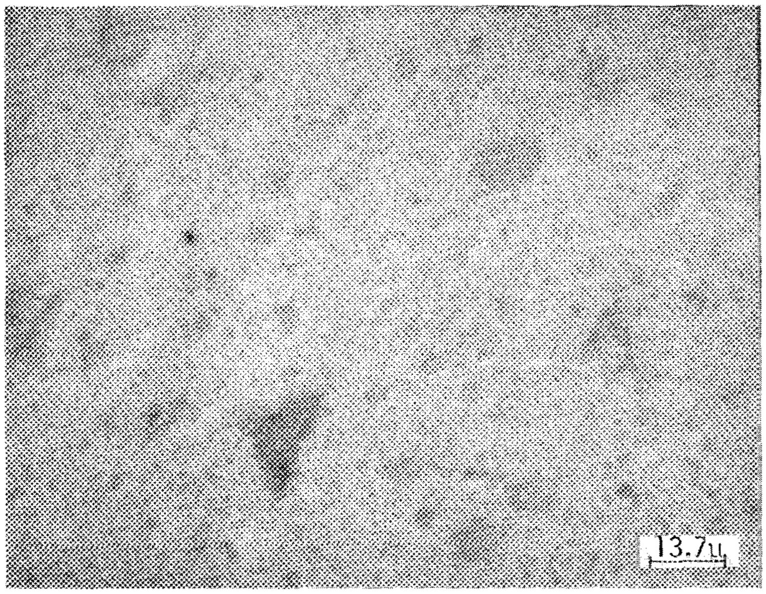

Fig. 1.2.1. Polished and etched section of material XS241 at 730X (etchant a solution of HF and $NaHF_2$).

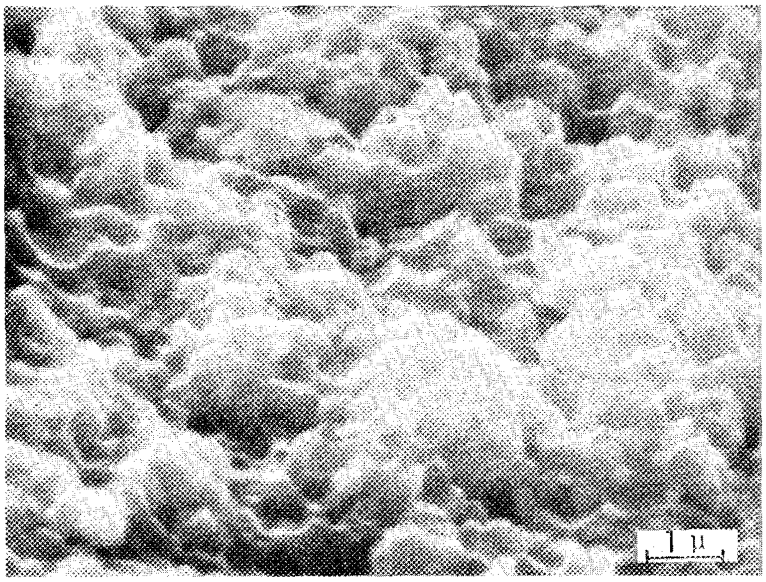

Fig. 1.2.2. SEM photograph of a fractured section of material XS241 at 10,000X.

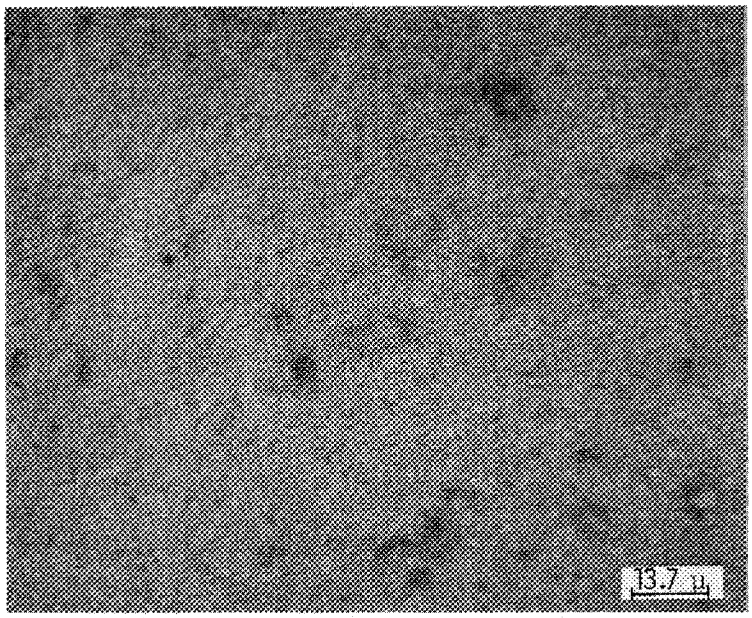

Fig. 1.2.3. Polished and etched section of material XS121 at 730X (etchant a solution of HF and $NaHF_2$).

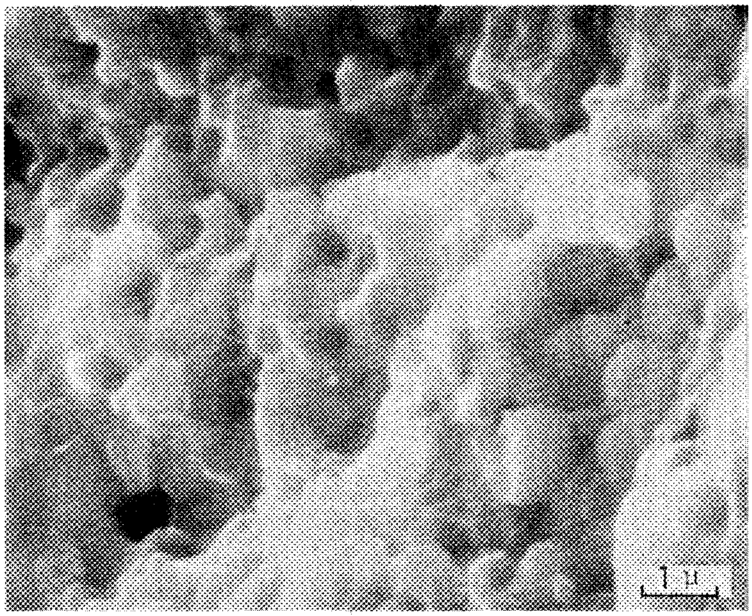

Fig. 1.2.4. SEM photograph of a fractured section of material XS121 at 10,000X.

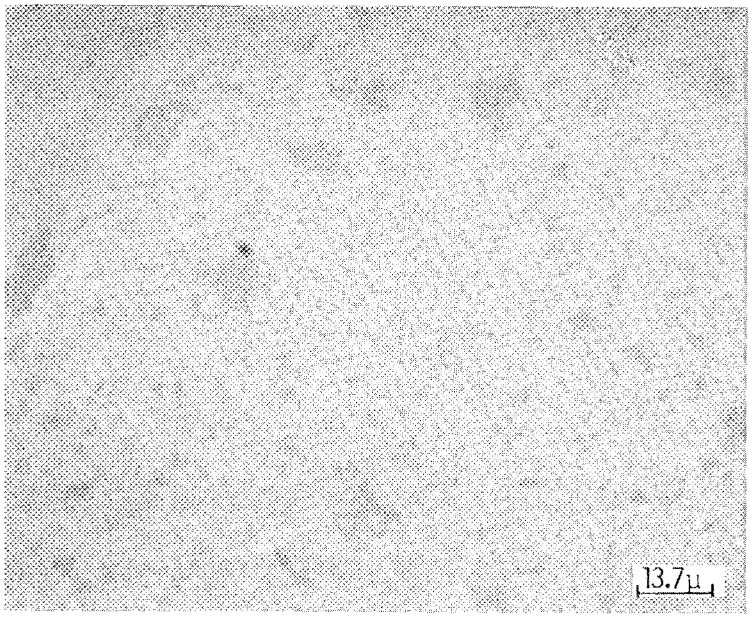

Fig. 1.2.5. Polished and etched section of material CTZP at 730X (etchant a solution of HF and $NaHF_2$).

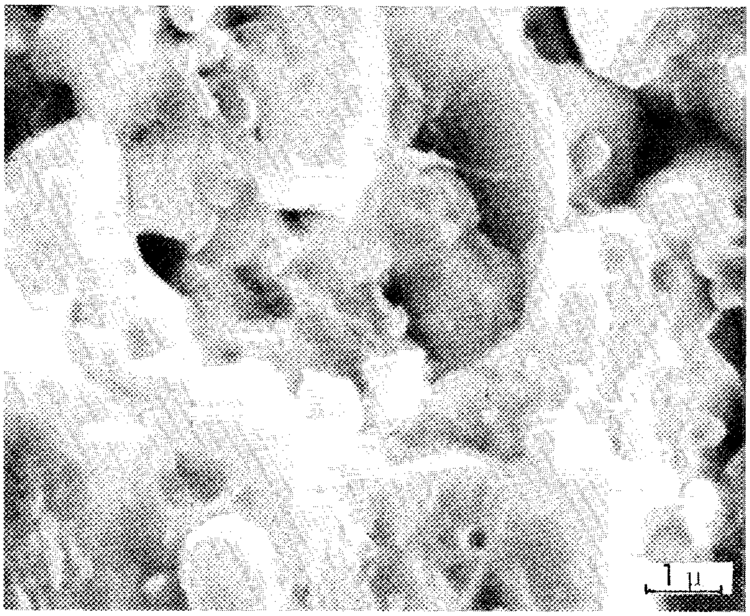

Fig. 1.2.6. SEM photograph of a fractured section of material CTZP at 10,000X.

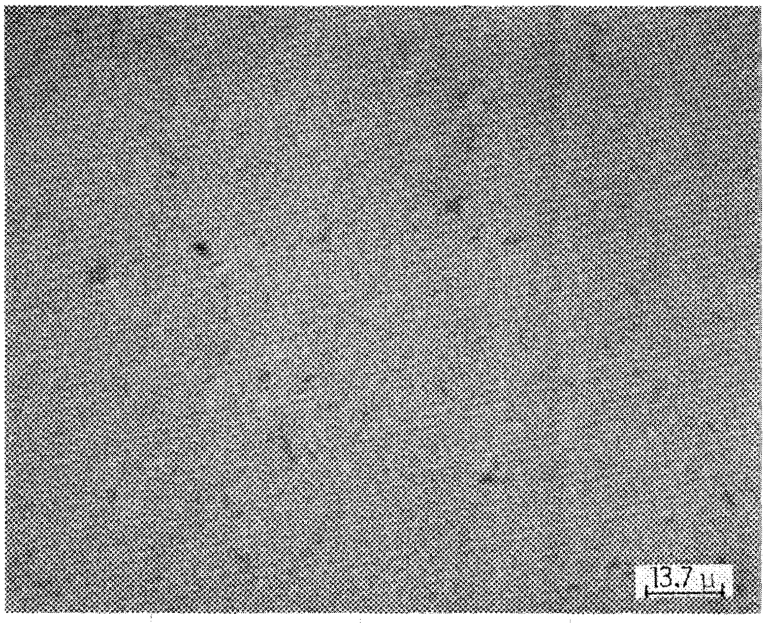

Fig. 1.2.7. Polished and etched section of material Z191 at 730X (etchant a solution of HF and $NaHF_2$).

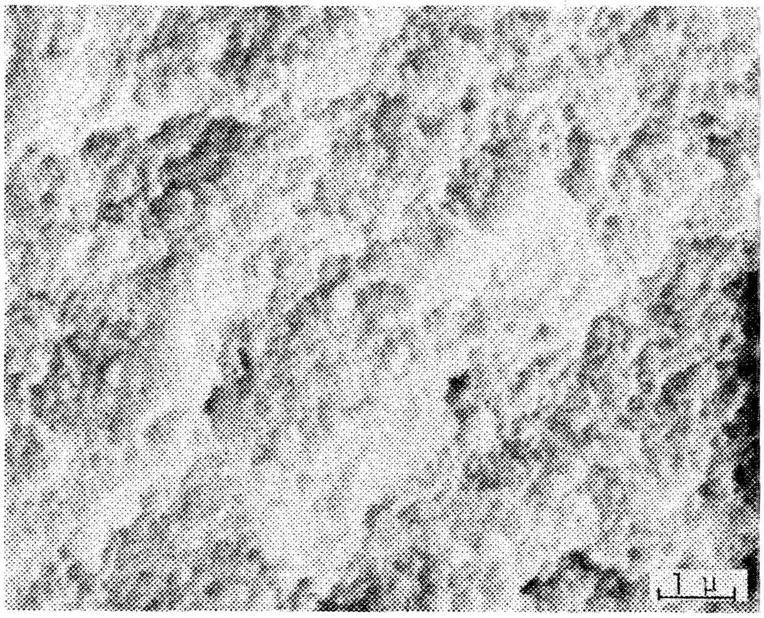

Fig. 1.2.8. SEM photograph of a fractured section of material Z191 at 10,000X.

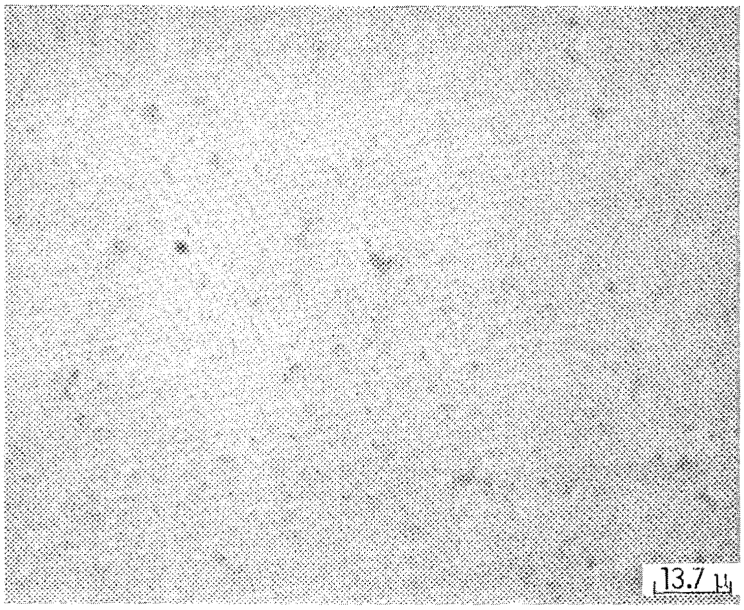

Fig. 1.2.9. Polished and etched section of material Z201 at 730X (etchant H_2PO_4).

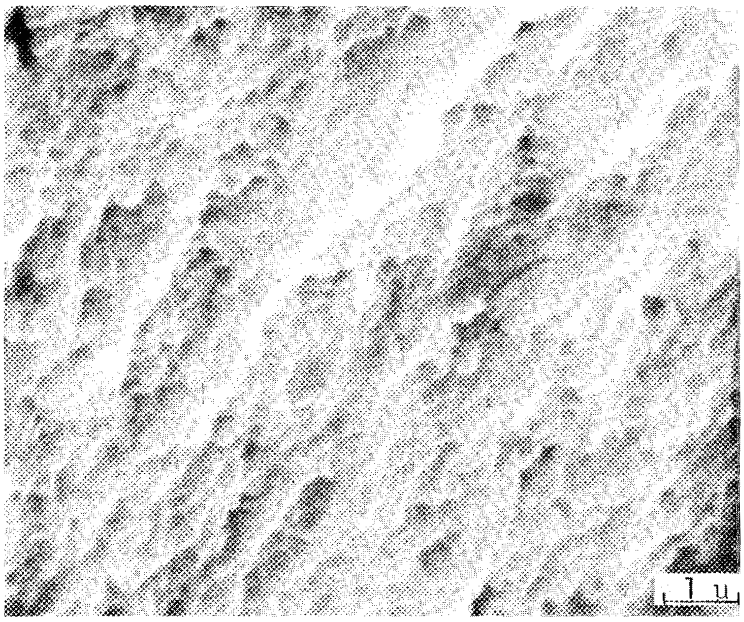

Fig. 1.2.10. SEM photograph of a fractured section of material Z201 at 10,000X.

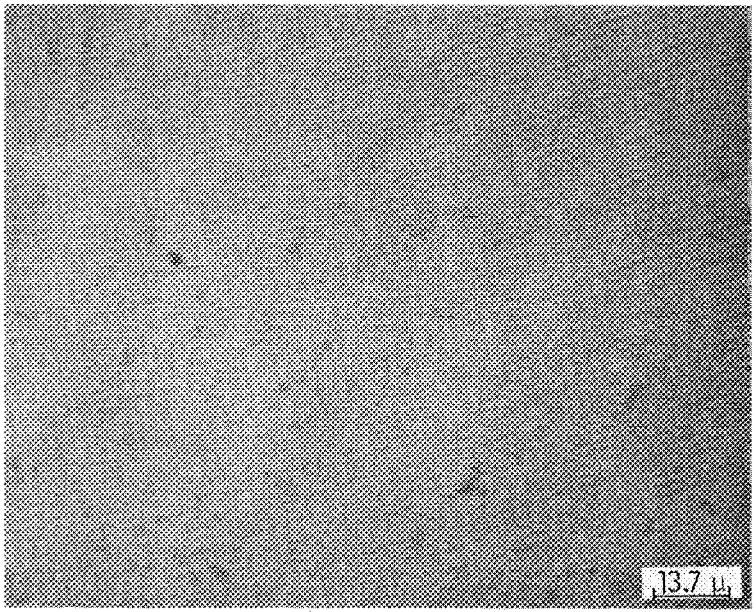

Fig. 1.2.11. Polished and etched section of material AZ301 at 730X (etchant H_2PO_4).

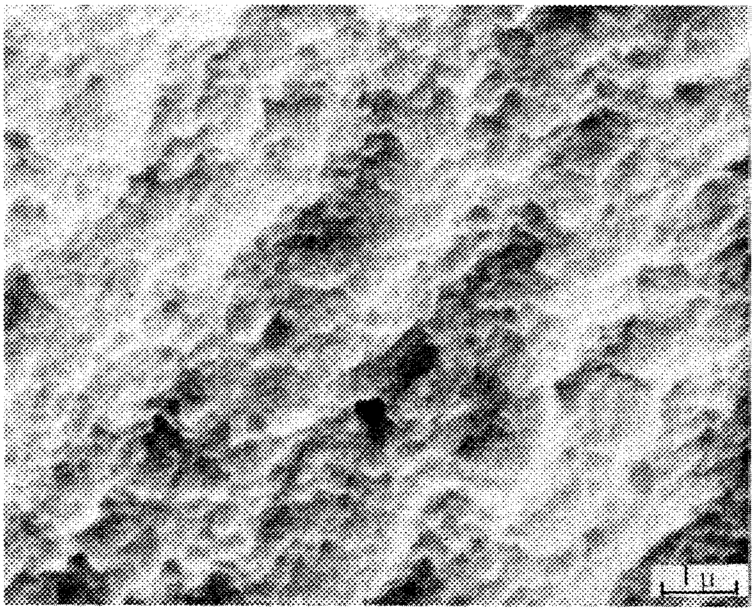

Fig. 1.2.12. SEM photograph of a fractured surface of material AZ301 at 10,000X.

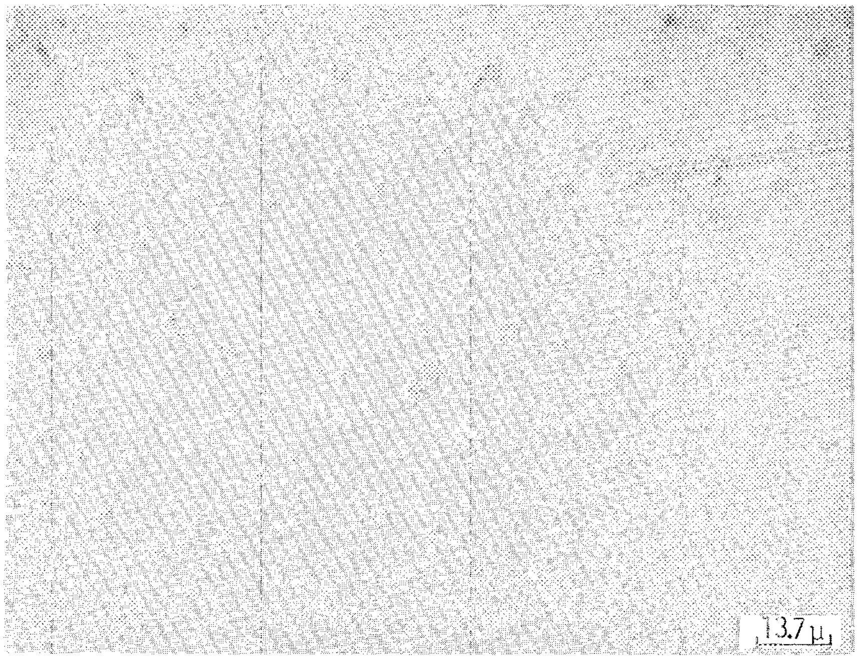

Fig. 1.2.13. Polished and etched section of material MS-PSZ at 730X (etchant H_2PO_4).

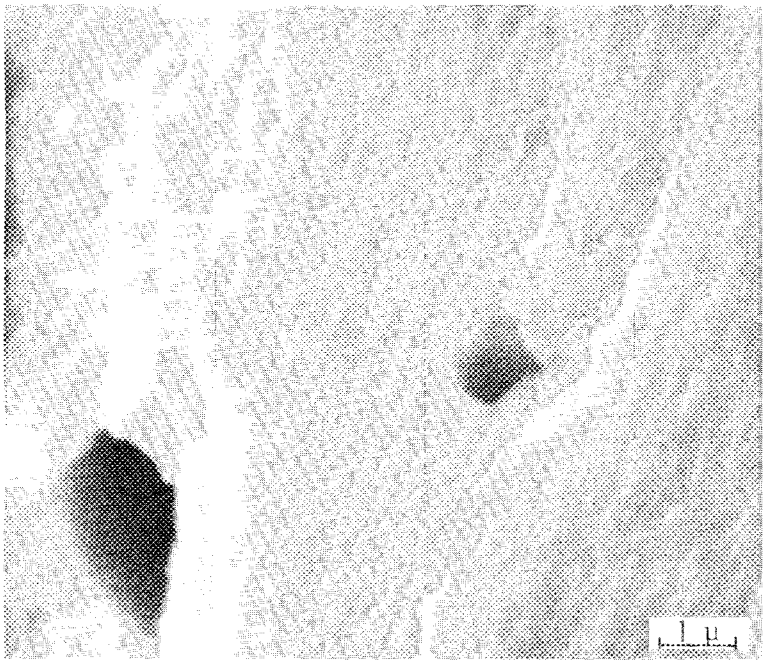

Fig. 1.2.14. SEM photograph of a fractured section of material MS-PSZ at 10,000X.

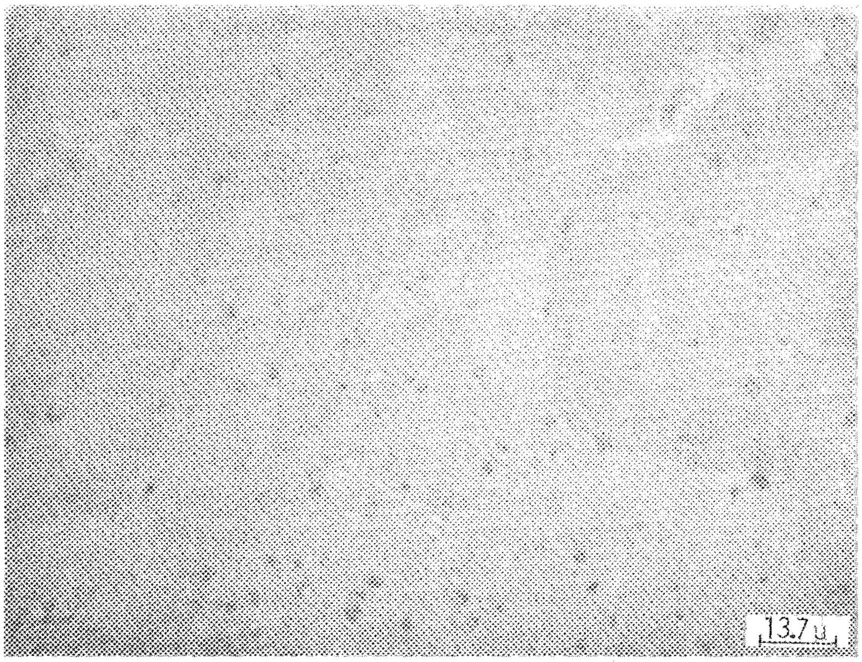

Fig. 1.2.15. Polished and etched section of material TS-PSZ at 730X (etchant H_2PO_4).

Fig. 1.2.16. SEM photograph of a fractured section of material TS-PSZ at 10,000X.

Table 1.2.4. Summary analysis of microstructural features.

Material Designation	Description
ZTA-XS121	A two-phase system of fine grained material with a grain size of 0.5 - 1.5 μ. The material contains a uniform distribution of varying size pores (0.2 - 1.5 μ).
YTZP-XS241	A two-phased material where the second phase is a fine grained material (0.1 - 0.3 μ) which is uniformly dispersed in a matrix of irregular shaped particles 0.5 - 1.5 μ in size. Distributed through the matrix is an array of small pores (0.5 - 5 μ).
CTZP	A two-phase material where a second phase of fine grained material is dispersed uniformly through the matrix phase. The matrix phase consists of irregular or angular platelets 1 - 3 μ in size. The matrix also contains a relatively uniform distribution of irregular shaped pores. This material also appears to contain a network of microcracks.
PSZ-Z201	A very dense material with a dispersion of very small pores (0.1 - 0.3 μ). The grain size of the material ranged from 0.2 - 0.5 μ with a few grains up to 1 μ in size.
DTA-AZ301	A very dense two-phase material with few pores. The second phase has a grain size of 0.1 - 0.3 μ and the matrix has a particle size of 0.3 - 1 μ.
Z191	A very dense material containing fine sized pores sparsely dispersed through the material. The individual grains are difficult to differentiate and have an estimated particle size of 3 - 10 μ.
MS-PSZ	A coarse grained and highly porous material with a grain size ranging from 30-60 μ. The pores are uniformly distributed throughout the bulk of the material and range in size from 1 - 10 μ (and average 2 - 3 μ).
TS-PSZ	A coarse grained and highly porous material with a grain size ranging from 30 - 60 μ. The pores are uniformly distributed throughout the bulk of the material and range in size from 1 - 10 μ (and average 2 - 3 μ).

1.2.3. Chemistry and Crystal Structure

The chemical composition and the crystal structure of the constituents present in the eight candidate materials was determined by the use of energy dispersive x-ray analysis (EDAX) and x-ray diffraction analysis (XRD). A tabulation of the components identified by EDAX is presented in Table 1.2.5. An XRD procedure was developed to identify the ZrO_2 crystal phases present and their approximate relative quantities. XRD analysis was performed on representative samples from each group of materials in the as-received condition, after aging, and after mechanical testing.

Table 1.2.5. Identification of components present in the TTC materials by EDAX.

Material Designation	ZTA-XS121	YTZP -XS241	CTZP	PSZ -Z201	DTA -AZ301	Z191	MS-PSZ	TS-PSZ
Major Constituent	Al_2O_3	ZrO_2	ZrO_2	ZrO_2	Al_2O_3	ZrO_2	ZrO_2	ZrO_2
Dispersant	ZrO_2	—	—	—	ZrO_2	—	—	—
Stabilizer	—	Y_2O_3	CeO_2	Y_2O_3	—	Y_2O_3	MgO	MgO
Secondary Constituents	SiO_2	Al_2O_3	SiO_2 Al_2O_3	—	—	—	—	—
Trace Constituents	K_2O CaO	—	K_2O CaO	—	SiO_2	SiO_2 Al_2O_3	—	—

The XRD analysis was not able to detect changes in the ZrO_2 crystal structure after mechanical testing since the method used is only effective on flat surfaces and not sensitive to the transformation which is reported to occur only in a very small zone along the edge of the fracture. However, the effects of aging on the ZrO_2 crystal structure could be determined by XRD and was measured on the samples subjected to aging. A summary of the XRD data obtained is presented in Table 1.2.6.

It had been planned that during the characterization and screening protocol, fired but unground and unpolished tabs of each candidate material would also be evaluated by x-ray, SEM, RMS, and OM. However, only four tabs were received and preliminary analysis showed these tabs to have essentially the same chemistry and crystal structure as the ground and polished samples used in the screening evaluation.

1.2.4. Mechanical Property Measurements

Flexure strength and fracture toughness was measured for each of the candidate materials at room temperature. The results of the flexure strength measurements are summarized in Table 1.2.7 and shown schematically in Figure 1.2.17. The results of the fracture toughness measurements are summarized in Table 1.2.8.

Table 1.2.6. Summary of XRD Results.

No.	Material Designation	Material Condition	Percent Monoclinic*
1	YTZP-XS141	As Received	10 (4-20)
		After Aging	42 (40-45)
2	ZTA-XS121	As Received	30
		After Aging	60
3	CTZP	As Received	4 (0-6)
		After Aging	0
4	Z191	As Received	7 (0-8)
		After Aging	10 (9-11)
5	DTA-AZ301	As Received	28 (25-32)
		After Aging	28
6	PSZ-Z201	As Received	4 (0-12)
		After Aging	4
7	MS-PSZ	As Received	23 (22-26)
		After Aging	33
8	TS-PSZ	As Received	33 (30-35)
		After Aging	44

*For materials 1 through 6, the predominate ZrO_2 crystal phase is tetragonal with little or no cubic phase present. For materials 7 and 8, the tetragonal phase ranged from 30-50% and the cubic phase ranged from 20-30%

Table 1.2.7. Summary of Flexure Strength Measurements at Room Temperature.

Material Designation	Fast Fracture MPa	Fast Fracture St. Dev.	Slow Fracture MPa	Slow Fracture St. Dev.	After Aging MPa	After Aging St. Dev.
ZTA-XS121	556	20	567	35	556	144$^+$
YTZP-XS241	777	145	761	100	729	74$^+$
CTZP	481	17	472	7	481	24$^+$
PSZ-Z201	957	52	832	67	791	124$^+$
DTA-AZ301	1265	136	1084	107	1206	118$^+$
Z191	1004	157	1014	94	957	165$^+$
MS-PSZ	679	39	621	44	674	16*
TS-PSZ	677	22	583	19	608	22*

$^+$Samples aged for 25 hrs. at 300°C.
*Samples aged for 200 hrs. at 800°C.

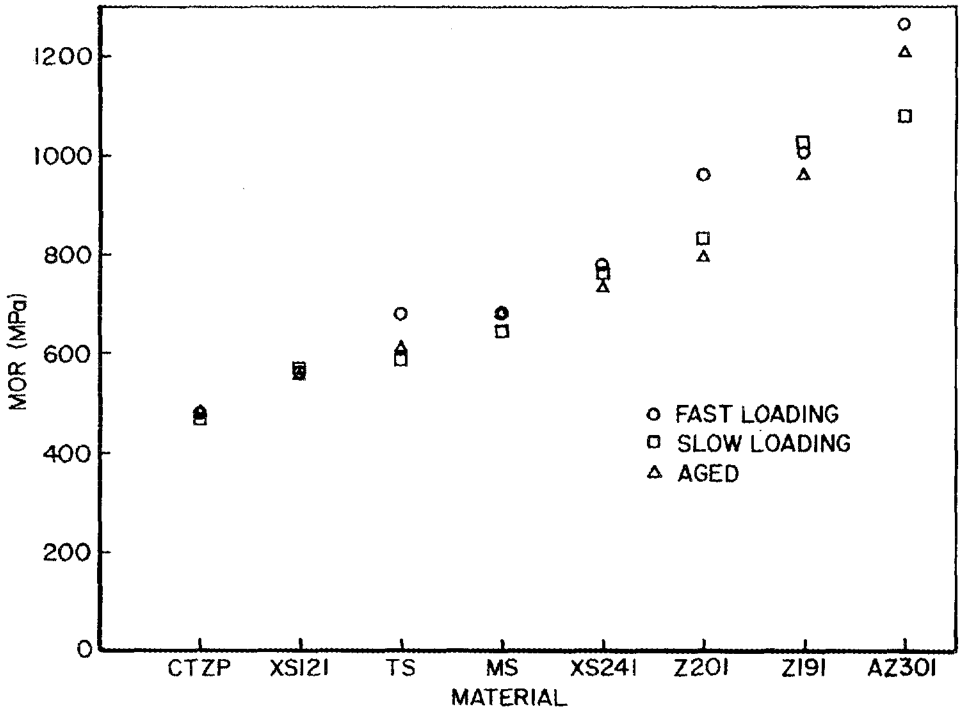

Fig. 1.2.17. Comparison of MOR test results.

Table 1.2.8. Summary of Fracture Toughness Measurements by the Controlled Surface Flaw Technique.

Material Designation	Fracture Toughness (MPa $\sqrt{m}$)
ZTA-XS121	2.8
YTZP-XS241	4.8
CTZP*	—
PSZ-Z201	5.4
DTA-AZ301	2.4
Z191	5.5
MS-PSZ*	—
TS-PSZ*	—

*Valid fracture toughness values could not be obtained by the measurement method employed.

The controlled surface flaw technique used for measuring fracture toughness also provides data for calculating surface hardness. Hardness is determined by measurement of the diagonal of the Vickers indent made at a known load. The results of these hardness calculations are summarized in Table 1.2.9.

Table 1.2.9. Average Vickers Hardness Measurements.

Material Designation	Vickers Hardness kg/mm^2	St. Deviation kg/mm^2
TZP-XS241	1120	22
ZTA-XS121	1172	99
CTZP	864	69
Z191	1292	53
PSZ-Z201	1282	35
DTA-AZ301	1939	133
MS-PSZ	1099	78
TS-PSZ	1025	54

Fracture toughness measurements for five of the eight materials evaluated were very straight forward, however, valid toughness measurements could not be readily obtained for the Ceramatec CTZP material and the Nilcra MS and TS materials. All of the samples tested failed outside of the indent region, and it was only possible to locate the site of fracture origin for one of the CTZP test samples.

Photomicrographs were taken of the indents made for the fracture toughness measurement and the subsequent fracture surfaces. Typical photomicrographs are presented in Figures 1.2.18 through 1.2.20.

It was observed that fracture origin for most of the samples tested in flexure was at the tensile surface of the sample and due primarily to the presence of cracks or large pores at the surface. However, a small number of flexure test samples failed from internal imperfections (pores, cracks, inhomogeneities, etc.). It should also be noted that there was no obvious correlation between fracture mode and flexure test procedure (pre-test aging, rapid loading, or slow loading). SEM photographs of typical fracture origin sites are presented in Figures 1.2.21 through 1.2.25.

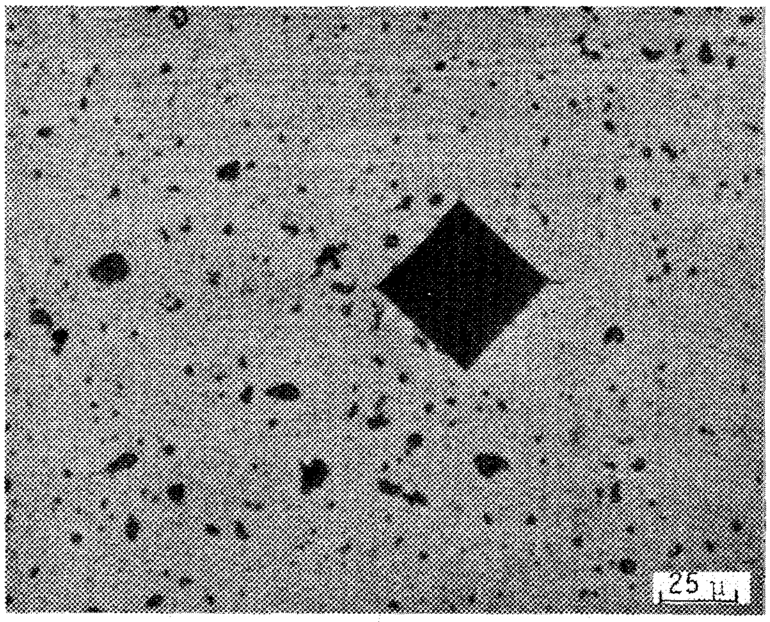

Fig. 1.2.18. Typical fracture toughness indent (material XS241 at 400X).

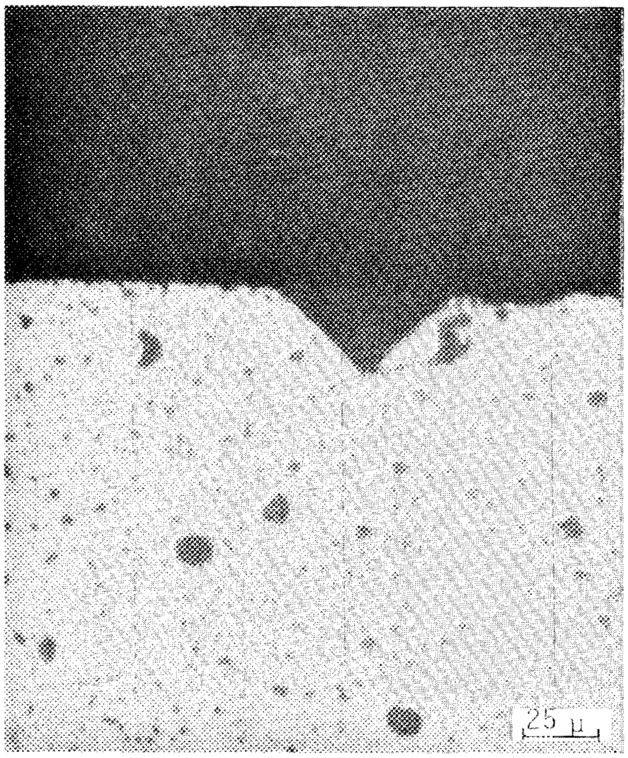

Fig. 1.2.19. Typical fracture line emanating from indent (material XS241 at 400X).

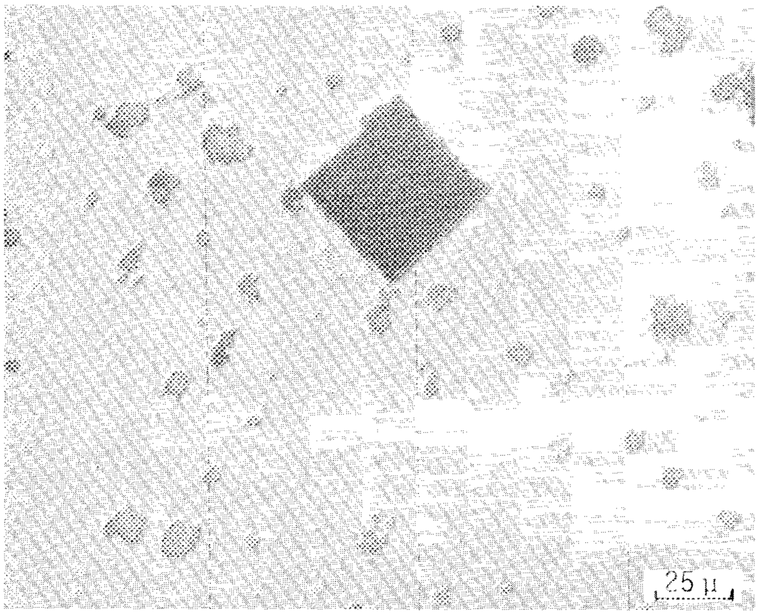

Fig. 1.2.20. Typical crack pattern observed around indent of CTZP material (at 400X).

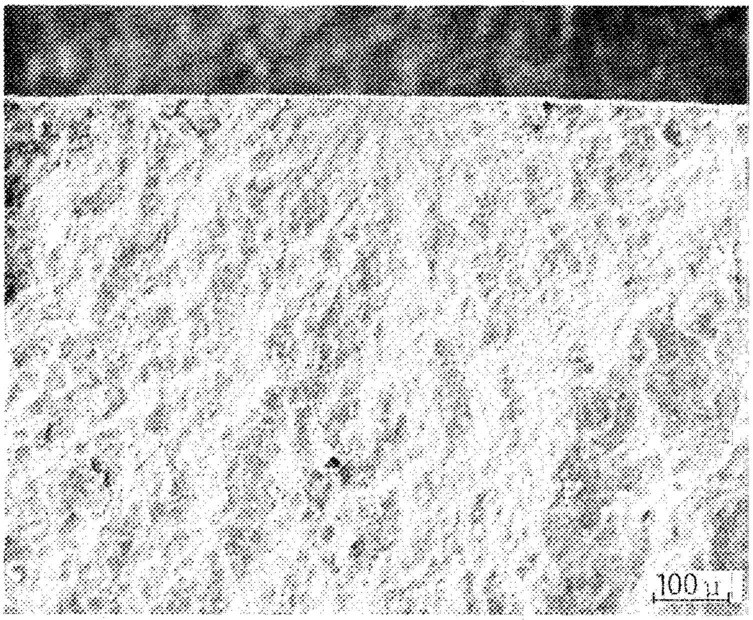

Fig. 1.2.21. SEM photograph of fractured surface with fracture origin at surface (material Z191 at 100X).

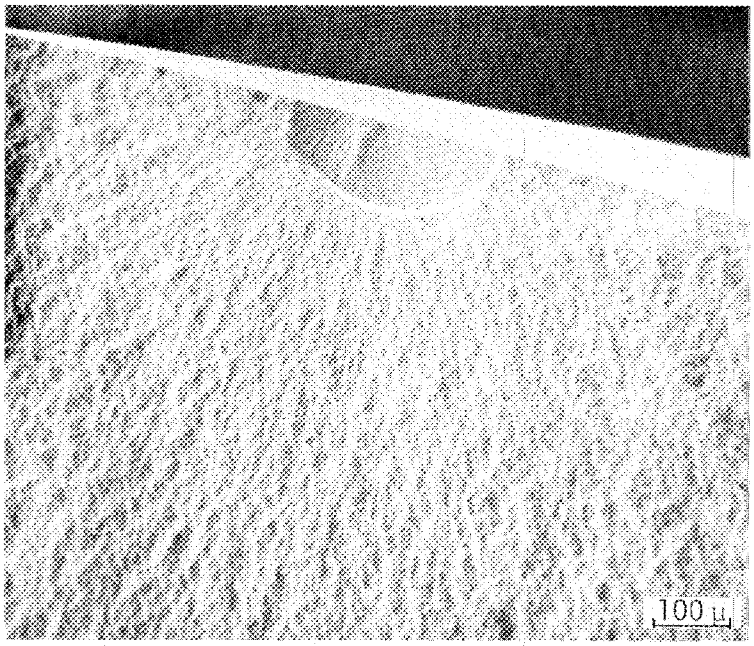

Fig. 1.2.22. SEM photograph of fractured surface with fracture origin at surface (material Z201 at 100X).

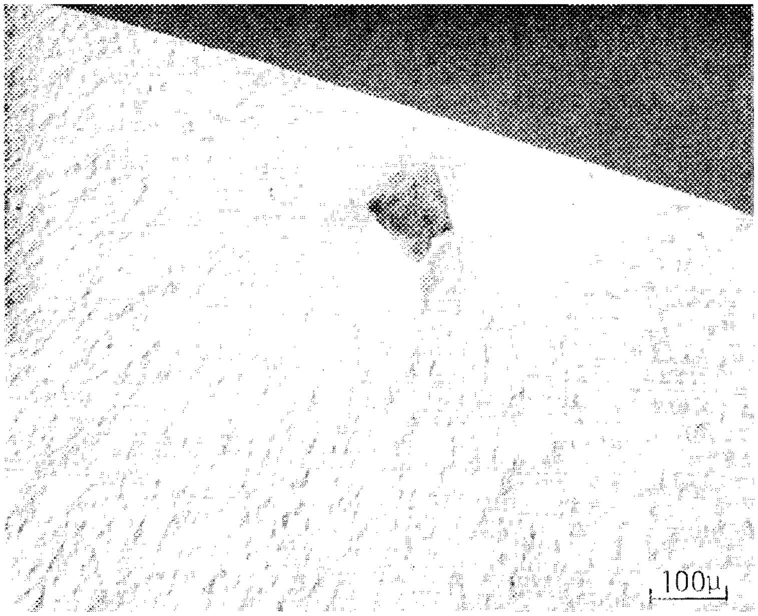

Fig. 1.2.23. SEM photograph of fractured surface with fracture origin at internal pore (material Z201 at 100X).

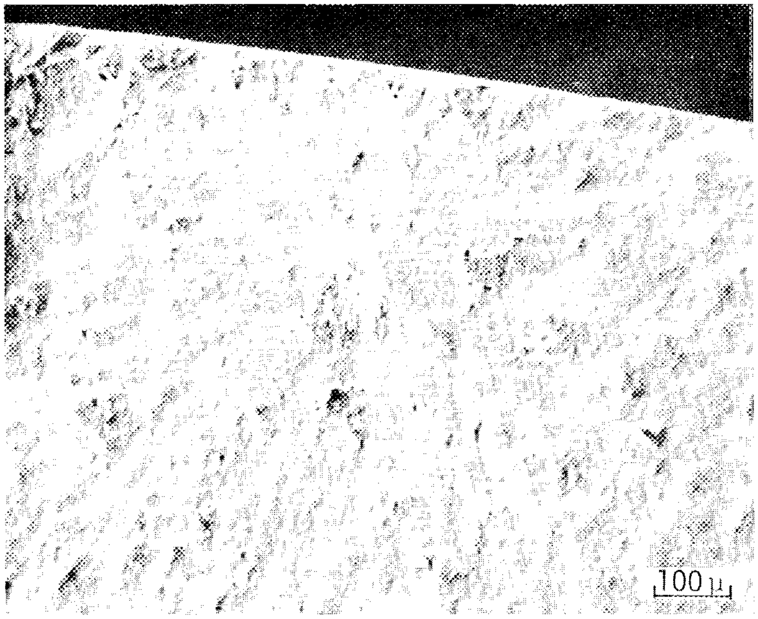

Fig. 1.2.24. SEM photograph of fractured surface with fracture origin at internal flaw (material Z191 at 100X).

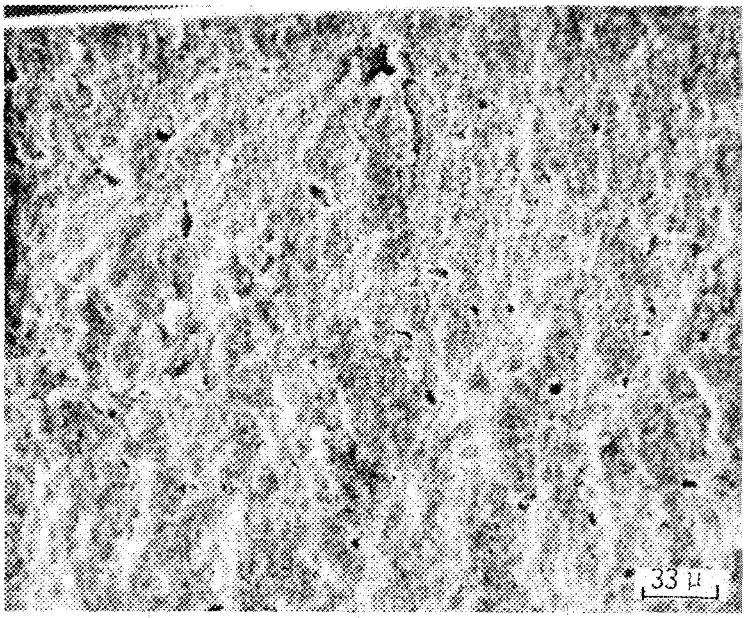

Fig. 1.2.25. SEM photograph of fractured surface with fracture origin at internal pore (material XS121 at 300X).

1.3 DISCUSSION OF RESULTS AND FUTURE PLANS

The initial task of this program is designed to verify manufacturers property data, further characterize candidate TTC materials, and establish a basis for the selection of the candidate materials to be further evaluated in the mini-matrix program. The results obtained in the screening studies will provide the basis for evaluating the candidate materials and validate supplier claims.

The modulus of rupture values measured at room temperature for the eight candidate materials evaluated were in general agreement with the data obtained from the supplier. By comparing the data in Table 1.2.1 with the data presented in Table 1.2.7, it can be seen that the room temperature modulus of rupture values measured are within 2 to 3% of that reported by the suppliers except for the Ceramatec XS121 and Nilcra MS-PSZ materials which were about 80% of the supplier's reported value. The modulus of rupture values measured for all of the different TTC materials were impressive. Even the 481 MPa MOR value measured for the Ceramatec CTZP is significantly higher than the MOR values reported for most conventional ceramic materials and is twice as high as the average modulus of rupture value reported for fully stabilized zirconium oxide materials. The 1265 MPa measured for the Kyocera AZ301 material was especially impressive since it is greater than the values reported for virtually all conventional ceramic materials.

Five of the eight candidate materials (XS212, XS241, CTZP, MS-PSZ, and Z191) showed no change when tested in flexure using the slow loading rates, however, the two Kyocera materials, Z201 and AZ301, both showed a 14% decrease as did the Nilcra TS-PSZ material. This magnitude of decrease may indicate the presence of slow crack growth in these two materials but further statistical evaluation is required.

Little or no strength decrease was observed for six of the eight candidate materials exposed to the aging treatments (XS121, XS241, CTZP, AZ301, MS-PSZ, and Z191). The Kyocera Z201 material showed a 17% decrease in the average flexure strength as a result of the aging treatment. The Nilcra TS-PSZ material showed a 10% decrease in average flexure strength as a result of the aging treatment.

Based on the x-ray data obtained, it was found that prior to aging the Y_2O_3 partially stabilized ZrO_2 materials were predominantly tetragonal with 0 - 10% monoclinic phase (see Table 1.2.5). The MgO partially stabilized ZrO_2 materials were 23 - 33% monoclinic, 30 - 50% tetragonal, and the remainder cubic. The two dispersion toughened alumina materials had a ZrO_2 dispersant that was approximately 70% tetragonal and 30% monoclinic. After the aging treatment, the Ceramatec XS121 and XS241 material showed significant change and the Nilcra TS-PSZ showed a moderate change. The XS121 dispersion toughened alumina had twice the amount of monoclinic ZrO_2 present after aging. The Y_2O_3 stabilized XS241 had a four-fold increase in the amount of monoclinic phase after aging. The Nilcra TS-PSZ (MgO stabilized) showed a 24% increase in the monoclinic crystal phase after aging. However, the modulus of rupture measured for the two Ceramatec materials did not show any decrease in flexure strength as a result of the aging treatment. The Nilcra TS-PSZ material had a 10% decrease in the flexure strength after the aging treatment. It is interesting to note that the Kyocera Z201 material, which showed a 17% decrease in modulus of rupture, showed no change in the monoclinic phase present as a result of the aging treatment.

With the exception of the fractured toughness values measured for the Kyocera Z201 material, all of the other fracture toughness (K_{IC}) measurements were found to be considerably (25 - 60%) lower than those reported by the suppliers. It is possible that this difference may be due to the difference in fracture toughness measurements methods employed. A number of investigators have reported that the controlled surface flaw technique for measuring fracture toughness will result in significantly lower K_{IC} values than those obtained by other measurement methods.[1-3] However, since the test methods used by the supplier are not cited, it is not possible to determine if the differences obtained are due to differences in measurement techniques. Although the fracture toughness values obtained were lower than those reported by the supplier, the values obtained are still somewhat higher than those reported for most convention ceramic materials.

Unfortunately, valid K_{IC} values could not be obtained for the Ceramatec CTZP material and the two Nilcra materials. All of the samples tested failed outside of the indent region, and it was only possible to identify fracture origin and initial crack size for one CTZP sample. As shown in Figure 1.2.20, an array of microcracks formed around the indent of the CTZP materials. It is suggested that the failure during fracture toughness testing occurred at one of these microcrack sites which had become a critical flaw during the testing process. A number of process modifications and alternative techniques were investigated in an attempt to obtain valid toughness measurements for the CTZP material, however, none of the methods used proved effective.

The Kyocera and NGK materials were very fine particle sized materials and had very high densities containing only a sparse dispersion of very small pores. The Ceramatec materials were also very fine particle size and had lower densities with a greater degree of porosity. The CeO_2 and Y_2O_3 stabilized materials (CTZP and XS241) appeared to contain several phases. In addition, the CTZP material appeared to contain a network of internal microcracks. The Nilcra MS/TS materials are MgO stabilized, relatively porous and coarse grained.

In summary, it would appear that the MOR data provided by the supplier were in agreement with the data obtained in the screening test. All of the materials evaluated had impressive flexure strength and fracture toughness values that are higher than commonly reported for conventional ceramic materials. The effect of aging treatments on modulus of rupture and increased formation of the monoclinic phase is not clear and will require further investigation.

1.4 FUTURE PLANS

A tabulation of the activities planned for the next several months is presented below:

1. Initiate MOR testing at the most critical temperature (1050°C) and moisture (10% H_2O) for three samples of each TTC material. These tests will provide insight about the material's behavior at this severe condition and aid in the selection of the candidates for further evaluation.
2. Measure thermal expansion of the candidate TTC materials. This added measurement should provide valuable information about their behavior.
3. Continue the statistical analysis of MOR data that has been initiated. The results of this analysis should be completed during the next reporting period.
4. Make the final selection of the candidate materials for the mini-matrix evaluation program.
5. After the candidate TTC materials are selected, the high temperature (1050°C) dynamic fatigue testing phase of the mini-matrix evaluation plan will be initiated.
6. Continue the development of an effective Raman microprobe spectroscopy procedure for evaluating the crystal structure at the fracture surface and small increments behind the fracture zone. A brief report describing the status of the developments to date has been prepared and is submitted under separate cover.

1.4 REFERENCES

1. J. J. Petrovic, R. A. Dirks, L. A. Jacobson, and M. G. Mendiratta, "Effects of Residual Stresses on Fracture from Controlled Surface Flaws," *J. Am. Ceram. Soc.* 59(3), 177-178 (1976).

2. J. J. Petrovic, L. A. Jacobson, P. K. Talty, and A. K. Vasudevan, "Controlled Surface Flaws in Hot-Pressed Si_3N_4," *J. Am. Ceram. Soc.* 58(3), 113-116 (1975).

3. R. R. Wills and J. M. Wimmer, "Controlled Surface Flaw-Initiated Fracture in Reaction-Densified Silicon Carbide," *J. Am. Ceram. Soc.* 59(9), 437-440 (1976).

3.4 FRACTURE MECHANICS

Improved Methods for Measuring the Fracture Resistance of Structural Ceramics

R. C. Bradt and A. S. Kobayashi (University of Washington)

Objective/Scope

The long-term goals of this study are to develop and demonstrate a technique comprising a single measurement, or a technique comprising a set of correlative measurements for structural ceramics including monolithic and composite materials which will allow the reliable and accurate determination of their resistance to fracture (crack propagation) over a broad temperature range from 25°C to 1400°C.

Technical Progress

The monolithic ceramic materials (a transparaent polycrystalline $MgAl_2O_4$, Coors; a sintered silicon carbide, Hexoloy, and a sintered silicon nitride, (GTE, A2Y6) have been received and are being prepared for testing. This includes introducing microflaws and also diamond sawing straight through notches and chevron notches. While these specimens are being prepared for testing, other preliminary testing is proceeding to refine the experimental procedures using the laser interferomatic strain guage (LISG) technique.

The LISG technique has now been coupled directly with an Instron floor model testing machine and successfully applied to compliance measurements and toughness measurements for alumina and silicon nitride specimens. In addition to unnotched and straight through notched specimens, the LISG method has also been recently applied to monitor the stable crack growth through chevron notched specimens. It is now evident that the LISG technique will be completely adaptable to determine fracture parameters through dimensionless load-displacement methods.

Finite element modelling of the chevron notched three point bend specimen is proceeding for a range of a/w values. The 'ANSYS' finite element code is being used, consisting of eight model (3 DOF/mode) bricks with 1000 degrees of freedom in the solution. Preliminary results show good agreement with the Bluhm slice model and the Sakai modified slice model, although the 3-D model is somewhat stiffer.

Several ceramic/ceramic composites have been obtaining for preliminary testing and screening for the composites portion of the program. These include two ARCO SiC whisker/Al_2O_3 matrix materials and three different continuous fiber/CVI SiC matrix bodies, including Nicalon, Nextel, and alumina fibers. Only the Nicalon/CVI-SiC matrix body has been tested to date and reported in the publication listed later.

Status of Milestones

The first year's milestones, which can be summarized as obtaining and initiating the testing of the monolithic ceramics and also obtaining the composites, are on schedule except for the composites. The difficulty with the composites is essentially the same as was experienced with the monolithic ceramics, namely the ready availability of compositions for which large numbers of specimens are obtainable. It is expected that this will catch-up during the second year of the program.

Publications

Four papers have been written during the year. They are:

Graphical Methods for Determining the Nonlinear Fracture Parameters of Silica and Graphite Refractory Composites
(VPI, Fracture Mechanics of Ceramics Symposium)

Toughness Anisotorpy of a SiC/SiC Laminar Composite
(Penn State, Multiphase Ceramics Meeting)

The Toughness of Polycrystalline $MgAl_2O_4$
(ACerS, PCRM at Irvine)

Fracture Toughness Testing of Ceramics with an LISG
(ACerS, PCRM at Irvine)

Testing and Evaluation of Advanced Ceramics at High Temperature in Uniaxial Tension

J. Sankar and V. S. Avva (North Carolina A&T State University)

Objectives/Scope

The purpose of this effort will be to test and evaluate advanced ceramic materials at temperatures up to 1500°C in uniaxial tension. Testing may include fast fracture strength, stepped static fatigue strength, and cyclic fatigue strength, along with analysis of fracture surfaces by scanning electron microscopy. This effort will comprise the following tasks:

Task 1. Specifications for Testing Machine and Controls + (Procurement)
Task 2. Identification of Test Material (s) + (Procurement of Specimens)
Task 3. Identification of Test Specimen Configuration
Task 4. Specifications for Testing Grips and Extensometer + (Procurement)
Task 5. Specifications for Testing Furnance and Controls + (Procurement)
Task 6. Development of Test Plan
Task 7. High Temperature Tensile Testing
Task 8. Reporting (Periodic)
Task 9. Final Report

It is anticipated that this two (2) year program will help in understanding the behavior of ceramic materials at very high temperatures in uniaxial tension.

Technical Progress

Both specification and identification of a suitable testing machine for ceramic tensile testing and the test ceramic material for the program have been selected, identified and approvals were obtained from the ORNL project manager for both. The selected machine with excellent force transducer and control systems seems to have the expected alignment, stiffness and stability required for the uniaxial tension testing of ceramics. As far as the candidate material is concerned, GTE SN-1000 Silicon Nitride is selected as the test material for the program.

During this reporting period attention was continued to be given to Tasks 3-5. A trip to ORNL was carried out to discuss these tasks with the project manager. A tensile specimen geometry with circular cross section, as shown on Figure 1 was decided for use in this program. Right now negotiations are being carried out with GTE, California to fabricate this geometry for GTE SN-1000 material.

During the ORNL trip, a fruitful discussion was also carried out with K. C. Liu regarding the gripping mechanism. It is planned to use his hydraulic self-aligning grip system idea for this project. Discussions are underway with fabricators to manufacture these grips for the present program.

The initial load train design is such that the ceramic pull rods (which will be holding the sample) will be connected to another set of water cooled stainless steel pull rods which in turn will be held by the self-aligning hydraulic grips. The ceramic pull rod portions of the load train will be within a ceramic retort tube to create an inert atmosphere and the whole set-up will be located in the middle of a silicon carbide split furnace capable of generating 1500°C. The initial design will also carry a ceramic extensometer with power supply and signal conditioner.

Status of Milestone

The procurement of the testing machine and control is already underway. The expected delivery date of this machine is in February, 1986. Procurement of tensile samples and grips is expected to start in the next 2 - 3 weeks.

Specimen Geometry

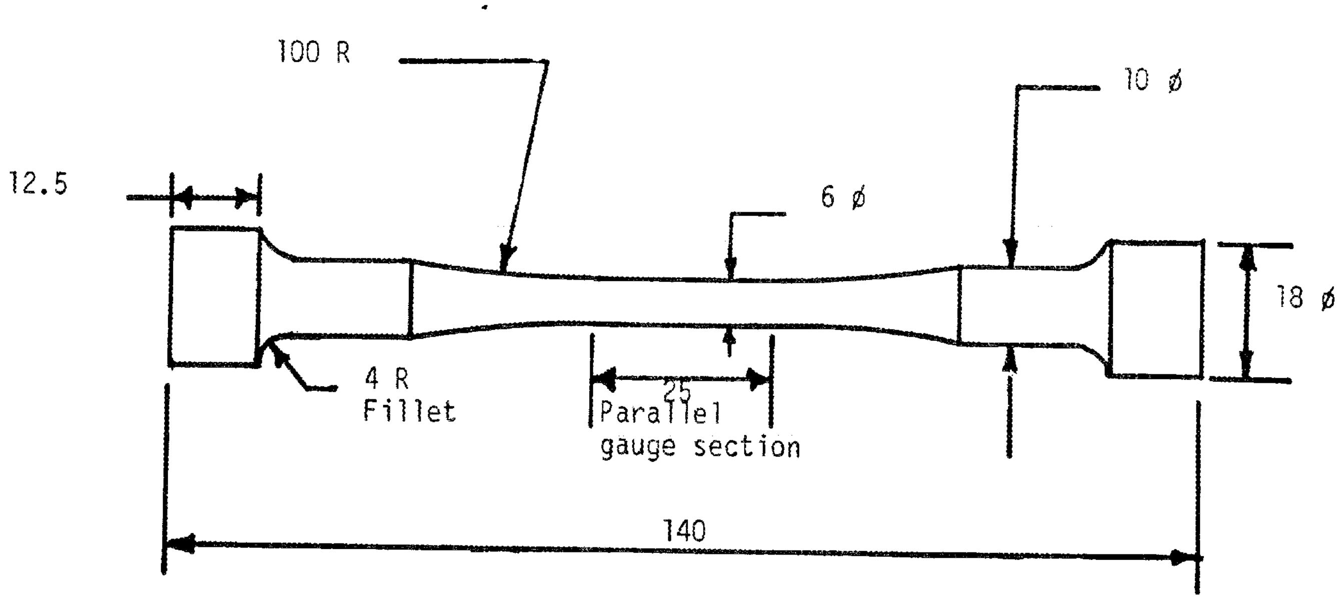

All Tolerances 0.01 mm
Surface finish 600 grit diamond ground

All Dimensions in mm
Scale:: 1 : 1

3.5 NONDESTRUCTIVE EVAULATION DEVELOPMENT

Nondestructive Characterization

R. W. McClung (Oak Ridge National Laboratory)

Objective/scope

The purpose of this program is to conduct nondestructive evaluation (NDE) development directed at identifying approaches for quantitative determination of conditions (including both properties and flaws) in ceramics that affect the structural performance. Those materials that have been seriously considered for application in advanced heat engines are all brittle materials whose fracture is affected by structural features whose dimensions are on the order of the dimensions of their microstructure. This work seeks to characterize those features using high-frequency ultrasonics and radiography to detect, size, and locate critical flaws and to measure nondestructively the elastic properties of the host material.

Technical progress

We have obtained several samples of partially stabilized zirconia (PSZ) from different sources that have been stabilized both with magnesium and with yttrium. Having found no large (>250 μm) discontinuities with low-frequency (20-MHz) ultrasonics, we examined these samples with a 50-MHz center frequency short-focus transducer, which is a relatively wide-band unit having significant energy above 80 MHz. This transducer is well suited for detecting small flaws, because the diameter of the ultrasonic beam in the region near focus is only about 60 μm in water and smaller still in the ceramic. Thus, even small flaws (~20 μm) will intercept a reasonable fraction of the total beam energy and be detectable.

Upon examining these samples with a 50-μm scan index, we located several discrete indications that, because they were detectable along a single scan line only (i.e., they were not detectable by adjacent scan lines), had to be smaller than 50 μm. The backscattering spectrum was then computed and found to peak at about 72 MHz, which is well down on the high-frequency tail of our 50-MHz transducer and implies that the scattering center is smaller than a wavelength at 50 MHz.

We next deconvolved these results with the transducer response to remove the effects of the unit and provide a record of the frequency-dependent scattering of the flaw alone. The result is shown in Fig. 1 and may be compared with the theoretical calculation previously given. The salient feature of the scattering is an approximate fourth-power increase with frequency to a turning point beyond which the scattering levels off. This point occurs when $ka \sim 1$, where k is the wave number and a the radius of the flaw. For the measured parameters of PSZ, this yields a flaw diameter of about 25 μm. This value is only approximate,

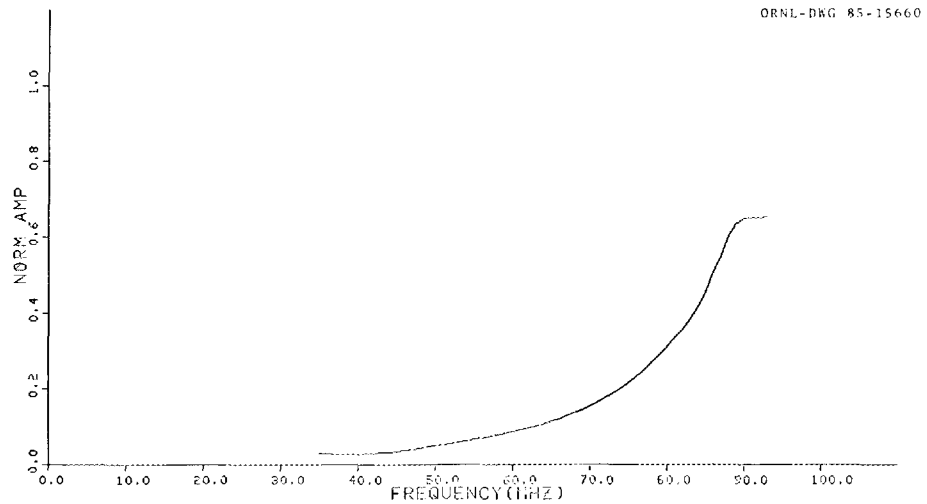

Fig. 1. Frequency dependence of scattering by a small flaw in partially stabilized zirconia.

because we assume spherical voids in the calculations. However, we are now confident that we can detect and approximately size voids in the 10- to 50-μm range with existing equipment.

One extremely useful capability toward which we have been striving is the ability to compute a material transfer function, or attenuation versus frequency response, which is independent of the transducer and test configuration used. This function is very useful in comparing different specimens, and we believe that the attenuation characteristic may be correlated with fracture properties of ceramics, although we have not demonstrated this yet. We routinely compute this response in low-frequency ultrasonics, but we have encountered difficulty in applying the algorithm to our ceramics work. We now believe that a modification to our diffraction-correction calculations and inclusion of coupling layer effects have solved these problems. The latter effect was completely unanticipated and arises because, in typical (low-frequency) contact ultrasonics, the effect of the very thin (~1 μm) layer of liquid used to couple energy from the transducer into the specimen is negligible. At 100 MHz, however, this layer is almost 0.1 wavelength thick and has a significant effect on the reflection and transmission coefficients. We therefore analytically examined a solid—liquid layer—solid structure and incorporated the results into our computer programs. Figure 2 shows the frequency dependence of the reflection coefficient for a 1-μm water couplant into silicon carbide. Because our original program assumed a constant value equal to that shown for zero frequency, the magnitude of the error is apparent. Our program now measures the thickness of the coupling layer from the input data and corrects for its frequency-dependent transmissivity.

Figure 3 shows the attenuation in an yttrium-stabilized zirconia. This curve is highly repeatable, even for samples that differ greatly in thickness, and is thus largely geometry-independent. The microstructure

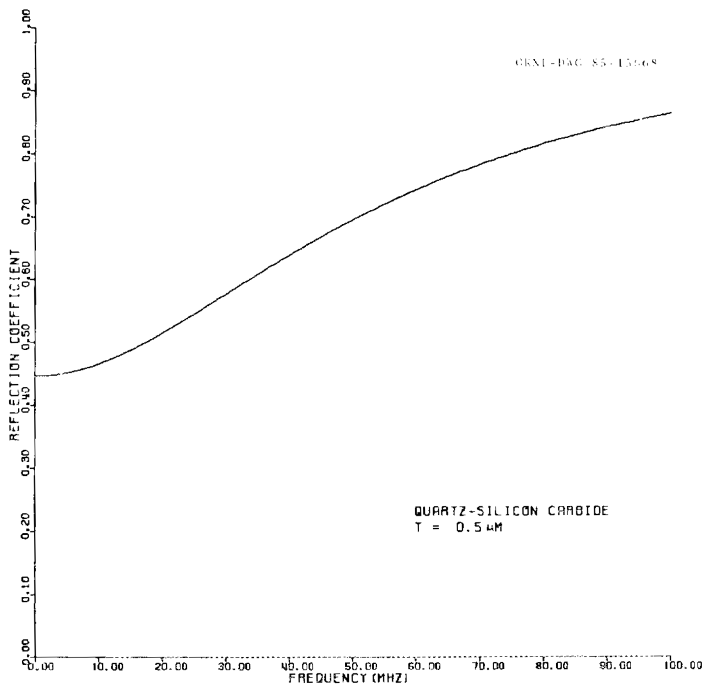

Fig. 2. Frequency dependence of the reflection coefficient at a quartz–silicon carbide interface coupled by 0.5 μm of water.

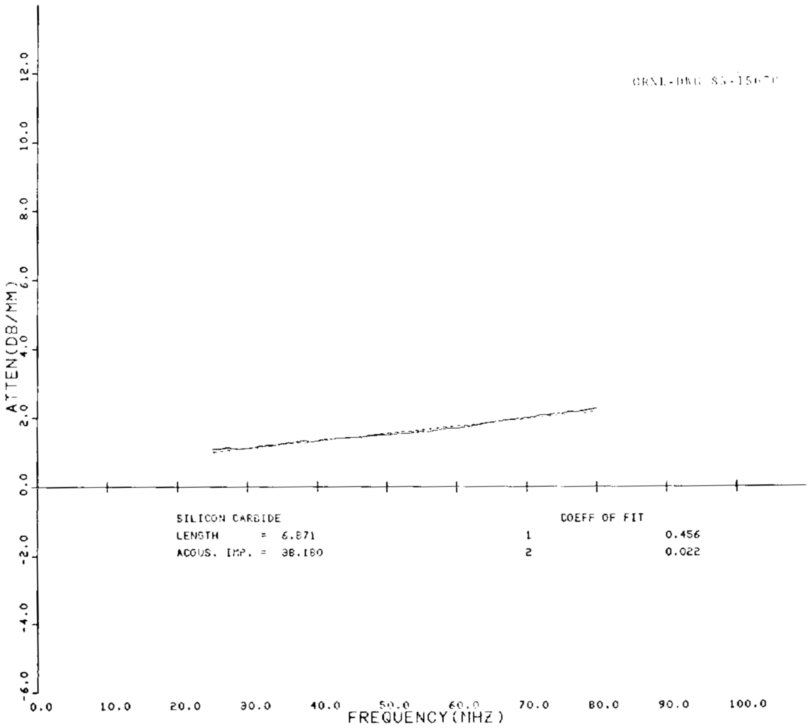

Fig. 3. Frequency dependence of attenuation in an yttrium-stabilized zirconia. Raw data (solid curve) and least-squares computer fit (dashed curve).

is largely tetragonal with a grain size of about 10 μm. The linear behavior of the attenuation characteristic indicates that scattering losses are not important in this frequency range, which is consistent with the grain size and ultrasonic wavelength. This material is amenable to ultrasonic examination for flaws having sizes of the order or 20 μm, because there is minimal contribution from grain boundary scattering.

Figure 4 shows the attenuation response for a magnesium-stabilized zirconia. Here the microstructure is largely cubic with a grain size of about 100 μm. The attenuation is much more severe and more strongly frequency-dependent than for the tetragonal microstructure. In this material, the detection of small flaws is much more difficult because of the severe grain boundary scattering in the frequency range of interest.

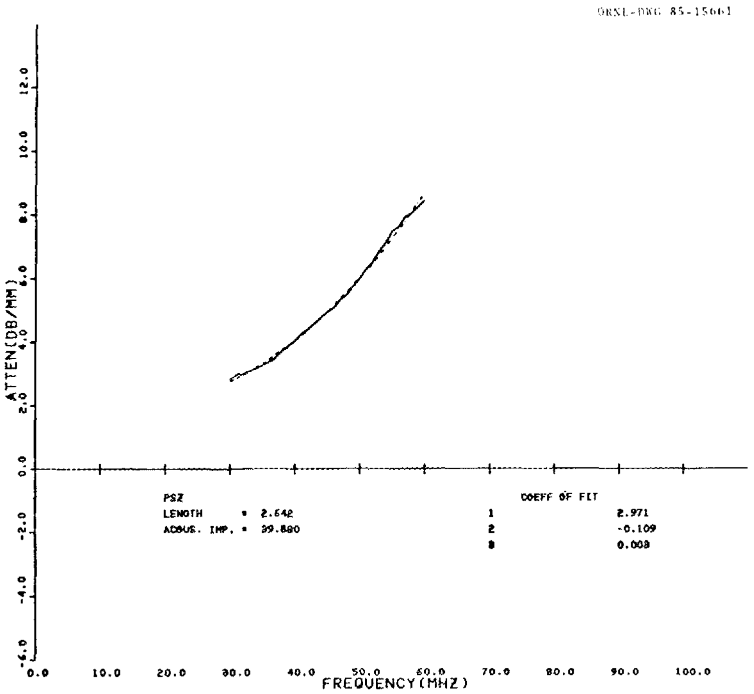

Fig. 4. Frequency dependence of attenuation in a magnesium-stabilized zirconia. Raw data (solid curve) and least-squares computer fit (dashed curve).

Initial experiments were conducted to determine the thickness sensitivity that could be achieved on silicon nitride modulus of rupture (MOR) bars using conventional radiographic techniques for future comparison with microfocus and tomographic techniques. Two silicon nitride MOR bars were obtained with no apparent discontinuities. In one of the bars, we placed three holes that were 0.25 mm in diameter with depths of 12.5, 20, and 43 μm in the 2.5-mm thickness separated by 1.25 cm. In the other bar, we placed three holes that were 0.125 mm in diameter with depths of 10, 20, and 37 μm in the 2.5-mm thickness separated by 1.25 cm.

The radiographic technique that was used included 35-kVCP energy, 25-mA current, 2.5-mm focal spot size, 1.37-m film-to-focal distance, type M film with no front screen in a vacuum cassette, and 8.5-min exposure time. Five of the six holes were imaged. The 10-μm-deep hole was not imaged. A thickness sensitivity of 0.5% was obtained, as evidenced by imaging the 12.5-μm-deep hole.

Smaller diameter (50-μm) holes will be placed in a third sample for assessment of the level of detectability with the conventional radiography.

Status of milestones

Milestone 351101 was completed as scheduled.

Publications

None.

4.0 TECHNOLOGY TRANSFER

Technology Transfer

D. R. Johnson (Oak Ridge National Laboratory)

Technology transfer in the Ceramic Technology Project is accomplished by a number of mechanisms including the following:

Trade shows. A portable display describing the program has been built and used at several trade shows and technical meetings, most recently at the Annual Meeting of the American Ceramic Society, May 5–7, 1985, in Cincinnati, Ohio.

Newsletter. A Ceramic Technology Newsletter is published bimonthly and sent to a large distribution.

Reports. Semiannual technical reports, which include contributions by all participants in the program, are published and sent to a large distribution. Informal bimonthly management and technical reports are distributed to the participants in the program. Open-literature reports are required of all research and development participants.

Direct Assistance. Direct assistance is provided to subcontractors in the program via access to unique characterization and testing facilities at the Oak Ridge National Laboratory.

Workshops. Topical workshops are held on subjects of vital concern to our community. During this period plans were completed for a workshop on material requirements for advanced heat engines, to be held during the Automotive Technology Development Contractors Coordination Meeting, October 21–24, 1985.

International Cooperation. Our program is actively involved in and supportive of the cooperative work being done by researchers in West Germany, Sweden, and the United States under an agreement with the International Energy Agency. That work, ultimately aimed at development of international standards, includes physical, morphological, and microstructural characterization of ceramic powders and dense ceramic bodies, and mechanical characterization of dense ceramics. Detailed planning and procurement of ceramic powders and flexural test bars were accomplished during this reporting period.

INTERNAL DISTRIBUTION

1–2. Central Research Library
3. Document Reference Section
4–5. Laboratory Records Department
6. Laboratory Records, ORNL RC
7. ORNL Patent Section
8. S. Baik
9. P. F. Becher
10. J. Bentley
11. T. M. Besmann
12. A. Bleier
13. E. E. Bloom
14. K. W. Boling
15. W. D. Bond
16. R. A. Bradley
17. C. R. Brinkman
18. V. R. Bullington
19. A. J. Caputo
20. R. S. Carlsmith
21. P. T. Carlson
22. J. A. Carpenter, Jr.
23. J. V. Cathcart
24. R. H. Cooper
25. S. A. David
26. J. H. DeVan
27. W. P. Eatherly
28. J. I. Federer
29. W. Fulkerson
30. R. L. Graves
31. D. L. Greene
32. M. A. Janney
33–37. D. R. Johnson
38. R. R. Judkins
39. M. A. Karnitz
40. M. P. Kertesz
41. T. B. Lindemer
42. K. C. Liu
43. E. L. Long, Jr.
44. R. W. McClung
45. D. L. McElroy
46. J. W. Michel
47. A. J. Moorhead
48. J. L. Rich
49. C. R. Richmond
50. J M Robbins
51. M. W. Rosenthal
52–98. A. C. Schaffhauser
99. J. H. Schneibel
100. J. L. Scott
101. G. M. Slaughter
102. E. J. Soderstrom
103–105. P. T. Thornton
106. T. N. Tiegs
107. J. R. Weir, Jr.
108. F. W. Wiffen
109. C. S. Yust
110. A. Zucker

EXTERNAL DISTRIBUTION

111. Donald F. Adams
Composite Materials
Research Group
Mechanical Engineering
Department
University of Wyoming
Laramie, WY 82071

112. Richard T. Alpaugh
Department of Energy
Office of Transportation
Systems
Forrestal Building CE-151
1000 Independence Avenue
Washington, DC 20585

113. H. Arbabi
Brunel University
Department of Materials
Technology
Uxbridge Middlesex UB8 3PH
United Kingdom

114. James P. Arnold
U.S. Army Belvoir
R&D Center
ATTN: FTRBE-EMP
Fort Belvoir, VA 22060

115. V. S. Avva
North Carolina Agricultural and Technical State University
Department of Mechanical Engineering
Greensboro, NC 27411

116. John M. Bailey
Research Consultant, Research Dept.
Technical Center
Caterpillar Tractor Company
100 NE Adams
Peoria, IL 61629

117. Murray Bailey
NASA Lewis Research Center
21000 Brookpark Road, MS 77-6
Cleveland, OH 44135

118. R. R. Baker
34819 Lyndon Street
Livonia, MI 48154

119. J. Gary Baldoni
GTE Laboratories, Inc.
40 Sylvan Road
Waltham, MA 02254

120. Ken Baumert
Air Products and Chemicals, Inc.
Box 538
Allentown, PA 18105

121. Ronald L. Beatty
ARCO Chemicals, Silag Operation
Route 6, Box A
Greer, SC 29651

122. A. L. Bement, Jr.
Vice President, Technical Resources
TRW, Inc.
23555 Euclid Avenue
Cleveland, OH 44117

123. M. Bentele
Xamag, Inc.
259 Melville Avenue
Fairfield, CT 06430

124. Clifton G. Bergeron
Head, Department of Ceramic Engineering
University of Illinois
204 Ceramics Building
Urbana, IL 61801

125. William D. Bjorndahl
TRW, Inc.
TRW Energy Development Group
Materials Characterization and Chemical Analysis Dept.
One Space Park
Building 01, Room 2060
Redondo Beach, CA 90278

126. Paul N. Blumberg
President
Integral Technologies Inc.
415 E. Plaza Drive
Westmont, IL 60559

127. Wolfgang D. G. Boecker
Sohio Engineered Materials Company
Niagara Falls R&D Center
PO Box 832
Niagara Falls, NY 14302

128. Seymour A. Bortz
Manager, Nonmetallic Materials and Composites
Materials and Manufacturing Technology
IIT Research Institute
10 West 35th Street
Chicago, IL 60616

129. H. K. Bowen
Department of Materials Science and Engineering
Room 12-009
Massachusetts Institute of Technology
Cambridge, MA 02139

130. Richard C. Bradt, Chairman,
Materials Science and Engrg.
University of Washington
Dept. of Materials Science and Engineering
Roberts Hall, FB-10
Seattle, WA 98195

131. Raymond J. Bratton
Manager, Ceramic Science
Westinghouse Electric Corporation
R&D Center
1310 Beulah Road
Pittsburgh, PA 15235

132. Catherine E. Brown
E. I. DuPont de Nemours & Company
Experimental Station
Information Center E302/301
Wilmington, DE 19898

133. W. Bryzik
U.S. Army Tank Automotive Command
R&D Center
Warren, MI 48090

134. S. T. Buljan
GTE Laboratories, Inc.
40 Sylvan Road
Waltham, MA 02254

135. Donald J. Campbell
Air Force Wright Aeronautical Laboratory
AFWAL/POX
Wright-Patterson AFB, OH 45433

136. Harry W. Carpenter
Rockwell International
Rocketdyne Division
J39-169:HC92
6633 Canoga Avenue
Canoga Park, CA 91304

137. David Carruthers
Garrett Turbine Engine Company
111 South 34 Street
PO Box 5217
Phoenix, AZ 85010

138. Se-Tak Chang
GTE Laboratories
40 Sylvan Road
Dept. 312
Waltham, MA 02254

139. R. J. Charles, Manager
Ceramics Branch
Physical Chemistry Laboratory
General Electric Company
PO Box 8
Schenectady, NY 12301

140. Albert A. Chesnes
Director, Heat Engine Propulsion Division
Office of Transportation Systems
Department of Energy
Forrestal Building CE-151
1000 Independence Avenue
Washington, DC 20585

141. Gilbert Y. Chin
Bell Telephone Laboratories
Research & Development
Murray Hill, NJ 07974

142. Melvin H. Chiogioji
Director, Office of Transportation Systems
Department of Energy
Forrestal Building CE-15
1000 Independence Avenue, SW
Washington, DC 20585

143. William L. Cleary
Associate Division Director
ORI, Inc.
1375 Piccard Drive
Rockville, MD 20850

144. Philip R. Compton
Energy Systems Office
National Aeronautics and Space Administration
Code REC-1
Washington, DC 20546

145. Harry E. Cook
Director, Automotive Research and Technical Planning
Chrysler Corporation
PO Box 857, CIMS: 414-01-22
Detroit, MI 48288

146. John A. Coppola
Representative Director
Executive Vice President
Hitachi-Carborundum Company
Shinjuku-Mitsui Building
No. 1-1, 2-Chome
Nishishinjuku
Shinjuku-ku, Tokyo 160
Japan

147. Charles H. Craig
Senior Materials Engineer
Office of Transportation Systems
Department of Energy
Forrestal Building CE-151
Washington, DC 20585

148. William J. Croft
U.S. Army Materials Technology Laboratory
Arsenal Street
Watertown, MA 02172

149. Gary M. Crosbie
Ford Motor Company
PO Box 2053, Room S-2079
Ceramics Materials Department
Dearborn, MI 48121

150. Floyd W. Crouse, Jr.
Department of Energy
Morgantown Energy Technology Center
PO Box 880
Morgantown, WV 26505

151. Raymond Cutler
Ceramatec, Inc.
163 W. 1700 South
Salt Lake City, UT 84115

152. Stanley J. Dapkunas
Technical Coordination Staff
Office of Fossil Energy
FE-14 GTN
Department of Energy
Washington, DC 20545

153. Robert F. Davis
North Carolina State University
Materials Engineering Department
232 Riddick Laboratory
Raleigh, NC 27607

154. Alan L. Dragoo
Materials Scientist, Inorganic Materials Division
National Bureau of Standards
Center for Materials Science
Gaithersburg, MD 20899

155. Keith F. Dufrane
Battelle Columbus Laboratories
505 King Avenue
Columbus, OH 43201

156. Robert J. Eagan
Manager, Chemistry and Ceramics Department 1840
Sandia National Laboratories
Albuquerque, NM 87185

157. Christopher A. Ebel
Program Manager, High Performance Ceramics
Norton Company
Goddard Road
Northboro, MA 01532

158. J. J. Eberhardt
Office of Energy Utilization Research
Department of Energy
Forrestal Building CE-142
1000 Independence Avenue
Washington, DC 20585

159. E. E. Ecklund
Office of Transportation Systems
Department of Energy
Forrestal Building CE-151
1000 Independence Avenue
Washington, DC 20585

160. William A. Ellingson
Argonne National Laboratory
9700 South Cass Avenue
Argonne, IL 60439

161. Director, Applied Technology Laboratory
U.S. Army Research and Technology Laboratory (AVSCOM)
ATTN: SAVDL-ATL-ATP
(Mr. Graydon A. Elliott)
Fort Eustis, VA 23604

162. A. Erdely
Chemical Engineer
26 Av. Gare des Eaux-vives
1208 Geneva
Switzerland

163. Charles D. Estes
U.S. Senate
Professional Staff Member
Committee on Appropriations
SD-152 Dirksen Senate Office Building
Washington, DC 20510

164. Anthony G. Evans
Lawrence Berkeley Laboratory
University of California
264 Hearst Mining Building
Berkeley, CA 94720

165. Robert C. Evans
Asst. Manager, Vehicular Gas Turbine and Diesel Project Office
NASA Lewis Research Center
21000 Brookpark Road
Cleveland, OH 44135

166. Katherine T. Faber
Assistant Professor of Ceramic Engineering
Ohio State University
2041 College Road
Columbus, OH 43210

167. John Facey
National Aeronautics and Space Administration
Energy Systems Office
Washington, DC 20546

168. John W. Fairbanks
Office of Transportation Systems
Department of Energy
Forrestal Building CE-151
Washington, DC 20585

169. Larry Farrell
Babcock and Wilcox
PO Box 1260
Lynchburg, VA 24505

170. M. K. Ferber
University of Illinois
105 S. Goodwin Avenue
203 Ceramic Building
Urbana, IL 61801

171. R. E. Fisher
President
Amercom, Inc.
8948 Fullbright Avenue
Chatsworth, CA 91311

172. H. W. Foglesong
Dow Corning Corporation
3901 S. Saginaw Road
Midland, MI 48640

173. Thomas F. Foltz
Manager, Product Applications
Avco
Special Materials Division
Two Industrial Avenue
Lowell, MA 01851

174. Robert G. Frank
Manager, Non-Metallic Materials
General Electric Company
One Neumann Way, Mail Drop M-87
PO Box 156301
Cincinnati, OH 45215-6301

175. Frank Gac
Department of Materials Science and Engineering
University of Washington
Seattle, WA 98195

176. George E. Gazza
U.S. Army Materials Technology Laboratory
Arsenal Street
Watertown, MA 02172

177. Charles M. Gilmore
Department of Civil, Mechanical, and Environmental Engineering
The George Washington University
Washington, DC 20052

178. Paul Glance
Director, R&D
Concept Analysis Corporation
9145 General Court
Plymouth, MI 48170

179. Joseph W. Glatz
Naval Air Propulsion Test Center
Science and Technology Group
Systems Technology Division
Box 7176, PE 34
Trenton, NJ 08628

180. Stephen T. Gonczy
Signal UOP Corporate Research Center
Materials Science Department
50 UOP Plaza
Des Plaines, IL 60016-6187

181. Robert J. Gottschall
Office of Material Sciences
Department of Energy
ER-131 GTN
Washington, DC 20545

182. Kenneth Green
Senior Development Engineer
Coors Porcelain Company
Golden, CO 80401

183. Michael Greenfield
National Aeronautics and Space Administration
Energy Systems Office
Washington, DC 20546

184. Lance E. Groseclose
General Motors Corporation
Allison Gas Turbine Division
PO Box 420
Indianapolis, IN 46206-0420

185. T. D. Gulden
Manager, Ceramics and Chemistry
GA Technologies, Inc.
PO Box 81608
San Diego, CA 92138

186. M. D. Gurney
NIPER
PO Box 2128
Bartlesville, OK 74005

187. J. J. Habeeb
Senior Chemist, Research Division
Esso Petroleum Canada
PO Box 3022
Sarina, Ontario
Canada N7T 7M1

188. H. T. Hahn
Department of Mechanical Engineering
Washington University at St. Louis
Lindell and Skinker
Box 1087
St. Louis, MO 63130

189. Nabil S. Hakim
Staff Research Engineer,
Engrg R&D
General Motors Corporation
Detroit Diesel Allison Div.
36880 Ecorse Road
Romulus, MI 48174

190. John W. Halloran
Ceramic Process Systems
128 Spring Street
Lexington, MA 02173

191. John M. Halstead
Manager, Business Development
Structural Ceramics Division
Sohio Engineered Materials Company
1625 Buffalo Avenue, Bldg. 91-2
PO Box 1054
Niagara Falls, NY 14302

192. R. A. Harmon
25 Schalren Drive
Latham, NY 12110

193. Stephen D. Hartline
Norton Company
High Performance Ceramics
Goddard Road
Northboro, MA 01532

194. Willard E. Hauth
Section Manager, Composite Development Ceramics Program
Dow Corning Corporation
Midland, MI 48640

195. Norman L. Hecht
University of Dayton Research Institute
300 College Park
Dayton, OH 45469-0001

196. S. S. Hecker
Deputy Division Leader
Material Science and Technology Division, G-756
Los Alamos National Lab.
PO Box 1663
Los Alamos, NM 87545

197. Peter W. Heitman
General Motors Corporation
Allison Gas Turbine Operations
PO Box 420, W-5
Indianapolis, IN 46206-0420

198. H. E. Helms
General Motors Corporation
Allison Gas Turbine Operations
PO Box 420
Indianapolis, IN 46206-0420

199. Thomas L. Henson
Director of Research and Engineering
Chemical & Metallurgical Div.
GTE Products Corporation
Hawes Street
Towanda, PA 18848-0504

200. Thomas P. Herbell
NASA Lewis Research Center
21000 Brookpark Road, MS 001
Cleveland, OH 44135

201. Ben Heshmatpour
Thermo Electron Corporation
101 First Avenue
Waltham, MA 02154

202\. Robert V. Hillery
Manager, Coating Materials
and Processes
General Electric Company
Cincinnati, OH 45215

203\. Jonathan W. Hinton
Vice President and
General Manager
Structural Ceramics Division
Sohio Engineered Materials
Company
PO Box 1054
Niagara Falls, NY 14302

204\. Stephen M. Hsu
Chemical Stability and
Corrosion Division
Center for Materials Science
National Measurements Lab.
National Bureau of Standards
Gaithersburg, MD 20899

205\. Joseph E. Hunter, Jr.
General Motors Corporation
Research Labs, Metallurgy
Department
12 Mile and Mound Roads
Warren, MI 48090-9055

206\. Louis C. Ianniello
Director, Office of Materials
Sciences
Department of Energy
ER-13 GTN
Washington, DC 20545

207\. Curt A. Johnson
General Electric Company
PO Box 8, Ceramics Branch
Schenectady, NY 12301

208\. Larry Johnson, Director
Center for Transportation
Research
Argonne National Laboratory
9700 S. Cass Avenue,
Building 362
Argonne, IL 60439
Indianapolis, IN 46206-0420

209\. R. A. Johnson
General Motors Corporation
Allison Gas Turbine Division
PO Box 420
Indianapolis, IN 46206-0420

210\. L. A. Joo
Associate Director of Research
Great Lakes Research
Corporation
PO Box 1031
Elizabethton, TN 37643

211\. Roy Kamo, President
Adiabatics, Inc.
630 S. Mapleton
Columbus, IN 47201

212\. Allan Katz
Air Force Wright Aeronautical
Laboratory
Materials Laboratory
AFWAL/MLLM
Metals and Ceramics Division
Wright-Patterson AFB,
OH 45433

213\. R. N. Katz
Chief, Ceramics Research
Division
U.S. Army Materials
Technology Laboratory
Arsenal Street
Watertown, MA 02172

214. P. Victor Kelsey
Ceramics Technical Leader
Materials Science Division
Alcoa Aluminum Company of America
Alcoa Technical Center B
Alcoa Center, PA 15061

215. Frederick L. Kennard III
Supervisor, Ceramic Research
General Motors Corporation
AC Spark Plug Division Dept. 32-24
1300 N. Dort Highway
Flint, MI 48556

216. J. R. Kidwell
AGT101 Assistant Project Engineer
Garrett Turbine Engine Company
111 S. 34th Street
PO Box 5217
Phoenix, AZ 85010

217. Max Klein, Senior Scientist
Thermodynamics
Gas Research Institute
8600 West Bryn Mawr Avenue
Chicago, IL 60631

218. C. E. Knapp
Norton Company
8001 Daly Street
Niagara Falls, Ontario
Canada

219. A. S. Kobayashi
University of Washington
Dept. of Mechanical Engineering, MS FU10
Seattle, WA 98195

220. David M. Kotchick
AiResearch Manufacturing Co.
2525 W. 190th Street
Torrance, CA 90509

221. Saunders B. Kramer
Manager, AGT Program
Office of Transportation Systems
Department of Energy
Forrestal Building CE-151
1000 Independence Avenue
Washington, DC 20585

222. D. M. Kreiner
AGT101 Project Manager
Garrett Turbine Engine Company
111 S. 34th Street
PO Box 5217
Phoenix, AZ 85010

223. Pieter Krijgsman
Ceramic Design Int. Hold., Ltd.
PO Box 68
8050 AB Hattem
The Netherlands

224. Everett A. Lake
Air Force Wright Aeronautical Laboratory
AFWAL/POOS
Wright-Patterson AFB, OH 45433

225. Fred F. Lange
Science Center
Rockwell International
1049 Camino Dos Rios
PO Box 1085
Thousand Oaks, CA 91360

226. John G. Lanning
Corning Glass Works
Advanced Engine Components, HP-BB-2
Corning, NY 14830

227. David C. Larsen
Corning Glass Works
Materials Research Department
Sullivan Park, FR-51
Corning, NY 14831

228. Patrick Lauzon
Ontario Research Foundation
Glass and Ceramics Centre
Materials Division
Sheridan Park Research
Community
Mississauga, Ontario
Canada L5K 183

229. Alan Lawley
Drexel University
Materials Engineering
Piladelphia, PA 19104

230. Daniel Lee
Temescon
2850 7th Street
Berkeley, CA 94710

231. E. M. Lenoe
Office of Naval Research
Air Force Office of Scientific
Research
Liaison Office, Far East
APO San Francisco, CA
96503-0110

232. Stanley R. Levine
NASA Lewis Research Center
21000 Brookpark Road
Cleveland, OH 44135

233. David Lewis
Naval Research Laboratory
Code 6360, Materials Science
and Technology Division
4555 Overlook Avenue, SW
Washington, DC 20375

234. Winston W. Liang
Project Manager
Industrial Materials Research
Gas Research Institute
8600 W. Bryn Mawr Avenue
Chicago, IL 60631

235. Bill Long
Babcock and Wilcox
PO Box 1260
Lynchburg, VA 24505

236. L. A. Lott
EG&G, Inc.
Idaho National Engineering
Laboratory
PO Box 1625
Idaho Falls, ID 83415

237. Bryan K. Luftglass
Staff Consultant
Chem Systems, Inc.
303 S. Broadway
Tarrytown, NY 10591

238. Tai-il Mah
Technical Manager, Ceramics
and Composites Research
Universal Energy Systems
4401 Dayton-Xenia Road
Dayton, OH 45432

239. William R. Martin
General Manager, Ceramic
Packaging Business Unit
Cabot Technical Ceramics
87 John L. Dietsch Boulevard
Attleboro, MA 02110

240. John Mason
Vice President, Engineering
The Garrett Corporation
9851 Sepulveda Boulevard
PO Box 92248
Los Angeles, CA 90009

241. Richard A. Matula
Dean, College of Engineering
Louisiana State University
Baton Rouge, LA 70803-6401

242. K. S. Mazdiyasni
Air Force Wright Aeronautical
Laboratory
Materials Laboratory,
AFWAL/MLLM
Metals and Ceramics Division
Wright-Patterson AFB,
OH 45433-6533

243. J. McCauley
U.S. Army Materials
Technology Laboratory
DRXMR-MC
Arsenal Street
Watertown, MA 02172

244. William J. McDonough
Department of Energy
Office of Transportation
Systems
Forrestal Building CE-151
1000 Independence Avenue
Washington, DC 20585

245. Thomas D. McGee
Iowa State University
Department of Materials
Science and Engineering
Ames, IA 50011

246. Malcolm G. McLaren
Head, Department of Ceramics
Rutgers University
Busch Campus
Bowser Road, Box 909
Piscataway, NJ 08854

247. Arthur F. McLean
Manager, Ceramics Materials
Department
Ford Motor Company
20000 Rotunda Drive
Dearborn, MI 48121

248. B. L. Mehosky
Development Engineer, R&D
Sohio Research and Development
4440 Warrensville Center Road
Cleveland, OH 44128

249. P. K. Mehrotra
Kennametal, Inc.
PO Box 639
Greensburg, PA 15601

250. D. Messier
U.S. Army Materials
Technology Laboratory
DRXMR-MC
Arsenal Street
Watertown, MA 02172

251. Arthur G. Metcalfe
Director, Research Department
Solar Turbines, Inc.
2200 Pacific Highway
PO Box 80966
San Diego, CA 92138

252. Thomas N. Meyer
Senior Technical Specialist
Alumina, Chemicals and
Ceramics Div.
Alcoa Aluminum Company of
America
Alcoa Technical Center
Alcoa Center, PA 15069

253. W. Miloscia
Sohio
Research and Development
4440 Warrensville Center Road
Cleveland, OH 44128

254. Bill Moehle
Ethyl Corporation
451 Florida Blvd.
Ethyl Tower
Baton Rouge, LA 70801

255. Helen Moeller
Babcock and Wilcox
PO Box 11165
Lynchburg, VA 24506

256. Peter E. D. Morgan
Member Technical Staff
Structural Ceramics
Rockwell International
Science Center
1049 Camino Dos Rios
PO Box 1085
Thousand Oaks, CA 91360

257. James I. Mueller
University of Washington
Ceramic Engineering Dept.,
MS FB10
Seattle, WA 98195

258. Solomon Musikant
General Electric Company
Space Systems Division
PO Box 8555, Mail Stop U-1219
Philadelphia, PA 19101

259. Pero Nannelli
Pennwalt Corporation
900 First Avenue, PO Box C
King of Prussia, PA
19406-0018

260. Dale E. Niesz
Manager, Materials Department
Battelle Columbus Laboratories
505 King Avenue
Columbus, OH 43201

261. William D. Nix
Stanford University
Dept. of Materials Science
and Engineering
Stanford, CA 94305

262. W. Richard Ott
New York State College of
Ceramics
Alfred University
Alfred, NY 14802

263. Muktesh Paliwal
GTE Products Corporation
Hawes Street
Towanda, PA 18848

264. Hayne Palmour III
North Carolina State
University
Engineering Research Services
Division
2158 Burlington Engineering
Laboratories
PO Box 5995
Raleigh, NC 27607

265. Joseph N. Panzarino
Norton Company
Director, R&D, High
Performance Ceramics
Goddard Road
Northboro, MA 01532-2545

266. Pellegrino Papa
Manager, Technical and
Business Development
Corning Technical Products
Division
Corning Glass Works
Corning, NY 14831

267. Arvid E. Pasto
Member of Technical Staff
Precision Materials
Technology
GTE Laboratories, Inc.
40 Sylvan Road
Waltham, MA 02254

268. James W. Patten, Director
Materials Engineering
Cummins Engine Company, Inc.
Box 3005, Mail Code 50183
Columbus, IN 47201

269. Dan Petrak
Babcock and Wilcox
PO Box 1260
Lynchburg, VA 24505

270. R. Byron Pipes
University of Delaware
Center for Composite Materials
2001 Spencer Laboratory
Newark, DE 19716

271. Robert C. Pohanka
Office of Naval Research
800 N. Quincy Street, Code 431
Arlington, VA 22217

272. Stephen C. Pred
Product Manager
ICD Group, Inc.
641 Lexington Avenue
New York, NY 10022

273. Karl M. Prewo
United Technologies Corporation
Research Center
Silver Lane, MS 24
East Hartford, CT 06108

274. Hubert B. Probst
Chief Scientist,
Materials Div., MS 49-1
NASA Lewis Research Center
21000 Brookpark Road
Cleveland, OH 44135

275. Carr Lane Quackenbush
Norton Company
High Performance Ceramics
Goddard Road
Northboro, MA 01532

276. George Quinn
U.S. Army Materials
Technology Laboratory
Arsenal Street
Watertown, MA 02172

277. Dennis T. Quinto
Kennametal, Inc.
Phillip M. McKenna Laboratory
PO Box 639
Greensburg, PA 15601

278. Dennis Readey
Department Chairman,
Ceramic Engineering
Ohio State University
2041 College Road
Columbus, OH 43210

279. Robert R. Reeber
U.S. Army Research Office
PO Box 12211
Research Triangle Park, NC
27709

280. K. L. Reifsnider
Virginia Polytechnic
Institute and State
University
Department of Engineering
Science and Mechanics
Blacksburg, VA 24061

281. K. T. Rhee
Rutgers University
College of Engineering
PO Box 909
Piscataway, NJ 08854

282. Roy W. Rice
W. R. Grace and Company
7379 Route 32
Columbus, MD 21044

283. David W. Richerson
Ceramatec, Inc.
163 West 1700 South
Salt Lake City, UT 84115

284. Paul Rieth
Ferro Corporation
661 Willet Road
Buffalo, NY 14218

285. Michael A. Rigdon
Babcock and Wilcox
1735 Eye Street, NW
Washington, DC 20006

286. John E. Ritter, Jr.
University of Massachusetts
Mechanical Engineering Dept.
Amherst, MA 01003

287. Giulio A. Rossi
Norton Company
High Performance Ceramics
Goddard Road
Northboro, MA 01532

288. Barry R. Rossing
Alcoa Aluminum Company of
America
Alcoa Technical Center
Alcoa Center, PA 15069

289. David J. Rowcliffe
SRI International
333 Ravenswood Avenue
Menlo Park, CA 94025

290. Donald W. Roy
Manager, Carbide and Optical
Material
Research and Development
Coors Porcelain Company
Golden, CO 80401

291. Bruce Rubinger
Gobal
50 Milk Street, 15th Floor
Boston, MA 02109

292. Robert Ruh
Air Force Wright Aeronautical Laboratory
Materials Laboratory, AFWAL/MLLM
Metals and Ceramics Division
Wright-Patterson AFB, OH 45433

293. Robert J. Russell, Sr.
Divisional Vice President, Technology and Planning
High Performance Ceramics
Norton Company
Goddard Street
Northboro, MA 01532

294. George P. Safol
Westinghouse Electric Corp.
R&D Center
Pittsburgh, PA 15235

295. J. Sankar
North Carolina Agricultural and Technical State University
Department of Mechanical Engineering
Greensboro, NC 27411

296. Maxine Savitz
Assistant to Vice President, Engineering
The Garrett Corporation
PO Box 92248
Los Angeles, CA 90009

297. Richard Schapery
Texas A&M University
Civil Engineering Department
College Station, TX 77843

298. L. J. Schioler
Aerojet Tech Systems Company
PO Box 13222
Dept. 9990, Bldg. 2001
Sacramento, CA 95813

299. Matthew Schreiner
Gas Research Institute
8600 W. Bryn Mawr Avenue
Chicago, IL 60631

300. John Schuldies
Industrial Ceramic Technology, Inc.
141 Enterprise Drive
Ann Arbor, MI 48103

301. R. B. Schulz
Department of Energy
Office of Transportation Systems
Forrestal Building CE-151
1000 Independence Avenue
Washington, DC 20585

302. Wesley J. C. Schuster
President
Thermo Electron Corporation
Metals Division
115 Eames Street, PO Box 340
Wilmington, MA 01887

303. Murray A. Schwartz
Bureau of Mines
2401 I Street, N.W.
Washington, DC 20241

304. Thomas M. Sebestyen
U.S. Army Tank-Automotive Command
AMSTA-RGRT
Warren, MI 48397-5000

305. Brian Seegmiller
Senior Development Engineer
Coors Porcelain Company
17750 North 32 Street
Golden, CO 80401

306. S. G. Seshadri
Research Associate
Sohio Engineered Materials Company
Niagara Falls R&D Center
PO Box 832
Niagara Falls, NY 14302

307. Peter T. B. Shaffer
Executive Vice President
Advanced Refractory Technologies, Inc.
699 Hertel Avenue
Buffalo, NY 14207

308\. Maurice E. Shank
Director, Engineering
Technology Assessment
United Technologies Corp.
Pratt and Whitney Engrg.
Div., MS 162-31
East Hartford, CT 06108

309\. Jack D. Sibold
Coors Porcelain Company
17750 North 32 Street
Golden, CO 80401

310\. Neal Sigmon
Appropriations Committee
Subcommittee on Interior and
Related Events
U.S. House of Representatives
Rayburn Building, Room B308
Washington, DC 20515

311\. Richard Silberglitt
DHR, Inc.
6849 Old Dominion Drive
Suite 228
McLean, VA 22101

312\. Maurice J. Sinnott
University of Michigan
Chemical and Metallurgical
Engineering
438 W. Engineering Building
Ann Arbor, MI 48109

313\. S. R. Skaggs
Los Alamos National Lab.
PO Box 1663
MS F-682, Program Office
Los Alamos, NM 87545

314\. J. Thomas Smith
Director, Precision
Materials Tech.
GTE Laboratories, Inc.
40 Sylvan Road
Waltham, MA 02254

315\. Jay R. Smyth
Senior Materials Engineer
Garrett Turbine Engine Co.
111 South 34th Street
Phoenix, AZ 85010

316\. Rafal Sobotowski
Sohio Research and
Development
3092 Broadway Avenue
Cleveland, OH 44115

317\. Boyd W. Sorenson
E. I. DuPont de Nemours & Co.
Planning Manager,
New Ventures Dept.
Wilmington, DE 19898

318\. Richard M. Spriggs
National Materials
Advisory Board
National Research Council
2101 Constitution Avenue
Washington, DC 20418

319\. M. Srinivasan
Sohio Engineered Materials Co.
Niagara Falls R&D Center
PO Box 832
Niagara Falls, NY 14302

320\. Gordon L. Starr
Manager, Metallic/Ceramic
Materials Dept.
Cummins Engine Company, Inc.
Box 3005, Mail Code 50183
Columbus, IN 47202-3005

321\. Harold L. Stocker, Manager
Low Heat Rejection Program
General Motors Corporation
Allison Gas Turbine Operations
PO Box 420, T-23
Indianapolis, IN 46206-0420

322\. Roger Storm, Director
Niagara Falls R&D Center
Sohio Engineered Materials Co.
PO Box 832
Niagara Falls, NY 14302

323\. E. E. Strain
Program Manager AGT-101
Garrett Turbine Engine Company
111 S. 34th Street
PO Box 5217, Mail Stop 301-2N
Phoenix, AZ 85010

324. Thomas N. Strom
NASA Lewis Research Center
21000 Brookpark Road, 77-6
Cleveland, OH 44135

325. Karsten Styhr
AiResearch Casting Company
19800 Van Ness Avenue
Torrance, CA 90509

326. Paul Sutor
425 Volker Blvd.
Kansas City, MO 64116

327. Lewis Swank
Ford Motor Company
PO Box 2053
Building SRL, Room E3172
Dearborn, MI 48121

328. Anthony C. Taylor
Staff Director, Subcommittee
on Transportation, Aviation,
& Materials
Committee on Science and
Technology
U.S. House of Representatives
Rayburn Building, Room 2321
Washington, DC 20515

329. W. H. Thielbahr
Chief, Energy Programs Branch
Department of Energy
Idaho Operations Office
550 2nd Street
Idaho Falls, ID 83401

330. John K. Tien
Director of Center for
Strategic Materials
Columbia University
1137 SW Mudd Building
New York, NY 10027

331. T. Y. Tien
University of Michigan
Materials and Metallurgical
Engineering
Dow Building
Ann Arbor, MI 48109-2136

332. Nancy J. Tighe
National Bureau of Standards
Inorganic Materials
Division 420
Building 223, Room A331
Gaithersburg, MD 20899

333. Julian M. Tishkoff
Air Force Office of
Scientific Research
Directorate of Aerospace
Sciences
Bolling AFB
Washington, DC 20332

334. Maurice L. Torti
Senior Scientist
High Performace Ceramics
Norton Company
Goddard Road
Northboro, MA 01532-2545

335. Louis E. Toth
National Science Foundation
Division of Materials Research
1800 G Street, NW
Washington, DC 20550

336. Richard E. Tressler
Chairman, Ceramic Science and
Engineering Department
The Pennsylvania State
University
201 Steidle Building
University Park, PA 16802

337. Donald R. Uhlmann, Professor
Ceramics and Polymers
Department of Materials
Science and Engrg.
Massachusetts Institute of
Technology
Cambridge, MA 02139

338. Thomas Vasilos, Manager
Electro Chemical Facility
Avco Corporation
201 Towell Street
Wilmington, MA 01887

339. V. Venkateswaran
Sohio Engineered Materials Co.
PO Box 832
Niagara Falls, NY 14302

354. Charles Zeh
Department of Energy
Morgantown Energy Technology
Center
PO Box 880
Morgantown, WV 26505

355. Klaus M. Zwilsky
Executive Director
National Materials Advisory
Board
National Research Council
2101 Constitution Avenue
Washington, DC 20418

356. Department of Energy
Oak Ridge Operations Office
Office of Assistant Manager
for Energy Research and
Development
PO Box E
Oak Ridge, TN 37831

357– 384. Department of Energy
Technical Information Center
Office of Information Services
PO Box 62
Oak Ridge, TN 37831

For distribution by microfiche
as shown in DOE/TIC-4500,
Distribution Category UC-95
(Energy Conservation).

340. John B. Wachtman, Jr.
Director, Center for Ceramics Research
Rutgers University
PO Box 909
Piscataway, NJ 08854

341. Richard B. Wallace
Manager, Government Research and Development Programs
General Motors Corporation
Detroit Diesel Allison Division
36880 Ecorse Road
Romulus, MI 48174

342. Harlan L. Watson
Subcommittee on Energy Research and Production
U.S. House of Representatives
Committee on Science and Technology
Rayburn Building, Suite 2321
Washington, DC 20515

343. Steven G. Wax
Department of Defense
Advanced Research Projects Agency
Materials Science Division
1400 Wilson Boulevard
Arlington, VA 22209

344. Albert R. C. Westwood
Corporate Director, R&D
Martin Marietta Laboratories
1450 South Rolling Road
Baltimore, MD 21227

345. Sheldon M. Wiederhorn
U.S. Department of Commerce
National Bureau of Standards
Inorganic Materials Division
Mechanical Properties Group
Gaithersburg, MD 20899

346. Roger Wills
TRW, Inc.
Automotive Worldwide Sector, Valve Division
Cleveland, OH 44110

347. J. M. Wimmer
Supervisor, Nonmetallic Materials Group
Garrett Turbine Engine Company
111 S. 34th Street
PO Box 5217
Phoenix, AZ 85010

348. David Wirth
VP, Technical Operations & Engineering
Coors Porcelain Company
17750 North 32 Street
Golden, CO 80401

349. Thomas J. Wissing
Manager, Government Contract Administration
Eaton Corporation
Engineering & Research Center
26201 Northwestern Highway
PO Box 766
Southfield, MI 48037

350. James C. Wood
NASA Lewis Research Center
21000 Brookpark Road
MS 500-210
Cleveland, OH 44135

351. Hun C. Yeh
Ceramic Supervisor
AiResearch Casting Company
19800 Van Ness Avenue
Torrance, CA 90509

352. Thomas M. Yonushonis
Cummins Engine Company, Inc.
Box 3005, Mail Code 50183
Columbus, IN 47202-3005

353. Don Zabierek
Air Force Wright Aeronautical Laboratory
AFWAL/POTC
Wright-Patterson AFB, OH 45433